



TECHNISCHE UNIVERSITÄT MÜNCHEN
TUM School of Engineering and Design

Fast Multipole Boundary Element Techniques for Acoustic and Vibroacoustic Problems

Christopher Jelich

Vollständiger Abdruck der von der TUM School of Engineering and Design der
Technischen Universität München zur Erlangung des akademischen Grades eines

Doktors der Ingenieurwissenschaften (Dr.-Ing.)

genehmigten Dissertation.

Vorsitzender: Prof. Dr.-Ing. Wolfgang A. Wall
Prüfer der Dissertation: 1. Prof. Dr.-Ing. Steffen Marburg
2. Prof. Dr. rer. nat. Matthias Voigt

Die Dissertation wurde am 15.03.2022 bei der Technischen Universität München eingereicht
und durch die TUM School of Engineering and Design am 08.08.2022 angenommen.

Abstract

Computational methods that precisely describe the acoustic and elastodynamic wave propagation are an important tool of engineers. They allow to accurately predict vibroacoustic quantities such as the radiated sound power and the transmission loss ahead of production. Finite element and boundary element methods constitute a powerful measure in this regard. They facilitate a cost efficient design process of various technical products such as industrial machines, aircraft engines and noise barriers. Despite ongoing research efforts, limitations of these methods are still present today. First, the full-scale analysis of periodic structures necessitates substantial computational effort with currently available techniques. Second, discretizations of parameterized structural acoustic problems lead to linear systems with parameter and implicit frequency dependence. Their repeated evaluation for all parameter and frequency values of interest is laborious. Lastly, existing methods lack efficient strategies for boundary element discretized acoustic problems with multiple load cases.

This cumulative thesis presents accurate and efficient numerical formulations for acoustic and vibroacoustic analyses that address the aforementioned limitations. Two novel fast multipole boundary element formulations for the acoustic analysis of finite periodic structures are developed. They allow to analyze large-scale periodic arrangements in three dimensional space with quasi-linear complexity in time and memory. In contrast to existing approaches, the incident wave field and the solution are neither required to be periodic nor quasi-periodic. Furthermore, a greedy reduced basis scheme for parameter and implicitly frequency dependent structural acoustic problems is introduced. It approximates the solution within the discretized parameter domain by a linear combination of the responses of the high-fidelity system at a few parameter samples. Contrary to most of the existing techniques, the presented algorithm does not rely on an a priori choice but chooses the samples iteratively based on a greedy choice. Lastly, the use of iterative solvers for the solution of boundary element discretized acoustic problems with multiple load cases is evaluated. The performance of three variants is compared and recommendations on their choice are given based on the study of two numerical examples.

Altogether, the presented computational methods constitute an efficient strategy to evaluate parameter and implicitly frequency dependent vibroacoustic systems, to solve problems with multiple load cases and to evaluate the acoustic scattering by finite periodic structures. Their performance is assessed on the basis of a noise barrier design study, the analysis of a satellite structure subject to a diffuse sound field, the prediction of aeroacoustic noise and the eigenvalue analysis of an acoustic metamaterial.

Kurzzusammenfassung

Die numerische Berechnung von akustischen und elastodynamischen Wellenausbreitungsphänomenen ist eine wichtige Methodik in Wissenschaft und Industrie. Sie erlaubt es, strukturalakustische Eigenschaften wie die abgestrahlte Schalleistung oder das Schalldämmmaß weit vor der Prototypenfertigung zu bestimmen. Die Finite Elemente und Randelementmethode haben sich in diesem Zusammenhang bewährt, ermöglichen sie doch eine zeit- und kosteneffiziente Entwicklung technischer Produkte in Bereichen wie dem Maschinenbau, Flugzeugbau und Verkehrswesen. Trotz des immerwährenden wissenschaftlichen Fortschritts sind die Einsatzmöglichkeiten der Methoden limitiert. Zum einen geht die akustische Berechnung von großskaligen, dreidimensionalen Strukturen mit einem erheblichen Rechenaufwand einher. Des Weiteren führt die Diskretisierung von parametrisierten strukturalakustischen Systemen zu Gleichungssystemen, die parameter- und implizit frequenzabhängig sind. Ihre wiederkehrende Auswertung für eine Vielzahl von Parameter- und Frequenzwerten ist mit untragbarem Aufwand verbunden. Außerdem werden effiziente iterative Gleichungslöser für akustische Randelementsysteme mit einer Vielzahl an rechten Seiten benötigt.

Die vorliegende Arbeit präsentiert robuste und effiziente numerische Verfahren für akustische und strukturalakustische Berechnungen, welche die vorher genannten Limitierungen bestehender Methoden beseitigt. Es werden zwei innovative Fast Multipol Randelementformulierungen für die akustische Berechnung von periodischen Strukturen vorgestellt. Sie ermöglichen die Berechnung von großskaligen, periodischen Anordnungen im dreidimensionalen Raum mit quasi-linearem Zeit- und Speicherbedarf. Im Gegensatz zu bestehenden Verfahren erfordern die entwickelten Formulierungen keine Periodizität der Anregung oder des Lösungsfelds. Des Weiteren wird ein Verfahren zur Modellordnungsreduktion von parameter- und implizit frequenzabhängigen strukturalakustischen Systemen präsentiert. Das Verfahren approximiert die Lösung im diskretisierten Parametergebiet durch eine Linearkombination von Lösungen des Ausgangssystems für einige wenige Parameterwerte. Im Gegensatz zu bestehenden Methoden werden diese Auswertepunkte nicht a priori gewählt, sondern iterativ durch den Algorithmus selbst. Abschließend werden drei iterative Gleichungslöser zur Lösung von akustischen Randelementsystemen mit vielen rechten Seiten anhand von zwei numerischen Beispielen untersucht und verglichen.

Insgesamt stellen die entwickelten numerischen Verfahren eine effiziente Strategie zur Lösung von Systemen mit Parameter- und impliziter Frequenzabhängigkeit, mit einer Vielzahl an unterschiedlichen Lastfällen und mit periodischen Geometrien dar. Die Leistungsfähigkeit der Methoden wird anhand von Anwendungsbeispielen aufgezeigt. Diese umfassen die akustische Bewertung von Schallschutzwänden, die Analyse einer Satellitenstruktur in einem diffusen Schallfeld, die Abschätzung der Schallabstrahlung eines umströmten Tragflächenprofils und die Lösung eines nichtlinearen Eigenwertproblems.

Danksagung

Meine Zeit am Lehrstuhl für Akustik mobiler Systeme der Technischen Universität München war vor allem von schönen, lustigen und lehrreichen Momenten geprägt. Ein großes Danke gebührt von Herzen all den lieben Mitmenschen, die innerhalb und außerhalb des akademischen Umfeldes sowohl im Großen als auch im Kleinen diese Momente ermöglicht haben.

Ein besonderer Dank gilt meinem Doktorvater Prof. Dr.-Ing. Steffen Marburg für das Vertrauen, das er in mich gehabt hat. Ich bin insbesondere dankbar für den großen Gestaltungsfreiraum, den du mir eingeräumt hast und die vielen Gestaltungsmöglichkeiten, die du mir aufgezeigt hast.

Besonders bedanke ich mich auch bei Prof. Dr. Matthias Voigt. Zum einen für die Übernahme des Zweitgutachtens, zum anderen für den stets lehrreichen Austausch mit dir und deinen erfrischend mathematischen Blick auf unsere Ingenieursproblemstellungen.

Danke an Prof. Dr.-Ing. Wolfgang A. Wall für die Übernahme des Prüfungsvorsitzes und die äußerst angenehme Prüfungsatmosphäre.

Ein großer Dank gebührt darüber hinaus allen Kolleginnen und Kollegen des Lehrstuhls, die mir auch in turbulenten Zeiten immer in offener und herzlicher Weise entgegengekommen sind. Hervorheben möchte ich Suhaib Koji Baydoun-Hidding. Obwohl unsere Sichtachse durch unsere Bildschirme getrennt war, warst du stets für einen kurzen – oder oftmals auch längeren – Austausch offen. Danke dir, Koji, für die kleinen Ablenkungen im Arbeitsalltag und die vielen lustigen Momente.

Im Hinblick auf die etlichen organisatorischen Belange richte ich einen weiteren Dank an die Kollegen, die sich in einer aufopfernden Hingabe und einem entsprechenden Zeitaufwand um die IT des Lehrstuhls gekümmert haben und weiterhin kümmern. Mein Dank gilt auch den Kolleginnen im Sekretariat für ihre allzeit vertrauensvolle Unterstützung.

I express my deepest gratitude to Prof. Nicole Kessissoglou, Prof. Marion Burgess and Michael Burgess for their hospitality and support during my research stay in Sydney. Nicole, I'm very thankful for your time, guidance and support. I highly value the time that I have spent with your group at the University of New South Wales. Thank you very much for this opportunity. Marion and Michael, your hospitality is tremendous. I thoroughly enjoyed every day that we have spent together and am grateful for your trust, patience and generosity.

Mein größter Dank gilt meinen Freunden und meiner Familie. Ihr bereichert mein Leben in so unbeschreiblicher Weise. Ich bin euch von Herzen dankbar für euer Vertrauen, euren Rückhalt und jeden wundervollen Moment, den wir zusammen verbringen.

Contents

1	Introduction	1
1.1	State of the art	2
1.1.1	Fast boundary element methods	2
1.1.2	Periodic structures and acoustic metamaterials	3
1.1.3	Parameter dependent structural acoustic problems	5
1.1.4	Iterative solvers of linear systems with many right-hand sides	6
1.2	Contributions and accomplishments	7
2	Governing equations and numerical methods	9
2.1	Wave equations of linear acoustics and elastodynamics	9
2.1.1	Linear time-harmonic acoustics	9
2.1.2	Linear time-harmonic elastodynamics	10
2.2	Acoustic boundary element method	12
2.2.1	Boundary element formulation	12
2.2.2	Fast multipole method	14
2.2.3	Periodic boundary element formulation	17
2.3	Parameterized structural acoustic problems	20
2.3.1	Fully coupled FEM-BEM formulation	20
2.4	Structural acoustic problems with many right-hand sides	21
2.4.1	Diffuse sound field excitation	22
2.4.2	Nonlinear acoustic eigenvalue analysis	23
2.4.3	Block Krylov subspace methods	24
2.4.4	Global Krylov subspace methods	25
3	Summary of publications	27
3.1	Paper A	29
3.2	Paper B	31
3.3	Paper C	33
4	Discussion and conclusion	35
	Bibliography	39
A	Appended publications	55
A.1	Paper A	57
A.2	Paper B	83
A.3	Paper C	107

1 Introduction

The pressure fluctuations around the ambient atmospheric pressure in a fluid is what we understand as sound. Whether the sound that we perceive is delightful, pleasant, distracting or even hurtful, is subjective to every human being. Although our body is capable of centering our attention away from unwanted sound, the pressure fluctuations themselves might still inflict damage on our ears, harm our health or impair our well-being. Avoiding the exposition to unwanted sound – or in other words noise – is a task that we follow daily in our life. Be it the use of noise canceling headphones when commuting, closing the windows the minute the neighbor starts mowing the lawn or covering our ears when an ambulance passes by. Various factors determine the success of these actions. In most cases, mitigation efforts are best to take place close or directly at the noise source. Designing quieter aircraft engines and automotive vehicles or constructing more efficient noise barriers benefits all of us without the need to take everyday actions as an individual [1, 2].

Similar to the mitigation of noise, the precise design of sound impressions has a great influence on our daily life. The sound that a product emits controls how we perceive its quality. The way a car's door closes, the clicking of a button or the clink of two glasses are signs of quality. Designing a product that holds up to high standards thus goes hand in hand with mitigating unpleasant audio impressions and creating a sound characteristic that leads to an appearance of high value [3]. Aside from its importance in our daily life, sound can also inflict damage on structural components. The launch of spacecrafts generates intense acoustic noise that excites the surrounding structural components including the payload consisting of satellites and delicate measurement equipment [4]. Assessing the noise levels upfront and introducing measures for their attenuation is vital for the success of the whole operation.

These examples fundamentally show that the mitigation of noise and the specific design of vibrating structures are key tasks within the product development process. An essential requirement is the knowledge of the acoustic and vibroacoustic properties of the product ahead of production. Assessing them in the early design stages is crucial since applying changes in the later stages becomes increasingly expensive. Performing experimental investigations early on, however, is only seldom possible or vastly laborious. This is where numerical methods represent a remedy. The number of different designs that can be evaluated are tremendous and simplify reaching well-founded design decisions. Many noise and vibration complaints of prototypes and of the final product can be resolved upfront. The need of expensive modifications introduced in the later design stages is anticipated and eliminated.

The overarching goal of this thesis is to develop accurate and robust computational methods within the fields of acoustics and vibroacoustics. With the ongoing development of numerical algorithms, the quantity of techniques is manifold. They range from analytical models [5, 6] that generate solutions in an instant to sophisticated numerical models [7–9] that are tailored to supercomputers and address immensely large models. Often, analytical models are a good measure to gain a first impression of a system's behavior but they are seldom applicable to complex geometries. On the other hand, the availability of supercomputers is limited. Hence, the focus of the this work lies on developing methods that are capable of solving engineering problems of today and tomorrow on widely available computer architectures. Three specific applications are considered in this regard: The acoustic analysis of periodic structures such as noise barriers and metamaterials, the solution of parameterized structural acoustic problems which are omnipresent within the product development process and the calculation of the acoustic responses to multiple load cases emerging from a turbulent boundary layer excitation.

1.1 State of the art

The following sections review the state of the art of the numerical methods that represent the foundation of this work. This includes finite element and boundary element formulations for acoustic and structural acoustic problems in unbound domains. In addition, an overview of the recent developments in modeling acoustic metamaterials is given and solution techniques for parameterized vibroacoustic problems are reviewed. Finally, iterative solvers for applications that involve multiple load cases are presented and the contributions of this thesis to the fields of acoustics and vibroacoustics are summarized.

1.1.1 Fast boundary element methods

The boundary element method (BEM) is an established and widely used numerical technique to solve linear time-harmonic acoustic problems [10, 11]. Its starting point is the weak formulation of the Helmholtz equation. Subsequent to integrating twice by parts, the fundamental solution or Green's function is identified as weight functions. This choice leads to the Kirchhoff-Helmholtz integral equation which solely consists of integrals over the boundary of the computational domain [12]. Therefore, only the boundary needs to be discretized and the problem's dimension is reduced by one. In addition, the Sommerfeld radiation condition is implicitly fulfilled, making the BEM especially attractive for exterior problems [10]. The boundary element discretization typically yields a system of linear equations with lower numbers of degrees of freedom N_{dof} compared to the finite element method (FEM). However, the system matrices are generally dense and implicitly frequency dependent [13]. Various textbooks introduce the BEM and discuss the details of the mathematical formulation, the computational framework and its applications [14–17].

Despite its advantages, the requirement of assembling the dense boundary element matrices restricts the application of the BEM. Only small-scale problems can be considered since the assembly and iterative solution of the corresponding system of linear equations requires order $\mathcal{O}(N_{\text{dof}}^2)$ operations [18]. Fortunately, fast boundary element techniques have emerged over the last decades. They utilize that certain matrix blocks within the generally dense boundary element system matrix admit a low-rank approximation [19]. This leads to a compression of the system matrices and reduces the asymptotic complexity of matrix-vector products to order $\mathcal{O}(N_{\text{dof}} \log(N_{\text{dof}}))$ in time and to order $\mathcal{O}(N_{\text{dof}})$ in memory at best [20, 21]. Fast boundary element techniques can be purely algebraic such as the hierarchical matrices (\mathcal{H} -matrices, [22, 23]) which perform an adaptive cross approximation (ACA, [24, 25]) of the low-rank matrix blocks. Others rely on an analytical approximation of the Green's function such as the fast multipole method (FMM, [26, 27]) and the precorrected fast Fourier transform (pFFT, [28]). In addition, wavelet-based methods exist which introduce an approximation based on wavelet transform matrices [29, 30]. A performance comparison between fast boundary element techniques is a challenging task. Most schemes share the same asymptotic complexity with a slight difference in the corresponding constant depending on their numerical implementation and the investigated problem [31].

The thesis at hand utilizes the fast multipole method which was originally introduced as a numerically scheme to evaluate the pair-wise interactions between large numbers of bodies [26]. Such interactions can be found in various fields including molecular dynamics [32], celestial mechanics [26], electromagnetics [33] but also acoustics [34]. In fact, the FMM efficiently accelerates the solution of the discretized Kirchhoff-Helmholtz boundary integral equation as demonstrated by Rokhlin [27] for two-dimensional problems and by Greengard et al. [34]

for three-dimensional problems. Since then, various variants of the FMM have been proposed [35–38]. They employ either a single-level or multi-level subdivision of the computational domain in order to identify clusters of degrees of freedom that are separated by a characteristic distance. Interactions between these degrees of freedom are called far-field interactions. For these, a multipole series expansion approximates the Green’s function in the corresponding boundary integral terms. In contrast, the remaining near field interactions between closely located clusters utilize the exact Green’s function. The additional approximation error is controlled by the number of terms n_t of the series expansion. Considering a large number of terms leads to more accurate results at the cost of an increased computational effort [39]. The low-frequency FMM [40, 41] scales order $\mathcal{O}(n_t^5)$ in time, whereas variants based on exponential plane-wave expansions scale of order $\mathcal{O}(n_t^3)$ in time [42, 43]. The multipole expansions of both variants are instable in the high-frequency region. In this case, either high-frequency variants [44–47] or broadband FMMs [37, 48, 49] can be used. The latter feature stable expansions at both low and high frequencies. Since most FMMs rely on specific series expansions of the Green’s function, they are tailored to specific problem types. In the case of half-space problems, a series expansion of the half-space Green’s function is employed in conjunction with a slightly modified geometric subdivision of the computational domain [50, 51].

Today, obtaining the solution of the boundary element discretized Helmholtz equation in quasi-linear time does not imply a significant challenge anymore. Recent improvements focus on high-performance computing [52–55], model order reduction [56–61], eigenvalue analysis [62, 63], layered media [64, 65], symmetry [51, 66] and periodicity [67–69]. The particular emphasize of the present work lies on introducing an efficient model order reduction technique, accelerating acoustic eigenvalue analyses and developing two periodic boundary element formulations.

1.1.2 Periodic structures and acoustic metamaterials

Periodic structures consist of a representative unit cell that is repeated an infinite amount of times in one or more directions of periodicity. They feature unusual acoustic properties due to the multiple scattering between the unit cells [70]. Whenever the unit cell is about half a wavelength in size, the destructive interference of the incident and scattered wave fields prohibits wave propagation at and around the corresponding frequency, the so-called Bragg frequency [71]. These frequency bands are denoted as stop bands and the periodic structures are termed phononic or sonic crystals [72]. The required length scale of the unit cell that is necessary to excite Bragg resonances, however, prevents a competitive manipulation of the wave propagation at low frequencies. Introducing local resonances to the unit cell design remedies this by creating band gaps that are an order of magnitude below the first Bragg frequency. In this spectrum, the propagation of sound waves is dominated by the acoustic behavior of a single unit cell [71]. Acoustic metamaterials with remarkable properties usually combine the destructive interference around the Bragg frequencies with the local resonances of the unit cells [73]. They are very efficient in modifying the propagation of sound waves in fluids [74, 75] and achieve an extraordinary sound attenuation [70, 76]. Modifying the size of the unit cell replications and their geometry influences the position and width of the stop bands, whereas adjusting the topology of the unit cell changes the local resonances and thus the position and width of the band gaps [77].

Acoustic metamaterials have been successfully employed in several applications over the last decade. This includes aircrafts [78], automobiles [79], sound absorbers [80], buildings [81]

and operas [82] to name but a few. A further promising application are noise barriers. With the increase in urbanization and population growth, railways and motorways inevitably get closer to commercial and residential areas leading to higher levels of noise exposition [83]. This asks for highly effective and compact structures that are capable of providing broadband noise attenuation since traffic-induced noise is present in a wide range of frequencies [84]. Road noise for instance is dominant between 700 Hz and 1300 Hz [85]. Various designs based on acoustic metamaterials have been proposed within the scientific community [86]. The periodic arrangement of cylindrical columns [75, 87, 88] and hollow, slotted, cylindrical tubes, so-called c-shapes [77, 89, 90], are commonly investigated. However, broadband attenuation usually requires more advanced designs. Van der Aa and Forssén [91] investigated the effect of inserting a porous core into perforated cylindrical tubes, whereas Fard et al. [92] embedded local resonators into a classic wall-like noise barrier design. A combination of sonic crystals and wall-like noise barriers is proposed and evaluated by Koussa et al. [93]. A significant broadband transmission loss can be realized by utilizing overlapping resonance effects [94–97]. This has been demonstrated by means of a railway noise barrier design [98]. Only achieving a broadband transmission loss allows the use of acoustic metamaterials as noise barriers since existing concepts with geometric variations of the top edge [99] or absorbing materials [100] are very well designed and competitive.

In order to quantify the performance of these designs, efficient numerical techniques need to be available. Assessing the acoustic behavior within a frequency range of interest requires the solution of the Helmholtz equation at distinct frequencies. Its solution can be found by the finite element method (FEM) [89, 101], the boundary element method (BEM) [102, 103], the multiple scattering theory [104] and the plane wave expansion [73]. Infinite periodic structures, although only existent as a numerical model and not present in reality, can be accurately described by a single unit cell. Applying Floquet-Bloch boundary conditions to the boundaries at which the unit cell is periodically repeated covers all possible modes of wave propagation [73]. These modes are then obtained by solving multiple eigenvalue problems within the irreducible Brillouin zone. Visualizing the dispersion curves indicates the frequency gaps at which wave propagation is eliminated [72]. Among others, the FEM [105] and the BEM [106, 107] can be employed for the discretization of the unit cell. In the case of the BEM, the eigenvalue problems are nonlinear due to the implicit frequency dependence of the system matrices. Although several powerful techniques of the last couple of years address this issue [108–110], their application is still challenging due to the difficult choice of the algorithmic parameters.

Aside from characterizing the acoustic performance in dispersion curves, the response to a given incident sound wave field is a very valuable information within the design process. This response can be found based on a discretization of a single unit cell when the assumption of quasi-periodic incident wave fields, scattering wave fields and boundary conditions is valid. The corresponding numerical model includes periodic boundary conditions at the unit cell boundaries perpendicular to the direction of periodicity as in the periodic FMM [111] and the periodic BEM [112]. The latter includes an infinite sum of Green's functions which leads to the quasi-periodic BEM [92, 113] when truncated with adequate choices of the truncation number reported by Jean and Defrance [87]. Approximating the truncated sum of Green's functions by fast multipole expansions further accelerates this scheme [114–116]. Otani and Nishimura [117] presented a corresponding approach for the two-dimensional Helmholtz equation that was later on extended to the three-dimensional case [68, 118].

The aforementioned approaches are of limited use for the analysis of periodic structures that are of finite extent. They neglect reflections from the ground and scattering effects at the edges of the finite periodic structure. This drawback is shared by the commonly employed two-

dimensional [77, 89, 98] and 2.5-dimensional modeling approaches [119]. Whenever these effects are of interest, full-scale acoustic analyses are necessary which entail enormous computational efforts. Recently, Karimi et al. [102] introduced a sophisticated boundary element formulation for the three-dimensional acoustic analysis of finite periodic structures. The formulation leads to boundary element matrices that are multilevel block Toeplitz matrices [120]. These are nested matrices with constant matrix blocks along each diagonal [121]. The number of levels corresponds to the number of directions of periodicity [90]. This exact representation of the system matrix reduces the scaling of the memory usage to order $\mathcal{O}(n_{\text{dof}}^2 n_{\text{cell}})$ with n_{dof} denoting the number of degrees of freedom per unit cell and n_{cell} denoting the number of unit cell repetitions. Further, the scaling of the assembly and matrix-vector operations is reduced to order $\mathcal{O}(n_{\text{dof}}^2 n_{\text{cell}} \log(n_{\text{cell}}))$ in time. Despite the significant reduction, the application of this formulation is still limited to finite periodic structures with small values of n_{dof} due to the associated quadratic complexity in memory and time. Amado-Mendes et al. [122] applied a similar concept to a finite periodic array of acoustic scatterers using a boundary element formulation based on hierarchical matrices. Although their approach effectively lowers the assembly time and memory usage, it does not succeed in accelerating the corresponding matrix-vector products. Efficient solution strategies for large-scale finite periodic structures are still missing.

1.1.3 Parameter dependent structural acoustic problems

The boundary element discretization of the Helmholtz equation leads to a system of linear equations that is implicitly frequency dependent. Evaluating the solution over a broad frequency range requires elaborate recalculations of the coefficient matrices at each frequency point of interest. This imposes substantial computational efforts which can be reduced by model order reduction techniques. Early approaches consist of assembling the boundary element system matrices only at a few sample points and interpolating in between [123–125] or performing a frequency interpolation of the Green's function itself [126]. More recently, Xie and Liu [56] proposed an approach based on a Taylor approximation of the Green's function. The resulting frequency-decoupled system matrices can then be reduced by a second order Arnoldi scheme. This approach has also been applied to FEM-BEM coupled linear systems [57] and equipped with an error estimator [60]. In addition, employing the Cauchy integral representation of the boundary element matrices leads to a rational approximation which enables fast frequency sweeps [58, 63, 127].

Aside from the frequency dependence, additional parameter dependencies can be considered. This is especially useful when evaluating a variety of different designs in the product development process. In the case of fully coupled problems, each physics domain can be addressed individually [128]. Finite element discretizations of the equation of linear elastodynamics lead to a second order dependence on the frequency which allows to reduce its frequency independent system matrices by Krylov subspace methods [129] or modal reduction [130]. However, considering additional parameters might lead to a non-affine representation, rendering the aforementioned approaches infeasible. A more general approach is represented by the discrete empirical interpolation method (DEIM). It approximates nonlinear parameter dependencies by an affine representation based on a few evaluations of the original system [131]. This allows to apply a range of projection-based parametric model order reduction (pMOR) schemes [132]. They reduce the number of degrees of freedom of the linear system in order to accelerate the solution process while adding only a small error to the approximate solution [133]. Negri et al. [134] applied the matrix DEIM to a finite element discretized Helmholtz problem with dependencies on the frequency and four geometry

parameters. Although Casenave et al. [135] present a successful application of the DEIM to the frequency dependent boundary element matrices, there is no indication in literature of applications to FEM-BEM coupled structural acoustic problems.

An alternative class of MOR techniques are reduced basis methods. They utilize that the solutions of the parameterized FEM-BEM system lie in lower-dimensional manifolds [136] due to the analytical parameter dependence [137]. Therefore, the solution can be expressed by superposing a small number of basis vectors [138]. The Proper Orthogonal Decomposition (POD) method evaluates the responses at a priori chosen sampling points within the parameter space. Concatenating the solution vectors and performing a singular value decomposition (SVD) yields singular vectors that can be utilized as basis vectors [139]. In contrast, greedy algorithms iteratively build a reduced basis and employ an optimality criterion for choosing the sampling points [140]. The basis vectors are simply represented by the system's response at these points. Once the reduced basis is constructed, approximate solutions at a possibly large number of new parameter values can be evaluated by a linear combination of the basis vectors [141]. Jiang et al. [142] built a reduced order model of the boundary element discretized Helmholtz equation using a POD scheme. Without an in-depth understanding of the system's behavior, the a priori sampling of the frequency domain represents a non-optimal choice. Baydoun et al. [61] showed that employing a greedy reduced basis method resolves this drawback and leads to small reduced order models of the frequency dependent boundary element system. Unfortunately, this approach requires the assembly and storage of the FEM-BEM system at all parameter samples of interest. This renders the approach infeasible for problems with high-dimensional parameter spaces. Casenave et al. [143] provides a remedy by combining the greedy reduced basis scheme with the empirical interpolation method. Alternatively, the approach of Hesthaven et al. [144] provides a bound to the memory usage and resolves the curse of dimensionality. The latter is followed in this work and a greedy reduced basis scheme for parameter and implicit frequency dependent vibroacoustic problems is presented. Particular emphasis lies on problems with many right-hand sides which are seldom covered in existing MOR techniques [145].

1.1.4 Iterative solvers of linear systems with many right-hand sides

Many engineering problems lead to systems of linear equations with multiple right-hand sides, so-called sequences of linear systems. They do not only arise in data analysis [146], Gaussian process modeling [147] and electromagnetics [148] but also in acoustic applications such as the optimization of high-intensity focused ultrasonic transducers [149] and the analysis of diffuse incident sound fields [150]. Recent advances of nonlinear eigenvalue solvers based on contour integration give rise to an additional application. The main computational burden of these eigensolvers lies in obtaining the solution of many sequences of linear systems [108–110]. Improving the computational efficiency of the solution process has the potential to significantly accelerate the estimation of the eigenvalues and eigenvectors [63].

Systems of linear equations can be solved by either direct or iterative solvers. The former scale of order $\mathcal{O}(N_{\text{dof}}^3)$ in time considering a dense boundary element system. This restricts their application to problems with small numbers of degrees of freedom. They additionally require that the system matrix admits a factorization which is associated with substantial computational efforts for the fast multipole BEM [8]. Hence, large-scale boundary element simulations using the FMM rely on iterative solvers of which Krylov subspace methods are the most commonly used techniques [151]. In each iteration, they obtain an approximate solution by minimizing the current residual over a Krylov subspace. This subspace is built

iteratively and spanned by the initial residual and additional vectors that are the result of repeated multiplications of the initial residual with the system matrix. Many different variants exist and the optimal choice depends on the specific problem type and the available memory. Marburg and Schneider [152] compared the performance of four different Krylov subspace solvers applied to the boundary element discretized Helmholtz equation. Their study indicates that the Generalized Minimal Residual (GMRes, [153]) method is the preferable technique and that the convergence behavior is highly influenced by the wavenumber, boundary conditions and surface smoothness. Yasuda et al. [154] highlighted the effect of the chosen boundary element formulation on the convergence which was studied in great detail by Marburg [155]. More recently, Marchand et al. [156] analyzed the effect of the frequency on the number of GMRes iterations for scattering objects containing cavities. Besides the particular choice of the Krylov subspace solver, the preconditioning of the linear system has a great influence on the solution time [157]. Gumerov and Duraiswami [37] proposed a low-accuracy fast multipole scheme as a preconditioner within the flexible inner-outer GMRes algorithm introduced by Saad [158]. This scheme belongs to the class of algebraic preconditioners and is also applicable in the case of the hierarchical BEM [159]. Other methods include the sparse approximate inverse [160] and the inverse fast multipole method [161]. In contrast, analytical preconditioners do not require the access to the discretized system of linear equations but are based on the boundary integral operators itself. Examples are the OSRC preconditioning [162] and the Calderón preconditioning [163].

Considering sequences of linear systems, standard Krylov subspace solvers can be applied sequentially to each linear system. The solution to each right-hand side is obtained individually without carrying over information of previous solution processes. Significant improvements of the solution time can be realized by more sophisticated methods, namely by seed, recycling, global and block Krylov subspace methods [164]. Seed methods solve the first system within the sequence of linear systems and store the generated Krylov subspace. The residuals of the remaining linear systems are then projected onto this subspace which often leads to a good approximate solution [165]. Recycling methods additionally augment or deflate the subspace or both [166, 167]. Their efficiency in solving the finite element discretized Helmholtz equation and the boundary element discretized Maxwell's equations is demonstrated in [168] and [169, 170], respectively. Instead of sequentially solving each system, global and block Krylov solvers obtain the solution to all right-hand sides simultaneously [164, 171]. Their advantage lies in performing more computationally efficient matrix-matrix multiplications and building much larger Krylov subspaces which usually yield solutions in less iterations [172, 173]. Malhotra et al. [174] solved the finite element discretized Helmholtz equation by means of the block quasi minimal residual method, whereas Calandra et al. [175] and Elman et al. [168] employed the block GMRes method. Successful applications to the boundary element discretized Helmholtz equation are limited to the work of Zheng et al. [62] which rely on a block Induced Dimension Reduction (block IDR(s), [176]) scheme. The proper choice of the Krylov subspace method for boundary element discretized Helmholtz problems with multiple right-hand sides is still unclear.

1.2 Contributions and accomplishments

This cumulative thesis contributes to the fields of computational acoustics and vibroacoustics. Three peer-reviewed publications form the core of this work, introducing accurate and robust computational methods that efficiently address the application cases highlighted at the

beginning of [Chapter 1](#). The publications are denoted by [Paper A](#) [177], [Paper B](#) [178] and [Paper C](#) [179] in the remainder of this work. The major accomplishments can be briefly summarized as follows:

- Two novel fast multipole boundary element formulations are developed that efficiently predict the scattering of acoustic waves by finite periodic structures. [Paper A](#) derives the mathematical formulation, discusses numerical solution techniques and provides two numerical examples for validation. In addition, it presents a comparison of three noise barrier designs based on full-scale, three-dimensional acoustic analyses.
- In [Paper B](#), a greedy reduced basis scheme for the solution of fully coupled FEM-BEM systems with parameter and implicit frequency dependence is proposed. An extension to vibroacoustic problems with multiple load cases is presented and two numerical examples are provided for validation.
- Finally, three Krylov subspace solvers for the solution of the boundary element discretized Helmholtz equation with multiple excitations are evaluated in [Paper C](#). They are employed to accelerate the prediction of aeroacoustic noise and the solution of a nonlinear acoustic eigenvalue problem.

[Chapter 3](#) presents a detailed summary of the publications [Paper A](#), [Paper B](#) and [Paper C](#) along with the individual contributions of the authors. Reprints of the full texts are provided in [Appendix A](#).

2 Governing equations and numerical methods

The mathematical formulations and computational methods that represent the foundation of this thesis are outlined in this chapter. [Section 2.1](#) presents the time-harmonic wave equations of linear acoustics and linear elastodynamics. This is followed by an introduction of the boundary element method for the Helmholtz equation in [Section 2.2](#). Particular emphasis lies on the fast multipole method and a formulation for periodic structures. [Section 2.3](#) reviews the numerical treatment of coupled structural acoustic problems by means of a fully coupled finite element and boundary element formulation. Lastly, structural acoustic problems with multiple right-hand sides are examined and Krylov subspace methods for their solution are presented in [Section 2.4](#).

2.1 Wave equations of linear acoustics and elastodynamics

2.1.1 Linear time-harmonic acoustics

Sound waves are propagating dynamic disturbances of the ambient pressure within a compressible fluid. In linear acoustics, the fluctuations are assumed to be significantly smaller than the atmospheric pressure and are represented by the sound pressure $\tilde{p}(\mathbf{x}, t)$. Its distribution within a homogeneous fluid is described by a hyperbolic second order partial differential equation, the acoustic wave equation

$$\nabla^2 \tilde{p}(\mathbf{x}, t) = \frac{1}{c^2} \frac{\partial^2 \tilde{p}(\mathbf{x}, t)}{\partial t^2}, \quad (2.1)$$

with speed of sound c and the assumption of isentropic fluid flow. Its derivation stems from the balance of mass, the balance of momentum and an equation of state that relates the density perturbation to the sound pressure and the speed of sound [180].

The time-dependent wave equation (2.1) can be transferred into the frequency domain by separation of variables. This introduces a time-harmonic ansatz such as

$$\tilde{p}(\mathbf{x}, t) = \Re \{ p(\mathbf{x}) e^{-i\omega t} \}, \quad (2.2)$$

where i is the imaginary unit and $\omega = 2\pi f$ is the circular frequency of the sound pressure oscillation with the frequency f . The sign of the exponent in the ansatz describes the direction of the traveling wave which is pointing outwards in this case. Inserting the ansatz (2.2) into the wave equation (2.1) yields the Helmholtz equation

$$\nabla^2 p(\mathbf{x}) + k^2 p(\mathbf{x}) = 0, \quad (2.3)$$

an elliptic second-order partial differential equation with wave number $k = \omega/c$.

Accompanying the Helmholtz equation (2.3) with suitable boundary conditions defines a boundary value problem. Its solution describes the spatial sound pressure field $p(\mathbf{x})$ within the domain Ω . The boundary value problem is well-stated if a boundary condition is prescribed on every part of the boundary Γ that encloses Ω which itself is a bounded Lipschitz domain. Three different types of boundary conditions are distinguished [180]. The Dirichlet boundary condition

$$p(\mathbf{x}) = p_D(\mathbf{x}), \quad \mathbf{x} \in \Gamma_D, \quad (2.4)$$

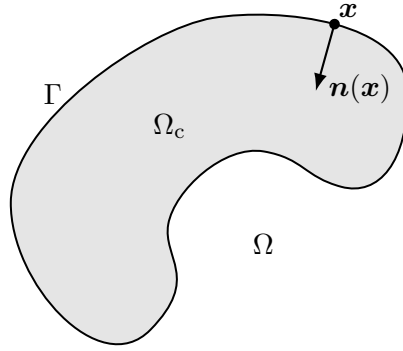


Figure 2.1: Unbound computational domain Ω with its boundary Γ . The normal vector $\mathbf{n}(\mathbf{x})$ is perpendicular to the boundary at \mathbf{x} and points into the complementary domain Ω_c .

prescribes a sound pressure field $p_D(\mathbf{x})$ on the boundary Γ_D , whereas the Neumann boundary condition

$$\frac{1}{i\omega\rho_0} \frac{\partial p(\mathbf{x})}{\partial \mathbf{n}(\mathbf{x})} = v_f(\mathbf{x}), \quad \mathbf{x} \in \Gamma_N, \quad (2.5)$$

prescribes the normal derivative of the sound pressure field on the boundary Γ_N . The latter depends on the normal fluid particle velocity v_f , the fluid density ρ_0 and the normal vector $\mathbf{n}(\mathbf{x})$ that points into the complementary domain Ω_c as visualized in Fig. 2.1. Both boundary conditions can be derived from the Robin boundary condition

$$Y(\mathbf{x}) p(\mathbf{x}) = v_f(\mathbf{x}) - v_s(\mathbf{x}), \quad \mathbf{x} \in \Gamma_R, \quad (2.6)$$

which relates the sound pressure to the fluid particle velocity v_f and the structural particle velocity v_s by the acoustic boundary admittance Y on the boundary Γ_R . The value of the boundary admittance usually needs to be determined experimentally and depends on the material properties and surface characteristics [181]. The union of the three boundary parts yields the whole boundary, i.e., $\Gamma = \Gamma_D \cup \Gamma_N \cup \Gamma_R$.

When considering exterior acoustic problems, an additional boundary condition applies on all boundaries at infinity. It is known as Sommerfeld radiation condition and reads

$$\lim_{|\mathbf{x}| \rightarrow \infty} |\mathbf{x}|^{\frac{d-1}{2}} \left(\frac{\partial}{\partial |\mathbf{x}|} - ik \right) p(\mathbf{x}) = 0, \quad (2.7)$$

with the dimension d of Ω and the Euclidean norm $|\cdot|$. Fulfilling the radiation condition (2.7) ensures that the sound pressure field exhibits free field behavior at infinity [182].

2.1.2 Linear time-harmonic elastodynamics

Linear elastodynamics describes the deformation and rigid-body displacements of elastic solids under the assumption of linear elasticity and geometric linearity. The balance of linear momentum, the balance of angular momentum and the constitutive equation of linear elasticity yield the Navier-Lamé equation [183, 184]

$$\mu \nabla^2 \tilde{\mathbf{u}}(\mathbf{x}, t) + (\lambda + \mu) \nabla (\nabla \cdot \tilde{\mathbf{u}}(\mathbf{x}, t)) + \mathbf{f}_v(\mathbf{x}, t) = \rho \frac{\partial^2 \tilde{\mathbf{u}}(\mathbf{x}, t)}{\partial t^2}. \quad (2.8)$$

It relates the time-dependent displacement field $\tilde{\mathbf{u}}(\mathbf{x}, t)$ measured from an undeformed configuration or equilibrium position to its second order time derivative and the body forces $\mathbf{f}_v(\mathbf{x}, t)$.

The material density reads ρ and the Lamé constants are given as

$$\lambda = \frac{\nu E}{(1 + \nu)(1 - 2\nu)}, \quad (2.9)$$

and

$$\mu = \frac{E}{2(1 + \nu)}, \quad (2.10)$$

where E denotes the elastic modulus and ν denotes the Poisson's ratio [184].

The displacement vector $\tilde{\mathbf{u}}(\mathbf{x}, t)$ can be decomposed into the sum of the irrotational part and the solenoidal part according to the Helmholtz decomposition [185], i.e.,

$$\tilde{\mathbf{u}}(\mathbf{x}, t) = -\nabla\varphi(\mathbf{x}, t) + \nabla \times \boldsymbol{\psi}(\mathbf{x}, t). \quad (2.11)$$

The longitudinal component of $\tilde{\mathbf{u}}$ is described by the first term, whereas the second term describes its transversal component. Inserting Eq. (2.11) into the Navier-Lamé equation (2.8) and setting the body forces to zero yields

$$-\nabla \left(\rho \frac{\partial^2 \varphi(\mathbf{x}, t)}{\partial t^2} - (\lambda + 2\mu) \nabla^2 \varphi(\mathbf{x}, t) \right) + \nabla \times \left(\rho \frac{\partial^2 \boldsymbol{\psi}(\mathbf{x}, t)}{\partial t^2} - \mu \nabla^2 \boldsymbol{\psi}(\mathbf{x}, t) \right) = \mathbf{0}. \quad (2.12)$$

Enforcing that the relations in both brackets equal to zero yields the elastodynamic wave equations

$$\frac{\partial^2 \varphi(\mathbf{x}, t)}{\partial t^2} - c_L^2 \nabla^2 \varphi(\mathbf{x}, t) = 0 \quad (2.13)$$

and

$$\frac{\partial^2 \boldsymbol{\psi}(\mathbf{x}, t)}{\partial t^2} - c_T^2 \nabla^2 \boldsymbol{\psi}(\mathbf{x}, t) = \mathbf{0}. \quad (2.14)$$

Displacements in the direction of the wave propagation are longitudinal waves $\varphi(\mathbf{x}, t)$, also referred to as compression waves, that propagate with the velocity

$$c_L = \sqrt{\frac{\lambda + 2\mu}{\rho}}. \quad (2.15)$$

In contrast, displacements perpendicular to the direction of the propagation are transversal waves $\boldsymbol{\psi}(\mathbf{x}, t)$, or shear waves, that propagate with the velocity

$$c_T = \sqrt{\frac{\mu}{\rho}}. \quad (2.16)$$

The remainder of the present work considers the time-harmonic Navier-Lamé equations. By assuming that the time-dependent displacement field $\tilde{\mathbf{u}}(\mathbf{x}, t)$ follows a time-harmonic ansatz in the form of

$$\tilde{\mathbf{u}}(\mathbf{x}, t) = \Re \{ \mathbf{u}(\mathbf{x}) e^{-i\omega t} \}, \quad (2.17)$$

the time-dependent Navier-Lamé equation (2.8) is transferred into the frequency domain. Inserting Eq. (2.17) into Eq. (2.8) and assuming that the body forces vanish yields

$$\mu \nabla^2 \mathbf{u}(\mathbf{x}) + (\lambda + \mu) \nabla (\nabla \cdot \mathbf{u}(\mathbf{x})) + \rho \omega^2 \mathbf{u}(\mathbf{x}) = \mathbf{0}, \quad (2.18)$$

with the spatial displacement field $\mathbf{u}(\mathbf{x})$. Accompanying Eq. (2.18) with Dirichlet, Neumann and Robin boundary conditions yields a well posed boundary value problem.

2.2 Acoustic boundary element method

The boundary element method (BEM) is an efficient measure to solve exterior Helmholtz problems. Its starting point is the weak formulation of the Helmholtz equation that originates from applying the method of weighted residuals. Integrating twice by parts and identifying the weight functions as the fundamental solution, also known as Green's function, yields the Kirchhoff-Helmholtz integral equation. It is discretized by a collocation boundary element method and accompanied with sufficient boundary conditions. Introducing a spatial discretization of the domain's boundary and of the physical quantities results in a dense, complex-valued system of linear equations. Combining the BEM with the fast multipole method (FMM) yields a computational efficient scheme for solving large-scale acoustic problems. A further acceleration can be achieved in the special case of periodic geometries. The system matrices become block Toeplitz matrices and matrix-vector products can be expressed by circular convolutions.

2.2.1 Boundary element formulation

Applying the method of weighted residuals to the Helmholtz equation (2.3), that is multiplying Eq. (2.3) by the a weight function w which is restricted to Sobolev spaces and integrating over the computational domain Ω , leads to the weak formulation

$$\int_{\Omega} w(\mathbf{x}) [\nabla^2 p(\mathbf{x}) + k^2 p(\mathbf{x})] d\Omega = 0. \quad (2.19)$$

Integrating Eq. (2.19) twice by parts yields

$$\int_{\Gamma} w(\mathbf{x}) \frac{\partial p(\mathbf{x})}{\partial \mathbf{n}(\mathbf{x})} - \frac{\partial w(\mathbf{x})}{\partial \mathbf{n}(\mathbf{x})} p(\mathbf{x}) d\Gamma + \int_{\Omega} [\nabla^2 w(\mathbf{x}) + k^2 w(\mathbf{x})] p(\mathbf{x}) d\Omega = 0, \quad (2.20)$$

in which the Helmholtz operator is applied to the weight function in the second integral. This domain integral can be reformulated by introducing the fundamental solution $G(\mathbf{x}, \mathbf{y})$ as weight function for which

$$\nabla^2 G(\mathbf{x}, \mathbf{y}) + k^2 G(\mathbf{x}, \mathbf{y}) = -\delta(\mathbf{x}, \mathbf{y}), \quad (2.21)$$

holds. The right-hand side term $\delta(\mathbf{x}, \mathbf{y})$ corresponds to the Dirac function and the fundamental solution $G(\mathbf{x}, \mathbf{y})$ describes the sound pressure at the field point \mathbf{x} subject to a monopole source at the source point \mathbf{y} under free field conditions. With Eq. (2.21), the domain integral in Eq. (2.20) simplifies to

$$\int_{\Omega} [\nabla^2 G(\mathbf{x}, \mathbf{y}) + k^2 G(\mathbf{x}, \mathbf{y})] p(\mathbf{x}) d\Omega = \int_{\Omega} -\delta(\mathbf{x}, \mathbf{y}) p(\mathbf{x}) d\Omega = -c(\mathbf{y}) p(\mathbf{y}), \quad (2.22)$$

with the integral-free term $c(\mathbf{y})$. Therefore, the domain integral of Eq. (2.20) vanishes and the boundary integral equation

$$c(\mathbf{y}) p(\mathbf{y}) + \int_{\Gamma} \frac{\partial G(\mathbf{x}, \mathbf{y})}{\partial \mathbf{n}(\mathbf{x})} p(\mathbf{x}) d\Gamma - \int_{\Gamma} G(\mathbf{x}, \mathbf{y}) \frac{\partial p(\mathbf{x})}{\partial \mathbf{n}(\mathbf{x})} d\Gamma = 0, \quad (2.23)$$

is obtained [12]. Equation (2.23) is known as Kirchhoff-Helmholtz integral equation in the case of $\mathbf{y} \in \Gamma$ with $c(\mathbf{y}) = 0.5$ if the boundary is smooth around \mathbf{y} . Its solution implicitly fulfills the Sommerfeld radiation condition (2.7) due to choosing a weight function that is a solution to the Helmholtz equation itself. This constitutes a major advantage of the boundary

element method compared to other numerical methods since they usually require specialized techniques to fulfill the radiation condition [186, 187]. For $\mathbf{y} \in \Omega \setminus \Gamma$, the integral-free term corresponds to either 0 or 1 and the sound pressure at any field point can be calculated based on the Dirichlet and Neumann data on the boundary Γ .

The choice of the fundamental solution $G(\mathbf{x}, \mathbf{y})$ depends on the shape of the computational domain Ω . The present work considers three-dimensional full- and half-space acoustic problems for which the Green's functions read

$$G(\mathbf{x}, \mathbf{y}) = \frac{1}{4\pi} \frac{e^{ik|\mathbf{x}-\mathbf{y}|}}{|\mathbf{x}-\mathbf{y}|}, \quad \mathbf{x}, \mathbf{y} \in \mathbb{R}^3, \quad (2.24)$$

and

$$G_h(\mathbf{x}, \mathbf{y}) = \frac{1}{4\pi} \frac{e^{ik|\mathbf{x}-\mathbf{y}|}}{|\mathbf{x}-\mathbf{y}|} + R_p \frac{1}{4\pi} \frac{e^{ik|\hat{\mathbf{x}}-\mathbf{y}|}}{|\hat{\mathbf{x}}-\mathbf{y}|}, \quad \mathbf{x}, \hat{\mathbf{x}}, \mathbf{y} \in \mathbb{R}^3, \quad (2.25)$$

respectively [12]. Herein, R_p is the reflection coefficient and $\hat{\mathbf{x}}$ is the mirror image of the field point \mathbf{x} with respect to the plane that divides both half-spaces.

Taking the derivative of the boundary integral equation (2.23) with respect to the normal vector $\mathbf{n}(\mathbf{y})$ and assuming that the boundary is smooth around \mathbf{y} yields the hypersingular boundary integral equation

$$c(\mathbf{y}) \frac{\partial p(\mathbf{y})}{\partial \mathbf{n}(\mathbf{y})} + \int_{\Gamma} \frac{\partial^2 G(\mathbf{x}, \mathbf{y})}{\partial \mathbf{n}(\mathbf{x}) \partial \mathbf{n}(\mathbf{y})} p(\mathbf{x}) d\Gamma = \int_{\Gamma} \frac{\partial G(\mathbf{x}, \mathbf{y})}{\partial \mathbf{n}(\mathbf{y})} \frac{\partial p(\mathbf{x})}{\partial \mathbf{n}(\mathbf{x})} d\Gamma. \quad (2.26)$$

The linear combination of Eq. (2.23) and Eq. (2.26) yields the Burton and Miller formulation [188]

$$\begin{aligned} c(\mathbf{y})p(\mathbf{y}) + \int_{\Gamma} \left[\frac{\partial G(\mathbf{x}, \mathbf{y})}{\partial \mathbf{n}(\mathbf{x})} + \alpha \frac{\partial^2 G(\mathbf{x}, \mathbf{y})}{\partial \mathbf{n}(\mathbf{x}) \partial \mathbf{n}(\mathbf{y})} \right] p(\mathbf{x}) d\Gamma \\ + \alpha c(\mathbf{y}) \frac{\partial p(\mathbf{y})}{\partial \mathbf{n}(\mathbf{y})} - \int_{\Gamma} \left[G(\mathbf{x}, \mathbf{y}) + \alpha \frac{\partial G(\mathbf{x}, \mathbf{y})}{\partial \mathbf{n}(\mathbf{y})} \right] \frac{\partial p(\mathbf{x})}{\partial \mathbf{n}(\mathbf{x})} d\Gamma = 0, \end{aligned} \quad (2.27)$$

which exhibits unique solutions at all frequencies [189]. The coupling parameter α is a complex scalar with a non-vanishing imaginary part, i.e., $\text{Im}(\alpha) \neq 0$. A value of $-i/k$ is optimal in the present case [155].

In order to solve Eq. (2.27) numerically, the method of weighted residuals is applied a second time. Multiplying the equation by an additional set of weight functions and integrating over the boundary Γ yields the weak formulation of Eq. (2.27). Different choices for the weight functions lead to different boundary element formulations. In the thesis at hand, the collocation BEM is employed in which the second set of weight functions corresponds to the Dirac function $\delta(\mathbf{x}, \mathbf{z})$ with the collocation points $\mathbf{z} \in \Gamma$. Therefore, the weak formulation is enforced in a strong sense at a number of discrete points. Its numerical solution only requires the spatial discretization of the geometry and of the physical quantities on the boundary Γ . A common choice for the discretization are discontinuous boundary elements. They approximate the geometry by continuous polynomials, whereas the physical quantities are approximated by discontinuous polynomials [190, 191]. In the usual case, the discontinuous nodes coincide with the collocation points [12]. An in-depth error analysis with respect to frequency, element size and the location of the discontinuous nodes is presented in [192]. Introducing the admittance boundary condition (2.6) and the aforementioned spatial discretization into Eq. (2.27) yields the following system of linear equations

$$(\mathbf{H} - \mathbf{G}\mathbf{Y}) \mathbf{p} = \mathbf{G}\mathbf{v}_s + \mathbf{p}^{\text{inc}}. \quad (2.28)$$

Herein, $\mathbf{H} \in \mathbb{C}^{N_{\text{dof}} \times N_{\text{dof}}}$ and $\mathbf{G} \in \mathbb{C}^{N_{\text{dof}} \times N_{\text{dof}}}$ are the dense boundary element coefficient matrices with the number of collocation points N_{dof} . Choosing a piecewise constant approximation of the boundary admittance leads to a block diagonal admittance matrix $\mathbf{Y} \in \mathbb{C}^{N_{\text{dof}} \times N_{\text{dof}}}$. Furthermore, the vectors $\mathbf{p} \in \mathbb{C}^{N_{\text{dof}}}$, $\mathbf{p}^{\text{inc}} \in \mathbb{C}^{N_{\text{dof}}}$ and $\mathbf{v}_s \in \mathbb{C}^{N_{\text{dof}}}$ store the sound pressure values, incident sound pressure values and structural particle velocity values at the collocation points, respectively. Note that \mathbf{p}^{inc} arises from considering the inhomogeneous Helmholtz equation, i.e., including a source term on the right-hand side of Eq. (2.3). Details on the numerical treatment of the inhomogeneous Helmholtz equation can be found in [10].

2.2.2 Fast multipole method

The fast multipole method (FMM) is an elegant numerical technique to evaluate the pair-wise interactions of a large number of bodies, commonly referred to as N -body problem [26]. The boundary element discretized Helmholtz equation constitutes a problem of this type and significantly benefits from its application [27, 34]. Applying the multilevel variant of the FMM to three-dimensional acoustic problems approximates the matrix-vector multiplications of Eq. (2.28) in order $\mathcal{O}(N_{\text{dof}} \log(N_{\text{dof}}))$ time and order $\mathcal{O}(N_{\text{dof}})$ memory at best [20]. The basis of the algorithm is a hierarchical subdivision of the computational domain and its representation in a tree structure. A bounding box is spanned around the boundary Γ and subdivided into smaller boxes of equal size. These boxes are repeatedly subdivided until either the number of degrees of freedom within the specific box is below a predefined limit or a certain number of subdivisions is reached. The hierarchical structure is stored into a tree where the root corresponds to the bounding box and each tree level represents an additional level of subdivision [55]. Figure 2.2a shows a bounding box around the two-dimensional boundary Γ with dots indicating the locations of the degrees of freedom. Adding two additional levels of subdivisions leads to the formation shown in Fig. 2.2b. Each box at a level l lies within a specific box of the previous level $l-1$. The box at level $l-1$ is denoted as parent box, whereas the box at level l is denoted as its child box.

A pair of boxes is called well-separated when it fulfills the admissibility criterion

$$|\mathbf{x}_c - \mathbf{y}_c| \geq 2r, \quad (2.29)$$

with the characteristic length r of the boxes and their center points \mathbf{x}_c and \mathbf{y}_c . The interaction between degrees of freedom of well-separated boxes are referred to as far-field interactions. They can be approximated by employing a multipole series expansion of the Green's function. In contrast, pairs of boxes which do not fulfill the admissibility criterion of Eq. (2.29) are referred to as neighboring boxes. The interaction between their degrees of freedom are near-field interactions and are represented using the exact description of the Green's function. Figure 2.2c indicates the relationship for a specific box highlighted in olive at the second level of subdivision. Its neighboring boxes are colored in blue, whereas the so-called interacting boxes are colored in gray. Figure 2.2d presents the relationship at an additional level of subdivision. Again, blue boxes denote neighboring boxes of the olive box and gray boxes denote the interacting boxes. Note that the latter does not include all well-separated boxes. Only the cousins of the olive box are considered. These correspond to the child boxes of the parent's neighboring boxes, i.e., to boxes that are located within one of the blue boxes of the previous level of subdivision visualized in Fig. 2.2c. Determining these relations can be performed by bit-interleaving [193].

Following these rules, the neighboring and well-separated boxes of each box at the levels $l \geq 2$ are identified. Whenever Eq. (2.29) holds for a given pair of boxes, the Green's

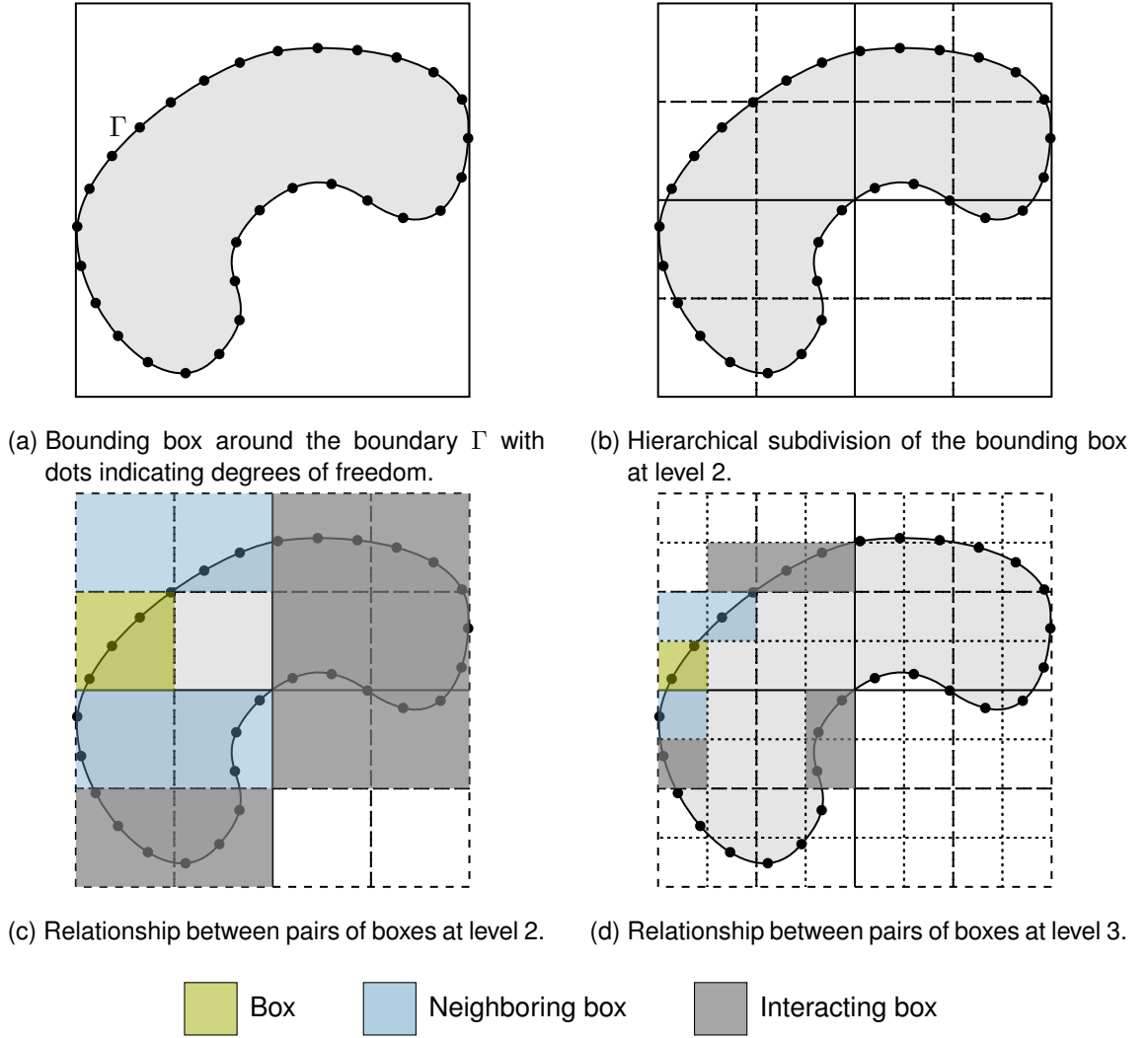


Figure 2.2: Two-dimensional boundary Γ and the uniform hierarchical subdivision of its bounding box at levels 0, 2 and 3.

function can be approximated by a series expansion around the center of one of the boxes. The truncated series expansion of the full-space Green's function (2.24) around the center \mathbf{x}_c close to \mathbf{x} reads [194]

$$G(\mathbf{x}, \mathbf{y}) \approx \frac{ik}{4\pi} \sum_{n=0}^{n_t} (2n+1) \sum_{m=-n}^n O_n^m(\mathbf{y} - \mathbf{x}_c) \bar{I}_n^m(\mathbf{x} - \mathbf{x}_c), \quad (2.30)$$

where \bar{I}_n^m denotes the complex conjugate of I_n^m and n_t is the expansion order. Both O_n^m and I_n^m are given as

$$O_n^m(\mathbf{x}) = h_n^{(1)}(|\mathbf{x}|) Y_n^m \left(\frac{\mathbf{x}}{|\mathbf{x}|} \right) \quad (2.31)$$

and

$$I_n^m(\mathbf{x}) = j_n(|\mathbf{x}|) Y_n^m \left(\frac{\mathbf{x}}{|\mathbf{x}|} \right), \quad (2.32)$$

with the n -th order spherical Hankel function of the first kind $h_n^{(1)}$, the n -th order spherical Bessel function of the first kind j_n and the spherical harmonics Y_n^m [41]. Taking the derivative of Eq. (2.30) with respect to the normal vector $\mathbf{n}(\mathbf{x})$ yields

$$\frac{\partial G(\mathbf{x}, \mathbf{y})}{\partial \mathbf{n}(\mathbf{x})} \approx \frac{ik}{4\pi} \sum_{n=0}^{n_t} (2n+1) \sum_{m=-n}^n O_n^m(\mathbf{y} - \mathbf{x}_c) \frac{\partial \bar{I}_n^m(\mathbf{x} - \mathbf{x}_c)}{\partial \mathbf{n}(\mathbf{x})}. \quad (2.33)$$

A combination of a box of field points enclosing the boundary $\Gamma_{\mathbf{x}} \subset \Gamma$ and a box of source points enclosing the boundary $\Gamma_{\mathbf{y}} \subset \Gamma$ is considered and it is assumed that the admissibility criterion (2.29) holds for both boxes. In this case, the far-field interaction between the field points on $\Gamma_{\mathbf{x}}$ and the source points on $\Gamma_{\mathbf{y}}$ can be approximated by a product of five fast multipole operators. They are obtained by inserting the truncated series expansions into the boundary integrals of Eq. (2.23) or Eq. (2.27), respectively. This yields the following multipole expansion for the double-layer potential [41]

$$\int_{\Gamma_{\mathbf{x}}} \frac{\partial G(\mathbf{x}, \mathbf{y})}{\partial \mathbf{n}(\mathbf{x})} p(\mathbf{x}) d\Gamma \approx \frac{ik}{4\pi} \sum_{n=0}^{n_t} (2n+1) \sum_{m=-n}^n O_n^m(\mathbf{y} - \mathbf{x}_c) M_n^m(\mathbf{x}_c), \quad (2.34)$$

with $\mathbf{y} \in \Gamma_{\mathbf{y}}$ and $\mathbf{x} \in \Gamma_{\mathbf{x}}$. The expansion translates the contribution within the field box to the multipole moments according to the particle-to-moment (P2M) translation

$$M_n^m(\mathbf{x}_c) = \int_{\Gamma_{\mathbf{x}}} \frac{\partial \bar{I}_n^m(\mathbf{x} - \mathbf{x}_c)}{\partial \mathbf{n}(\mathbf{x})} p(\mathbf{x}) d\Gamma. \quad (2.35)$$

Subsequently, the multipole moments of the field box are shifted to the center point $\mathbf{x}_{c'}$ of the parent box by the moment-to-moment (M2M) translation

$$M_n^m(\mathbf{x}_{c'}) = \sum_{n'=0}^{n_t} (2n'+1) \sum_{m'=-n'}^{n'} \sum_{l \in N} (-1)^{m'} W_{n',n,m',m,l} I_l^{-m-m'}(\mathbf{x}_c - \mathbf{x}_{c'}) M_{n'}^{-m'}(\mathbf{x}_c). \quad (2.36)$$

The set N is defined by [41]

$$N := \left\{ l \mid l \in \mathbb{Z}, n + n' - l : \text{even}, \max\{|m + m'|, |n - n'|\} < l < n + n' \right\}, \quad (2.37)$$

and $W_{n',n,m',m,l}$ is given as

$$W_{n',n,m',m,l} = (2l+1) i^{n-n'+l} \begin{pmatrix} n & n' & l \\ 0 & 0 & 0 \end{pmatrix} \begin{pmatrix} n & n' & l \\ m & m' & -m - m' \end{pmatrix}, \quad (2.38)$$

where $(\begin{smallmatrix} \cdot \\ \cdot \\ \cdot \end{smallmatrix})$ denotes the Wigner 3j-symbol [195]. The M2M translation is applied to all boxes within the levels $l \geq 2$ starting at the lowest level. Subsequently, the multipole moments of the field box are transferred to the local expansion coefficients of the source box by the moment-to-local (M2L) translation [41]

$$L_n^m(\mathbf{y}_c) = \sum_{n'=0}^{n_t} (2n'+1) \sum_{m'=-n'}^{n'} (-1)^{m+m'} \sum_{l \in N} W_{n',n,m',m,l} O_l^{m+m'}(\mathbf{y}_c - \mathbf{x}_c) M_{n'}^{m'}(\mathbf{x}_c). \quad (2.39)$$

The local expansion coefficients are then translated down the tree until the lowest level of subdivision is reached using the local-to-local (L2L) translation

$$L_n^m(\mathbf{y}_{c'}) = (-1)^m \sum_{n'=0}^{n_t} (2n'+1) \sum_{m'=-n'}^{n'} \sum_{l \in N} W_{n',n,m',m,l} I_l^{m-m'}(\mathbf{y}_{c'} - \mathbf{y}_c) L_{n'}^{m'}(\mathbf{y}_c). \quad (2.40)$$

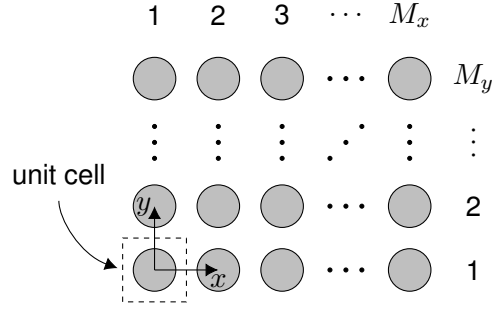


Figure 2.3: A finite periodic structure with periodicity in the x - and y -direction. The unit cell is highlighted by the dashed box and repeated M_x and M_y times in the x and y directions, respectively.

Expanding the Green's function around the center point \mathbf{y}_c close to \mathbf{y} , yields an expression for the local expansion [41]

$$\int_{\Gamma_x} \frac{\partial G(\mathbf{x}, \mathbf{y})}{\partial \mathbf{n}(\mathbf{x})} p(\mathbf{x}) d\Gamma \approx \frac{ik}{4\pi} \sum_{n=0}^{n_t} (2n+1) \sum_{m=-n}^n \bar{I}_n^m(\mathbf{y} - \mathbf{y}_c) L_n^m(\mathbf{y}_c), \quad (2.41)$$

with $\mathbf{y} \in \Gamma_y$ and $\mathbf{x} \in \Gamma_x$. This local-to-particle (L2P) translation shifts the local expansion coefficients of the leaf boxes to the particle contributions.

These five operators represent an approximation of the interactions between the degrees of freedom of well-separated boxes. Its accuracy is determined by the choice of the truncation number n_t [20]. Although the discretized operators can be precomputed and assembled into matrices as in [161], matrix-free implementations of the fast multipole method are far more common [196].

2.2.3 Periodic boundary element formulation

The collocation boundary element discretization yields a system of linear equations in the form of Eq. (2.28). The system matrices \mathbf{H} and \mathbf{G} are fully populated which leads to infeasible assembly and storage costs in the case of medium to large-scale problems. Although fast boundary element methods such as the FMM reduce this cost, more efficient representations exist for particular use cases. One of these cases is the acoustic analysis of finite periodic structures. In the present work, the term finite periodic structure denotes structures that consist of a finite number of replications of a unit cell. Figure 2.3 shows an example consisting of an array of circular objects. The unit cell is spanned around a single object and repeated M_x and M_y times in the x and y directions, respectively. Consequently, the structure consists of $n_{\text{cell}} = M_x M_y$ unit cells.

Applying a collocation boundary element discretization to a finite periodic structure yields the system of linear equations (2.28) with the system matrix $\mathbf{H} - \mathbf{G}\mathbf{Y}$. Arranging the degrees of freedom according to the underlying periodicity allows to represent both matrices \mathbf{H} and \mathbf{G} by structured matrices. Due to the translation invariance of the Green's function and its normal derivative, c.f. Eq. (2.24), interactions between equally spaced replications of the unit cell are identical [102]. Therefore, the system matrices that store these interactions feature constant blocks along each diagonal. Matrices of this type are known as block Toeplitz matrix. When considering periodicity in multiple directions, the system matrices become multilevel block Toeplitz matrices which implies that each matrix block is a block Toeplitz matrix itself.

Additionally assuming that the boundary admittance is periodic and thus uniquely defined on a unit cell, the whole system matrix $(\mathbf{H} - \mathbf{G}\mathbf{Y})$ becomes a multilevel block Toeplitz matrix which is abbreviated by \mathbf{T} in the following. Considering the structure shown in Fig. 2.3, \mathbf{T} is of size $M_x M_y n_{\text{dof}} \times M_x M_y n_{\text{dof}}$, where n_{dof} denotes the number of degrees of freedom of the unit cell. The matrix reads

$$\mathbf{T} = \begin{bmatrix} \mathbf{T}_0^1 & \mathbf{T}_{-1}^1 & \cdots & \cdots & \mathbf{T}_{1-M_y}^1 \\ \mathbf{T}_1^1 & \mathbf{T}_0^1 & \mathbf{T}_{-1}^1 & \cdots & \mathbf{T}_{2-M_y}^1 \\ \vdots & \mathbf{T}_1^1 & \ddots & \ddots & \vdots \\ \vdots & \vdots & \ddots & \ddots & \mathbf{T}_{-1}^1 \\ \mathbf{T}_{M_y-1}^1 & \mathbf{T}_{M_y-2}^1 & \cdots & \mathbf{T}_1^1 & \mathbf{T}_0^1 \end{bmatrix} \quad (2.42)$$

and stores constant matrix blocks \mathbf{T}_j^1 on each diagonal. The superscript $(\cdot)^1$ denotes the first level of periodicity and \mathbf{T} features $2M_y - 1$ unique matrix blocks. These are block Toeplitz matrices itself with a size of $M_x n_{\text{dof}} \times M_x n_{\text{dof}}$ and read

$$\mathbf{T}_j^1 = \begin{bmatrix} \mathbf{T}_0^2 & \mathbf{T}_{-1}^2 & \cdots & \cdots & \mathbf{T}_{1-M_x}^2 \\ \mathbf{T}_1^2 & \mathbf{T}_0^2 & \mathbf{T}_{-1}^2 & \cdots & \mathbf{T}_{2-M_x}^2 \\ \vdots & \mathbf{T}_1^2 & \ddots & \ddots & \vdots \\ \vdots & \vdots & \ddots & \ddots & \mathbf{T}_{-1}^2 \\ \mathbf{T}_{M_x-1}^2 & \mathbf{T}_{M_x-2}^2 & \cdots & \mathbf{T}_1^2 & \mathbf{T}_0^2 \end{bmatrix}_j \quad (2.43)$$

The $2M_x - 1$ unique $n_{\text{dof}} \times n_{\text{dof}}$ matrix blocks $[\mathbf{T}_i^2]_j$ are fully populated and coincide with the corresponding entries of the discretized boundary integral equation. Since the multilevel block Toeplitz representation is an exact representation, $(\mathbf{H} - \mathbf{G}\mathbf{Y})\mathbf{p} = \mathbf{T}\mathbf{p}$ holds. In contrast of storing all $(M_x M_y n_{\text{dof}})^2$ matrix entries, only $(2M_x - 1)(2M_y - 1)n_{\text{dof}}^2$ entries are assembled and stored. An extension to the acoustic analysis of structures with an arbitrary number of periodic directions is given by Karimi et al. [120].

Aside from the reduction of the storage costs, the representation of the system matrix as a multilevel block Toeplitz matrix reduces the computation cost of the associated matrix-vector multiplications. The multiplication of an $N_{\text{dof}} \times N_{\text{dof}}$ multilevel block Toeplitz matrix with a vector can be expressed by circular convolutions which leads to a quasi-linear scaling in time [121]. Since the present block Toeplitz matrix \mathbf{T} stores dense and non-structured matrices on its lowest level, an asymptotic complexity of order $\mathcal{O}(n_{\text{dof}}^2 n_{\text{cell}} \log(n_{\text{cell}}))$ is obtained. This scaling is achieved by embedding the matrix \mathbf{T} into a multilevel block circulant matrix \mathbf{C} which is a special type of multilevel block Toeplitz matrix. Each block row of \mathbf{C} is a rightward cyclic permutation of its first block row [197, 198]. The 2-level block circulant matrix of the problem visualized in Fig. 2.3 reads

$$\mathbf{C} = \begin{bmatrix} \mathbf{C}_0^1 & \mathbf{C}_{-1}^1 & \cdots & \mathbf{C}_2^1 & \mathbf{C}_1^1 \\ \mathbf{C}_1^1 & \mathbf{C}_0^1 & \mathbf{C}_{-1}^1 & \cdots & \mathbf{C}_2^1 \\ \vdots & \mathbf{C}_1^1 & \ddots & \ddots & \vdots \\ \mathbf{C}_{-2}^1 & \vdots & \ddots & \ddots & \mathbf{C}_{-1}^1 \\ \mathbf{C}_{-1}^1 & \mathbf{C}_{-2}^1 & \cdots & \mathbf{C}_1^1 & \mathbf{C}_0^1 \end{bmatrix} \quad (2.44)$$

It stores block circulant matrices \mathbf{C}_j^1 , which are defined as

$$\mathbf{C}_j^1 = \begin{bmatrix} \mathbf{T}_0^2 & \mathbf{T}_{-1}^2 & \cdots & \mathbf{T}_2^2 & \mathbf{T}_1^2 \\ \mathbf{T}_1^2 & \mathbf{T}_0^2 & \mathbf{T}_{-1}^2 & \cdots & \mathbf{T}_2^2 \\ \vdots & \mathbf{T}_1^2 & \ddots & \ddots & \vdots \\ \mathbf{T}_{-2}^2 & \vdots & \ddots & \ddots & \mathbf{T}_{-1}^2 \\ \mathbf{T}_{-1}^2 & \mathbf{T}_{-2}^2 & \cdots & \mathbf{T}_1^2 & \mathbf{T}_0^2 \end{bmatrix}_j, \quad (2.45)$$

and include the $n_{\text{dof}} \times n_{\text{dof}}$ matrix blocks $[\mathbf{T}_i^2]_j$. The first block row of \mathbf{C}_j^1 consists of all unique matrix blocks of \mathbf{T}_j^1 defined in Eq. (2.43). Concatenating the blocks into a matrix \mathbf{Q} reads

$$\mathbf{Q} = (\mathbf{T}_0^2 \quad \mathbf{T}_{-1}^2 \quad \cdots \quad \mathbf{T}_{1-M_x}^2 \quad \mathbf{T}_{M_x-1}^2 \quad \cdots \quad \mathbf{T}_2^2 \quad \mathbf{T}_1^2). \quad (2.46)$$

Rightward shifts of \mathbf{Q} build the block rows of \mathbf{C}_j^1 . Subsequently concatenating the unique entries of \mathbf{C}_j^1 and introducing rightward shifts for each block row then yields the multilevel block circulant matrix \mathbf{C} defined in Eq. (2.44).

Applying the Fourier transform \mathfrak{F} and the inverse Fourier transform \mathfrak{F}^{-1} block diagonalizes the multilevel block circulant matrix \mathbf{C} [121], i.e.,

$$\mathbf{C} = \mathfrak{F}^{-1} \mathbf{\Lambda} \mathfrak{F}. \quad (2.47)$$

The entries of the block diagonal matrix

$$\mathbf{\Lambda} = \text{diag}(\mathbf{e}_0^1, \mathbf{e}_1^1, \dots, \mathbf{e}_{-2}^1, \mathbf{e}_{-1}^1), \quad (2.48)$$

correspond to the discrete Fourier transform of the first block column of \mathbf{C} , which reads

$$[\mathbf{e}_0^1 \quad \mathbf{e}_1^1 \quad \cdots \quad \mathbf{e}_{-2}^1 \quad \mathbf{e}_{-1}^1] = \mathfrak{F} [\mathbf{C}_0^1 \quad \mathbf{C}_1^1 \quad \cdots \quad \mathbf{C}_{-2}^1 \quad \mathbf{C}_{-1}^1]. \quad (2.49)$$

The discrete Fourier transform and its inverse are given by

$$\mathfrak{F} = \mathbf{F}_{2M_y-1} \otimes \mathbf{F}_{2M_x-1} \otimes \mathbf{I}_{n_{\text{dof}}}, \quad (2.50)$$

$$\mathfrak{F}^{-1} = \mathbf{F}_{2M_y-1}^{-1} \otimes \mathbf{F}_{2M_x-1}^{-1} \otimes \mathbf{I}_{n_{\text{dof}}}. \quad (2.51)$$

Herein, \otimes denotes the Kronecker product, $\mathbf{I}_{n_{\text{dof}}}$ denotes the $n_{\text{dof}} \times n_{\text{dof}}$ identity matrix and the Fourier matrix \mathbf{F}_m as well as its inverse \mathbf{F}_m^{-1} read

$$\mathbf{F}_m = \left(\left(e^{-i2\pi/m} \right)^{ij} \right)_{i,j=0,\dots,m-1}, \quad (2.52)$$

$$\mathbf{F}_m^{-1} = \frac{1}{m} \mathbf{F}_m^*. \quad (2.53)$$

The block diagonalization of \mathbf{C} allows to rewrite multiplications of the multilevel block Toeplitz matrix with the vector \mathbf{p} as

$$\mathbf{T}\mathbf{p} = \tilde{\mathfrak{F}}^{-1} \mathbf{\Lambda} \tilde{\mathfrak{F}} \mathbf{p}, \quad (2.54)$$

with the incomplete Fourier transformations $\tilde{\mathfrak{F}}$ and $\tilde{\mathfrak{F}}^{-1}$. They are determined by [120]

$$\tilde{\mathfrak{F}} = \tilde{\mathbf{F}}_{2M_y-1} \otimes \tilde{\mathbf{F}}_{2M_x-1} \otimes \mathbf{I}_{n_{\text{dof}}}, \quad (2.55)$$

$$\tilde{\mathfrak{F}}^{-1} = \tilde{\mathbf{F}}_{2M_y-1}^{-1} \otimes \tilde{\mathbf{F}}_{2M_x-1}^{-1} \otimes \mathbf{I}_{n_{\text{dof}}}, \quad (2.56)$$

and consider the incomplete Fourier matrices $\tilde{\mathbf{F}}_{2M_x-1}$ and $\tilde{\mathbf{F}}_{2M_y-1}$. These only contain the first M columns of \mathbf{F}_{2M-1} and the first M rows of \mathbf{F}_{2M-1}^{-1} , respectively, with M being a placeholder for either M_x or M_y in the present case. Based on the identity of Eq. (2.54), multiplications of the system matrix are performed in order $\mathcal{O}(n_{\text{dof}}^2 M_x M_y \log(M_x M_y))$ time [121]. Although the block diagonal matrix Λ requires the storage of $(2M_x - 1)(2M_y - 1)n_{\text{dof}}^2$ matrix entries, the overall memory requirements are not increased since the original block Toeplitz matrix \mathbf{T} can be freed from the memory.

The periodic boundary element formulation addresses small-scale acoustic problems with finite periodic geometries more efficiently than conventional and fast boundary element methods [90]. However, the assembly and storage of the block Toeplitz matrices becomes infeasible for medium to large-scale problems due to the quadratic complexity on the number of degrees of freedom n_{dof} of the unit cell.

2.3 Parameterized structural acoustic problems

Many technical applications involve vibrating structures that induce sound waves into the surrounding fluid. In some cases, the structures themselves are subject to surface pressure loads from incident sound waves. The interaction between structural parts and the surrounding acoustic fluid is described by the coupled equations of acoustics and elastodynamics. Two configurations are usually distinguished: Strong coupling and weak coupling. In the former case, the equations of elastodynamics and acoustics are solved simultaneously, taking the mutual interaction between both physical fields into account. The second case is a simplification in which the fluid loading that acts on the solid is negligible. This allows to solve the equations of elastodynamics in-vacuo and subsequently solve the acoustic wave equation in the surrounding fluid imposing the obtained structural solution as a boundary condition.

2.3.1 Fully coupled FEM-BEM formulation

The present work considers either lightweight structures in air or structures submerged in dense fluids such as water. Both contribute to strongly coupled structural acoustic problems for which a combined approach of finite and boundary element methods is a common modeling technique [199–201]. The finite element method discretizes the time-harmonic equations of linear elastodynamics (2.18) leading to [183]

$$(\mathbf{K}(\boldsymbol{\lambda}) - \omega^2 \mathbf{M}(\boldsymbol{\lambda})) \mathbf{u} = \mathbf{f}_s + \mathbf{f}_f, \quad (2.57)$$

with the vector of unknown displacements $\mathbf{u} \in \mathbb{C}^{\hat{N}_{\text{dof}}}$ at the \hat{N}_{dof} structural degrees of freedom. The stiffness matrix $\mathbf{K}(\boldsymbol{\lambda}) \in \mathbb{R}^{\hat{N}_{\text{dof}} \times \hat{N}_{\text{dof}}}$ and mass matrix $\mathbf{M}(\boldsymbol{\lambda}) \in \mathbb{R}^{\hat{N}_{\text{dof}} \times \hat{N}_{\text{dof}}}$ depend on $n_p - 1$ design parameters concatenated into

$$\boldsymbol{\lambda} = [\lambda_1, \dots, \lambda_{n_p-1}]. \quad (2.58)$$

They represent variations of the material parameters, thickness or boundary conditions but do not alter the geometry of the sound radiating boundary. In addition, the linear system explicitly depends on the angular frequency $\omega = 2\pi f$ with frequency f . Equation (2.57) includes two distinct forces that excite the solid. They are structural nodal forces $\mathbf{f}_s \in \mathbb{C}^{\hat{N}_{\text{dof}}}$ and the acoustic loading $\mathbf{f}_f \in \mathbb{C}^{\hat{N}_{\text{dof}}}$ caused by the sound pressure that acts on the sound radiating boundary.

The time-harmonic equations of linear acoustics (2.3) are discretized by the collocation boundary element method as outlined in Section 2.2. This leads to [12]

$$\mathbf{H}(\omega)\mathbf{p} = \mathbf{G}(\omega)\mathbf{v}_s + \mathbf{p}^{\text{inc}}, \quad (2.59)$$

under the assumptions of a vanishing boundary admittance. The vector $\mathbf{p} \in \mathbb{C}^{N_{\text{dof}}}$ contains the unknown sound pressure values at the acoustic degrees of freedom N_{dof} . The boundary element system matrices $\mathbf{G}(\omega) \in \mathbb{C}^{N_{\text{dof}} \times N_{\text{dof}}}$ and $\mathbf{H}(\omega) \in \mathbb{C}^{N_{\text{dof}} \times N_{\text{dof}}}$ are implicitly frequency dependent but do not depend on λ . The acoustic fluid is subject to an excitation by means of the structural particle velocity $\mathbf{v}_s \in \mathbb{C}^{N_{\text{dof}}}$ and the incident sound pressure field $\mathbf{p}^{\text{inc}} \in \mathbb{C}^{N_{\text{dof}}}$.

The acoustic loading \mathbf{f}_f and the structural particle velocity \mathbf{v}_s couples the structural and acoustic domains on the mutual interface. The coupling conditions read

$$\mathbf{f}_f = \mathbf{C}_{\text{sf}}\mathbf{p} \quad \text{and} \quad \mathbf{v}_s = -i\omega\mathbf{C}_{\text{fs}}\mathbf{u}, \quad (2.60)$$

introducing the mesh coupling matrices $\mathbf{C}_{\text{sf}} \in \mathbb{R}^{\hat{N}_{\text{dof}} \times N_{\text{dof}}}$ and $\mathbf{C}_{\text{fs}} \in \mathbb{R}^{N_{\text{dof}} \times \hat{N}_{\text{dof}}}$ which are obtained by a Galerkin projection [202]. Inserting Eq. (2.60) into Eqs. (2.57) and (2.59) leads to the fully coupled system of linear equations

$$\begin{bmatrix} \mathbf{K}(\lambda) - \omega^2\mathbf{M}(\lambda) & -\mathbf{C}_{\text{sf}} \\ i\omega\mathbf{G}(\omega)\mathbf{C}_{\text{fs}} & \mathbf{H}(\omega) \end{bmatrix} \begin{bmatrix} \mathbf{u} \\ \mathbf{p} \end{bmatrix} = \begin{bmatrix} \mathbf{f}_s \\ \mathbf{p}^{\text{inc}} \end{bmatrix}. \quad (2.61)$$

Obtaining a solution of Eq. (2.61) can be difficult in the case of heavy fluid loading or lightweight structures since the system matrix is generally ill-conditioned [58, 199, 201]. Forming the Schur complement with respect to \mathbf{p} provides a remedy and leads to

$$\left[i\omega\mathbf{G}(\omega)\mathbf{C}_{\text{fs}} (\mathbf{K}(\lambda) - \omega^2\mathbf{M}(\lambda))^{-1} \mathbf{C}_{\text{sf}} + \mathbf{H}(\omega) \right] \mathbf{p} = \hat{\mathbf{f}}_s(\omega, \lambda) \quad (2.62)$$

where the right-hand side is given as

$$\hat{\mathbf{f}}_s(\omega, \lambda) = -i\omega\mathbf{G}(\omega)\mathbf{C}_{\text{fs}} (\mathbf{K}(\lambda) - \omega^2\mathbf{M}(\lambda))^{-1} \mathbf{f}_s + \mathbf{p}^{\text{inc}}. \quad (2.63)$$

Iterative solvers are well suited for this Schur complement formulation since the finite element matrix $\mathbf{K}(\lambda) - \omega^2\mathbf{M}(\lambda)$ admits a sparse LU factorization. However, solving the FEM-BEM system for a broad range of parameter values and possibly high-dimensional parameter domains requires sophisticated numerical techniques. The present work will introduce a model order reduction technique based on a greedy reduced basis scheme.

2.4 Structural acoustic problems with many right-hand sides

The solution of a discretized system of linear equations can be obtained by either direct or iterative solvers. Sparse system matrices as well as small dense system matrices admit efficient factorizations and thus direct solvers are preferably applied. This particularly holds for linear systems with multiple right-hand sides. Once a factorization is computed, the solution to each right-hand side is obtained at a low cost. Unfortunately, the memory requirements of direct solvers scales cubic with respect to the size of the dense system matrices. This prevents their application to even medium-scale boundary element discretized linear systems. Although the fast multipole method avoids the assembly of the fully populated system matrix, the resulting algebraic structure of the linear system limits the computational efficiency of direct solvers [8]. A remedy is found by iterative solvers which obtain the solution of the linear

system based on matrix-vector products. They do not require a fully assembled system matrix and work well with matrix-free formulations. Krylov subspace solvers are widely used variants of iterative solvers which combine low memory requirements with favorable convergence properties [151]. They iteratively build and extend a Krylov subspace. It is spanned by the initial residual and by additional vectors that are the result of repeated multiplications of the initial residual with the system matrix. The present work employs two advanced algorithms that are especially tailored for linear systems with multiple right-hand sides. Contrary to standard Krylov solvers, they rely on either block or global Krylov subspaces. Prior to introducing them, the following sections review two applications within the field of acoustics and vibroacoustics that lead to linear systems with multiple right-hand sides.

2.4.1 Diffuse sound field excitation

The sound transmission loss of structures such as panels and windows is experimentally measured in coupled anechoic-reverberant chambers. A diffuse sound field within the reverberant chamber excites the structural component located at the mutual interface of both chambers and intensity probes within the anechoic chamber allow to determine the transmitted sound energy. These studies are expensive and time-consuming, especially when performing an optimization of the structural components. Numerical methods constitute a more efficient approach to evaluate the sound transmission behavior of various designs. A finite element model describes the dynamic behavior of the structure, whereas a boundary element model reflects the acoustic behavior within the anechoic chamber and the reverberant room. Only the structural components and its sound radiating surfaces need to be discretized. The BEM straightforwardly represents free field conditions and the approach of Rafaely [150] describes the diffuse sound field excitation by superposing n_{pw} plane waves from uniformly distributed directions. The response to a diffuse sound field excitation is given by the mean responses to multiple incident sound pressure fields. They are given as

$$p^{\text{inc}}(\mathbf{x}) = \frac{1}{\sqrt{n_{\text{pw}}}} \sum_{i=1}^{n_{\text{pw}}} A_i e^{\mathbf{k}_i \cdot \mathbf{x} + \varphi_i}, \quad (2.64)$$

for the coordinates $\mathbf{x} \in \mathbb{R}^3$. The values of A_i and φ_i are randomly chosen amplitudes and phase angles, respectively. The wave vector $\mathbf{k}_i \in \mathbb{R}^3$ is described in spherical coordinates with the radius $r = \omega/c$, incident angle $\phi \in [0, \pi)$ and azimuth angle $\theta \in [0, 2\pi)$ of each plane wave. The values of both angles are uniformly distributed and $n_{\text{pw}} = 1145$ is chosen according to [150].

In the present thesis, a total of n_{rhs} incident wave fields in the form of Eq. (2.64) are sampled for the calculation of the structural acoustic response to a diffuse sound field excitation. Therefore, the solution of the fully coupled FEM-BEM system in Eq. (2.62) with multiple right-hand sides needs to be obtained. It is abbreviated by

$$\mathbf{A}(\boldsymbol{\mu})\mathbf{X}(\boldsymbol{\mu}) = \mathbf{B}(\boldsymbol{\mu}), \quad (2.65)$$

with the system matrix $\mathbf{A}(\boldsymbol{\mu})$, solution matrix $\mathbf{X}(\boldsymbol{\mu})$ and right-hand side matrix $\mathbf{B}(\boldsymbol{\mu})$. Furthermore, the d -dimensional parameter vector

$$\boldsymbol{\mu} = [\boldsymbol{\lambda}, \omega] = [\lambda_1, \dots, \lambda_{d-1}, \omega]. \quad (2.66)$$

includes the dependencies on the frequency and additional structural parameters. The right-hand side matrix \mathbf{B} contains n_{rhs} column vectors. They store the sound pressure values of

the individual incident pressure fields as well as possible structural loads at the degrees of freedom according to Eq. (2.63). The total response to the diffuse sound pressure field is given by the mean of the column vectors stored in \mathbf{X} . Since a larger number of realizations of the incident wave field yields better approximations of the diffuse sound field, a large number of right-hand sides needs to be considered. Hence, computationally efficient iterative solution techniques for sequences of linear systems are required.

2.4.2 Nonlinear acoustic eigenvalue analysis

The eigenfrequencies and modal damping values of acoustic or structural acoustic systems are crucial design criteria. They provide valuable insight on the dynamics of the system and assist in describing physical effects such as radiation damping [203]. Determining the modal parameters by means of an eigenvalue analysis is common practice when designing acoustic metamaterials [73, 105, 107]. Locally resonant periodic structures usually accomplish a high sound attenuation in the close vicinity of their eigenfrequencies [98].

Obtaining the eigenvalues and eigenvectors of boundary element discretized Helmholtz problems requires the solution of a nonlinear eigenvalue problem (NLEVP). Applying the periodic boundary element formulation, the NLEVP reads

$$\mathbf{T}(\tilde{\omega})\Phi = \mathbf{0}, \quad (2.67)$$

with the multilevel block Toeplitz matrix \mathbf{T} and the nonzero eigenvector Φ as well as the corresponding complex eigenvalue parameter $\tilde{\omega}$. The eigenfrequency coincides with the real part of $\tilde{\omega}$, whereas the modal damping is given by its imaginary part.

An efficient class of techniques to solve Eq. (2.67) are contour integral methods. They extract all eigenvalues and corresponding eigenvectors that lie within a contour of the complex plane, visualized in Fig. 2.4. The block Sakurai Sugiura (block-SS, [108]) is one of many variants [109, 110, 204, 205]. It transforms the nonlinear eigenvalue problem into the generalized eigenvalue problem

$$(\mathbf{H}_2 - \hat{\omega}\mathbf{H}_1)\hat{\Phi} = \mathbf{0}, \quad (2.68)$$

with Hankel matrices \mathbf{H}_1 and \mathbf{H}_2 of size $KL \times KL$. Both K and L are parameters of the eigensolver and their product is significantly smaller than the size of the system matrix in the original nonlinear eigenvalue problem. The solution of the generalized eigenvalue problem Eq. (2.68) involves only little computational effort and yields the complex eigenvalue parameters $\hat{\omega}$. They coincide with those eigenvalue parameters $\tilde{\omega}$ of Eq. (2.67) that lie inside the contour \mathcal{C} . Setting up Eq. (2.68) requires the assembly of the Hankel matrices given by

$$\mathbf{H}_1 = [\mathbf{M}_{i+j-2}]_{i,j=1}^K \quad \text{and} \quad \mathbf{H}_2 = [\mathbf{M}_{i+j-1}]_{i,j=1}^K, \quad (2.69)$$

with a positive integer K and the sequence of moments

$$\mathbf{M}_k = \frac{1}{2\pi i} \oint_{\mathcal{C}} z^k \mathbf{V}^* \mathbf{T}(z)^{-1} \mathbf{V} dz, \quad k = 0, 1, \dots, 2K - 1. \quad (2.70)$$

Herein, the complex coordinate z parameterizes the contour \mathcal{C} , \mathbf{V} is a random, complex-valued matrix of size $N_{\text{dof}} \times L$ and \mathbf{V}^* denotes its conjugate transpose. Applying the trapezoidal rule to the contour integral leads to an approximation of the moments by

$$\mathbf{M}_k \approx \frac{1}{N_c} \sum_{j=0}^{N_c-1} \rho \left(\frac{z_j - \gamma}{\rho} \right)^{k+1} \mathbf{V}^* \mathbf{T}(z_j)^{-1} \mathbf{V}, \quad (2.71)$$

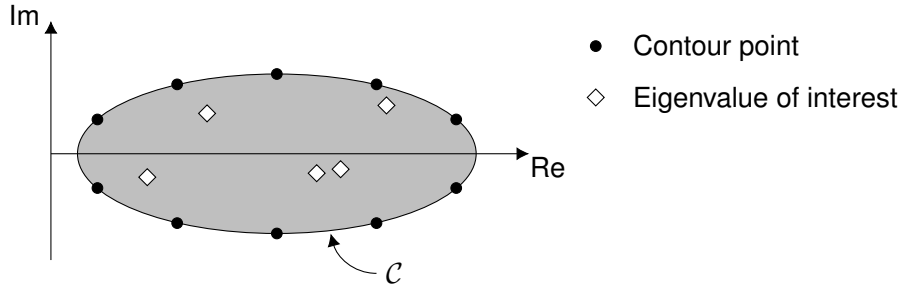


Figure 2.4: Contour points z_j on the contour \mathcal{C} that encloses all eigenvalues of interest.

with the N_c contour points $z_j = \gamma + \rho e^{i\theta_j}$ along a circular contour in polar coordinates with center γ , radius ρ , and angle θ_j [108]. Once the generalized eigenvalue problem of Eq. (2.68) is solved, the determined eigenvectors $\hat{\Phi}$ are transferred back to obtain Φ .

Evaluating the sequence of moments given by Eq. (2.71) contributes to a large fraction of the computational effort due to the need of solving the discretized system of linear equations for all columns in \mathbf{V} . Both the number of contour points N_c and the value of L mainly determine the accuracy of the contour integral method. Choosing a large number of contour points results in a more accurate approximation of the sequence of moments, whereas higher values of L enlarge the subspace in which the eigenvalues are sought. This has a direct impact on the computational efficiency since the linear system $\mathbf{T}(z_j)^{-1}\mathbf{V}$ is solved at each of the N_c contour points and for each of the L right-hand sides. Therefore, efficient solution techniques for linear systems with many right-hand sides are required in order to achieve highly accurate estimations of the eigenvalues and eigenvectors at reasonable computational costs. This similarly holds for other contour integral methods such as the block-SS with resolvent sampling [206] or nonlinear FEAST algorithms [110]. The details on two efficient iterative solution techniques are outlined in the following.

2.4.3 Block Krylov subspace methods

Consider a system of linear equations $\mathbf{A}\mathbf{X} = \mathbf{B}$ where the matrix \mathbf{B} stores n_{rhs} right-hand sides as column vectors. Block Krylov subspace solvers create an intermediate solution \mathbf{X}_k within each iteration k that fulfills the relation

$$\mathbf{X}_k - \mathbf{X}_0 \in \mathcal{K}_k^\square(\mathbf{A}, \mathbf{R}_0), \quad (2.72)$$

with an initial estimate \mathbf{X}_0 of the solution. The initial residual is given by $\mathbf{R}_0 = \mathbf{B} - \mathbf{A}\mathbf{X}_0$ and the block Krylov subspace of iteration k is denoted by $\mathcal{K}_k^\square(\mathbf{A}, \mathbf{R}_0)$. The superscript $(\)^\square$ indicates the block nature of the subspace which is given by

$$\mathcal{K}_k^\square(\mathbf{A}, \mathbf{R}_0) = \left\{ \sum_{i=0}^{k-1} \mathbf{A}^i \mathbf{R}_0 \gamma_i; \gamma_i \in \mathbb{C}^{n_{\text{rhs}} \times n_{\text{rhs}}}, i = 0, \dots, k-1 \right\}, \quad (2.73)$$

following the notation of Gutknecht [164]. The repeated multiplications of the system matrix \mathbf{A} with itself and the initial residual \mathbf{R}_0 are weighted by the $n_{\text{rhs}} \times n_{\text{rhs}}$ matrices γ_i . They span the block Krylov subspace and approximate each column of the matrix $\mathbf{X}_k - \mathbf{X}_0$ by a linear combination. The size of the block Krylov subspace is larger than the size of the subspaces built by standard Krylov methods. Each iteration adds up to n_{rhs} additional Krylov vectors to the subspace. Therefore, a larger number of vectors is available for the approximation of the solution

which generally leads to a convergence of the solution in less iterations [164]. Building a block Krylov subspace not only increases the memory requirements but might also result in linearly or nearly linearly dependent columns within the block Krylov subspace. This requires deflation in order to detect and delete linearly dependent columns and prevent breakdowns [207]. In addition, the computational burden can be reduced by detecting linearly dependent right-hand side vectors upfront. Performing a truncated singular value decomposition of the right-hand side matrix allows to reduce the number of columns of \mathbf{B} , and thus the computational effort [169].

Employing the block Arnoldi process for obtaining the block Krylov basis leads to the block GMRes method presented by Vital [208]. Storing and extending this space in every iteration accounts for a significant part of the computational cost and memory at high iterations counts. This can be resolved by restarting the solver after a certain number of iterations [209] or by preconditioning the linear system [175, 210].

2.4.4 Global Krylov subspace methods

Global Krylov subspace solvers construct an intermediate solution \mathbf{X}_k in each iteration k such that

$$\mathbf{X}_k - \mathbf{X}_0 \in \mathcal{K}_k(\mathbf{A}, \mathbf{R}_0), \quad (2.74)$$

holds. Contrary to block methods, a matrix Krylov subspace $\mathcal{K}_k(\mathbf{A}, \mathbf{R}_0)$ is built which is defined as [164]

$$\mathcal{K}_k(\mathbf{A}, \mathbf{R}_0) = \left\{ \sum_{i=0}^{k-1} \mathbf{A}^i \mathbf{R}_0 \gamma_i; \gamma_i \in \mathbb{C}, i = 0, \dots, k-1 \right\}. \quad (2.75)$$

The matrices that span the subspace of Eq. (2.75) are weighted by the scalars γ_i in order to approximate the entire matrix $\mathbf{X}_k - \mathbf{X}_0$. This substantially differs from the methodology of the aforementioned block methods where each column of the matrix is approximated independently. The search space of the global methods is much smaller which leads to slower convergence. However, the memory requirements are less demanding [164].

Orthogonalizing the basis by means of the global Arnoldi process leads to the global GMRes method introduced by Jbilou et al. [171]. The matrices \mathbf{V}_i that store the basis vectors of each iteration i are F -orthonormal, i.e., $\text{tr}(\mathbf{V}_i^* \mathbf{V}_j) = 0$ for $i \neq j$ and $i, j = 0, \dots, k-1$ with $\text{tr}(\cdot)$ denoting the trace. In contrast to block methods, linearly dependence does not occur.

3 Summary of publications

This chapter provides a brief summary of the publications [Paper A \[177\]](#), [Paper B \[178\]](#) and [Paper C \[179\]](#). It highlights their key results and indicates the authors' individual contributions. Reprints of the full texts are provided in [Appendix A](#).

3.1 Paper A

Fast multipole boundary element method for the acoustic analysis of finite periodic structures

Christopher Jelic, Wenchang Zhao, Haibo Chen, Steffen Marburg

Summary

Periodic arrangements of locally resonant structures are very efficient in modifying the propagation of sound. They are referred to as acoustic metamaterials when exhibiting macroscopic properties that are not found in naturally occurring materials. This includes the formation of frequency bands at which sound propagation is prohibited in certain directions. Established by local resonances of the individual structural components but also by arranging the components periodically, a very high sound attenuation can be achieved in these frequency bands at the macroscopic scale [73]. Precisely tailoring the design of acoustic metamaterials offers great potential for compact and effective vibroacoustic structures. Numerical methods play a crucial role in this process due to the complexity of the designs. Most schemes consider a metamaterial composed of identical substructures that are described by a representative volume element or unit cell. In addition, they assume that the metamaterial is of infinite extent. Under these assumptions, the characteristics of the wave propagation within the metamaterial are obtained by solving multiple eigenvalue problems of the unit cell with specialized boundary conditions. Unfortunately, these approaches do not incorporate any diffraction at edges of the eventually finite-sized metamaterial or scattering by the ground. These effects are only covered by a full-scale, three-dimensional analysis of the acoustic metamaterial.

To this end, two fast multipole boundary element formulations are presented for the acoustic analysis of finite periodic structures. Existing strategies either rely on the aforementioned assumptions and are thus not feasible or demand excessive computational resources. The proposed methods subdivide the geometry into boxes which coincide with the unit cell. Boundary elements discretize the unit cells and the fast multipole method approximates the interactions between well-separated boxes. Due to the periodic layout, the fast multipole operators assemble into structured matrices such as block diagonal and block Toeplitz matrices. This representation secures fast matrix-vector products and significantly reduces the memory requirements; thus permitting simulations of large-scale metamaterials.

Two numerical examples demonstrate the computational efficiency of the presented formulations. The first example considers a periodic arrangement of spherical scatterers with small unit cell discretizations sharing only a few thousand degrees of freedom. The first formulation outperforms state-of-the-art approaches by an order of magnitude in both time and memory. A similar performance is reported for the second formulation which is especially suited for unit cell discretizations sharing large numbers of degrees of freedom. It features a more favorable asymptotic scaling due to applying an additional level of fast multipole expansions to the near-field interactions. The second example consists of a noise barrier design study which compares the sound attenuation achieved by a wall noise barrier and two sonic crystal noise barriers. The formulations allow to depict the acoustic behavior in a broad frequency range and validate the noise barrier designs at full scale.

Altogether, the two proposed formulations efficiently describe the acoustic wave propagation in metamaterials and periodically arranged structures. This holds for both small-scale metamaterials as well as large arrangements with unit cell discretizations that feature tens of thousands of degrees of freedom. Further development could include applying the same

concept to rotationally arranged structures such as ducts, mufflers and fans. In addition, taking visco-thermal losses or structural acoustic coupling into account would extend the computational possibilities of the presented formulations even further. Finally, local defects or disturbances of the periodic arrangement could be represented by low-rank updates of the corresponding fast multipole operators.

Contribution

Christopher Jelic contributed to the conceptualization and derivation of the numerical algorithms. Christopher Jelic and Wenchang Zhao carried out the code implementation. Christopher Jelic conducted the numerical simulations and prepared the draft of the manuscript. Christopher Jelic and Wenchang Zhao contributed to the discussion of the results. All authors provided critical feedback and approved the final version of the manuscript.

Reference

C. Jelic, W. Zhao, H. Chen and S. Marburg. Fast multipole boundary element method for the acoustic analysis of finite periodic structures. *Computer Methods in Applied Mechanics and Engineering*, 391:114528, 2022.

3.2 Paper B

A greedy reduced basis algorithm for structural acoustic systems with parameter and implicit frequency dependence

Christopher Jelich, Suhaib Koji Baydoun, Matthias Voigt, Steffen Marburg

Summary

The process of designing quiet machines and vehicles relies on an efficient evaluation of vibroacoustic properties such as the radiated sound power and the transmission loss prior to manufacturing. The coupled finite element method (FEM) and boundary element method (BEM) offer great potential in this regard. Despite recent advances, analyzing the dynamics of a system for a variety of design parameters and frequencies is still computationally challenging. The usual approach requires repeated evaluations of the coupled FEM-BEM system at each frequency and each set of parameter values of interest. Model order reduction (MOR) methods aim to reduce this computational effort. However, many techniques are infeasible to apply due to the implicit frequency dependence of the FEM-BEM system.

To this end, the present publication proposes a greedy reduced basis scheme for the solution of fully coupled FEM-BEM systems with parameter and implicit frequency dependence. The time-harmonic equations of linear elastodynamics and acoustics are discretized by the finite element and boundary element method, respectively. This leads to an implicitly frequency dependent system of linear equations. Aside from the frequency, an additional set of parameters is considered which spans a high-dimensional parameter space. In the present work, variations of the material parameters and the rotational stiffness values of joints that connect the individual structural components are considered. The developed MOR scheme obtains the solution within the parameter domain by a linear combination of reduced basis vectors. This basis is built iteratively and each basis vector coincides with the response of the FEM-BEM system at certain parameter samples. The samples are chosen in a greedy fashion, i.e., at the parameter combination at which the solution is currently approximated worst. Considering high-dimensional parameter spaces or large-scale vibroacoustic problems leads to infeasible memory requirements. The algorithm remedies this by starting on a small subset of the discretized parameter domain. Hence, only a limited number of FEM-BEM systems needs to be assembled at the same time. In addition, the reduced basis scheme includes an extension to address parameter dependent systems with multiple right-hand sides. In each iteration, a truncated singular value decomposition (SVD) of the responses is computed to extract its major components. The corresponding left singular vectors are then added to the reduced basis.

The computational efficiency of the proposed greedy reduced basis scheme is demonstrated in two numerical examples. The first example considers a point-excited spherical shell that is submerged in water and made of a homogeneous linear elastic material. Both frequency and Young's modulus span the parameter domain which is discretized by 89 and 11 points in each direction, respectively. The proposed scheme outperforms the conventional approach of solving each system sequentially. Furthermore, the results indicate that starting on a small subset of the discretized parameter domain is more beneficial than starting on the full set. The second numerical example considers a simplified satellite structure that consists of six aluminum honeycomb panels. The panels are connected by joints that are represented by a series of linear elastic springs. Their stiffness values span a three-dimensional parameter space together with the frequency. A diffuse incident field acts on the structure which is

modeled by a large number of incident plane waves. This leads to a parameterized problem with multiple right-hand sides. The results validate the computational efficiency of the greedy reduced basis scheme. The extension to cases with multiple excitations manages to maintain a small basis containing vectors with high approximation power. Suitable truncation values for the singular value decomposition are indicated.

In conclusion, the proposed greedy reduced basis scheme is an efficient measure to solve parameter and implicitly frequency dependent vibroacoustic problems. An extension of the algorithm covers the case of multiple right-hand sides. Following the results of [Paper C \[179\]](#), the block GMRes method is incorporated into this extension in order to accelerate the solution of the FEM-BEM system. The algorithm paves the way for highly productive parameter studies within the design processes of vibroacoustic structures. This is owed to its efficiency in obtaining an approximate solution for all samples of the discretized parameter domain at a predefined accuracy.

Contribution

Christopher Jelic, Suhaib Koji Baydoun and Matthias Voigt conceived the general concept of the model order reduction method. Christopher Jelic carried out the code implementation, performed the numerical simulations and prepared the draft of the manuscript. Christopher Jelic, Matthias Voigt and Suhaib Koji Baydoun contributed to the discussion of the results. All authors provided critical feedback and approved the final version of the manuscript.

Reference

C. Jelic, S. K. Baydoun, M. Voigt and S. Marburg. A greedy reduced basis algorithm for structural acoustic systems with parameter and implicit frequency dependence. *International Journal of Numerical Methods in Engineering*, 122(24):7409–7430, 2021.

3.3 Paper C

Efficient solution of block Toeplitz systems with multiple right-hand sides arising from a periodic boundary element formulation

Christopher Jelich, Mahmoud Karimi, Nicole Kessissoglou, Steffen Marburg

Summary

Studying the aeroacoustic behavior of structures subject to fluid flow is of great importance. It allows to find designs that ensure structural integrity but also comply with regulations and consumer demands. Passenger aircrafts for instance are obliged to be durable but also quiet. In many cases, the turbulent flow in the vicinity of the bounding surfaces contributes to the major source of flow-induced noise. This turbulent boundary layer (TBL) excitation can be modeled using a set of uncorrelated wall pressure waves (UWPW) based on the description of the surrounding flow by either empirical models, experimental data or a steady-state Reynolds-averaged Navier-Stokes solution [211]. The flow-induced noise is then obtained by solving a series of structural acoustic scattering problems with realizations of the UWPW as incident field [212]. Accelerating this subsequent analysis step improves the computational efficiency of the overall numerical scheme which is especially useful when using empirical models or experimental data for the characterization of the UWPW.

The need of obtaining the acoustic responses to a variety of excitations is also present in recently introduced nonlinear eigenvalue solvers based on contour integration. They require the solution at various frequency points along a contour in the complex plane. This contributes to the main computational burden since multiple right-hand sides need to be considered at each frequency point. Accelerating the solution process paves the way for more accurate and less time consuming solutions of nonlinear eigenvalue problems.

To this end, an efficient numerical scheme to solve acoustic scattering problems subject to multiple excitations is presented in this publication. The structural components are assumed to be rigid and thus, only the unbound acoustic domain is discretized. Employing the boundary element method and considering structures that are composed of periodically arranged unit cells yields a computationally efficient representation of the discretized linear system. The system matrices become block Toeplitz matrices which feature a reduced asymptotic complexity in time and memory for assembly and matrix-vector multiplications. This benefit can be utilized to its full extent by employing iterative solvers. Three Krylov subspace solvers are implemented for the solution of the block Toeplitz systems with multiple right-hand sides. The first variant is one of the most commonly used Krylov subspace solvers, the generalized minimal residual (GMRes) method [153]. It sequentially obtains the solution to each individual right-hand side without taking information of the previous solutions into account. The remaining two methods are the global and block variants of the GMRes method which obtain a solution to all right-hand side at once, utilizing similarities of the solutions to different right-hand sides [171, 208]. The performance of all three schemes is assessed in terms of the wall clock time of the iterative solution process, the number of multiplications with the block Toeplitz system matrix and the peak memory usage.

Two case studies are presented to demonstrate the approach: The evaluation of the aeroacoustic noise from turbulent flow around a flat plate airfoil and a nonlinear eigenvalue analysis of a sonic crystal noise barrier. Both numerical examples indicate a significant reduction of the solution time by employing global and block GMRes. Their solution times scale more favorably with respect to the number of right-hand sides which encourages their application to problems

with a large number of different excitations. Noteworthy, the standard and global GMRes methods obtain the solution within the same number of iterations. Therefore, the speedup of the global GMRes can be attributed to performing matrix-matrix instead of matrix-vector products. In the case of the block GMRes method, less iterations are required to obtain the solution due to extending the search space by a larger quantity of Krylov vectors in each iteration.

Altogether, the present work applies global and block GMRes to solve boundary element discretized Helmholtz problems with multiple right-hand sides and provides a comparison to the standard GMRes method. The numerical results show that employing the block variant significantly increases the efficiency of two numerical schemes that predict aeroacoustic noise and solve nonlinear acoustic eigenvalue problems. The findings of the present work encouraged the introduction of the block GMRes into a recently introduced subspace iteration eigensolver based on Cauchy integrals [63] and into the nonlinear model order reduction technique presented in [Paper B \[178\]](#).

Contribution

Christopher Jelic and Mahmoud Karimi conceived the general concept of the proposed numerical scheme. Christopher Jelic carried out the code implementation, performed the numerical simulations and prepared the draft of the manuscript. Christopher Jelic, Mahmoud Karimi and Nicole Kessissoglou contributed to the discussion of the results. All authors provided critical feedback and approved the final version of the manuscript.

Reference

C. Jelic, M. Karimi, N. Kessissoglou, and S. Marburg. Efficient solution of block Toeplitz systems with multiple right-hand sides arising from a periodic boundary element formulation. *Engineering Analysis with Boundary Elements*, 130:135–144, 2021.

4 Discussion and conclusion

Highly efficient computational methods that precisely describe acoustic and elastodynamic wave propagation phenomena are an important tool of today's engineers. They open up the possibility to investigate the acoustic and vibroacoustic properties of a broad variety of product designs ahead of production. Combined with optimization algorithms, these numerical analysis techniques pave the way for finding the optimal design that complies with multi-disciplinary objectives. These objectives might include the structural integrity under various load cases but also acoustic properties such as a broadband sound attenuation or a specific sound characteristic. Existing strategies for solving vibroacoustic problems at low frequencies usually rely on finite element methods or coupled finite and boundary element methods. The latter is especially convenient for the commonly occurring case of unbound computational domains. Despite the research efforts of the previous decades, limitations of finite element and boundary element methods are still present today. First, currently available techniques for the full-scale analysis of periodic structures necessitate substantial computational efforts; rendering their application infeasible. Second, solving parameterized structural acoustic problems with a FEM-BEM approach yields a system of linear equations with parameter and implicit frequency dependencies. Its repeated evaluation for all frequencies and parameter values of interest comes at a significant cost. Lastly, existing methodologies lack efficient strategies to address multiple load cases.

This cumulative thesis provides remedies to the aforementioned limitations of finite element and boundary element methods in acoustics and vibroacoustics. [Paper A \[177\]](#) presents two fast multipole boundary element formulations for the acoustic analysis of structures with finite periodicity. Both formulations fully utilize the special matrix structure that arises from applying the boundary element method to periodic structures. By incorporating the fast multipole method, large-scale problems with millions of degrees of freedom can be addressed. In addition, [Paper B \[178\]](#) introduces a novel greedy reduced basis scheme for structural acoustic problems with parameter and implicit frequency dependencies. It obtains an approximate solution within the possibly high-dimensional parameter space by a linear combination of a few high-fidelity solutions. Lastly, [Paper C \[179\]](#) investigates the application of sophisticated Krylov subspace solvers to obtain the solution to acoustic problems with multiple right-hand sides. This approach is validated in a calculation of flow-induced noise around an airfoil and an eigenvalue analysis of an acoustic metamaterial. In summary, the present work introduces three methodologies that accelerate acoustic and vibroacoustic analyses using finite element and boundary element methods. They are successfully applied to a range of applications including the parameter study of a satellite structure, the prediction of flow-induced noise and the design of noise barriers.

Optimizing structural components to achieve a desired acoustic behavior is an omnipresent task of engineers. Noise barriers are a prominent example where the intent is to accomplish high levels of sound abatement. Current designs consist of vertical screens that are supported by metal profiles sitting on a concrete foundation. They mitigate traffic-induced noise along roads and railways by intercepting the propagating sound waves [213]. Being located at close distance to the noise emitting source, their height allows to restrict direct passage of acoustic waves while attenuating the diffraction in a way that critical reflections between the barrier and the noise emitting source are avoided [214]. More recent efforts intent to incorporate additional physical effects in order to keep up with the increasing requirements on the performance of noise barriers. Periodically arranging locally resonant structures has been

proven to yield noise barrier designs that achieve an excellent sound attenuation over broad frequency ranges [86, 98]. Assessing these quantities upfront by means of numerical methods is still challenging. Existing techniques are not capable of modeling large-scale noise barrier designs in three-dimensional space. Designers instead rely on simplified models based on a single unit cell representation [92, 107] or on 2d [77, 89, 98] and 2.5d models [119]. These approaches impose strict requirements on the incident sound field, the boundary conditions and the solution. They must either be constant, periodic or quasi-periodicity in certain directions. Furthermore, reflections from the ground and edge effects are neglected. To this end, [Paper A](#) introduces two fast multiple periodic boundary element formulations for the three-dimensional acoustic analysis of finite periodic structures. Both formulations rely on subdividing the geometry into unit cells to which the fast multipole boundary element method is applied. The discretized system of linear equations features structured matrices due to periodic layout of the unit cells. This leads to a small memory footprint as well as matrix-vector products with a quasi-linear complexity in time. In conjunction with an acoustic half-space formulation, the presented methodology allows to efficiently assess the sound attenuation properties of periodic noise barrier designs within typical frequency ranges of interest. Contrary to the aforementioned modeling approaches, the developed formulations allow accurate and computational efficient analysis of full scale, three-dimensional periodic structures. [Paper A](#) paves the way for a reliable validation of noise barrier designs prior to prototyping. However, its application goes beyond the validation of noise barrier designs and covers general acoustic problems with finite periodic geometry. This includes acoustic metamaterials which are often based on a periodic arrangement of locally resonant structures. They exhibit extraordinary properties and might find their way into various structural designs in the near future. In this regard, extending the presented formulations to visco-thermal losses would be a worthwhile contribution [215, 216]. Furthermore, local defects could be incorporated by introducing cost-efficient low-rank updates of the system matrices.

The product development process involves studying various different designs and evaluating their performance with respect to multidisciplinary objectives. Expressing the design parameters within the governing equations allows to set up a parameterized system of linear equations. Parametric model order reduction methods then allow to obtain the solution for a broad range of parameter samples with high efficiency [132]. Unfortunately, their application to the FEM-BEM system of vibroacoustic problems is limited due to the implicit frequency dependence of the boundary element matrices. The discrete empirical interpolation method (DEIM) provides a remedy by approximating the nonlinear parameter dependence by an affine representation based on a few evaluations of the original system [131]. Alternatively, Proper Orthogonal Decomposition (POD) schemes evaluate the high-fidelity solutions at a priori chosen sampling points in order to generate a basis for the solution within the parameter domain [139]. More recently, Panagiotopoulos et al. [60] leveraged a series expansion of the Green's function to generate an affine representation of frequency dependent system matrix. Contrary to the aforementioned approaches, [Paper B](#) contributes an adaptively enriching greedy reduced basis scheme. The algorithm does not rely on the costly determination of an approximate affine representation or a series expansion that is meticulously tailored to the specific parameter dependence. Instead, it obtains a solution to a predefined number of parameter samples within a possibly high-dimensional parameter domain by a linear combination of a few basis vectors. The vectors correspond to the responses of the high-fidelity system at carefully chosen parameter samples. In contrast to POD schemes, these samples are chosen by the algorithm. In each iteration, the algorithm evaluates the high-fidelity system for the parameter sample at which the solution is currently approximated worst. This leads to

basis vectors with high approximation power without the need of providing an a priori choice. In addition, the greedy reduced basis scheme addresses vibroacoustic problems subject to multiple load cases. Instead of considering all responses, the algorithm reduces them based on a truncated singular value decomposition before appending the basis. The greedy reduced basis scheme presented in [Paper B](#) constitutes a powerful tool for efficiently obtaining the solution of parametrized vibroacoustic problems. Incorporating the scheme into an optimization algorithm could prove to be beneficial. The repeated evaluations of the system for slightly changing parameter values could be used to build a reduced basis which eventually accelerates the solution process with increasing iterations of the optimization algorithm. Possible improvements of the presented scheme include to start on a coarse discretization of the parameter domain and performing subsequent refining steps as in multigrid methods [217].

Acoustic and structural acoustic problems with multiple load cases arise in many applications. This includes the optimization of high-intensity focused ultrasonic transducers [149], the calculation of the sound transmission loss in coupled anechoic-reverberant chambers [218] and, more generally, the acoustic eigenvalue analysis by contour integral methods [219]. Usually, the response to each load case is obtained by sequentially solving each individual system independently using well-known iterative solvers such as the GMRes method [153]. However, more sophisticated variants exist such as global and block Krylov subspace methods [164]. Although block Krylov subspace methods show a superior performance in solving comparable electromagnetic problems [168, 169, 175], their application to boundary element discretized Helmholtz problems is still limited to the work of Zheng et al. [62]. To this end, [Paper C](#) presents the first comparison of block and global Krylov subspace methods for the solution of acoustic boundary element systems with multiple right-hand sides. The numerical studies indicate a significant reduction of the solution time when applying the global and block GMRes method instead of the standard GMRes solver. Assessing the memory requirements and asymptotic scalings in great detail is a valuable contribution of this work, easing the choice of the iterative solver for other members of the acoustic community. The results of [Paper C](#) inspired the use within an eigenvalue solver for vibroacoustic problems in unbound domains [63]. In addition, the nonlinear model order reduction method presented in [Paper B](#) [178] builds upon this work and utilizes the block GMRes method for obtaining the structural acoustic response to a diffuse incident sound field.

To conclude, the present thesis introduces accurate and efficient computational methods for acoustic and vibroacoustic analysis using finite element and boundary element methods. The applications are taken from the field of acoustics, aeroacoustics and vibroacoustics and validate the performance of the presented schemes. The work presents two fast multipole boundary element techniques for the acoustic analysis of finite periodic structures commonly found in noise barrier designs and acoustic metamaterials. Furthermore, a parameter model order reduction method is introduced that allows to efficiently obtain the solution for a large of number of parameter samples within a possibly high-dimensional parameter space. Lastly, this thesis addresses solution techniques for multiple load cases arising from turbulent boundary layer excitations in aeroacoustics, diffuse sound field excitations in vibroacoustics and random excitations featured in contour integral methods.

Bibliography

- [1] D. A. Bies, C. H. Hansen, and C. Q. Howard. *Engineering noise control*. CRC Press, 2017.
- [2] G. H. Koopmann and J. B. Fahline. *Designing quiet structures*. Elsevier, 1997.
- [3] H. Fastl and E. Zwicker. *Psychoacoustics*. Springer, Berlin, Heidelberg, 2007.
- [4] Z. Rarata, A. Dacko, T. Barciński, S. Polak, J. Musiał, S. Kubacki, T. Kowalski, A. Sikorski, and J. Baran. Vibro-acoustic response of spacecraft instrument subjected to diffuse sound field: Numerical simulations and experimental verification. *Applied Acoustics*, 184:108338, 2021.
- [5] M. C. Junger and D. Feit. *Sound, structures, and their interaction*. MIT Press, Cambridge, 1986.
- [6] F. P. Mechel, ed.. *Formulas of acoustics*. Springer, Berlin, Heidelberg, 2008.
- [7] T. Wang, C. D. Cooper, T. Betcke, and L. A. Barba. High-productivity, high-performance workflow for virus-scale electrostatic simulations with Bempp-Exafmm. *arXiv:2103.01048v2*, 2021.
- [8] T. Takahashi, C. Chen, and E. Darve. Parallelization of the inverse fast multipole method with an application to boundary element method. *Computer Physics Communications*, 247:106975, 2020.
- [9] M. Kravčenko, M. Merta, and J. Zapletal. Distributed fast boundary element methods for Helmholtz problems. *Applied Mathematics and Computation*, 362:124503, 2019.
- [10] S. Marburg and B. Nolte. A unified approach to finite and boundary element discretization in linear time-harmonic acoustics. In: S. Marburg and B. Nolte, eds., *Computational acoustics of noise propagation in fluids. Finite and boundary element methods*, pp. 1–34. Springer, Berlin, Heidelberg, 2008.
- [11] S. Kirkup. The boundary element method in acoustics: A survey. *Applied Sciences*, 9(8):1642, 2019.
- [12] S. Marburg. Boundary element method for time-harmonic acoustic problems. In: M. Kaltenbacher, ed., *Computational acoustics*, pp. 69–158. Springer, Wien, 2018.
- [13] I. Harari and T. J. R. Hughes. A cost comparison of boundary element and finite element methods for problems of time-harmonic acoustics. *Computer Methods in Applied Mechanics and Engineering*, 97(1):77–102, 1992.
- [14] O. von Estorff, ed.. *Boundary elements in acoustics: Advances and applications*. WIT Press, Southampton, 2000.
- [15] T. W. Wu, ed.. *Boundary element acoustics: Fundamentals and computer codes*. WIT Press, Southampton, 2000.
- [16] R. D. Ciskowski and C. A. Brebbia, eds.. *Boundary element methods in acoustics*. Springer Netherlands, 1991.

- [17] S. Kirkup. *The boundary element method in acoustics*. Integrated Sound Software, 2007.
- [18] T. Sakuma, S. Schneider, and Y. Yasuda. Fast solution methods. In: S. Marburg and B. Nolte, eds., *Computational acoustics of noise propagation in fluids. Finite and boundary element methods*, pp. 333–366. Springer, Berlin, Heidelberg, 2008.
- [19] M. Bebendorf and S. Rjasanow. Adaptive low-rank approximation of collocation matrices. *Computing*, 70(1):1–24, 2003.
- [20] E. Darve. The fast multipole method I: Error analysis and asymptotic complexity. *SIAM Journal on Numerical Analysis*, 38(1):98–128, 2000.
- [21] S. Börm, L. Grasedyck, and W. Hackbusch. Introduction to hierarchical matrices with applications. *Engineering Analysis with Boundary Elements*, 27(5):405–422, 2003.
- [22] W. Hackbusch. A sparse matrix arithmetic based on H-matrices. Part I: Introduction to H-matrices. *Computing*, 62(2):89–108, 1999.
- [23] M. Bebendorf. Approximation of boundary element matrices. *Numerische Mathematik*, 86(4):565–589, 2000.
- [24] M. Bebendorf. *Hierarchical matrices: A means to efficiently solve elliptic boundary value problems*. Springer, Berlin, Heidelberg, 2008.
- [25] W. Hackbusch. *Hierarchische Matrizen: Algorithmen und Analysis*. Springer, Berlin, Heidelberg, 2009.
- [26] L. Greengard and V. Rokhlin. A fast algorithm for particle simulations. *Journal of Computational Physics*, 73(2):325–348, 1987.
- [27] V. Rokhlin. Rapid solution of integral equations of scattering theory in two dimensions. *Journal of Computational Physics*, 86(2):414–439, 1990.
- [28] J. R. Phillips and J. K. White. A precorrected-FFT method for electrostatic analysis of complicated 3-D structures. *IEEE Transactions on Computer-Aided Design of Integrated Circuits and Systems*, 16(10):1059–1072, 1997.
- [29] J. Tausch. Sparse BEM for potential theory and Stokes flow using variable order wavelets. *Computational Mechanics*, 32(4-6):312–318, 2003.
- [30] G. Beylkin, R. Coifman, and V. Rokhlin. Fast wavelet transforms and numerical algorithms. In: *Fundamental Papers in Wavelet Theory*, pp. 741–783. Princeton University Press, 2009.
- [31] D. Brunner, M. Junge, P. Rapp, M. Bebendorf, and L. Gaul. Comparison of the fast multipole method with hierarchical matrices for the Helmholtz-BEM. *Computer Modeling in Engineering & Sciences*, 58(2):131–160, 2010.
- [32] D. C. Rapaport. *The art of molecular dynamics simulation*. Cambridge University Press, 2004.
- [33] R. Coifman, V. Rokhlin, and S. Wandzura. The fast multipole method for the wave equation: A pedestrian prescription. *IEEE Antennas and Propagation Magazine*, 35(3):7–12, 1993.

-
- [34] L. Greengard, J. Huang, V. Rokhlin, and S. Wandzura. Accelerating fast multipole methods for the Helmholtz equation at low frequencies. *IEEE Computational Science and Engineering*, 5(3):32–38, 1998.
- [35] N. Nishimura. Fast multipole accelerated boundary integral equation methods. *Applied Mechanics Reviews*, 55(4):299–324, 2002.
- [36] W. C. Chew, H. Y. Chao, T. J. Cui, C. C. Lu, S. Ohnuki, Y. C. Pan, J. M. Song, S. Velamparambil, and J. S. Zhao. Fast integral equation solvers in computational electromagnetics of complex structures. *Engineering Analysis with Boundary Elements*, 27(8):803–823, 2003.
- [37] N. A. Gumerov and R. Duraiswami. A broadband fast multipole accelerated boundary element method for the three dimensional Helmholtz equation. *The Journal of the Acoustical Society of America*, 125(1):191–205, 2009.
- [38] Y. J. Liu, S. Mukherjee, N. Nishimura, M. Schanz, W. Ye, A. Sutradhar, E. Pan, N. A. Dumont, A. Frangi, and A. Saez. Recent advances and emerging applications of the boundary element method. *Applied Mechanics Reviews*, 64(3), 2011.
- [39] S. Ohnuki and W. C. Chew. Truncation error analysis of multipole expansion. *SIAM Journal on Scientific Computing*, 25(4):1293–1306, 2004.
- [40] N. A. Gumerov and R. Duraiswami. *Fast multipole methods for the Helmholtz equation in three dimensions*. Elsevier Series in Electromagnetism. Elsevier, 2004.
- [41] Y. Liu. *Fast multipole boundary element method: Theory and applications in engineering*. Cambridge University Press, 2009.
- [42] R. Beatson and L. Greengard. A short course on fast multipole methods. In: *Wavelets, Multilevel Methods and Elliptic PDEs*, pp. 1–37. Oxford University Press, 1997.
- [43] C. A. White and M. Head-Gordon. Derivation and efficient implementation of the fast multipole method. *The Journal of Chemical Physics*, 101(8):6593–6605, 1994.
- [44] V. Rokhlin. Diagonal forms of translation operators for the Helmholtz equation in three dimensions. *Applied and Computational Harmonic Analysis*, 1(1):82–93, 1993.
- [45] M. Messner, M. Schanz, and E. Darve. Fast directional multilevel summation for oscillatory kernels based on Chebyshev interpolation. *Journal of Computational Physics*, 231(4):1175–1196, 2012.
- [46] B. Engquist and L. Ying. Fast directional multilevel algorithms for oscillatory kernels. *SIAM Journal on Scientific Computing*, 29(4):1710–1737, 2007.
- [47] B. Engquist and L. Ying. Fast directional algorithms for the Helmholtz kernel. *Journal of Computational and Applied Mathematics*, 234(6):1851–1859, 2010.
- [48] W. R. Wolf and S. K. Lele. Wideband fast multipole boundary element method: Application to acoustic scattering from aerodynamic bodies. *International Journal for Numerical Methods in Fluids*, 67(12):2108–2129, 2010.

- [49] H. Cheng, W. Y. Crutchfield, Z. Gimbutas, L. F. Greengard, J. F. Ethridge, J. Huang, V. Rokhlin, N. Yarvin, and J. Zhao. A wideband fast multipole method for the Helmholtz equation in three dimensions. *Journal of Computational Physics*, 216(1):300–325, 2006.
- [50] M. S. Bapat, L. Shen, and Y. J. Liu. Adaptive fast multipole boundary element method for three-dimensional half-space acoustic wave problems. *Engineering Analysis with Boundary Elements*, 33(8-9):1113–1123, 2009.
- [51] Y. Yasuda, K. Higuchi, T. Oshima, and T. Sakuma. Efficient technique in low-frequency fast multipole boundary element method for plane-symmetric acoustic problems. *Engineering Analysis with Boundary Elements*, 36(10):1493–1501, 2012.
- [52] T. Takahashi and T. Hamada. GPU-accelerated boundary element method for Helmholtz equation in three dimensions. *International Journal for Numerical Methods in Engineering*, 80(10):1295–1321, 2009.
- [53] I. Lashuk, G. Biros, A. Chandramowlishwaran, H. Langston, T.-A. Nguyen, R. Sampath, A. Shringarpure, R. Vuduc, L. Ying, and D. Zorin. A massively parallel adaptive fast-multipole method on heterogeneous architectures. In: *Proceedings of the Conference on High Performance Computing Networking, Storage and Analysis - SC '09*, pp. 1–12. ACM Press, 2009.
- [54] T. Wang, R. Yokota, and L. Barba. ExaFMM: a high-performance fast multipole method library with C++ and Python interfaces. *Journal of Open Source Software*, 6(61):3145, 2021.
- [55] N. A. Gumerov and R. Duraiswami. Fast multipole methods on graphics processors. *Journal of Computational Physics*, 227(18):8290–8313, 2008.
- [56] X. Xie and Y. Liu. An adaptive model order reduction method for boundary element-based multi-frequency acoustic wave problems. *Computer Methods in Applied Mechanics and Engineering*, 373:113532, 2021.
- [57] X. Xie and Y. Liu. Efficient multi-frequency solutions of FE–BE coupled structural–acoustic problems using Arnoldi-based dimension reduction approach. *Computer Methods in Applied Mechanics and Engineering*, 386:114126, 2021.
- [58] T. Liang, J. Wang, J. Xiao, and L. Wen. Coupled BE-FE based vibroacoustic modal analysis and frequency sweep using a generalized resolvent sampling method. *Computer Methods in Applied Mechanics and Engineering*, 345:518–538, 2019.
- [59] S. Dirckx, D. Huybrechs, and K. Meerbergen. Frequency extraction for BEM-matrices arising from the 3D scalar Helmholtz equation. *arXiv:2012.14287v1*, 2020.
- [60] D. Panagiotopoulos, E. Deckers, and W. Desmet. Krylov subspaces recycling based model order reduction for acoustic BEM systems and an error estimator. *Computer Methods in Applied Mechanics and Engineering*, 359:112755, 2020.
- [61] S. K. Baydoun, M. Voigt, C. Jelich, and S. Marburg. A greedy reduced basis scheme for multifrequency solution of structural acoustic systems. *International Journal for Numerical Methods in Engineering*, 121(2):187–200, 2020.

- [62] C.-J. Zheng, H.-F. Gao, L. Du, H.-B. Chen, and C. Zhang. An accurate and efficient acoustic eigensolver based on a fast multipole BEM and a contour integral method. *Journal of Computational Physics*, 305:677–699, 2016.
- [63] S. K. Baydoun, M. Voigt, B. Goderbauer, C. Jelich, and S. Marburg. A subspace iteration eigensolver based on Cauchy integrals for vibroacoustic problems in unbounded domains. *International Journal for Numerical Methods in Engineering*, 2021.
- [64] M. H. Cho and A. H. Barnett. Robust fast direct integral equation solver for quasi-periodic scattering problems with a large number of layers. *Optics Express*, 23(2):1775, 2015.
- [65] B. Wang, D. Chen, B. Zhang, W. Zhang, M. H. Cho, and W. Cai. Taylor expansion based fast multipole method for 3-D Helmholtz equations in layered media. *Journal of Computational Physics*, 401:109008, 2020.
- [66] C. Zheng, H. Chen, and L. Chen. A wideband fast multipole boundary element method for half-space/plane-symmetric acoustic wave problems. *Acta mechanica sinica*, 29(2):219–232, 2013.
- [67] Y. Otani and N. Nishimura. A periodic FMM for Maxwell’s equations in 3D and its applications to problems related to photonic crystals. *Journal of Computational Physics*, 227(9):4630–4652, 2008.
- [68] H. Ziegelwanger, P. Reiter, and M. Conter. The three-dimensional quasi-periodic boundary element method: Implementation, evaluation, and use cases. *International Journal of Computational Methods and Experimental Measurements*, 5(3):404–414, 2017.
- [69] N. Yoshii, Y. Andoh, and S. Okazaki. Fast multipole method for three-dimensional systems with periodic boundary condition in two directions. *Journal of Computational Chemistry*, 41(9):940–948, 2020.
- [70] R. Martínez-Sala, J. Sancho, J. V. Sánchez, V. Gómez, J. Llinares, and F. Meseguer. Sound attenuation by sculpture. *Nature*, 378(6554):241–241, 1995.
- [71] S. A. Cummer, J. Christensen, and A. Alù. Controlling sound with acoustic metamaterials. *Nature Reviews Materials*, 1:16001, 2016.
- [72] M. I. Hussein, M. J. Leamy, and M. Ruzzene. Dynamics of phononic materials and structures: Historical origins, recent progress, and future outlook. *Applied Mechanics Review*, 66(4):040802, 2014.
- [73] N. Jiménez, O. Umnova, and J.-P. Groby, eds.. *Acoustic waves in periodic structures, metamaterials, and porous media*. Springer International Publishing, 2021.
- [74] M. Maldovan. Sound and heat revolutions in phononics. *Nature*, 503(7475):209–217, 2013.
- [75] V. Romero-García, R. Picó, A. Cebreco, V. J. Sánchez-Morcillo, and K. Staliunas. Enhancement of sound in chirped sonic crystals. *Applied Physics Letters*, 102(9):091906, 2013.

- [76] M. Sigalas, M. S. Kushwaha, E. N. Economou, M. Kafesaki, I. E. Psarobas, and W. Steurer. Classical vibrational modes in phononic lattices: Theory and experiment. *Zeitschrift für Kristallographie - Crystalline Materials*, 220(9-10):765–809, 2005.
- [77] L. Chalmers, D. P. Elford, F. V. Kusmartsev, and G. M. Swallowe. Acoustic band gap formation in two-dimensional locally resonant sonic crystals comprised of Helmholtz resonators. *International Journal of Modern Physics B*, 23(20n21):4234–4243, 2009.
- [78] F. Langfeldt. *Membrane-type acoustic metamaterials for aircraft noise shields*. Ph.D. thesis, Hamburg University of Technology, 2018.
- [79] L. V. Belle, L. Sangiuliano, N. G. R. de Melo Filho, M. C. Villanueva, R. Boukadia, S. Ahsani, F. A. Pires, Z. Zhang, C. Claeys, E. Deckers, B. Pluymers, and W. Desmet. Vibro-acoustic metamaterials for improved interior NVH performance in vehicles. In: *Future Interior Concepts*, pp. 31–51. Springer International Publishing, 2020.
- [80] S. Kumar and H. Lee. The present and future role of acoustic metamaterials for architectural and urban noise mitigations. *Acoustics*, 1(3):590–607, 2019.
- [81] S.-H. Kim and S.-H. Lee. Air transparent soundproof window. *AIP Advances*, 4(11):117123, 2014.
- [82] A. Melnikov, M. Maeder, N. Friedrich, Y. Pozhanka, A. Wollmann, M. Scheffler, S. Oberst, D. Powell, and S. Marburg. Acoustic metamaterial capsule for reduction of stage machinery noise. *The Journal of the Acoustical Society of America*, 147(3):1491–1503, 2020.
- [83] L. Goines and L. Hagler. Noise pollution: A modern plague. *Southern Medical Journal*, 100(3):287–294, 2007.
- [84] D. Thompson. *Railway noise and vibration*. Elsevier, 2009.
- [85] U. Sandberg. The multi-coincidence peak around 1000 Hz in tyre/road noise spectra. *Euronoise Naples*, 89:1–8, 2003.
- [86] L. Fredianelli, A. D. Pizzo, and G. Licitra. Recent developments in sonic crystals as barriers for road traffic noise mitigation. *Environments*, 6(2):14, 2019.
- [87] P. Jean and J. Defrance. Sound propagation in rows of cylinders of infinite extent: Application to sonic crystals and thickets along roads. *Acta Acustica united with Acustica*, 101(3):474–483, 2015.
- [88] F. Morandi, M. Miniaci, A. Marzani, L. Barbaresi, and M. Garai. Standardised acoustic characterisation of sonic crystals noise barriers: Sound insulation and reflection properties. *Applied Acoustics*, 114:294–306, 2016.
- [89] D. P. Elford, L. Chalmers, F. V. Kusmartsev, and G. M. Swallowe. Matryoshka locally resonant sonic crystal. *The Journal of the Acoustical Society of America*, 130(5):2746–2755, 2011.
- [90] M. Karimi, P. Croaker, and N. Kessissoglou. Acoustic scattering for 3D multi-directional periodic structures using the boundary element method. *The Journal of the Acoustical Society of America*, 141(1):313–323, 2017.

- [91] B. Van der Aa and J. Forssén. Scattering by an array of perforated cylinders with a porous core. *The Journal of the Acoustical Society of America*, 136(5):2370–2380, 2014.
- [92] S. B. Fard, H. Peters, S. Marburg, and N. Kessissoglou. Acoustic performance of a barrier embedded with Helmholtz resonators using a quasi-periodic boundary element technique. *Acta Acustica united with Acustica*, 103(3):444–450, 2017.
- [93] F. Koussa, J. Defrance, P. Jean, and P. Blanc-Benon. Acoustical efficiency of a sonic crystal assisted noise barrier. *Acta Acustica united with Acustica*, 99(3):399–409, 2013.
- [94] A. Lardeau, J.-P. Groby, and V. Romero-García. Broadband transmission loss using the overlap of resonances in 3D sonic crystals. *Crystals*, 6(5):51, 2016.
- [95] C. Rubio, S. Castiñeira-Ibáñez, A. Uris, F. Belmar, and P. Candelas. Numerical simulation and laboratory measurements on an open tunable acoustic barrier. *Applied Acoustics*, 141:144–150, 2018.
- [96] D. Panda and A. R. Mohanty. Bandgaps creation with high acoustic losses in gradient-based sonic crystals. *Acoustics Australia*, 49(3):473–484, 2021.
- [97] H. Q. Nguyen, Q. Wu, H. Chen, J. J. Chen, Y. K. Yu, S. Tracy, and G. L. Huang. A Fano-based acoustic metamaterial for ultra-broadband sound barriers. *Proceedings of the Royal Society A*, 477:20210024, 2021.
- [98] T. Cavalieri, A. Cebrecos, J.-P. Groby, C. Chaufour, and V. Romero-García. Three-dimensional multiresonant lossy sonic crystal for broadband acoustic attenuation: Application to train noise reduction. *Applied Acoustics*, 146:1–8, 2019.
- [99] T. Ishizuka and K. Fujiwara. Performance of noise barriers with various edge shapes and acoustical conditions. *Applied Acoustics*, 65(2):125–141, 2004.
- [100] M. Baulac, J. Defrance, and P. Jean. Optimisation with genetic algorithm of the acoustic performance of T-shaped noise barriers with a reactive top surface. *Applied Acoustics*, 69(4):332–342, 2008.
- [101] L. Moheit, S. Anthis, J. Heinz, F. Kronowetter, and S. Marburg. Analysis of scattering by finite sonic crystals in free field with infinite elements and normal modes. *Journal of Sound and Vibration*, 476:115291, 2020.
- [102] M. Karimi, P. Croaker, and N. Kessissoglou. Boundary element solution for periodic acoustic problems. *Journal of Sound and Vibration*, 360:129–139, 2016.
- [103] L. Godinho, D. Soares, and P. G. Santos. Efficient analysis of sound propagation in sonic crystals using an ACA–MFS approach. *Engineering Analysis with Boundary Elements*, 69:72–85, 2016.
- [104] F. A. Amirkulova and A. N. Norris. Acoustic multiple scattering using recursive algorithms. *Journal of Computational Physics*, 299:787–803, 2015.
- [105] B. R. Mace and E. Manconi. Modelling wave propagation in two-dimensional structures using finite element analysis. *Journal of Sound and Vibration*, 318(4-5):884–902, 2008.

- [106] H. Isakari, T. Takahashi, and T. Matsumoto. Periodic band structure calculation by the Sakurai-Sugiura method with a fast direct solver for the boundary element method with the fast multipole representation. *Engineering Analysis with Boundary Elements*, 68:42–53, 2016.
- [107] H. Gao, L. Chen, H. Lian, C. Zheng, H. Xu, and T. Matsumoto. Band structure analysis for 2D acoustic phononic structure using isogeometric boundary element method. *Advances in Engineering Software*, 149:102888, 2020.
- [108] J. Asakura, T. Sakurai, H. Tadano, T. Ikegami, and K. Kimura. A numerical method for nonlinear eigenvalue problems using contour integrals. *JSIAM Letters*, 1:52–55, 2009.
- [109] W.-J. Beyn. An integral method for solving nonlinear eigenvalue problems. *Linear Algebra and its Applications*, 436(10):3839–3863, 2012.
- [110] B. Gavin, A. Międlar, and E. Polizzi. FEAST eigensolver for nonlinear eigenvalue problems. *Journal of Computational Science*, 27:107–117, 2018.
- [111] P. Reiter, R. Wehr, and H. Ziegelwanger. Simulation and measurement of noise barrier sound-reflection properties. *Applied Acoustics*, 123:133–142, 2017.
- [112] Y. W. Lam. A boundary integral formulation for the prediction of acoustic scattering from periodic structures. *The Journal of the Acoustical Society of America*, 105(2):762–769, 1999.
- [113] S. M. B. Fard, H. Peters, N. Kessissoglou, and S. Marburg. Three-dimensional analysis of a noise barrier using a quasi-periodic boundary element method. *The Journal of the Acoustical Society of America*, 137(6):3107–3114, 2015.
- [114] V. Rokhlin and S. Wandzura. The fast multipole method for periodic structures. In: *Proceedings of IEEE Antennas and Propagation Society International Symposium and URSI National Radio Science Meeting*, pp. 424–426. IEEE, 1994.
- [115] M. Challacombe, C. White, and M. Head-Gordon. Periodic boundary conditions and the fast multipole method. *The Journal of Chemical Physics*, 107(23):10131–10140, 1997.
- [116] N. A. Gumerov and R. Duraiswami. A method to compute periodic sums. *Journal of Computational Physics*, 272:307–326, 2014.
- [117] Y. Otani and N. Nishimura. An FMM for periodic boundary value problems for cracks for Helmholtz equation in 2D. *International Journal for Numerical Methods in Engineering*, 73(3):381–406, 2007.
- [118] K. Niino and N. Nishimura. Preconditioning based on Calderon’s formulae for periodic fast multipole methods for Helmholtz’ equation. *Journal of Computational Physics*, 231(1):66–81, 2012.
- [119] D. Duhamel. Efficient calculation of the three-dimensional sound pressure field around a noise barrier. *Journal of Sound and Vibration*, 197(5):547–571, 1996.
- [120] M. Karimi, P. Croaker, N. Peake, and N. Kessissoglou. Acoustic scattering for rotational and translational symmetric structures in nonuniform potential flow. *AIAA Journal*, 55(10):3318–3327, 2017.

-
- [121] G. H. Golub and C. F. Van Loan. *Matrix computations*. Johns Hopkins University Press, 1989.
- [122] P. Amado-Mendes, L. Godinho, J. Carbajo, and J. Ramis-Soriano. Numerical modelling of finite periodic arrays of acoustic resonators using an efficient 3D BEM model. *Engineering Analysis with Boundary Elements*, 102:73–86, 2019.
- [123] G. W. Benthien and H. A. Schenk. Structural-acoustic coupling. In: R. D. Ciskowski and C. A. Brebbia, eds., *Boundary Element Methods in Acoustics*, chapter Structural-acoustic coupling. Computational Mechanics Publications, Elsevier Applied Science, 1991.
- [124] S. M. Kirkup and D. J. Henwood. Methods for speeding up the boundary element solutions of acoustic radiation problems. *Journal of Vibration and Acoustics*, 144(3):347–380, 1992.
- [125] S. M. Kirkup and S. Amini. Solution of the Helmholtz eigenvalue problem via the boundary element method. *International Journal for Numerical Methods in Engineering*, 36(2):321–330, 1993.
- [126] T. W. Wu, W. L. Li, and A. F. Seybert. An efficient boundary element algorithm for multi-frequency acoustical analysis. *Journal of Acoustical Society of America*, 94(1):447–452, 1993.
- [127] M. El-Guide, A. Międlar, and Y. Saad. A rational approximation method for solving acoustic nonlinear eigenvalue problems. *Engineering Analysis with Boundary Elements*, 111:44–54, 2020.
- [128] H. Peters, N. Kessissoglou, and S. Marburg. Modal decomposition of exterior acoustic-structure interaction problems with model order reduction. *Journal of Acoustical Society of America*, 135(5):2706–2717, 2014.
- [129] U. Hetmaniuk, R. Tezaur, and C. Farhat. Review and assessment of interpolatory model order reduction methods for frequency response structural dynamics and acoustics problems. *International Journal for Numerical Methods in Engineering*, 90:1636–1662, 2012.
- [130] J. A. Wolf. Modal synthesis for combined structural-acoustic systems. *AIAA Journal*, 15(5):743–745, 1977.
- [131] S. Chaturantabut and D. C. Sorensen. Nonlinear model reduction via discrete empirical interpolation. *SIAM Journal on Scientific Computing*, 32(5):2737–2764, 2010.
- [132] P. Benner, S. Gugercin, and K. Willcox. A survey of projection-based model reduction methods for parametric dynamical systems. *SIAM Review*, 57(4):483–531, 2015.
- [133] A. C. Antoulas. *Approximation of large-scale dynamical systems*. Society for Industrial and Applied Mathematics, 2005.
- [134] F. Negri, A. Manzoni, and D. Amsallem. Efficient model reduction of parametrized systems by matrix discrete empirical interpolation. *Journal of Computational Physics*, 303:431–454, 2015.

- [135] F. Casenave, A. Ern, and T. Lelièvre. A nonintrusive reduced basis method applied to aeroacoustic simulations. *Advances in Computational Mathematics*, 41(5):961–986, 2014.
- [136] M. Fares, J. S. Hesthaven, Y. Maday, and B. Stamm. The reduced basis method for the electric field integral equation. *Journal of Computational Physics*, 230(14):5532–5555, 2011.
- [137] D. Kressner and C. Tobler. Low-rank tensor Krylov subspace methods for parametrized linear systems. *SIAM Journal on Matrix Analysis and Applications*, 32(4):1288–1316, 2011.
- [138] A. Quarteroni, A. Manzoni, and F. Negri. *Reduced basis methods for partial differential equations*. Springer International Publishing, 2016.
- [139] Y. C. Liang, H. P. Lee., S. P. Lim, W. Z. Lin, K. H. Lee, and C. G. Wu. Proper orthogonal decomposition and its applications - Part I: Theory. *Journal of Sound and Vibration*, 252(3):527–544, 2002.
- [140] P. Binev, A. Cohen, W. Dahmen, R. DeVore, G. Petrova, and P. Wojtaszczyk. Convergence rates for greedy algorithms in reduced basis methods. *SIAM Journal on Mathematical Analysis*, 43(3):1457–1472, 2011.
- [141] A. Buffa, Y. Maday, A. T. Patera, C. Prud'homme, and G. Turinici. A priori convergence of the greedy algorithm for the parametrized reduced basis method. *ESAIM: Mathematical Modelling and Numerical Analysis*, 46:595–603, 2012.
- [142] H. Jiang, X. Zhang, and X. Huang. Reduced-basis boundary element method for efficient broadband acoustic simulation. *Journal of Sound and Vibration*, 456:374–385, 2019.
- [143] F. Casenave, A. Ern, and T. Lelièvre. Accurate and online-efficient evaluation of the a posteriori error bound in the reduced basis method. *ESAIM: Mathematical Modelling and Numerical Analysis*, 48(1):207–229, 2014.
- [144] J. S. Hesthaven, B. Stamm, and S. Zhang. Efficient greedy algorithms for high-dimensional parameter spaces with applications to empirical interpolation and reduced basis methods. *ESAIM: Mathematical Modelling and Numerical Analysis*, 48(1):259–283, 2014.
- [145] A. S. Wixom and J. G. McDaniel. Fast frequency sweeps with many forcing vectors through adaptive interpolatory model order reduction. *International Journal for Numerical Methods in Engineering*, 100:442–457, 2014.
- [146] V. Kalantzis, A. C. I. Malossi, C. Bekas, A. Curioni, E. Gallopoulos, and Y. Saad. A scalable iterative dense linear system solver for multiple right-hand sides in data analytics. *Parallel Computing*, 74:136–153, 2018.
- [147] J. Chen, T. L. H. Li, and M. Anitescu. A parallel linear solver for multilevel Toeplitz systems with possibly several right-hand sides. *Parallel Computing*, 40(8):408–424, 2014.

- [148] J. Cavillot, D. Tihon, C. Craeye, E. de Lera Acedo, and N. Razavi-Ghods. Fast simulation technique for antenna installed on a finite ground plane. In: *2019 International Conference on Electromagnetics in Advanced Applications (ICEAA)*, pp. 0742–0745. IEEE, 2019.
- [149] E. van’t Wout, P. Gélat, T. Betcke, and S. Arridge. A fast boundary element method for the scattering analysis of high-intensity focused ultrasound. *The Journal of the Acoustical Society of America*, 138(5):2726–2737, 2015.
- [150] B. Rafaely. Spatial-temporal correlation of a diffuse sound field. *The Journal of the Acoustical Society of America*, 107(6):3254–3258, 2000.
- [151] Y. Saad. *Iterative methods for sparse linear systems*. Society for Industrial and Applied Mathematics, 2003.
- [152] S. Marburg and S. Schneider. Performance of iterative solvers for acoustic problems. Part I. Solvers and effect of diagonal preconditioning. *Engineering Analysis with Boundary Elements*, 27(7):727–750, 2003.
- [153] Y. Saad and M. H. Schultz. GMRES: A generalized minimal residual algorithm for solving nonsymmetric linear systems. *SIAM Journal on Scientific and Statistical Computing*, 7(3):856–869, 1986.
- [154] Y. Yasuda, S. Sakamoto, Y. Kosaka, T. Sakuma, N. Okamoto, and T. Oshima. Numerical analysis of large-scale sound fields using iterative methods. Part I: Application of Krylov subspace methods to boundary element analysis. *Journal of Computational Acoustics*, 15(04):449–471, 2007.
- [155] S. Marburg. The Burton and Miller method: Unlocking another mystery of its coupling parameter. *Journal of Computational Acoustics*, 24(01):1550016, 2016.
- [156] P. Marchand, J. Galkowski, A. Spence, and E. A. Spence. Applying GMRES to the Helmholtz equation with strong trapping: how does the number of iterations depend on the frequency? *arXiv:2102.05367v3*, 2021.
- [157] S. Schneider and S. Marburg. Performance of iterative solvers for acoustic problems. Part II. Acceleration by ILU-type preconditioner. *Engineering Analysis with Boundary Elements*, 27(7):751–757, 2003.
- [158] Y. Saad. A flexible inner-outer preconditioned GMRES algorithm. *SIAM Journal on Scientific Computing*, 14(2):461–469, 1993.
- [159] F. Kpadonou, S. Chaillat, and P. Ciarlet. On the efficiency of nested GMRES preconditioners for 3D acoustic and elastodynamic H-matrix accelerated boundary element methods. *Computers & Mathematics with Applications*, 80(3):471–489, 2020.
- [160] K. Chen and P. J. Harris. Efficient preconditioners for iterative solution of the boundary element equations for the three-dimensional Helmholtz equation. *Applied Numerical Mathematics*, 36(4):475–489, 2001.
- [161] T. Takahashi, P. Coulier, and E. Darve. Application of the inverse fast multipole method as a preconditioner in a 3D Helmholtz boundary element method. *Journal of Computational Physics*, 341:406–428, 2017.

- [162] M. Darbas, E. Darrigrand, and Y. Lafranche. Combining analytic preconditioner and fast multipole method for the 3-D Helmholtz equation. *Journal of Computational Physics*, 236:289–316, 2013.
- [163] E. van't Wout, S. R. Haqshenas, P. Gélat, T. Betcke, and N. Saffari. Benchmarking preconditioned boundary integral formulations for acoustics. *International Journal for Numerical Methods in Engineering*, 122(20):5873–5897, 2021.
- [164] M. H. Gutknecht. Block Krylov space methods for linear systems with multiple right-hand sides: An introduction. In: A. H. Siddiqi, I. Duff, and O. Christensen, eds., *Modern Mathematical Models, Methods and Algorithms for Real World Systems*, pp. 1–22. Anamaya Publishers, 2007.
- [165] T. F. Chan and W. L. Wan. Analysis of projection methods for solving linear systems with multiple right-hand sides. *SIAM Journal on Scientific Computing*, 18(6):1698–1721, 1997.
- [166] M. L. Parks, E. de Sturler, G. Macker, D. D. Johnson, and S. Maiti. Recycling Krylov subspaces for sequences of linear systems. *SIAM Journal on Scientific Computing*, 28(5):1651–1674, 2006.
- [167] A. Gaul. *Recycling Krylov subspace methods for sequences of linear systems*. Ph.D. thesis, TU Berlin, 2014.
- [168] H. C. Elman, O. G. Ernst, D. P. O'Leary, and M. Stewart. Efficient iterative algorithms for the stochastic finite element method with application to acoustic scattering. *Computer Methods in Applied Mechanics and Engineering*, 194(9-11):1037–1055, 2005.
- [169] J. Langou. *Iterative methods for solving linear systems with multiple right-hand sides*. Ph.D. thesis, L'Institut National des Sciences Appliquées de Toulouse, 2003.
- [170] L. Giraud, S. Gratton, and E. Martin. Incremental spectral preconditioners for sequences of linear systems. *Applied Numerical Mathematics*, 57(11-12):1164–1180, 2007.
- [171] K. Jbilou, A. Messaoudi, and H. Sadok. Global FOM and GMRES algorithms for matrix equations. *Applied Numerical Mathematics*, 31(1):49–63, 1999.
- [172] A. El Guennouni, K. Jbilou, and H. Sadok. A block version of BiCGSTAB for linear systems with multiple right-hand sides. *Electronic Transactions on Numerical Analysis*, 16(2):129–142, 2003.
- [173] V. Puzyrev and J. M. Cela. A review of block Krylov subspace methods for multi-source electromagnetic modelling. *Geophysical Journal International*, 202(2):1241–1252, 2015.
- [174] M. Malhotra, R. W. Freund, and P. M. Pinsky. Iterative solution of multiple radiation and scattering problems in structural acoustics using a block quasi-minimal residual algorithm. *Computer Methods in Applied Mechanics and Engineering*, 146(1-2):173–196, 1997.
- [175] H. Calandra, S. Gratton, R. Lago, X. Vasseur, and L. M. Carvalho. A modified block flexible GMRES method with deflation at each iteration for the solution of non-Hermitian linear systems with multiple right-hand sides. *SIAM Journal on Scientific Computing*, 35(5):S345–S367, 2013.

- [176] L. Du, T. Sogabe, B. Yu, Y. Yamamoto, and S.-L. Zhang. A block IDR(s) method for nonsymmetric linear systems with multiple right-hand sides. *Journal of Computational and Applied Mathematics*, 235(14):4095–4106, 2011.
- [177] C. Jelich, W. Zhao, H. Chen, and S. Marburg. Fast multipole boundary element method for the acoustic analysis of finite periodic structures. *Computer Methods in Applied Mechanics and Engineering*, 391:114528, 2022.
- [178] C. Jelich, S. K. Baydoun, M. Voigt, and S. Marburg. A greedy reduced basis algorithm for structural acoustic systems with parameter and implicit frequency dependence. *International Journal for Numerical Methods in Engineering*, 122(24):7409–7430, 2021.
- [179] C. Jelich, M. Karimi, N. Kessissoglou, and S. Marburg. Efficient solution of block Toeplitz systems with multiple right-hand sides arising from a periodic boundary element formulation. *Engineering Analysis with Boundary Elements*, 130:135–144, 2021.
- [180] M. Kaltenbacher, ed.. *Computational acoustics*. Springer, 2018.
- [181] S. Marburg and H.-J. Hardtke. A study on the acoustic boundary admittance. Determination, results and consequences. *Engineering Analysis with Boundary Elements*, 23(9):737–744, 1999.
- [182] F. Ihlenburg, ed.. *Finite element analysis of acoustic scattering*. Springer Science & Business Media, 2006.
- [183] O. C. Zienkiewicz, R. L. Taylor, and D. Fox. *The finite element method for solid and structural mechanics*. Butterworth-Heinemann, 2014.
- [184] M. Kaltenbacher. *Numerical simulation of mechatronic sensors and actuators*, volume 3. Springer, Berlin, Heidelberg, 2015.
- [185] L. D. Landau, L. P. Pitaevskii, A. M. Kosevich, and E. M. Lifshitz. *Theory of elasticity*, volume 7. Pergamon Press, Oxford, New York, 1986.
- [186] I. Harari. A survey of finite element methods for time-harmonic acoustics. *Computer Methods in Applied Mechanics and Engineering*, 195(13-16):1594–1607, 2006.
- [187] L. Thompson. A review of finite-element methods for time-harmonic acoustics. *Journal of Acoustical Society of America*, 119:1315–1330, 2006.
- [188] A. J. Burton and G. F. Miller. The application of integral equation methods to the numerical solution of some exterior boundary-value problems. *Proceedings of the Royal Society A: Mathematical, Physical and Engineering Sciences*, 323(1553):201–210, 1971.
- [189] W. L. Meyer, W. A. Bell, B. T. Zinn, and M. P. Stallybrass. Boundary integral solutions of three dimensional acoustic radiation problems. *Journal of Sound and Vibration*, 59(2):245–262, 1978.
- [190] K. E. Atkinson. *The numerical solution of integral equations of the second kind*. Cambridge University Press, 1997.
- [191] G. A. Chandler. *Superconvergence of numerical solutions to second kind integral equations*. Ph.D. thesis, Australian National University, 1979.

- [192] S. Marburg and S. Schneider. Influence of element types on numeric error for acoustic boundary elements. *Journal of Computational Acoustics*, 11(03):363–386, 2003.
- [193] N. A. Gumerov, R. Duraiswami, and E. A. Borovikov. Data structures, optimal choice of parameters, and complexity results for generalized multilevel fast multipole methods in d dimensions. Technical Report, UMIACS Technical Report TR 2003-28, University of Maryland, 2003.
- [194] M. A. Epton and B. Dembart. Multipole translation theory for the three-dimensional Laplace and Helmholtz equations. *SIAM Journal on Scientific Computing*, 16(4):865–897, 1995.
- [195] B. W. Shore and D. H. Menzel. *Principles of atomic spectra*. John Wiley & Sons Inc, 1968.
- [196] R. Yokota, H. Ibeid, and D. Keyes. Fast multipole method as a matrix-free hierarchical low-rank approximation. In: *Lecture Notes in Computational Science and Engineering*, pp. 267–286. Springer International Publishing, 2017.
- [197] P. J. Davis. *Circulant matrices*. AMS Chelsea Publishing Series. Chelsea, 1994.
- [198] R. M. Gray. Toeplitz and circulant matrices: A review. *Foundations and Trends in Communications and Information Theory*, 2(3):155–239, 2005.
- [199] C. J. Zheng, C. X. Bi, C. Zhang, H. F. Gao, and H. B. Chen. Free vibration analysis of elastic structures submerged in an infinite or semi-infinite fluid domain by means of a coupled FE-BE solver. *Journal of Computational Physics*, 359:183–198, 2018.
- [200] D. Brunner, M. Junge, and L. Gaul. A comparison of FE-BE coupling schemes for large-scale problems with fluid-structure interaction. *International Journal of Numerical Methods in Engineering*, 77(5):664–688, 2009.
- [201] D. Fritze, S. Marburg, and H.-J. Hardtke. FEM-BEM-coupling and structural-acoustic sensitivity analysis for shell geometries. *Computers & Structures*, 83(2-3):143–154, 2005.
- [202] H. Peters, S. Marburg, and N. Kessissoglou. Structural-acoustic coupling on non-conforming meshes with quadratic shape functions. *International Journal for Numerical Methods in Engineering*, 91(1):27–38, 2012.
- [203] S. K. Baydoun and S. Marburg. Investigation of radiation damping in sandwich structures using finite and boundary element methods and a nonlinear eigensolver. *The Journal of the Acoustical Society of America*, 147(3):2020–2034, 2020.
- [204] A. Kimeswenger, O. Steinbach, and G. Unger. Coupled finite and boundary element methods for fluid-solid interaction eigenvalue problems. *SIAM Journal on Numerical Analysis*, 52(5):2400–2414, 2014.
- [205] J. Xiao, S. Meng, C. Zhang, and C. Zheng. Resolvent sampling based Rayleigh-Ritz method for large-scale nonlinear eigenvalue problems. *Computer Methods in Applied Mechanics and Engineering*, 310:33–57, 2016.

- [206] S. Yokota and T. Sakurai. A projection method for nonlinear eigenvalue problems using contour integrals. *JSIAM Letters*, 5:41–44, 2013.
- [207] E. Agullo, L. Giraud, and Y.-F. Jing. Block GMRES method with inexact breakdowns and deflated restarting. *SIAM Journal on Matrix Analysis and Applications*, 35(4):1625–1651, 2014.
- [208] B. Vital. *Etude de quelques méthodes de résolution de problèmes linéaires de grande taille sur multiprocesseur*. Ph.D. thesis, Université de Rennes, 1990.
- [209] R. B. Morgan. GMRES with deflated restarting. *SIAM Journal on Scientific Computing*, 24(1):20–37, 2002.
- [210] A. H. Baker, J. M. Dennis, and E. R. Jessup. On improving linear solver performance: A block variant of GMRES. *SIAM Journal on Scientific Computing*, 27(5):1608–1626, 2006.
- [211] L. Maxit. Simulation of the pressure field beneath a turbulent boundary layer using realizations of uncorrelated wall plane waves. *The Journal of the Acoustical Society of America*, 140(2):1268–1285, 2016.
- [212] M. Karimi, P. Croaker, L. Maxit, O. Robin, A. Skvortsov, S. Marburg, and N. Kessissoglou. A hybrid numerical approach to predict the vibrational responses of panels excited by a turbulent boundary layer. *Journal of Fluids and Structures*, 92:102814, 2020.
- [213] G. R. Watts, D. H. Crombie, and D. C. Hothersall. Acoustic performance of new designs of traffic noise barriers: Full scale tests. *Journal of Sound and Vibration*, 177(3):289–305, 1994.
- [214] A. Peplow, P. Persson, and L. V. Andersen. Evaluating annoyance mitigation in the screening of train-induced noise and ground vibrations using a single-leaf traffic barrier. *Science of The Total Environment*, 790:147877, 2021.
- [215] M. Molerón, M. Serra-Garcia, and C. Daraio. Visco-thermal effects in acoustic metamaterials: from total transmission to total reflection and high absorption. *New Journal of Physics*, 18(3):033003, 2016.
- [216] V. C. Henríquez, V. M. García-Chocano, and J. Sánchez-Dehesa. Viscothermal losses in double-negative acoustic metamaterials. *Physical Review Applied*, 8(1), 2017.
- [217] U. Baur and P. Benner. Model reduction for parametric systems using balanced truncation and interpolation. *at - Automatisierungstechnik*, 57(8):411–419, 2009.
- [218] P. Rong, M. Abele, and O. von Estorff. Comparison of different methods for simulating acoustic diffuse field excitations. *Acta Acustica united with Acustica*, 99(6):931–939, 2013.
- [219] A. Leblanc and A. Lavie. Solving acoustic nonlinear eigenvalue problems with a contour integral method. *Engineering Analysis with Boundary Elements*, 37(1):162–166, 2013.

A Appended publications

A.1 Paper A

Fast multipole boundary element method for the acoustic analysis of finite periodic structures

Christopher Jelich, Wenchang Zhao, Haibo Chen and Steffen Marburg

Reprinted from C. Jelich, W. Zhao, H. Chen and S. Marburg. Fast multipole boundary element method for the acoustic analysis of finite periodic structures. *Computer Methods in Applied Mechanics and Engineering*, 391:114528, 2022.

Copyright © 2022 Elsevier. Reprinted with permission.



ELSEVIER



Available online at www.sciencedirect.com

ScienceDirect

Comput. Methods Appl. Mech. Engrg. 391 (2022) 114528

**Computer methods
in applied
mechanics and
engineering**

www.elsevier.com/locate/cma

Fast multipole boundary element method for the acoustic analysis of finite periodic structures

Christopher Jelich^a, Wenchang Zhao^{b,*}, Haibo Chen^b, Steffen Marburg^a

^a Chair of Vibroacoustics of Vehicles and Machines, School of Engineering and Design, Technical University of Munich, Boltzmannstraße 15, Garching 85748, Germany

^b CAS Key Laboratory of Mechanical Behavior and Design of Materials, Department of Modern Mechanics, University of Science and Technology of China, Hefei 230026, Anhui, PR China

Received 2 April 2021; received in revised form 22 October 2021; accepted 21 December 2021

Available online xxxx

Abstract

In this work, two fast multipole boundary element formulations for the linear time-harmonic acoustic analysis of finite periodic structures are presented. Finite periodic structures consist of a bounded number of unit cell replications in one or more directions of periodicity. Such structures can be designed to efficiently control and manipulate sound waves and are referred to as acoustic metamaterials or sonic crystals. Our methods subdivide the geometry into boxes which correspond to the unit cell. A boundary element discretization is applied and interactions between well separated boxes are approximated by a fast multipole expansion. Due to the periodicity of the underlying geometry, certain operators of the expansion become block Toeplitz matrices. This allows to express matrix–vector products as circular convolutions which significantly reduces the computational effort and the overall memory requirements. The efficiency of the presented techniques is shown based on an acoustic scattering problem. In addition, a study on the design of sound barriers is presented where the performance of a wall-like sound barrier is compared to the performance of two sonic crystal sound barriers.

© 2021 Elsevier B.V. All rights reserved.

Keywords: Acoustic scattering; Boundary element method; Fast multipole method; Block Toeplitz matrix; Sonic crystals; Sound barriers

1. Introduction

Periodic structures are known to be very efficient in modifying the propagation of sound waves in fluids [1,2]. This especially holds for the sound attenuation by periodic arrangements of scatterers which are classified as sonic crystals [1,3]. Sonic crystal sound barriers can lead to significant sound attenuation in certain frequency bands due to periodicity and local resonances [4,5]. Modifying the distance between the sonic crystals or changing their geometry influences the position and width of these frequency bands, which are referred to as band gaps in the case of infinite periodic arrangements. The performance of sonic crystal sound barriers is usually compared to standard wall-like sound barriers which often can be seen as periodic structures, too. Various design improvements have been proposed for wall-like sound barriers over the years, including geometric variations of the top edge [6] and adding

* Corresponding author.

E-mail address: Jsukya@mail.ustc.edu.cn (W. Zhao).

absorbing materials [7]. Similar analyses have been carried out for sonic crystal sound barriers [8,9], see [10] for a recent review. In order to quantify the performance of designs, the acoustic behavior of the periodic structure has to be assessed within the frequency range of interest. This is described by the Helmholtz equation which can be solved by the finite element method (FEM) [8,11], the boundary element method (BEM) [12,13] and the multiple scattering theory [14].

Periodic arrangements consist of identical structures that are repeated an infinite amount of times in the directions of periodicity. Their acoustic behavior can be predicted by solving multiple acoustic eigenvalue problems of the unit cell with Floquet–Bloch boundary conditions using the FEM [15,16] or BEM [17]. However, this approach is not suitable for finite periodic arrangements, i.e., arrangements where an identical structure is repeated only a finite amount of times. It neglects possible scattering effects at the edges of the finite periodic arrangement as well as reflections from the ground. Other modeling approaches truncate the geometry such that only a sufficiently large section of the periodic arrangement is analyzed. Reiter et al. [18] proposed a periodic FEM which applies periodic boundary conditions to the unit cell. Analogously, Lam [19] introduced a periodic boundary element formulation which includes an infinite sum of Green’s functions. Truncating this sum yields the quasi-periodic BEM which is capable of sufficiently approximating the acoustic behavior within a unit cell [20,21]. A convergence study on the truncation number is reported by Jean and Defrance [9]. However, applying periodic boundary conditions is not suitable when only the geometry is periodic but the loading and the solution are assumed to be aperiodic. A third modeling approach is to assume an infinite extent of the periodic arrangement in one spatial direction. This leads to two-dimensional numerical models which neglect edge effects along the third dimension. Cavalieri et al. [22] employed the FEM to analyze an infinitely long sound barrier with a constant cross section in which Helmholtz resonators and quarter-wavelength resonators are horizontally placed. With respect to the BEM, Duhamel [23] extended the two-dimensional modeling approach by incoherent line sources and refers to it as 2.5-dimensional boundary element method. In contrast, Chalmers et al. [24] and Elford et al. [8] assumed that the height of the sonic crystals is infinite and that ground effects are negligible. This allows to modify the cross section of the sound barrier along its length. Whenever the aforementioned assumptions are not valid, a three-dimensional acoustic analysis has to be carried out. In this regard, two major characteristics of the BEM favor its application: The BEM implicitly fulfills the Sommerfeld radiation condition and reduces the problem’s dimension by one, such that only the sound radiating surface has to be discretized instead of the surrounding acoustic volume.

A recent attempt to reduce the computational effort of boundary element analyses of finite periodic arrangements was presented by Karimi et al. [12]. They identified that the boundary element discretization of a Helmholtz problem with periodic geometry yields a block Toeplitz system of linear equations. Utilizing this special matrix structure significantly accelerates the setup and solution times which enables three-dimensional analyses of various types of small periodic structures on today’s standard desktop computers [25,26]. Despite the significant reduction on the memory requirements, analyzing moderately large periodic structures with many degrees of freedom (dofs) is still infeasible. For periodicity in one direction, the storage of $2M_x - 1$ dense matrices of size $n_{\text{dof}} \times n_{\text{dof}}$ is required, with M_x denoting the number of unit cells in the x -direction and n_{dof} denoting the number of degrees of freedom of a unit cell. Considering periodicity in additional directions increases the storage costs even further which scale of order $\mathcal{O}(n_{\text{cells}}n_{\text{dof}}^2)$ with the total number of unit cells n_{cells} . Well-known techniques to reduce the computational complexity of boundary element analyses in both time and memory are fast boundary element formulations. They allow to express the dense system matrix as a function of sparse matrices. The most common approaches are the fast multipole method (FMM) [27,28] and hierarchical matrices [29,30]. Both are applicable to problems with arbitrary geometry but can be optimized for finite and infinite periodic arrangements. Analyzing the latter with the boundary element method involves an infinite sum of the Green’s function also denoted as periodic Green’s function, periodic sum or infinite lattice sum. This sum is usually truncated after a certain number of terms and evaluated by employing the FMM [31–33]. Otani and Nishimura [34] introduced an FMM for the two-dimensional Helmholtz equation with periodic geometries which is extended to the three-dimensional case in [35,36]. Similar approaches based on multipole expansions of the periodic Green’s function exist for the method of fundamental solutions (MFS) which is closely related to the BEM [37]. Furthermore, Yan and Shelley [38] introduced a kernel independent FMM for periodic Laplace and Stokes problems. In all approaches, the geometry is of infinite extent and the solution as well as boundary conditions and incident wave fields are assumed to be quasi-periodic. In the case of sound barriers, this assumption is often violated due to the limited height and width or aperiodic incident wave fields. Hence, finite periodic arrangements need to be analyzed. Amado-Mendes et al. [39] applied the hierarchical matrix BEM to a

finite periodic array of acoustic scatterers. They reported savings in the setup time and memory requirements due to the underlying Toeplitz structure but did not accelerate the matrix–vector products. Gumerov and Duraiswami [40] combined a T-matrix based approach and the FMM to accelerate the solution of acoustic problems that feature arrangements of arbitrarily shaped scatterers.

We propose two novel fast multipole boundary element formulations for acoustic problems with finite periodic geometries. They exhibit low memory requirements, fast matrix–vector multiplication and allow to efficiently analyze periodic structures of finite extent. The methods do not require any periodicity of the boundary conditions, incident fields or solutions. In contrast to the aforementioned approaches, our techniques rigorously make use of the multilevel block Toeplitz matrix structure which occurs when discretizing periodic structures with the BEM and applying the FMM. Identifying that the fast multipole operators are block Toeplitz matrices is a key point of the algorithms and drives its performance. The remainder of the paper is outlined as follows. Section 2 presents the periodic boundary element formulation of [12] and extends the formulation to specific symmetry problems. Section 3 outlines the low frequency fast multipole method and introduces our fast multipole periodic boundary element formulations. The formulations are validated numerically in terms of an acoustic scattering problem and a sound barrier design study in Section 4.

2. Boundary element method for finite periodic arrays

2.1. Boundary element formulation

Consider the acoustic Helmholtz equation

$$\nabla^2 p(\mathbf{x}) + k^2 p(\mathbf{x}) = 0, \quad \forall \mathbf{x} \in \Omega, \tag{1}$$

where ∇^2 is the Laplace operator, p is the acoustic pressure, $k = \omega/c$ is the wave number, $\omega = 2\pi f$ is the angular frequency with frequency f and c is the speed of sound of the acoustic medium within the domain Ω . The harmonic time dependence $e^{-i\omega t}$ with the imaginary unit i is omitted throughout this paper. The fluid particle velocity v_f on the boundary Γ of the acoustic domain is related to the sound pressure by

$$\frac{\partial p(\mathbf{x})}{\partial \mathbf{n}(\mathbf{x})} = i\omega\rho v_f(\mathbf{x}), \tag{2}$$

where $\mathbf{n}(\mathbf{x})$ is the outward pointing normal vector at $\mathbf{x} \in \Gamma$ and ρ is the fluid density. A well-posed problem is obtained by introducing the admittance boundary condition

$$i\omega\rho v_f(\mathbf{x}) = ik\beta(\mathbf{x})p(\mathbf{x}), \tag{3}$$

where β is the normalized surface admittance which can be expressed by the surface admittance Y through $Y(\mathbf{x}) = \beta(\mathbf{x})/\rho c$.

Applying Green’s second theorem yields the conventional boundary integral equation referred to as CBIE [41]

$$c(\mathbf{x})p(\mathbf{x}) + \int_{\Gamma} \frac{\partial G(\mathbf{x}, \mathbf{y})}{\partial \mathbf{n}(\mathbf{y})} p(\mathbf{y}) d\Gamma(\mathbf{y}) = \int_{\Gamma} G(\mathbf{x}, \mathbf{y}) \frac{\partial p(\mathbf{y})}{\partial \mathbf{n}(\mathbf{y})} d\Gamma(\mathbf{y}) + p^{\text{inc}}(\mathbf{x}), \tag{4}$$

where \mathbf{x} denotes the field point and \mathbf{y} denotes the source point. The solid angle $c(\mathbf{x})$ equals $1/2$ if the boundary around \mathbf{x} is smooth and equals 1 if $\mathbf{x} \in \Omega$. Further, $G(\mathbf{x}, \mathbf{y})$ denotes the Green’s function and $p^{\text{inc}}(\mathbf{x})$ is the incident acoustic pressure field. The Green’s functions of 3D full-space and half-space acoustic problems are given as

$$G(\mathbf{x}, \mathbf{y}) = \frac{1}{4\pi} \frac{e^{ik|\mathbf{x}-\mathbf{y}|}}{|\mathbf{x}-\mathbf{y}|}, \quad \mathbf{x}, \mathbf{y} \in \mathbb{R}^3, \tag{5}$$

$$G_h(\mathbf{x}, \mathbf{y}) = \frac{1}{4\pi} \frac{e^{ik|\mathbf{x}-\mathbf{y}|}}{|\mathbf{x}-\mathbf{y}|} + R_p \frac{1}{4\pi} \frac{e^{ik|\mathbf{x}-\hat{\mathbf{y}}|}}{|\mathbf{x}-\hat{\mathbf{y}}|}, \quad \mathbf{x}, \mathbf{y}, \hat{\mathbf{y}} \in \mathbb{R}^3, \tag{6}$$

respectively, where $|\cdot|$ is the l^2 -norm. Further, R_p is the reflection coefficient and $\hat{\mathbf{y}}$ is the mirror image of the source point \mathbf{y} with respect to the plane that divides both half-spaces. Taking the derivative of Eq. (4) with respect to the outward normal vector and assuming that the boundary around \mathbf{x} is smooth yields the hypersingular boundary integral equation (HBIE)

$$\frac{1}{2} \frac{\partial p(\mathbf{x})}{\partial \mathbf{n}(\mathbf{x})} + \int_{\Gamma} \frac{\partial^2 G(\mathbf{x}, \mathbf{y})}{\partial \mathbf{n}(\mathbf{x}) \partial \mathbf{n}(\mathbf{y})} p(\mathbf{y}) d\Gamma(\mathbf{y}) = \int_{\Gamma} \frac{\partial G(\mathbf{x}, \mathbf{y})}{\partial \mathbf{n}(\mathbf{x})} \frac{\partial p(\mathbf{y})}{\partial \mathbf{n}(\mathbf{y})} d\Gamma(\mathbf{y}) + \frac{\partial p^{\text{inc}}(\mathbf{x})}{\partial \mathbf{n}(\mathbf{x})}. \tag{7}$$

The linear combination of the CBIE and HBIE results in the Burton and Miller formulation, i.e.,

$$\begin{aligned} \frac{1}{2}p(\mathbf{x}) + \int_{\Gamma} \left[\frac{\partial G(\mathbf{x}, \mathbf{y})}{\partial \mathbf{n}(\mathbf{y})} + \alpha \frac{\partial^2 G(\mathbf{x}, \mathbf{y})}{\partial \mathbf{n}(\mathbf{x})\partial \mathbf{n}(\mathbf{y})} \right] p(\mathbf{y}) \, d\Gamma(\mathbf{y}) + \frac{\alpha}{2} \frac{\partial p(\mathbf{x})}{\partial \mathbf{n}(\mathbf{x})} \\ - \int_{\Gamma} \left[G(\mathbf{x}, \mathbf{y}) + \alpha \frac{\partial G(\mathbf{x}, \mathbf{y})}{\partial \mathbf{n}(\mathbf{x})} \right] \frac{\partial p(\mathbf{y})}{\partial \mathbf{n}(\mathbf{y})} \, d\Gamma(\mathbf{y}) = p^{\text{inc}}(\mathbf{x}) + \alpha \frac{\partial p^{\text{inc}}(\mathbf{x})}{\partial \mathbf{n}(\mathbf{x})}, \end{aligned} \tag{8}$$

which yields unique solutions at all frequencies [42]. The coupling parameter α is a complex-valued scalar with a non-vanishing imaginary part, i.e., $\text{Im}(\alpha) \neq 0$. A value of $-i/k$ is optimal in the present case [43].

The collocation boundary element method is applied to discretize Eq. (8). Quadrilateral boundary elements with second order, C^0 -continuous Lagrange polynomials approximate the geometry, whereas discontinuous Lagrange polynomials of variable order approximate the physical quantities, i.e., acoustic pressure, fluid particle velocity and boundary admittance. This leads to the following system of linear equations

$$(\mathbf{H} - \mathbf{G}\mathbf{Y}) \mathbf{p} = \mathbf{p}^{\text{inc}}, \tag{9}$$

where \mathbf{H} and \mathbf{G} are the dense boundary element coefficient matrices, \mathbf{Y} is the block diagonal admittance matrix and the vectors \mathbf{p}^{inc} and \mathbf{p} store the incident sound pressure values and unknown sound pressure values at the collocation points, respectively. The collocation boundary element method is described in great detail in [41,44].

2.2. BEM for finite periodic structures

Both the assembly and storage of the boundary element matrices become infeasible for medium to large-scale acoustic problems. A remedy is found by Karimi et al. [12] for problems which feature a finite periodic geometry. In such cases, the system matrix $(\mathbf{H} - \mathbf{G}\mathbf{Y})$ is a multilevel block Toeplitz matrix due to the translation invariance of the Green’s function, cf. Eq. (5). Block Toeplitz matrices are a special class of matrices which have constant blocks along each diagonal. Within this context, the term multilevel implies that the matrix blocks are block Toeplitz matrices itself. Representing the system matrix as a multilevel block Toeplitz matrix significantly reduces the storage cost.

Consider the finite periodic array of scatterers in Fig. 1. The scatterers are arranged in a regular pattern with M_x unit cells in the x -direction and M_y unit cells in the y -direction. Applying a boundary element discretization yields

$$\mathbf{T}\mathbf{p} = \mathbf{p}^{\text{inc}}, \tag{10}$$

where \mathbf{T} is a 2-level block Toeplitz matrix and an exact representation of $(\mathbf{H} - \mathbf{G}\mathbf{Y})$. It has a size of $M_x M_y n_{\text{dof}} \times M_x M_y n_{\text{dof}}$, with n_{dof} denoting the number of degrees of freedom of a unit cell and reads

$$\mathbf{T} = \begin{bmatrix} \mathbf{T}_0^1 & \mathbf{T}_{-1}^1 & \cdots & \cdots & \mathbf{T}_{1-M_y}^1 \\ \mathbf{T}_1^1 & \mathbf{T}_0^1 & \mathbf{T}_{-1}^1 & \cdots & \mathbf{T}_{2-M_y}^1 \\ \vdots & \mathbf{T}_1^1 & \ddots & \ddots & \vdots \\ \vdots & \vdots & \ddots & \ddots & \mathbf{T}_{-1}^1 \\ \mathbf{T}_{M_y-1}^1 & \mathbf{T}_{M_y-2}^1 & \cdots & \mathbf{T}_1^1 & \mathbf{T}_0^1 \end{bmatrix}. \tag{11}$$

The individual entries are block Toeplitz matrices \mathbf{T}_j^1 , $j = 1 - M_y, 2 - M_y, \dots, 0, \dots, M_y - 1$ itself with $(\cdot)^1$ denoting the first level of periodicity. The matrix blocks have a size of $M_x n_{\text{dof}} \times M_x n_{\text{dof}}$ and read

$$\mathbf{T}_j^1 = \begin{bmatrix} \mathbf{T}_0^2 & \mathbf{T}_{-1}^2 & \cdots & \cdots & \mathbf{T}_{1-M_x}^2 \\ \mathbf{T}_1^2 & \mathbf{T}_0^2 & \mathbf{T}_{-1}^2 & \cdots & \mathbf{T}_{2-M_x}^2 \\ \vdots & \mathbf{T}_1^2 & \ddots & \ddots & \vdots \\ \vdots & \vdots & \ddots & \ddots & \mathbf{T}_{-1}^2 \\ \mathbf{T}_{M_x-1}^2 & \mathbf{T}_{M_x-2}^2 & \cdots & \mathbf{T}_1^2 & \mathbf{T}_0^2 \end{bmatrix}_j \tag{12}$$

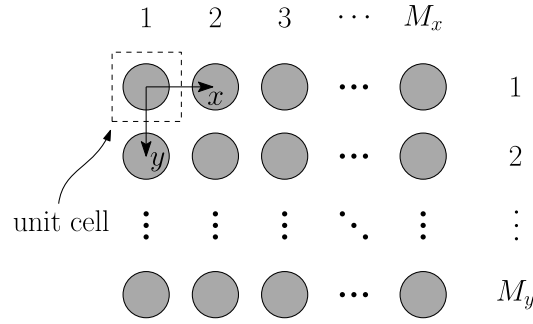


Fig. 1. A configuration of a finite periodic array of scatterers with periodicity in the x - and y -direction. The number of periodic segments in each direction is M_x and M_y . The geometry of each scatterer coincides with the geometry of the unit cell.

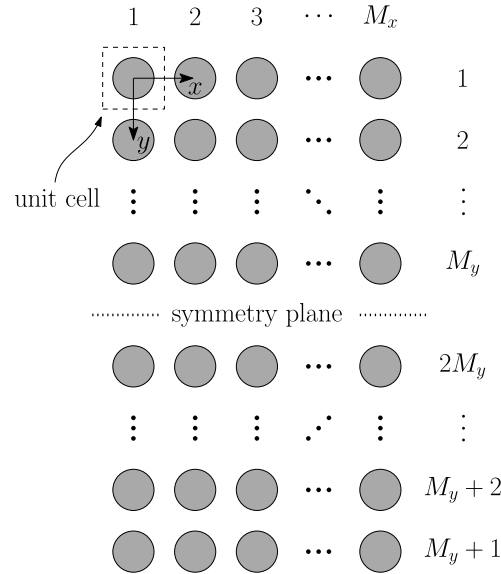


Fig. 2. A configuration of a finite periodic array of scatterers with periodicity in the x - and y -direction as well as symmetry along the xz -plane. The number of periodic segments in each direction is M_x and $2M_y$. The geometry of each scatterer coincides with the geometry of the unit cell.

They store dense $n_{\text{dof}} \times n_{\text{dof}}$ matrices \mathbf{T}_i^2 , $i = 1 - M_x, 2 - M_x, \dots, 0, \dots, M_x - 1$, which are defined by the corresponding entries of the discretized boundary integral equation (8).

Every multilevel block Toeplitz matrix is uniquely defined by its first block row and column in each level. Therefore, the periodic boundary element formulation requires the storage of $(2M_x - 1)(2M_y - 1)n_{\text{dof}}^2$ matrix entries. In contrast, the conventional boundary element method demands the storage of $(M_x M_y n_{\text{dof}})^2 = N_{\text{dof}}^2$ matrix entries where N_{dof} denotes the total number of dofs. The formulation will be referred to as periodic boundary element method (PBEM) throughout this work. It is referred to [12] for a more detailed derivation and to [25] for an extension to an arbitrary number of periodic directions and certain kinds of half-space problems. In either case, the storage cost scales of order $\mathcal{O}(n_{\text{cells}} n_{\text{dof}}^2)$ with n_{cells} denoting the number of periodic unit cells.

2.3. BEM for finite periodic structures in half-spaces

The system matrix $\mathbf{H} - \mathbf{G}\mathbf{Y}$ exhibits a block Toeplitz structure for periodic geometries in half-spaces as long as the half-space Green’s function (6) features translation invariance. This is the case whenever the directions of periodicity are parallel to the symmetry plane [25]. A periodic geometry for which this does not hold is shown in

Fig. 2. The scatterers' location is periodic in the x and y -direction and symmetric with respect to the xz -plane. A straightforward boundary element discretization of this problem does not yield a block Toeplitz system matrix since the periodicity in the y -axis is perpendicular to the xz -plane. This work introduces a remedy by taking the additive nature of the half-space Green's function (6) into account. The idea is to split the integrals of Eq. (8) into integrals including the first summand of the half-space Green's function and integrals including the second summand. This yields two separate matrices subsequent to applying the boundary conditions and the collocation boundary element discretization. The corresponding linear system of equations reads

$$\underbrace{(\mathbf{H} - \mathbf{G}\mathbf{Y})}_{\mathbf{T}} + \underbrace{(\hat{\mathbf{H}} - \hat{\mathbf{G}}\mathbf{Y})}_{\hat{\mathbf{T}}} \mathbf{p} = \mathbf{p}^{\text{inc}}. \tag{13}$$

The matrices \mathbf{H} and \mathbf{G} stem from the first summand of the half-space Green's function which corresponds to the full-space Green's function. Hence, the multilevel block Toeplitz matrix \mathbf{T} of Eq. (13) coincides with the system matrix of the corresponding full-space problem in Eq. (10). The matrices $\hat{\mathbf{H}}$ and $\hat{\mathbf{G}}$ stem from the second summand of the half-space Green's function and build the matrix $\hat{\mathbf{T}}$ which, in contrast to \mathbf{T} , has constant blocks along its anti-diagonals, i.e.,

$$\hat{\mathbf{T}} = \begin{bmatrix} \hat{\mathbf{T}}_0^1 & \hat{\mathbf{T}}_{-1}^1 & \cdots & \hat{\mathbf{T}}_{-M_y+1}^1 & \hat{\mathbf{T}}_{-M_y}^1 \\ \hat{\mathbf{T}}_{-1}^1 & \hat{\mathbf{T}}_{-2}^1 & \ddots & \ddots & \hat{\mathbf{T}}_{-M_y-1}^1 \\ \vdots & \ddots & \ddots & \ddots & \vdots \\ \hat{\mathbf{T}}_{-M_y+1}^1 & \ddots & \ddots & \hat{\mathbf{T}}_{-2M_y+2}^1 & \hat{\mathbf{T}}_{-2M_y+1}^1 \\ \hat{\mathbf{T}}_{-M_y}^1 & \hat{\mathbf{T}}_{-M_y-1}^1 & \cdots & \hat{\mathbf{T}}_{-2M_y+1}^1 & \hat{\mathbf{T}}_{-2M_y}^1 \end{bmatrix}. \tag{14}$$

Structured matrices in the form of Eq. (14) are referred to as multilevel block Hankel matrices. Since adding \mathbf{T} and $\hat{\mathbf{T}}$ leads to an unstructured matrix, the benefits of efficient memory storage as well as efficient matrix–vector products are only preserved when assembling and storing both matrices separately. The extension of the PBEM to this special type of symmetry condition therefore requires twice the storage, i.e., $2(2M_x - 1)(2M_y - 1)n_{\text{dof}}^2$ matrix entries in the present case.

2.4. Solution scheme for the periodic boundary element method

Both direct and iterative solvers are available for the solution of the multilevel block Toeplitz system (10). However, an efficient direct solution of Eq. (13) is infeasible since the system matrix is a sum of two structured matrices. Therefore, the focus is set on iterative solvers [45,46].

The computational effort of iterative solvers is driven by the efficiency of the matrix–vector product. Multiplying a multilevel block Toeplitz matrix by a vector scales quasi-linearly in time when expressed by circular convolutions [47]. The present block Toeplitz matrix \mathbf{T} features dense matrices on its lowest level which leads to an asymptotic complexity of $\mathcal{O}(n_{\text{dof}}^2 n_{\text{cells}} \log(n_{\text{cells}}))$. In order to achieve this complexity, the multilevel block Toeplitz matrix is embedded into a multilevel block circulant matrix. This is a special type of multilevel block Toeplitz matrix where each block row is a rightward circular shift of the first block row [48,49]. For a 2-level block Toeplitz matrix \mathbf{T} of the problem in Fig. 1 with periodicity in two directions, the corresponding 2-level block circulant matrix is defined as

$$\mathbf{C} = \begin{bmatrix} \mathbf{C}_0^1 & \mathbf{C}_{-1}^1 & \cdots & \mathbf{C}_2^1 & \mathbf{C}_1^1 \\ \mathbf{C}_1^1 & \mathbf{C}_0^1 & \mathbf{C}_{-1}^1 & \cdots & \mathbf{C}_2^1 \\ \vdots & \mathbf{C}_1^1 & \ddots & \ddots & \vdots \\ \mathbf{C}_{-2}^1 & \vdots & \ddots & \ddots & \mathbf{C}_{-1}^1 \\ \mathbf{C}_{-1}^1 & \mathbf{C}_{-2}^1 & \cdots & \mathbf{C}_1^1 & \mathbf{C}_0^1 \end{bmatrix}. \tag{15}$$

It stores 1-level block circulant matrices \mathbf{C}_j^1 , which reads

$$\mathbf{C}_j^1 = \begin{bmatrix} \mathbf{T}_0^2 & \mathbf{T}_{-1}^2 & \cdots & \mathbf{T}_2^2 & \mathbf{T}_1^2 \\ \mathbf{T}_1^2 & \mathbf{T}_0^2 & \mathbf{T}_{-1}^2 & \cdots & \mathbf{T}_2^2 \\ \vdots & \mathbf{T}_1^2 & \ddots & \ddots & \vdots \\ \mathbf{T}_{-2}^2 & \vdots & \ddots & \ddots & \mathbf{T}_{-1}^2 \\ \mathbf{T}_{-1}^2 & \mathbf{T}_{-2}^2 & \cdots & \mathbf{T}_1^2 & \mathbf{T}_0^2 \end{bmatrix}_j . \tag{16}$$

The first block row of \mathbf{C}_j^1 consists of the unique matrix blocks of \mathbf{T}_j^1 defined in Eq. (12). The blocks are concatenated into the matrix

$$\mathbf{Q} = (\mathbf{T}_0^2 \quad \mathbf{T}_{-1}^2 \quad \cdots \quad \mathbf{T}_{1-M_x}^2 \quad \mathbf{T}_{M_x-1}^2 \quad \cdots \quad \mathbf{T}_2^2 \quad \mathbf{T}_1^2) , \tag{17}$$

and shifted in a rightward direction to build the block rows of \mathbf{C}_j^1 . Concatenating the unique entries of \mathbf{C}_j^1 and introducing rightward shifts for each block row then builds the multilevel block circulant matrix \mathbf{C} as in Eq. (15). This matrix can be block diagonalized by applying Fourier transformations, i.e.,

$$\mathbf{C} = \mathfrak{F}^{-1} \mathbf{\Lambda} \mathfrak{F} . \tag{18}$$

The Fourier transform and inverse Fourier transform are defined as

$$\mathfrak{F} = \mathbf{F}_{2M_y-1} \otimes \mathbf{F}_{2M_x-1} \otimes \mathbf{I}_{n_{\text{dof}}} , \tag{19}$$

$$\mathfrak{F}^{-1} = \mathbf{F}_{2M_y-1}^{-1} \otimes \mathbf{F}_{2M_x-1}^{-1} \otimes \mathbf{I}_{n_{\text{dof}}} , \tag{20}$$

where \otimes denotes the Kronecker product and $\mathbf{I}_{n_{\text{dof}}}$ denotes the $n_{\text{dof}} \times n_{\text{dof}}$ identity matrix. The Fourier matrix as well as its inverse are given by

$$\mathbf{F}_m = \left((e^{-i2\pi/m})^{ij} \right)_{i,j=0, \dots, m-1} , \tag{21}$$

$$\mathbf{F}_m^{-1} = \frac{1}{m} \mathbf{F}_m^* , \tag{22}$$

with the complex conjugate transpose $(\cdot)^*$ [47]. The block diagonal matrix $\mathbf{\Lambda}$ of Eq. (18) reads

$$\mathbf{\Lambda} = \text{diag} (\mathfrak{C}_0^1, \mathfrak{C}_1^1, \dots, \mathfrak{C}_{-2}^1, \mathfrak{C}_{-1}^1) , \tag{23}$$

with $[\mathfrak{C}_0^1 \mathfrak{C}_1^1 \dots \mathfrak{C}_{-2}^1 \mathfrak{C}_{-1}^1] = \mathfrak{F} [\mathbf{C}_0^1 \mathbf{C}_1^1 \dots \mathbf{C}_{-2}^1 \mathbf{C}_{-1}^1]$, the discrete Fourier transform of the first block column of \mathbf{C} . By diagonalizing the block circulant matrix, the matrix–vector product $\mathbf{T}\mathbf{p}$ can be expressed as

$$\mathbf{T}\mathbf{p} = \tilde{\mathfrak{F}}^{-1} \mathbf{\Lambda} \tilde{\mathfrak{F}}\mathbf{p} , \tag{24}$$

employing the modified Fourier transform $\tilde{\mathfrak{F}}$ and its inverse $\tilde{\mathfrak{F}}^{-1}$, i.e.,

$$\tilde{\mathfrak{F}} = \tilde{\mathbf{F}}_{2M_y-1} \otimes \tilde{\mathbf{F}}_{2M_x-1} \otimes \mathbf{I}_{n_{\text{dof}}} , \tag{25}$$

$$\tilde{\mathfrak{F}}^{-1} = \tilde{\mathbf{F}}_{2M_y-1}^{-1} \otimes \tilde{\mathbf{F}}_{2M_x-1}^{-1} \otimes \mathbf{I}_{n_{\text{dof}}} . \tag{26}$$

The incomplete Fourier matrices $\tilde{\mathbf{F}}_{2M-1}$ and $\tilde{\mathbf{F}}_{2M-1}^{-1}$ contain the first M columns of \mathbf{F}_{2M-1} and the first M rows of \mathbf{F}_{2M-1}^{-1} , respectively [25]. Note that $\mathbf{\Lambda}$ is computed upfront by means of Eq. (23) and requires the storage of $(2M_x-1)(2M_y-1)n_{\text{dof}}^2$ matrix entries. This does not affect the storage costs of the PBEM since the corresponding multilevel block Toeplitz matrix can be freed from memory.

Employing this scheme, matrix–vector products with the system matrices in Eqs. (10) and (13) are determined in order $\mathcal{O}(n_{\text{dof}}^2 n_{\text{cells}} \log(n_{\text{cells}}))$ time. In the case of Eq. (13), multiplications with the first summand are performed as outlined above whereas the multiplications with the second summand, i.e., with the multilevel block Hankel matrix $\hat{\mathbf{T}}$, require a slight modification. Since Hankel matrices are column-permuted Toeplitz matrices, a permutation matrix \mathbf{P} can be applied such that $\hat{\mathbf{T}}\mathbf{P}$ is a block Toeplitz matrix. Therefore $\hat{\mathbf{T}}\mathbf{P}\mathbf{P}^T\mathbf{p} = \hat{\mathbf{T}}\mathbf{p}$ holds and the above scheme can also be used for multiplications with $\hat{\mathbf{T}}$ leading to the same asymptotic complexity.

3. Fast multipole boundary element method for finite periodic arrays

The PBEM introduces an efficient way of assembling and storing the boundary element system matrix in the case of problems with finite periodic geometry. Regardless of the problem's size, all unique interactions between the degrees of freedom are represented by dense matrices. This inflicts unnecessary computational costs since the interaction between degrees of freedom that are well-separated can be represented in a data sparse format using fast boundary element techniques such as the fast multipole method (FMM) [50,51].

3.1. Single level fast multipole method

The fast multipole method approximates the Green's function $G(\mathbf{x}, \mathbf{y})$ by a truncated series expansion whenever the distance between a field point \mathbf{x} and a source point \mathbf{y} is sufficiently large. This decision is made based on a subdivision of the geometry into n_{boxes} boxes of equal size. The part of the boundary that is enclosed by a box $\Omega_{\mathbf{x}}$ is assumed to be in the far field of the part of the boundary within a box $\Omega_{\mathbf{y}}$ if the admissibility criterion

$$|\mathbf{x}_c - \mathbf{y}_c| \geq 2r \quad (27)$$

holds [51]. Here, r is the characteristic size of a box and \mathbf{x}_c , \mathbf{y}_c are the center points of the boxes $\Omega_{\mathbf{x}}$ and $\Omega_{\mathbf{y}}$, respectively. Whenever Eq. (27) holds, the distance between a point $\mathbf{x} \in \Omega_{\mathbf{x}}$ and a point $\mathbf{y} \in \Omega_{\mathbf{y}}$ is sufficiently large and the Green's function can be approximated by an expansion around the center of one of the boxes. The truncated series expansion of the full-space Green's function around the center \mathbf{y}_c close to \mathbf{y} reads [52]

$$G(\mathbf{x}, \mathbf{y}) \approx \frac{ik}{4\pi} \sum_{n=0}^{n_t} (2n+1) \sum_{m=-n}^n O_n^m(\mathbf{x} - \mathbf{y}_c) \bar{I}_n^m(\mathbf{y} - \mathbf{y}_c), \quad |\mathbf{y} - \mathbf{y}_c| < |\mathbf{x} - \mathbf{y}_c|, \quad (28)$$

where \bar{I}_n^m is the complex conjugate of I_n^m and n_t is the truncation number. The functions O_n^m and I_n^m are given as

$$O_n^m(\mathbf{x}) = h_n^{(1)}(|\mathbf{x}|) Y_n^m\left(\frac{\mathbf{x}}{|\mathbf{x}|}\right), \quad (29)$$

$$I_n^m(\mathbf{x}) = j_n(|\mathbf{x}|) Y_n^m\left(\frac{\mathbf{x}}{|\mathbf{x}|}\right), \quad (30)$$

where $h_n^{(1)}$ denotes the n th order spherical Hankel function of the first kind, j_n denotes the n th order spherical Bessel function of the first kind and Y_n^m are the spherical harmonics [52].

Subsequent to discretizing Eq. (8), the integrals are split according to the admissibility criterion. Whenever the criterion holds, the truncated series expansion approximates the Green's function and allows to represent the integrals by three operators. These are the particle-to-moment (P2M), moment-to-local (M2L) and local-to-particle (L2P) operators [52]. First, the contribution of each source point \mathbf{y} within a box $\Omega_{\mathbf{y}}$ is translated to the center \mathbf{y}_c using the P2M operator. They are then translated to the center \mathbf{x}_c of the box $\Omega_{\mathbf{x}}$ by applying the M2L operator. Finally, the L2P operators translate the contribution from the center to the each field point \mathbf{x} within $\Omega_{\mathbf{x}}$. Whenever the admissibility criterion does not hold, the pairs of field and source points are assumed to be in the near field and the truncated series expansion is not valid. The exact Green's function is employed and the corresponding integrals are represented by the particle-to-particle (P2P) operator. Appendix presents the details of the fast multipole operators.

Assembling the discretized operators into matrices yields

$$\mathbf{H} - \mathbf{G}\mathbf{Y} \approx \mathbf{S} + \mathbf{U}\mathbf{K}\mathbf{V}. \quad (31)$$

The sparse $N_{\text{dof}} \times N_{\text{dof}}$ matrix \mathbf{S} represents the near field interactions and the matrix product $\mathbf{U}\mathbf{K}\mathbf{V}$ represents the far field interactions. \mathbf{U} and \mathbf{V} are block diagonal matrices of size $N_{\text{dof}} \times n_{\text{boxes}}(n_t + 1)^2$ and $n_{\text{boxes}}(n_t + 1)^2 \times N_{\text{dof}}$, respectively. They store the individual L2P and P2M operators of each box. Further, \mathbf{K} is an $n_{\text{boxes}}(n_t + 1)^2 \times n_{\text{boxes}}(n_t + 1)^2$ matrix which stores the M2L operators acting between each pair of boxes that fulfills the admissibility criterion. This decomposition is known as single level fast multipole method and allows to express matrix-vector multiplications at a complexity of $\mathcal{O}(N_{\text{dof}}^{3/2})$ [50]. A further reduction can be achieved in the case of problems with periodic geometries.

3.2. FMM for finite periodic structures

Consider the finite periodic geometry in Fig. 1 with M_x and M_y scatterers in the x and y -direction, respectively. Applying the single level fast multipole method, the geometry is subdivided into boxes which correspond to the unit cell of the periodic geometry, hence $n_{\text{boxes}} = n_{\text{cells}}$. One of the unit cells is marked by a dashed square in Fig. 1. Similar to the PBEM, the regularity of the periodic structure in conjunction with the translation invariance of the Green's function and of its multipole expansion in Eq. (A.1) leads to the formation of special matrices. The single level FMM representation of Eq. (31) reads

$$\left(\underbrace{\begin{bmatrix} \mathbf{S}_0^1 & \mathbf{S}_{-1}^1 & & & \\ \mathbf{S}_1^1 & \mathbf{S}_0^1 & \mathbf{S}_{-1}^1 & & \\ & \mathbf{S}_1^1 & \ddots & \ddots & \\ & & \ddots & \ddots & \mathbf{S}_{-1}^1 \\ & & & \mathbf{S}_1^1 & \mathbf{S}_0^1 \end{bmatrix}}_{\mathbf{S}} + \text{diag}(\mathbf{U}_0) \underbrace{\begin{bmatrix} \mathbf{K}_0^1 & \mathbf{K}_{-1}^1 & \cdots & \cdots & \mathbf{K}_{1-M_y}^1 \\ \mathbf{K}_1^1 & \mathbf{K}_0^1 & \mathbf{K}_{-1}^1 & \cdots & \mathbf{K}_{2-M_y}^1 \\ \vdots & \mathbf{K}_1^1 & \ddots & \ddots & \vdots \\ \vdots & \vdots & \ddots & \ddots & \mathbf{K}_{-1}^1 \\ \mathbf{K}_{M_y-1}^1 & \mathbf{K}_{M_y-2}^1 & \cdots & \mathbf{K}_{-1}^1 & \mathbf{K}_0^1 \end{bmatrix}}_{\mathbf{UKV}} \text{diag}(\mathbf{V}_0) \right) \mathbf{p} = \mathbf{p}^{\text{inc}} . \tag{32}$$

The matrix \mathbf{S} is a banded 2-level block Toeplitz matrix which represents the near field interactions. It consists of three unique banded block Toeplitz matrices which represent the interactions between boxes within the same row \mathbf{S}_0^1 and in neighboring rows $\mathbf{S}_{\pm 1}^1$. The superscript $(\cdot)^1$ denotes the first direction of periodicity which is the y -direction in the present case. In contrast, the subscript $(\cdot)_{\pm 1}$ indicates that the interaction points to the next row in positive or negative y -direction, respectively. The matrix product \mathbf{UKV} represents the far field interactions. Since each box corresponds to the unit cell, the P2M and L2P operators are the same for all boxes. This leads to block diagonal matrices \mathbf{U} and \mathbf{V} with constant blocks \mathbf{U}_0 and \mathbf{V}_0 , respectively. Since the translation invariance holds for the function $O_n^m(\mathbf{x})$, cf. Eq. (29), it additionally holds for the M2L operator defined in Eq. (A.4). Therefore, the matrix \mathbf{K} becomes a multilevel block Toeplitz matrix. It stores all the unique discretized M2L operators between boxes of the same row \mathbf{K}_0^1 and in different rows $\mathbf{K}_{j \neq 0}^1$.

Storing the interactions of unit cells and entire rows of unit cells in this nested approach leads to a very memory efficient representation of the system matrix as long as the unit cell features a small number of degrees of freedom n_{dof} . The presented scheme can be applied straightforwardly to geometries with periodicity in $d > 2$ directions. This yields d -level block Toeplitz matrices which store $(d - 1)$ -level block Toeplitz matrices itself. The inherent benefits are the same, i.e., the P2M and L2P operators are equal among every unit cell, the near field matrix is a banded block Toeplitz matrix and the matrix storing the M2L operators is a multilevel block Toeplitz matrix. Similar to the PBEM, dense matrices are stored on the lowest level of the multilevel block Toeplitz matrices. In the case of \mathbf{S} , they are of size $n_{\text{dof}} \times n_{\text{dof}}$, whereas in the case of \mathbf{K} , they are of size $(n_t + 1)^2 \times (n_t + 1)^2$. Therefore, the total storage cost asymptotically scales $\mathcal{O}(n_{\text{dof}}^2 + n_t^2 n_{\text{dof}} + n_t^4 M_x M_y)$ or, considering periodicity in an arbitrary number of directions, $\mathcal{O}(n_{\text{dof}}^2 + n_t^2 n_{\text{dof}} + n_t^4 n_{\text{cells}})$. This fast multipole periodic boundary element method (FMPBEM) features a more beneficial scaling than the scaling of the PBEM since $n_t \ll n_{\text{dof}}$ holds.

3.3. FMM for finite periodic structures with large unit cells

The quadratic dependence of the storage cost on n_{dof} limits the application to finite periodic structures with small to medium sized unit cell discretizations. A remedy is found by introducing an additional approximation to Eq. (32) that addresses the unique $n_{\text{dof}} \times n_{\text{dof}}$ matrix entries within the banded multilevel block Toeplitz matrix \mathbf{S} . Applying the multilevel fast multipole method to each of the unique entries in \mathbf{S} reduces its storing cost to $\mathcal{O}(n_{\text{dof}} \log(n_{\text{dof}}))$ [51]. This leads to a nested approximation scheme where the interaction between unit cells is approximated by a single level FMM and the identified near field interactions are further reduced by a multilevel FMM.

The approximation of the unique entries of \mathbf{S} requires the subdivision of the corresponding unit cells into boxes. These are then hierarchically subdivided until a certain level of subdivision is reached or the number of degrees

of freedom within a box is below a certain threshold. Boxes that are not further subdivided are called leaf boxes. Applying an admissibility criterion in the form of Eq. (27) allows to define the well-separated boxes on each level. The interactions are represented by P2P operators whenever the admissibility criterion does not hold. That is, the exact Green's function is employed. In contrast, interactions between well-separated boxes are represented by the truncated multipole expansion of Eq. (A.1). Since the unit cells are hierarchically subdivided into multiple levels, the contributions are first transferred to the leaf boxes by the previously introduced P2M operator. The contributions of all leaf boxes are then transferred upwards by M2M operators, cf. Eq. (A.8), and afterwards translated by the M2L operator. Subsequently, the contributions are transferred downwards by L2L operators, cf. Eq. (A.9), until the leaf boxes are reached. At this stage, the contributions of the leaf boxes are transferred by the L2P operators. Introducing the truncation number $n_{t,\text{near}}$ for the multipole expansion used in the multilevel FMM allows to choose its value independently of n_t . Hence, the error that is added on account of the approximation of \mathbf{S} can be controlled independently from the error that is added due to the approximation of the far-field interactions between the unit cells. It is referred to [50,51] for an in-depth analysis of the approximation error with respect to the truncation number and to [28,52] for details on the multilevel FMM.

The example in Fig. 1 considers a structure with finite two-dimensional periodicity. Applying the FMPBEM leads to the matrix structure of Eq. (32). Due to the quadratic shape of the unit cell in conjunction with the choice of the admissibility criterion in Eq. (27), the near field matrix \mathbf{S} consists of only 9 unique dense matrix blocks. Each of these blocks is approximated by the multilevel FMM scheme leading to the multilevel fast multipole periodic boundary element method, referred to as FMPBEM2. The complexity of the storage cost of \mathbf{S} is reduced to $\mathcal{O}(n_{\text{dof}} \log(n_{\text{dof}}))$ and therefore the total storage cost of the FMPBEM2 scales of order $\mathcal{O}(n_{\text{dof}} \log(n_{\text{dof}}) + n_t^2 n_{\text{dof}} + n_t^4 n_{\text{cells}})$ which is quasi-linear in n_{dof} and linear in n_{cells} . The FMPBEM2 does not require to store the discretized multilevel FMM operators, however, storing them significantly accelerates the matrix–vector products with \mathbf{S} . This adds an additional fourth-order dependence on the truncation number $n_{t,\text{near}}$ to the asymptotically complexity which is not included here since usually $n_{t,\text{near}} \ll n_{\text{dof}}$ holds. Whenever this does not hold, i.e., the finite periodic structure contains only a small unit cell discretization, applying the FMPBEM is more favorable than applying the FMPBEM2.

3.4. FMM for finite periodic structures in half-spaces

The FMPBEM and FMPBEM2 can also be applied to acoustic half-space problems. The geometry of one half-space is modeled and the reflection of sound waves at the symmetry plane is included by employing the half-space Green's function in Eq. (6). Whenever the symmetry plane is parallel to all directions of periodicity, the block Toeplitz matrix structure of Eq. (32) holds and a truncated series expansion of the half-space Green's function can be employed, cf. Eq. (A.7) in Appendix. In all other cases, the approach outlined in Section 2.3 is followed and the half-space Green's function is split into the first and the second summand. For the half-space problem shown in Fig. 2, the system matrix is approximated by

$$((\mathbf{S} + \mathbf{U}\mathbf{K}\mathbf{V}) + (\hat{\mathbf{S}} + \hat{\mathbf{U}}\hat{\mathbf{K}}\hat{\mathbf{V}}))\mathbf{p} = \mathbf{p}^{\text{inc}} . \quad (33)$$

The matrices \mathbf{S} , \mathbf{U} , \mathbf{K} and \mathbf{V} stem from applying the fast multipole boundary element method to the first summand of the half-space Green's function. Hence, the matrices coincide with the fast multipole matrices of a full-space problem for which the symmetry plane and the mirror images are neglected. These matrices are structured matrices as shown in (32). The matrices $\hat{\mathbf{S}}$, $\hat{\mathbf{U}}$, $\hat{\mathbf{K}}$ and $\hat{\mathbf{V}}$ stem from applying the fast multipole boundary element method to the second summand of the half-space Green's function. Appendix derives the corresponding fast multipole operators. The near field matrix $\hat{\mathbf{S}}$ is a multilevel banded block Hankel matrix whereas $\hat{\mathbf{U}}$ and $\hat{\mathbf{V}}$ are block diagonal matrices and $\hat{\mathbf{K}}$ is a multilevel block Hankel matrix. Note that $\mathbf{U} = \hat{\mathbf{U}}$ and $\mathbf{V} = \hat{\mathbf{V}}$ holds, since the L2P and P2M operators of both summands of the Green's function coincide. Note that the second summand includes the mirror image $\hat{\mathbf{y}}$ instead of \mathbf{y} and thus, an additional hierarchical subdivision of the mirrored boundary is required. Consequently, the admissibility criterion for the approximation of the integrals over the second summand changes to

$$|\mathbf{x}_c - \hat{\mathbf{y}}_c| \geq 2r . \quad (34)$$

Herein, $\hat{\mathbf{y}}_c$ is the center point of the box $\Omega_{\hat{\mathbf{y}}}$ that encloses a part of the mirrored boundary.

3.5. Solution scheme for the fast multipole periodic boundary element methods

The FMPBEM and FMPBEM2 yield a system of linear equations in the form of Eq. (32) or Eq. (33). In either case, the matrix structure prevents the direct solution and iterative solvers have to be applied.

In the case of full-space problems, the matrix–vector operation includes multiplications with the multilevel banded block Toeplitz matrix \mathbf{S} , with the block diagonal matrices \mathbf{U} and \mathbf{V} as well as with the multilevel block Toeplitz matrix \mathbf{K} . The latter can be embedded into a multilevel block circulant matrix $\tilde{\mathbf{C}}$ which can be block diagonalized by Fourier transforms similar to the scheme outlined in Section 2.4. This allows to rewrite Eq. (32) into

$$(\mathbf{S} + \mathbf{U}\tilde{\mathcal{F}}^{-1}\tilde{\mathbf{A}}\tilde{\mathcal{F}}\mathbf{V})\mathbf{p} = \mathbf{p}^{\text{inc}}, \quad (35)$$

where the block diagonal matrix $\tilde{\mathbf{A}}$ stores the Fourier transform of the first block column of $\tilde{\mathbf{C}}$ on its diagonal. The modified Fourier transforms $\tilde{\mathcal{F}}$ and $\tilde{\mathcal{F}}^{-1}$ are defined as

$$\tilde{\mathcal{F}} = \tilde{\mathbf{F}}_{2M_y-1} \otimes \tilde{\mathbf{F}}_{2M_x-1} \otimes \mathbf{I}_{(n_t+1)^2} \quad (36)$$

$$\tilde{\mathcal{F}}^{-1} = \tilde{\mathbf{F}}_{2M_y-1}^{-1} \otimes \tilde{\mathbf{F}}_{2M_x-1}^{-1} \otimes \mathbf{I}_{(n_t+1)^2}, \quad (37)$$

with the $(n_t + 1)^2 \times (n_t + 1)^2$ identity matrix $\mathbf{I}_{(n_t+1)^2}$ and the incomplete Fourier matrices as in Eqs. (25) and (26). This reduces the asymptotic complexity of matrix–vector operations with \mathbf{K} to $\mathcal{O}(n_t^4 n_{\text{cells}} \log(n_{\text{cells}}))$ time. Multiplications with the remaining matrices of Eq. (35) are implemented as sparse matrix operations. Consequently, the computational complexity scales of order $\mathcal{O}(n_{\text{cells}} n_{\text{dof}} n_t^2)$ for \mathbf{U} and \mathbf{V} as well as of order $\mathcal{O}(n_{\text{cells}} n_{\text{dof}}^2)$ for \mathbf{S} in the case of the FMPBEM. When employing the FMPBEM2, however, the asymptotic complexity of the multiplication with \mathbf{S} is further reduced to $\mathcal{O}(n_{\text{cells}} n_{\text{dof}} \log^2(n_{\text{dof}}))$ due to the multilevel approximation.

In the case of half-space problems for which Eq. (33) holds, the same technique as in Section 2.4 is applied. The matrix–vector multiplication is split into a multiplication involving the first summand and a multiplication involving the second summand. Since the first summand follows the structure of a full-space problem, i.e., of Eq. (32), this multiplication is performed as outlined above. The second summand involves block Hankel matrices and therefore a column permutation \mathbf{P} is applied to the matrix $\hat{\mathbf{K}}$ such that $\hat{\mathbf{K}}\mathbf{P}$ is a block Toeplitz matrix. This allows to address the matrix–vector product with a similar technique since $(\hat{\mathbf{S}} + \hat{\mathbf{U}}\hat{\mathbf{K}}\hat{\mathbf{V}})\mathbf{p} = (\hat{\mathbf{S}} + \hat{\mathbf{U}}\hat{\mathbf{K}}\mathbf{P}\mathbf{P}^T\hat{\mathbf{V}})\mathbf{p}$ holds.

4. Numerical examples

The proposed single level and multilevel fast multipole periodic boundary element methods are validated by means of two numerical examples. The first example is the scattering of a finite periodic array of spheres and the second example is a sound barrier design study. The computational efficiency of the proposed methods is compared to the conventional boundary element method (BEM), the multilevel fast multipole boundary element method (FMM, [52]) and the periodic boundary element method (PBEM). Both BEM and PBEM yield the same solution except for numerical round-off errors since the PBEM system matrix is an exact representation of the BEM system matrix. In contrast, the FMM, FMPBEM and FMPBEM2 are based on truncated multipole expansions and thus introduce additional errors. Our proposed approaches employ an optimized subdivision of the finite periodic geometry with either a single level scheme (FMPBEM) or a multilevel scheme (FMPBEM2). In contrast, the FMM uses the standard multilevel octree structure. All three methods evaluate matrix–vector products within an l^2 -error of less than 10^{-4} by choosing sufficiently large truncation numbers n_t as well as $n_{t,\text{near}}$ in the case of the FMPBEM2.

All methods employ the generalized minimal residual method (GMRes) to solve the system of linear equations. A converged solution is found whenever a relative tolerance of 10^{-4} is met. The calculations were performed on a desktop PC with 128 GB of RAM and 6 physical cores running at 3.5 GHz. The assembly and matrix–vector operations are fully parallelized using OpenMP with 6 threads.

4.1. Scattering of a finite periodic array of spheres

A periodic array of 25 acoustically rigid spheres with a radius of $r = 100$ mm is considered as first numerical example. The spheres are arranged in a two-dimensional pattern with $M_x = 5$ and $M_y = 5$ as shown in Fig. 3. The distance between the center points of neighboring scatterers in the x and y -direction equals 350 mm. The

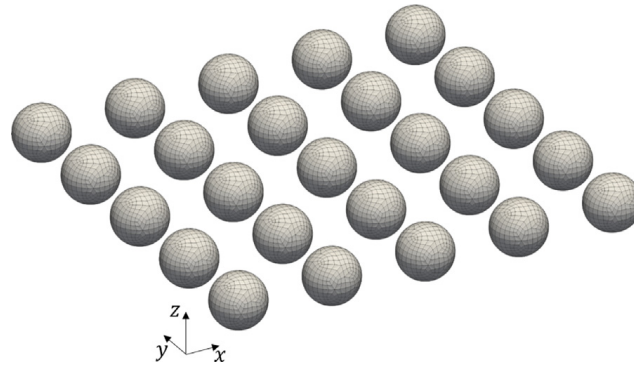


Fig. 3. Finite periodic array of spherical scatterers with $M_x = 5$ and $M_y = 5$. Each scatterer has a radius of $r = 100$ mm and the distance between the center points of neighboring scatterers equals 350 mm in the x and y -direction.

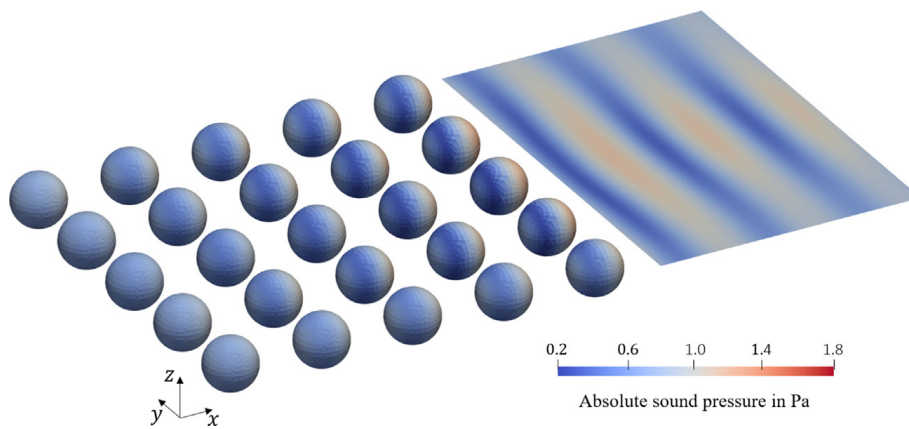


Fig. 4. Absolute sound pressure on the surface of the scatterers and on a plane in the back field at 500 Hz. Each sphere is discretized by 600 quadrilateral elements with constant discontinuous pressure approximation and excited by a plane wave traveling in the positive x -direction.

surrounding medium is air with speed of sound of $c = 343 \text{ m s}^{-1}$ and density of $\rho = 1.21 \text{ kg m}^{-3}$. A plane wave traveling in the x -direction with a source strength of $p_0 = 1 \text{ Pa}$ excites the spheres, i.e.,

$$p^{\text{inc}}(x) = p_0 e^{ikx} . \tag{38}$$

Each sphere is discretized using 600 quadrilateral boundary elements with constant discontinuous pressure approximation if not specified otherwise. This corresponds to 40 elements over the circumference and leads to a numerical model with 15 000 degrees of freedom (dofs) in total. Fig. 4 shows the absolute sound pressure on the surface of the scatterers and on a plane in the back field at $f = 500$ Hz. Up to this frequency, the FMM, FMPBEM and FMPBEM2 yield solutions with a relative error of less than 10^{-4} in the l^2 -norm compared to the PBEM solution by prescribing truncation numbers of $n_t = 8$ (FMM), $n_t = 4$ (FMPBEM) and $n_t = 4, n_{t,\text{near}} = 6$ (FMPBEM2).

The first study assesses the time spent for the assembly and matrix–vector computation as well as the memory usage with respect to the size of the periodic array. A variation of the number of unit cells in the y -direction, i.e., the value of M_y , is performed. Values between 5 and 100 are taken into account, resulting in periodic arrangements of 25 to 500 scatterers. This corresponds to numerical models with 15 000 to 300 000 dofs. Fig. 5(a) shows the time of the assembly process for the first four methods. The bottom axis represents the number of periodic elements M_y in the y -direction. This value relates to the total number of dofs by $N_{\text{dof}} = 3000M_y$ which is depicted on the top axis. The BEM is applied to the first three configurations only due to its excessive memory requirements. For the initial configuration, i.e., $M_y = 5$, the BEM is the slowest taking around 128.0 s followed by the FMM (19.9 s), the PBEM (19.4 s) and the FMPBEM (2.4 s). Increasing the number of unit cells in the y -direction, the assembly time complexity is found to be of order $\mathcal{O}(M_y^2)$ for the BEM and of order $\mathcal{O}(M_y \log(M_y))$ for the PBEM and FMM. In contrast, the assembly time of the FMPBEM seems to be constant. However, this is resolved in the more detailed plot of Fig. 5(b) where values of up to $M_y = 1000$ are considered. The assembly of \mathbf{S} , \mathbf{U} and \mathbf{V} is constant

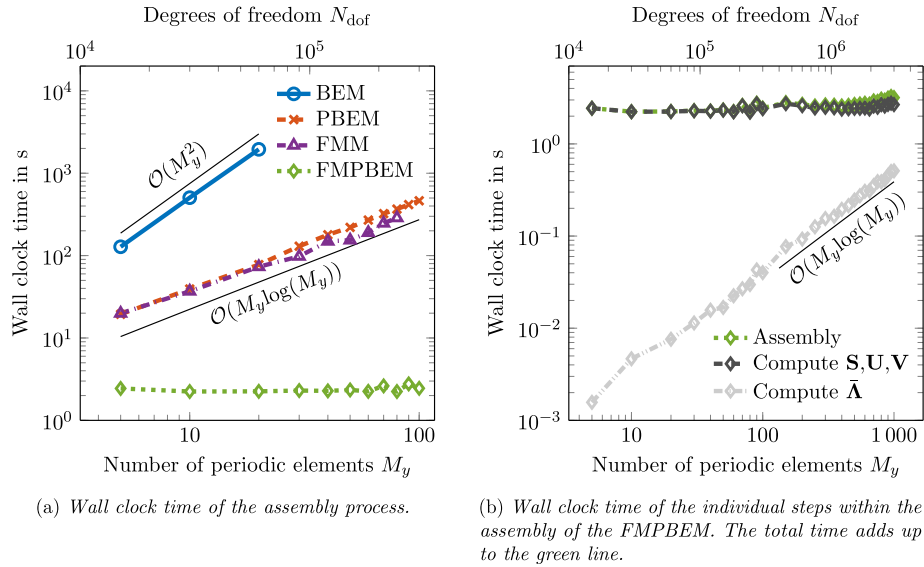


Fig. 5. Timings of the assembly for all five methods at $f = 500$ Hz. The size of the periodic arrangement is varied by prescribing values of M_y between 5 and 100. The numerical models consist of $N_{dof} = 3000M_y$ degrees of freedom.

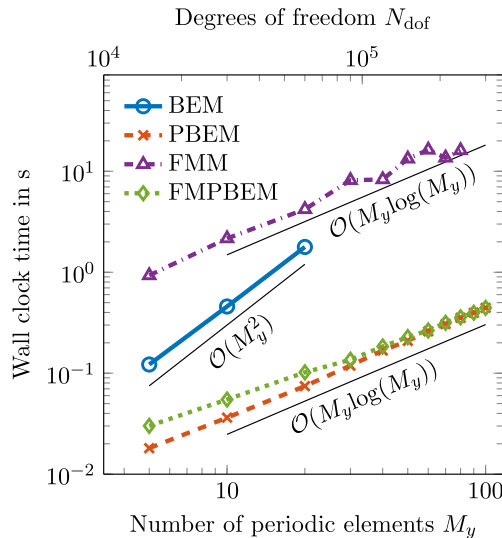


Fig. 6. Wall clock time of one matrix–vector product for the first four methods at $f = 500$ Hz. The size of the periodic arrangement is varied by prescribing values of M_y between 5 and 100. The numerical models consist of $N_{dof} = 3000M_y$ degrees of freedom.

in M_y , whereas the computation of $\bar{\mathbf{A}}$ scales quasi-linearly. Therefore, the assembly of the FMPBEM matrices asymptotically scales of order $\mathcal{O}(M_y \log(M_y))$. This complexity estimate equally holds for the FMPBEM2 since both methods differ only in the computation of \mathbf{S} .

Fig. 6 visualizes the time of one matrix–vector product for the first four methods. In the case of the initial configuration ($M_y = 5$), the FMM is the slowest taking around 0.930 s followed by the BEM (0.122 s), the FMPBEM (0.030 s) and the PBEM (0.018 s). Increasing the number of unit cells in the y -direction reveals the complexity of the matrix–vector products. It is of order $\mathcal{O}(M_y^2)$ for the BEM and of order $\mathcal{O}(M_y \log(M_y))$ for the PBEM and FMPBEM. The timings of the FMM follow its theoretical scaling of order $\mathcal{O}(M_y \log^2(M_y))$ [51] with slight fluctuations due to the changing depth of the octree subdivision with increasing M_y .

Fig. 7(a) shows the storage costs for the first four methods considering different sizes of the periodic arrangement. The BEM stores the fully populated system matrix which leads to a storage cost of $\mathcal{O}(M_y^2)$. The memory usage of the PBEM scales linear in M_y whereas the memory usage of the FMM scales close to its theoretical order

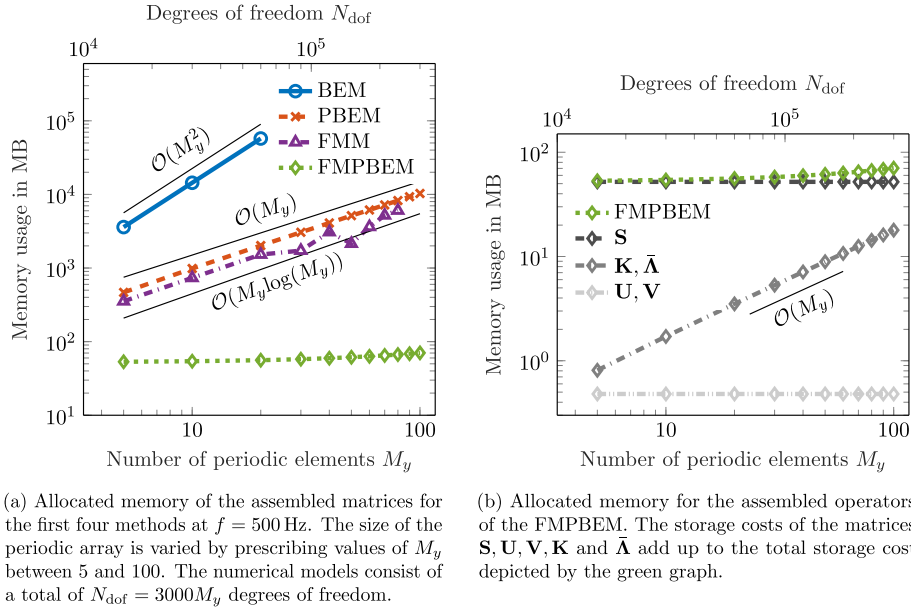


Fig. 7. Comparison of the memory with respect to the number of periodic elements M_y in the y -direction.

of $\mathcal{O}(M_y \log(M_y))$ [51]. The slight deviations can be attributed to the changing depth of the octree subdivision. Fig. 7(b) visualizes the memory usage of the FMPBEM in greater detail by illustrating the contribution of the individual matrices to the total storage costs. The allocated memory for \mathbf{S} , \mathbf{U} and \mathbf{V} is constant in M_y whereas the memory of \mathbf{K} , or equivalently $\bar{\Lambda}$, scales of order $\mathcal{O}(M_y)$. Hence, the storage cost complexity of the FMPBEM asymptotically converges to $\mathcal{O}(M_y)$.

The second study assesses the time spent for the assembly and matrix–vector computation as well as the memory usage with respect to the number of degrees of freedom n_{dof} within the unit cell. The layout of the periodic arrangement of scatters is held constant at $M_x = 5$ and $M_y = 10$ whereas the boundary element discretization of each scatterer is varied. An h -refinement is conducted to generate the numerical models. Each sphere is initially discretized using 24 boundary elements with quadratic pressure approximation featuring 192 sound pressure dofs. The largest problem that is solved in the first comparison features 388 800 dofs and stems from discretizing each spherical scatterer with 972 boundary elements with quadratic pressure approximation.

Fig. 8(a) visualizes the assembly time for the first four methods considering various unit cell discretizations. Not all methods are applied to every numerical model due to memory limitations. The assembly of the BEM matrices takes 11.1 s for the smallest problem which features a total of 9600 dofs. The assembly times of the FMM and PBEM are within one order of magnitude with 6.18 s and 1.56 s, respectively. The FMPBEM assembly is the fastest, taking only 0.16 s. An increase in the number of degrees of freedom n_{dof} within the unit cell reveals the quadratic complexity of the BEM, PBEM and FMPBEM assembly times in n_{dof} . In contrast, the FMM assembly time exhibits a scaling close to its theoretical value of $\mathcal{O}(n_{\text{dof}} \log(n_{\text{dof}}))$. Fig. 8(b) depicts the wall clock time of one matrix–vector product. The FMM takes the most time (0.60 s) in the case of the initial configuration followed by the BEM (0.053 s), the FMPBEM (0.007 s) and the PBEM (0.006 s). However, the timings of the latter three scale of order $\mathcal{O}(n_{\text{dof}}^2)$ which discourages their application to models featuring very large n_{dof} . The FMM features a scaling below the theoretical value of $\mathcal{O}(n_{\text{dof}} \log^2(n_{\text{dof}}))$ that is close to $\mathcal{O}(n_{\text{dof}})$. This might be attributed to the uneven distribution of the degrees of freedom within the $5 \times 10 \times 1$ pattern of the spherical scatterers. Employing a multilevel approximation of the near field matrix within the FMPBEM reduces the computational complexity of the assembly and matrix–vector computation. Figs. 9(a) and 9(b) visualize the performances of the FMPBEM in comparison to its extension, the FMPBEM2. For small unit cell discretizations, the FMPBEM is faster in both assembly and matrix–vector operations due to the additional overhead of the approximation of the near field matrix \mathbf{S} in the FMPBEM2. However, in the case of medium to large-scale unit cell discretizations, the FMPBEM2 achieves a significant reduction in computational time due to its more favorable scaling of order $\mathcal{O}(n_{\text{dof}} \log(n_{\text{dof}}))$. The largest problem features $n_{\text{dof}} = 194\,144$ degrees of freedom within each unit cell leading to a total of $N_{\text{dof}} = 9\,707\,200$

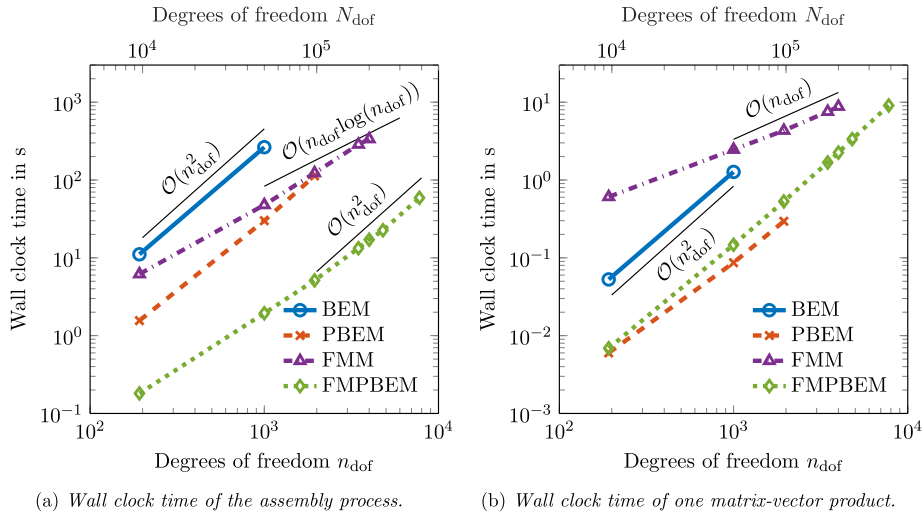


Fig. 8. Timings of the assembly and matrix–vector product for the first four methods at $f = 500$ Hz. The number of degrees of freedom n_{dof} is increased by performing an h -refinement. The size of the periodic arrangement is constant with $M_x = 5$ and $M_y = 10$.

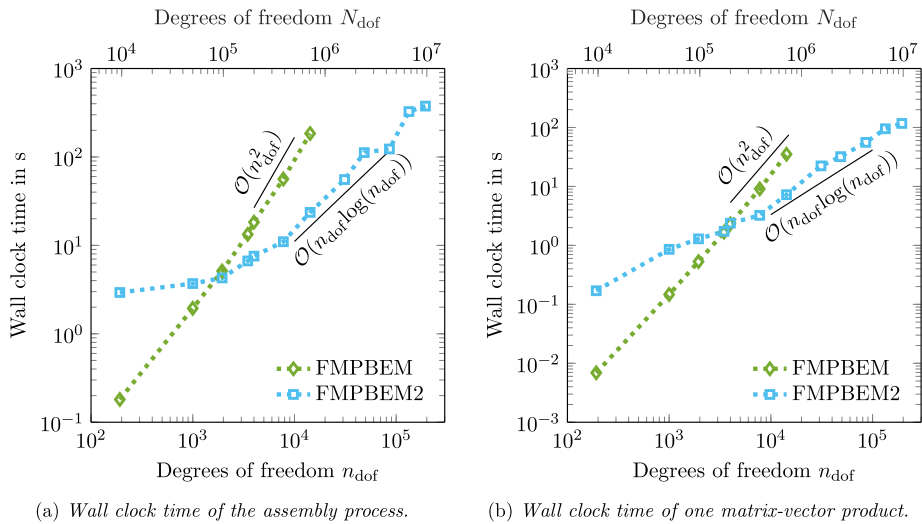


Fig. 9. Timings of the assembly and matrix–vector product of the FMPBEM and FMPBEM2 at $f = 500$ Hz considering large-scale unit cell discretizations. The number of degrees of freedom n_{dof} is increased by performing an h -refinement while the size of the periodic arrangement is constant with $M_x = 5$ and $M_y = 10$.

dofs. Its assembly takes 376 s and one matrix–vector product is computed in 117 s. The same problem cannot be solved with the FMM due to memory limitations.

Fig. 10(a) shows the memory usage of the first four methods considering varying unit cell discretizations. The BEM, PBEM and FMPBEM exhibit a quadratic scaling of the storage cost with respect to the number of degrees of freedom n_{dof} of the unit cell. In contrast, the FMM scales of order $\mathcal{O}(n_{\text{dof}} \log(n_{\text{dof}}))$. Although the FMPBEM features the lowest memory usage within the considered range of discretizations, the quadratic scaling prevents its application to finite periodic problems with large values of n_{dof} . This is resolved by the FMPBEM which introduces an additional approximation of the near field matrix \mathbf{S} . Fig. 10(b) visualizes the memory usage for large-scale unit cell discretizations with up to $n_{\text{dof}} = 194\,114$ degrees of freedom and indicates a complexity of $\mathcal{O}(n_{\text{dof}} \log(n_{\text{dof}}))$ for the storage cost within the FMPBEM2.

The third study analyzes the frequency dependent accuracy of the FMPBEM solution. The study includes a periodic arrangement with $M_x = 1$ and $M_y = 30$ and frequencies of up to 3000 Hz. Each sphere is discretized using 600 boundary elements with quadratic pressure approximation. This corresponds to about 7.3 elements per wavelength at 3 kHz. The GMRes tolerance is set to 10^{-14} and truncation numbers of $n_t = 2, 4, \dots, 12$ are

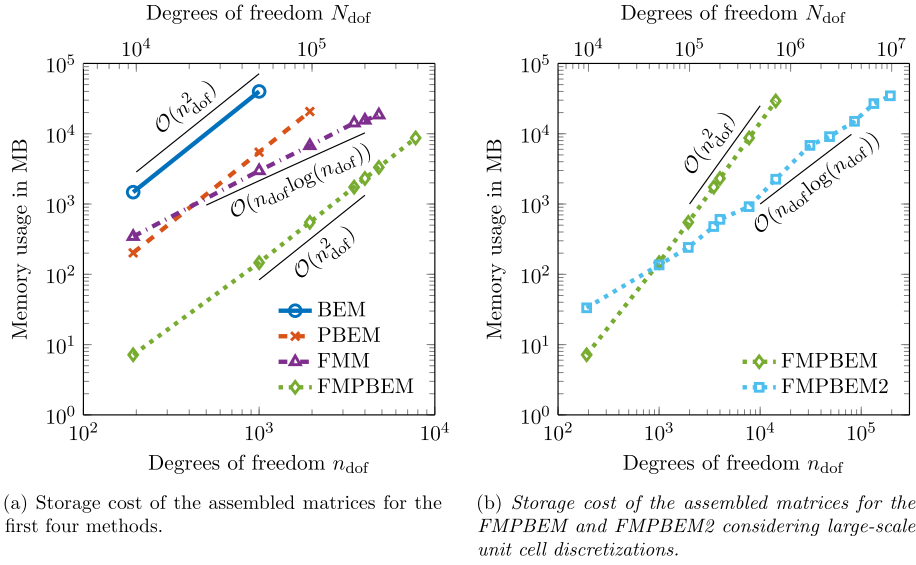


Fig. 10. Comparison of the storage cost with respect to the number of degrees of freedom n_{dof} at $f = 500$ Hz. The size of the periodic arrangement is constant with $M_x = 5$ and $M_y = 10$.

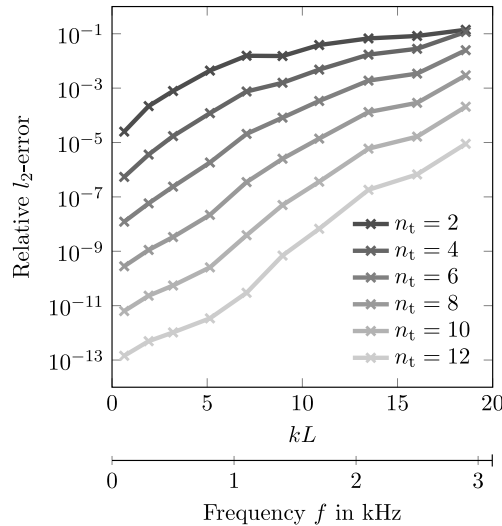


Fig. 11. Relative error of the FMPBEM solution to the BEM solution in the l_2 -norm as a function of the dimensionless wavenumber kL , with L denoting the characteristic unit cell length. A periodic arrangement with $M_x = 5$ and $M_y = 100$ is analyzed. Each sphere is discretized with 600 boundary elements with constant pressure approximation. Different values of the truncation number n_t are considered.

considered. Fig. 11 presents the relative error in the l_2 -norm of the FMPBEM solution to a reference solution determined by the PBEM. The x -axis shows both, the frequency f and the dimensionless wavenumber kL with the characteristic length $L = 350$ mm of the unit cells. A relative error of less than 10^{-4} is achieved for all considered truncation numbers at 100 Hz or $kL = 0.64$. With an increase in frequency, the accuracy of the FMPBEM deteriorates. A relative error of less than 10^{-4} at 1000 Hz requires six or more terms of the fast multipole expansion.

4.2. Sound barrier

A sound barrier design study is considered in the second numerical example. The general setup is shown in Fig. 12(a). Two monopole sources emit an incident sound pressure wave on the left-hand side, 1 m above the sound-hard ground. They differ in the source strength which is $p_1 = 2$ Pa for the source at $y_1 = 6.5$ m and $p_2 = 1$ Pa for the source at $y_2 = 3.5$ m. A sound barrier is located within the design space and ideally reduces the sound

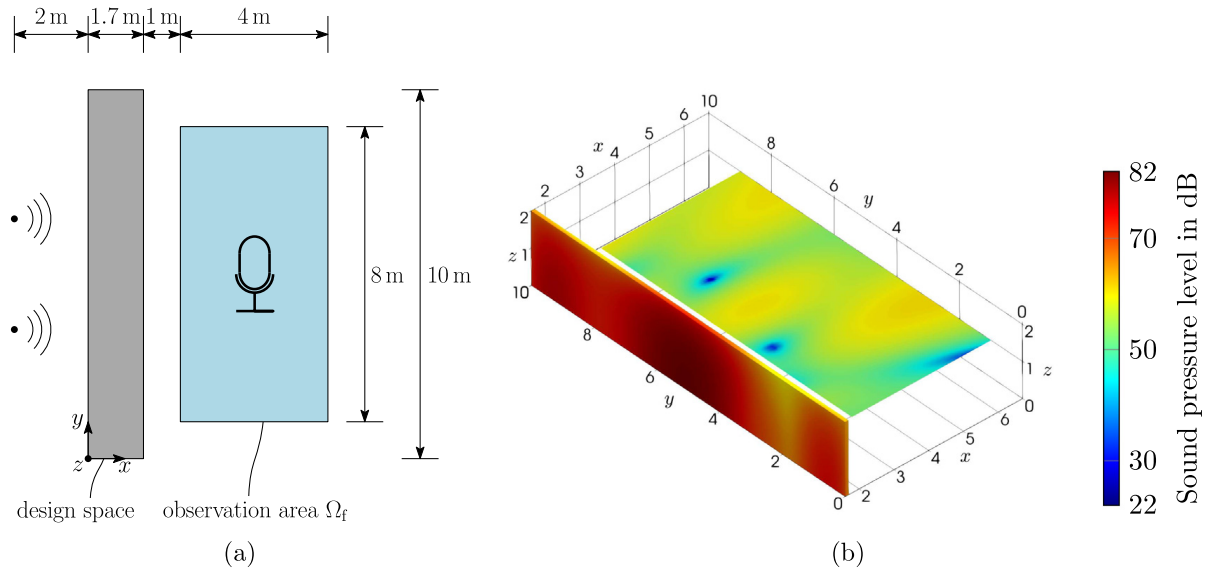


Fig. 12. Top view of the sound barrier setup (a) and sound pressure level ($0\text{ dB} = 2 \times 10^{-5}\text{ Pa}$) on the wall sound barrier and in the observation area at 100 Hz (b).

pressure within the observation area Ω_f . Assessing the insertion loss (IL) within the observation area quantifies the performance of different sound barrier designs. Following the work of [22], the IL reads

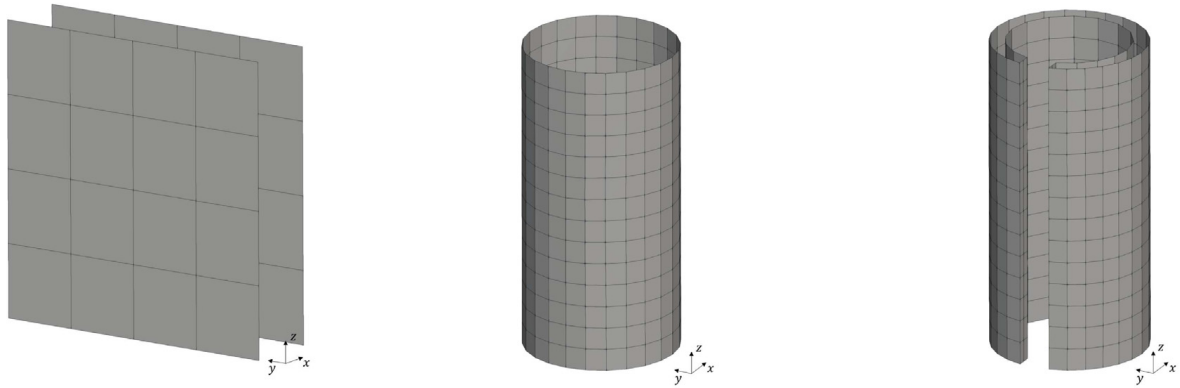
$$IL(f) = 20 \log_{10} \left(\frac{\sum_{i=1}^M |\mathbf{p}^{\text{inc}}(\mathbf{x}_i, f)|}{\sum_{i=1}^M |\mathbf{p}(\mathbf{x}_i, f)|} \right), \quad \mathbf{x}_i \in \Omega_f, \tag{39}$$

with the number of observation points M within Ω_f . In this study, $M = 3200$ uniformly distributed points are taken into account. A frequency range of 100 Hz to 500 Hz is analyzed with 81 uniformly distributed frequency samples.

The first sound barrier design is a sound-hard wall with constant rectangular cross section, height of 2 m, length of 10 m and a width of 0.1 m. It is located at the rightmost part of the design space. The full-scale wall model is shown in Fig. 12(b) and consists of 4140 boundary elements with quadratic pressure approximation. This equals 6.9 elements per wavelength at 500 Hz and a total of 33120 pressure dofs. The unit cell of the corresponding periodic wall model is shown in Fig. 13(a). It consists of two boundary element layers, one at the front and one at the back. The layers have a size of 0.2 m by 0.2 m and consist of four boundary elements with quadratic pressure approximation each. This also leads to 6.9 elements per wavelength at 500 Hz. The unit cell is extended by $M_y = 50$ cells in the y -direction, i.e., the length of the wall, and $M_z = 10$ cells in the z -direction, i.e., the height of the wall. Hence, a total of 500 periodic cells are considered. Note that the periodic model lacks the top and side surfaces of the wall and therefore only consists of 32000 dofs.

Fig. 14 shows the insertion loss of the sound-hard wall over the frequency range of 100 Hz to 500 Hz for both models, the full-scale wall model and the periodic wall model. The solution of the former is generated by the BEM whereas the FMPBEM is employed for solving the latter. Although the periodic model lacks the top and side surfaces of the wall, the insertion loss values are in good agreement with the results of the full-scale model and underestimate the IL only slightly. The insertion loss stays well above 10 dB up to 300 Hz with a peak value of 19.2 dB at 210 Hz. The minimum insertion loss value of 7.6 dB is found at 390 Hz. Fig. 12(b) shows the sound pressure levels on the sound barrier surface and in the observation area for $f = 100$ Hz.

The second sound barrier design considers a periodic array of cylinders where each cylinder has a radius of 0.1 m and a height of 2 m. A total of 75 cylinders are arranged in a rectangular pattern with $M_x = 3$ rows and $M_y = 25$ cylinders along the length of the barrier. With a distance of $d = 0.4$ m between neighboring cylinders in the x and y -direction, the footprint of the cylinder sound barrier wall is 9.8 m by 1 m. The unit cell has a height of 0.4 m, cf. Fig. 13(b), and is repeated $M_z = 5$ times in the z -direction, resulting in a total height of 2 m. Each unit cell is discretized with 12 boundary elements with linear sound pressure approximation along the circumference and 35 elements along its height. This corresponds to at least 12 elements per wavelength at 500 Hz and results in 126000 dofs in total.



(a) $0.2\text{ m} \times 0.2\text{ m} \times 0.1\text{ m}$
 $M_x = 1, M_y = 50, M_z = 10$

(b) $0.2\text{ m} \times 0.2\text{ m} \times 0.4\text{ m}$
 $M_x = 3, M_y = 25, M_z = 5$

(c) $0.2\text{ m} \times 0.2\text{ m} \times 0.4\text{ m}$
 $M_x = 3, M_y = 25, M_z = 5$

Fig. 13. Unit cells of the wall sound barrier (a), cylinder sound barrier (b) and c-shaped sound barrier (c). The outer dimensions of the unit cells and the number of cells in each direction of periodicity are given below the corresponding figures.

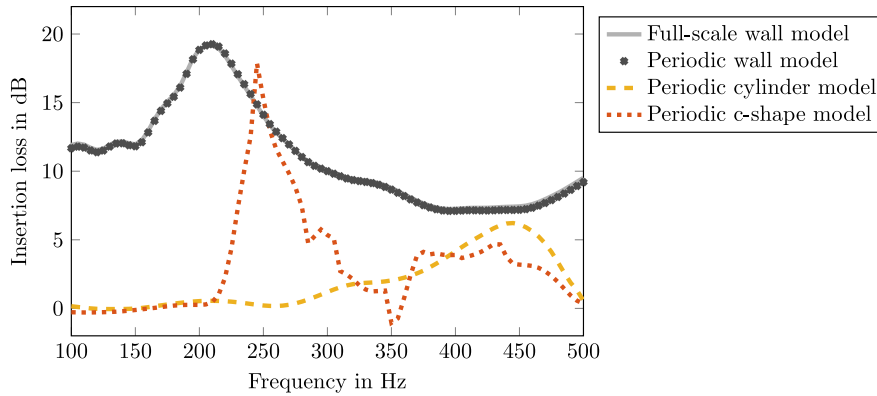


Fig. 14. Insertion loss (IL) in dB of the three sound barrier designs. The IL is assessed in the observation area Ω_f according to Eq. (39).

Although the cylinder sound barrier is not continuous along its length, a significant insertion loss is still expected due to standing waves forming between the cylinders. According to Bragg’s law, standing waves occur at

$$f_{\text{Bragg}} = \frac{nc}{2d \sin(\theta)}, \tag{40}$$

with a positive integer n and the incident angle θ . In the present case, the first Bragg frequency equals 428.75 Hz assuming perpendicular incidence, i.e., $\theta = \pi/2$. Note that $0.125\pi < \theta \leq \pi/2$ holds for the given monopole excitation and sound barrier setup. The insertion loss within the frequency range of interest is depicted in Fig. 14. The IL stays around 0 dB up to 280 Hz from which on it monotonically increases to its maximum of 6.5 dB at 440 Hz.

The third sound barrier design follows the idea of the second design but introduces an additional resonance by considering a c-shaped cross section. Each c-shape structure has an outer radius of 0.1 m, inner radius of 0.08 m, a slit width of 0.04 m and a height of 2 m. The unit cell of the periodic model has a height of 0.4 m and is depicted in Fig. 13(c). Its discretization features around 11.9 boundary elements with linear pressure approximation per wavelength at 500 Hz. Besides the standing waves around the Bragg frequency an additional resonance occurs since each c-shape structure acts as a Helmholtz resonator. The resonance frequency is estimated at $f_{\text{HR}} = 258.9\text{ Hz}$ based on a two-dimensional finite element simulation of the c-shaped cross section. The parameters of the periodic array remain unchanged with $M_x = 3, M_y = 25, M_z = 5$ and $d = 0.4\text{ m}$ which leads to the same estimate of the Bragg frequency f_{Bragg} and a total of 231000 dofs. The IL is shown in Fig. 14 and proceeds very similar to the IL of the cylinder sound barrier design up to around 210 Hz. From here on, the IL of the c-shaped design rises steeply to a maximum of 17.9 dB at 245 Hz. This is followed by an equally steep decline up to 320 Hz. A further significant IL is reported between 370 Hz and 440 Hz with values above 3.8 dB. Introducing a c-shaped cross section

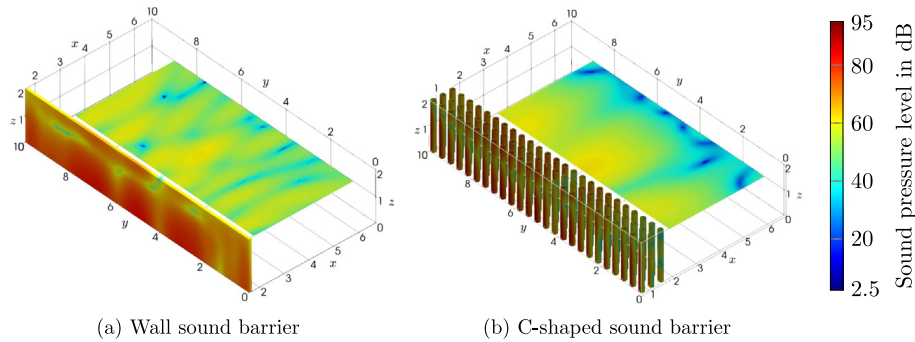


Fig. 15. Sound pressure level ($0\text{ dB} = 2 \times 10^{-5}\text{ Pa}$) on two sound barrier designs and in the observation area at 245 Hz.

significantly improves the insertion loss within a frequency region around f_{HR} while still utilizing the Bragg effects. Fig. 15 shows the sound pressure values of the wall sound barrier and the c-shaped sound barrier in a side-by-side comparison at a frequency of $f = 245\text{ Hz}$.

5. Conclusion and future work

Two fast multipole periodic boundary element methods have been proposed for the solution of time-harmonic acoustic problems of finite periodic structures. Both methods subdivide the geometry into boxes that correspond to the unit cells of the periodic geometry. A boundary element discretization is applied to each unit cell, i.e., each box. Interactions between well-separated boxes are approximated by a multipole expansion of the Green's function. On the other hand, either an exact representation of the Green's function is used for the interactions of neighboring boxes (FMPBEM) or an additional multilevel fast multipole method is employed (FMPBEM2). In both methods, the fast multipole operators acting between the unit cells become block Toeplitz matrices due to the periodicity of the geometry. These are matrices with constant blocks along each diagonal and therefore feature only a small memory footprint. In addition, matrix–vector products can be expressed by circular convolutions which significantly reduces their computational complexity. Certain configurations of half-space problems disturb the block Toeplitz structure. However, this contribution introduces a remedy by splitting the half-space Green's function into its summands and discretizing each summand separately. The first numerical example, the scattering of a periodic array of sound-hard spheres, indicated a quasi-linear scaling of the fast multipole periodic boundary element solution with respect to the number of unit cells. The solution time has been found to be an order of magnitude below comparable approaches such as the periodic boundary element method and the multilevel fast multipole method. The study indicated that the proposed methods perform especially well in cases where large periodic structures are considered. The application of the FMPBEM is favorable in the case of unit cells that feature small numbers of degrees of freedom, whereas the FMPBEM2 is more beneficial in the case of large-scale unit cell discretizations. The accuracy of our approach is set by the truncation number of the multipole expansions which also has been investigated in the first example. In the second example, the FMPBEM has been applied to a sound barrier design study in half-space. Both, wall sound barriers as well as sonic crystal sound barriers were analyzed. Although the periodic model of the wall barrier does not account for the top and side surfaces, the results were in good agreement with the results of a full-scale analysis. It has been shown that a comparison of sound barrier designs in three dimensional space is indeed feasible with the proposed methods.

The concept of the fast multipole periodic boundary element methods is based on the translation invariance of the Green's function. Applying the same concept to problems with a rotationally arranged unit cells would yield a method that, for instance, would be able to analyze the aeroacoustic behavior of ducted fans more efficiently. Furthermore, the presented approach can be applied likewise using the hierarchical boundary element method. With respect to the computational efficiency, further improvements are planned by representing the multilevel block Toeplitz matrices in the tensor train format, cf. [53] for details. Future work will involve taking visco-thermal losses into account and introducing a structural-acoustic coupling scheme. This will allow to analyze sound barriers that include acoustic energy harvesting as presented in [54]. In addition, the proposed methods can be extended to study local defects within the periodic structure by introducing cost-efficient low-rank updates of \mathbf{S} , \mathbf{U} and \mathbf{V} .

Declaration of competing interest

The authors declare that they have no known competing financial interests or personal relationships that could have appeared to influence the work reported in this paper.

Acknowledgments

This work is financially supported by the China Scholarship Council (CSC) (File No. 201706340085), the National Natural Science Foundation of China (NSFC) under Grant No. 11772322.

Appendix. Fast multipole expansions

A single integral of Eq. (8) over an arbitrary boundary part $\Gamma_c \subset \Gamma$ is picked as an example. All source points \mathbf{y} on the boundary Γ_c lie within the box Ω_y . This box is in the far field of the box Ω_x which encloses the field points \mathbf{x} . Based on the truncated series expansion of the full-space Green's function Eq. (28), the approximation of the integral reads [52]

$$\int_{\Gamma_c} \frac{\partial G(\mathbf{x}, \mathbf{y})}{\partial \mathbf{n}(\mathbf{y})} p(\mathbf{y}) d\Gamma(\mathbf{y}) \approx \frac{ik}{4\pi} \sum_{n=0}^{n_t} (2n+1) \sum_{m=-n}^n O_n^m(\mathbf{x} - \mathbf{y}_c) M_n^m(\mathbf{y}, \mathbf{y}_c), \quad (A.1)$$

$$|\mathbf{y} - \mathbf{y}_c| < |\mathbf{x} - \mathbf{y}_c|,$$

with the multipole moments M_n^m at the expansion point \mathbf{y}_c given as

$$M_n^m(\mathbf{y}_c) = \int_{\Gamma_c} \frac{\partial \bar{I}_n^m(\mathbf{y} - \mathbf{y}_c)}{\partial \mathbf{n}(\mathbf{y})} p(\mathbf{y}) d\Gamma(\mathbf{y}). \quad (A.2)$$

Eq. (A.1) is called multipole expansion and Eq. (A.2) is the particle-to-multipole (P2M) translation. The discretization of the latter equation leads the P2M operator.

Expanding the Green's function around a point \mathbf{x}_c close to \mathbf{x} instead yields the local expansion [52]

$$\int_{\Gamma_c} \frac{\partial G(\mathbf{x}, \mathbf{y})}{\partial \mathbf{n}(\mathbf{y})} p(\mathbf{y}) d\Gamma(\mathbf{y}) \approx \frac{ik}{4\pi} \sum_{n=0}^{n_t} (2n+1) \sum_{m=-n}^n \bar{I}_n^m(\mathbf{x} - \mathbf{x}_c) L_n^m(\mathbf{x}_c), \quad (A.3)$$

$$|\mathbf{x} - \mathbf{x}_c| < |\mathbf{y} - \mathbf{x}_c|,$$

with the local coefficients L_n^m at the expansion point \mathbf{x}_c given as

$$L_n^m(\mathbf{x}_c) = \sum_{n'=0}^{n_t} (2n'+1) \sum_{m'=-n'}^{n'} (-1)^{m+m'} \sum_{l \in N} W_{n',n,m',m,l} O_l^{m+m'}(\mathbf{x}_c - \mathbf{y}_c) M_{n'}^{m'}(\mathbf{y}_c). \quad (A.4)$$

Eq. (A.3) is the local-to-particle (L2P) translation and Eq. (A.4) is the multipole-to-local (M2L) translation. The set N is defined by [52]

$$N := \left\{ l \mid l \in \mathbb{Z}, n+n'-l : \text{even}, \max\{|m+m'|, |n-n'|\} < l < n+n' \right\}, \quad (A.5)$$

and $W_{n',n,m',m,l}$ is given as

$$W_{n',n,m',m,l} = (2l+1) i^{n'-n+l} \begin{pmatrix} n & n' & l \\ 0 & 0 & 0 \end{pmatrix} \begin{pmatrix} n & n' & l \\ m & m' & -m-m' \end{pmatrix}, \quad (A.6)$$

where $(\begin{smallmatrix} a & b & c \\ d & e & f \end{smallmatrix})$ denotes the Wigner 3j-symbol [55].

In the case of half-space problems, a truncated series expansion is employed for the second summand of the half-space Green's function Eq. (6). The expansion reads

$$G(\mathbf{x}, \hat{\mathbf{y}}) \approx R_p \frac{ik}{4\pi} \sum_{n=0}^{n_t} (2n+1) \sum_{m=-n}^n O_n^m(\mathbf{x} - \hat{\mathbf{y}}_c) \bar{I}_n^m(\hat{\mathbf{y}} - \hat{\mathbf{y}}_c), \quad |\hat{\mathbf{y}} - \hat{\mathbf{y}}_c| < |\mathbf{x} - \hat{\mathbf{y}}_c|. \quad (A.7)$$

The mirrored source points $\hat{\mathbf{y}}$ lie in the box $\Omega_{\hat{\mathbf{y}}}$ with center point $\hat{\mathbf{y}}_c$. Eq. (A.7) is valid whenever the admissibility criterion holds, i.e., when $\Omega_{\hat{\mathbf{y}}}$ is in the far field of Ω_x . The corresponding fast multipole operators can be derived

similarly to the aforementioned operators of the full-space problem by substituting \mathbf{y} and \mathbf{y}_c with its mirrored variants.

In the case of the multilevel fast multipole method, two additional operators are introduced. The moment-to-moment (M2M) translation shift the multipole moments from an expansion point \mathbf{y}_c to an expansion point $\mathbf{y}_{c'}$ following

$$\tilde{M}_n^m(\mathbf{y}_{c'}) = \sum_{n'=0}^{n_t} (2n' + 1) \sum_{m'=-n'}^{n'} \sum_{l \in N} (-1)^{m'} W_{n,n',m,m',l} I_l^{-m-m'}(\mathbf{y}_c - \mathbf{y}_{c'}) M_{n'}^{-m'}(\mathbf{y}_c). \quad (\text{A.8})$$

Similarly, the local-to-local (L2L) translation shifts the local coefficients from an expansion point $\mathbf{x}_{c'}$ to an expansion point \mathbf{x}_c by

$$L_n^m(\mathbf{x}_{c'}) = (-1)^m \sum_{n'=0}^{n_t} (2n' + 1) \sum_{m'=-n'}^{n'} \sum_{l \in N} W_{n',n,m',m,l} I_l^{m-m'}(\mathbf{x}_{c'} - \mathbf{x}_c) L_{n'}^{m'}(\mathbf{x}_c). \quad (\text{A.9})$$

References

- [1] R. Martínez-Sala, J. Sancho, J.V. Sánchez, V. Gómez, J. Llinares, F. Meseguer, Sound attenuation by sculpture, *Nature* 378 (6554) (1995) 241, <http://dx.doi.org/10.1038/378241a0>.
- [2] V. Romero-García, R. Picó, A. Cebrecos, V.J. Sánchez-Morcillo, K. Staliunas, Enhancement of sound in chirped sonic crystals, *Appl. Phys. Lett.* 102 (9) (2013) 091906, <http://dx.doi.org/10.1063/1.4793575>.
- [3] M. Sigalas, M.S. Kushwaha, E.N. Economou, M. Kafesaki, I.E. Psarobas, W. Steurer, Classical vibrational modes in phononic lattices: theory and experiment, *Z. Für Kristallographie - Cryst. Mater.* 220 (9–10) (2005) <http://dx.doi.org/10.1524/zkri.2005.220.9-10.765>.
- [4] M. Maldovan, Sound and heat revolutions in phononics, *Nature* 503 (7475) (2013) 209–217, <http://dx.doi.org/10.1038/nature12608>.
- [5] A. Melnikov, M. Maeder, N. Friedrich, Y. Pozhanka, A. Wollmann, M. Scheffler, S. Oberst, D. Powell, S. Marburg, Acoustic metamaterial capsule for reduction of stage machinery noise, *J. Acoust. Soc. Am.* 147 (3) (2020) 1491–1503, <http://dx.doi.org/10.1121/10.0000857>.
- [6] T. Ishizuka, K. Fujiwara, Performance of noise barriers with various edge shapes and acoustical conditions, *Appl. Acoust.* 65 (2) (2004) 125–141, <http://dx.doi.org/10.1016/j.apacoust.2003.08.006>.
- [7] M. Baulac, J. Defrance, P. Jean, Optimisation with genetic algorithm of the acoustic performance of T-shaped noise barriers with a reactive top surface, *Appl. Acoust.* 69 (4) (2008) 332–342, <http://dx.doi.org/10.1016/j.apacoust.2006.11.002>.
- [8] D.P. Elford, L. Chalmers, F.V. Kusmartsev, G.M. Swallowe, Matryoshka locally resonant sonic crystal, *J. Acoust. Soc. Am.* 130 (5) (2011) 2746–2755, <http://dx.doi.org/10.1121/1.3643818>.
- [9] P. Jean, J. Defrance, Sound propagation in rows of cylinders of infinite extent: Application to sonic crystals and thickets along roads, *Acta Acust. United Acust.* 101 (3) (2015) 474–483, <http://dx.doi.org/10.3813/aaa.918844>.
- [10] L. Fredianelli, A.D. Pizzo, G. Licitra, Recent developments in sonic crystals as barriers for road traffic noise mitigation, *Environments* 6 (2) (2019) 14, <http://dx.doi.org/10.3390/environments6020014>.
- [11] L. Moheit, S. Anthis, J. Heinz, F. Kronowetter, S. Marburg, Analysis of scattering by finite sonic crystals in free field with infinite elements and normal modes, *J. Sound Vib.* 476 (2020) 115291, <http://dx.doi.org/10.1016/j.jsv.2020.115291>.
- [12] M. Karimi, P. Croaker, N. Kessissoglou, Boundary element solution for periodic acoustic problems, *J. Sound Vib.* 360 (2016) 129–139, <http://dx.doi.org/10.1016/j.jsv.2015.09.022>.
- [13] L. Godinho, D. Soares, P.G. Santos, Efficient analysis of sound propagation in sonic crystals using an ACA–MFS approach, *Eng. Anal. Bound. Elem.* 69 (2016) 72–85, <http://dx.doi.org/10.1016/j.enganabound.2016.05.001>.
- [14] F.A. Amirkulova, A.N. Norris, Acoustic multiple scattering using recursive algorithms, *J. Comput. Phys.* 299 (2015) 787–803, <http://dx.doi.org/10.1016/j.jcp.2015.07.031>.
- [15] W. Axmann, P. Kuchment, An efficient finite element method for computing spectra of photonic and acoustic band-gap materials, *J. Comput. Phys.* 150 (2) (1999) 468–481, <http://dx.doi.org/10.1006/jcph.1999.6188>.
- [16] F. Morandi, M. Miniaci, A. Marzani, L. Barbaresi, M. Garai, Standardised acoustic characterisation of sonic crystals noise barriers: Sound insulation and reflection properties, *Appl. Acoust.* 114 (2016) 294–306, <http://dx.doi.org/10.1016/j.apacoust.2016.07.028>.
- [17] H. Gao, L. Chen, H. Lian, C. Zheng, H. Xu, T. Matsumoto, Band structure analysis for 2D acoustic phononic structure using isogeometric boundary element method, *Adv. Eng. Softw.* 149 (2020) 102888, <http://dx.doi.org/10.1016/j.advengsoft.2020.102888>.
- [18] P. Reiter, R. Wehr, H. Ziegelwanger, Simulation and measurement of noise barrier sound-reflection properties, *Appl. Acoust.* 123 (2017) 133–142, <http://dx.doi.org/10.1016/j.apacoust.2017.03.007>.
- [19] Y.W. Lam, A boundary integral formulation for the prediction of acoustic scattering from periodic structures, *J. Acoust. Soc. Am.* 105 (2) (1999) 762–769, <http://dx.doi.org/10.1121/1.426267>.
- [20] S.M.B. Fard, H. Peters, N. Kessissoglou, S. Marburg, Three-dimensional analysis of a noise barrier using a quasi-periodic boundary element method, *J. Acoust. Soc. Am.* 137 (6) (2015) 3107–3114, <http://dx.doi.org/10.1121/1.4921266>.
- [21] S.B. Fard, H. Peters, S. Marburg, N. Kessissoglou, Acoustic performance of a barrier embedded with Helmholtz resonators using a quasi-periodic boundary element technique, *Acta Acust. United Acust.* 103 (3) (2017) 444–450, <http://dx.doi.org/10.3813/aaa.919074>.

- [22] T. Cavaliere, A. Cebrecos, J.-P. Groby, C. Chaufour, V. Romero-García, Three-dimensional multiresonant lossy sonic crystal for broadband acoustic attenuation: Application to train noise reduction, *Appl. Acoust.* 146 (2019) 1–8, <http://dx.doi.org/10.1016/j.apacoust.2018.10.020>.
- [23] D. Duhamel, Efficient calculation of the three-dimensional sound pressure field around a noise barrier, *J. Sound Vib.* 197 (5) (1996) 547–571, <http://dx.doi.org/10.1006/jsvi.1996.0548>.
- [24] L. Chalmers, D.P. Elford, F.V. Kusmartsev, G.M. Swallowe, Acoustic band gap formation in two-dimensional locally resonant sonic crystals comprised of Helmholtz resonators, in: *Condensed Matter Theories, Internat. J. Modern Phys. B* 23 (20n21) (2009) 4234–4243, <http://dx.doi.org/10.1142/s0217979209063390>.
- [25] M. Karimi, P. Croaker, N. Kessissoglou, Acoustic scattering for 3D multi-directional periodic structures using the boundary element method, *J. Acoust. Soc. Am.* 141 (1) (2017) 313–323, <http://dx.doi.org/10.1121/1.4973908>.
- [26] C. Jelich, M. Karimi, N. Kessissoglou, S. Marburg, Efficient solution of block Toeplitz systems with multiple right-hand sides arising from a periodic boundary element formulation, *Eng. Anal. Bound. Elem.* 130 (2021) 135–144, <http://dx.doi.org/10.1016/jenganabound.2021.05.003>.
- [27] L. Greengard, V. Rokhlin, A fast algorithm for particle simulations, *J. Comput. Phys.* 73 (2) (1987) 325–348, [http://dx.doi.org/10.1016/0021-9991\(87\)90140-9](http://dx.doi.org/10.1016/0021-9991(87)90140-9).
- [28] N. Nishimura, Fast multipole accelerated boundary integral equation methods, *Appl. Mech. Rev.* 55 (4) (2002) 299–324, <http://dx.doi.org/10.1115/1.1482087>.
- [29] S. Börm, L. Grasedyck, W. Hackbusch, Introduction to hierarchical matrices with applications, *Eng. Anal. Bound. Elem.* 27 (5) (2003) 405–422, [http://dx.doi.org/10.1016/s0955-7997\(02\)00152-2](http://dx.doi.org/10.1016/s0955-7997(02)00152-2).
- [30] W. Hackbusch, S. Börm, H^2 -matrix approximation of integral operators by interpolation, *Appl. Numer. Math.* 43 (1–2) (2002) 129–143, [http://dx.doi.org/10.1016/s0168-9274\(02\)00121-6](http://dx.doi.org/10.1016/s0168-9274(02)00121-6).
- [31] V. Rokhlin, S. Wandzura, The fast multipole method for periodic structures, in: *Proceedings of IEEE Antennas and Propagation Society International Symposium and URSI National Radio Science Meeting, IEEE, 1994*, pp. 424–426, <http://dx.doi.org/10.1109/aps.1994.407723>.
- [32] M. Challacombe, C. White, M. Head-Gordon, Periodic boundary conditions and the fast multipole method, *J. Chem. Phys.* 107 (23) (1997) 10131–10140, <http://dx.doi.org/10.1063/1.474150>.
- [33] N.A. Gumerov, R. Duraiswami, A method to compute periodic sums, *J. Comput. Phys.* 272 (2014) 307–326, <http://dx.doi.org/10.1016/j.jcp.2014.04.039>.
- [34] Y. Otani, N. Nishimura, An FMM for periodic boundary value problems for cracks for Helmholtz equation in 2D, *Internat. J. Numer. Methods Engrg.* 73 (3) (2007) 381–406, <http://dx.doi.org/10.1002/nme.2077>.
- [35] K. Niino, N. Nishimura, Preconditioning based on Calderon's formulae for periodic fast multipole methods for Helmholtz' equation, *J. Comput. Phys.* 231 (1) (2012) 66–81, <http://dx.doi.org/10.1016/j.jcp.2011.08.019>.
- [36] H. Ziegelwanger, P. Reiter, M. Conter, The three-dimensional quasi-periodic boundary element method: Implementation, evaluation, and use cases, *Int. J. Comput. Methods Exper. Meas.* 5 (3) (2017) 404–414, <http://dx.doi.org/10.2495/cmeme-v5-n3-404-414>.
- [37] Y. Liu, A.H. Barnett, Efficient numerical solution of acoustic scattering from doubly-periodic arrays of axisymmetric objects, *J. Comput. Phys.* 324 (2016) 226–245, <http://dx.doi.org/10.1016/j.jcp.2016.08.011>.
- [38] W. Yan, M. Shelley, Flexibly imposing periodicity in kernel independent FMM: A multipole-to-local operator approach, *J. Comput. Phys.* 355 (2018) 214–232, <http://dx.doi.org/10.1016/j.jcp.2017.11.012>.
- [39] P. Amado-Mendes, L. Godinho, J. Carbajo, J. Ramis-Soriano, Numerical modelling of finite periodic arrays of acoustic resonators using an efficient 3D BEM model, *Eng. Anal. Bound. Elem.* 102 (2019) 73–86, <http://dx.doi.org/10.1016/jenganabound.2019.02.012>.
- [40] N.A. Gumerov, R. Duraiswami, Computation of scattering from clusters of spheres using the fast multipole method, *J. Acoust. Soc. Am.* 117 (4) (2005) 1744–1761, <http://dx.doi.org/10.1121/1.1853017>.
- [41] S. Marburg, *Computational acoustics*, in: M. Kaltenbacher (Ed.), *Computational Acoustics*, Springer, Wien, 2018, pp. 69–158.
- [42] A.J. Burton, G.F. Miller, The application of integral equation methods to the numerical solution of some exterior boundary-value problems, *Proc. R. Soc. A: Math. Phys. Eng. Sci.* 323 (1553) (1971) 201–210, <http://dx.doi.org/10.1098/rspa.1971.0097>.
- [43] S. Marburg, The Burton and Miller method: Unlocking another mystery of its coupling parameter, *J. Comput. Acoust.* 24 (01) (2016) 1550016, <http://dx.doi.org/10.1142/s0218396x15500162>.
- [44] T.W. Wu (Ed.), *Boundary element acoustics: Fundamentals and computer codes*, WIT Press, Southampton, 2000.
- [45] X. Jin, *Developments and Applications of Block Toeplitz Iterative Solvers*, Springer Netherlands, 2003.
- [46] R.H.-F. Chan, X.-Q. Jin, *An Introduction to Iterative Toeplitz Solvers*, Society for Industrial and Applied Mathematics, 2007, <http://dx.doi.org/10.1137/1.9780898718850>.
- [47] G.H. Golub, C.F. Van Loan, *Matrix Computations*, 2nd, Johns Hopkins University Press, 1989.
- [48] P.J. Davis, *Circulant Matrices*, in: *AMS Chelsea Publishing Series*, Chelsea, New York, 1994.
- [49] R.M. Gray, Toeplitz and circulant matrices: A review, *Found. Trends Commun. Inf. Theory* 2 (3) (2005) 155–239, <http://dx.doi.org/10.1561/0100000006>.
- [50] R. Coifman, V. Rokhlin, S. Wandzura, The fast multipole method for the wave equation: a pedestrian prescription, *IEEE Antennas Propag. Mag.* 35 (3) (1993) 7–12, <http://dx.doi.org/10.1109/74.250128>.
- [51] E. Darve, The fast multipole method: Numerical implementation, *J. Comput. Phys.* 160 (1) (2000) 195–240, <http://dx.doi.org/10.1006/jcph.2000.6451>.
- [52] Y. Liu, *Fast Multipole Boundary Element Method*, Cambridge University Press, 2009, <http://dx.doi.org/10.1017/cbo9780511605345>.
- [53] A.G. Polimeridis, J.K. White, On the compression of system tensors arising in FFT-VIE solvers, in: *2014 IEEE Antennas and Propagation Society International Symposium, APSURSI, IEEE, 2014*, <http://dx.doi.org/10.1109/aps.2014.6905399>.

- [54] Y. Wang, X. Zhu, T. Zhang, S. Bano, H. Pan, L. Qi, Z. Zhang, Y. Yuan, A renewable low-frequency acoustic energy harvesting noise barrier for high-speed railways using a Helmholtz resonator and a PVDF film, *Appl. Energy* 230 (2018) 52–61, <http://dx.doi.org/10.1016/j.apenergy.2018.08.080>.
- [55] B.W. Shore, D.H. Menzel, *Principles of Atomic Spectra*, John Wiley & Sons Inc, 1968.

A.2 Paper B

A greedy reduced basis algorithm for structural acoustic systems with parameter and implicit frequency dependence

Christopher Jelich, Suhaib Koji Baydoun, Matthias Voigt and Steffen Marburg

Reprinted from C. Jelich, S. K. Baydoun, M. Voigt and S. Marburg. A greedy reduced basis algorithm for structural acoustic systems with parameter and implicit frequency dependence. *International Journal of Numerical Methods in Engineering*, 122(24):7409–7430, 2021, licensed under the Creative Commons Attribution-NonCommercial-NoDerivatives 4.0 International license (<https://creativecommons.org/licenses/by-nc-nd/4.0/>).

A greedy reduced basis algorithm for structural acoustic systems with parameter and implicit frequency dependence

Christopher Jelich¹  | Suhaib Koji Baydoun¹  | Matthias Voigt² | Steffen Marburg¹

¹Chair of Vibroacoustics of Vehicles and Machines, Technische Universität München, Garching, Germany

²UniDistance Suisse, Brig, Switzerland

Correspondence

Christopher Jelich, Chair of Vibroacoustics of Vehicles and Machines, Technische Universität München, Boltzmannstraße 15, Garching 85748, Germany.
Email: c.jelich@tum.de

Funding information

Deutsche Forschungsgemeinschaft, Grant/Award Number: Priority Programme 1897 “Calm, Smooth and Smart”

Abstract

In this article, a greedy reduced basis algorithm is proposed for the solution of structural acoustic systems with parameter and implicit frequency dependence. The underlying equations of linear time-harmonic elastodynamics and acoustics are discretized using the finite element and boundary element method, respectively. The solution within the parameter domain is determined by a linear combination of reduced basis vectors. This basis is generated iteratively and given by the responses of the structural acoustic system at certain parameter samples. A greedy approach is followed by evaluating the next basis vector at the parameter sample which is currently approximated worst. The algorithm runs on a small training set which bounds the memory requirements and allows applications to large-scale problems with high-dimensional parameter domains. The computational efficiency of the proposed scheme is illustrated based on two numerical examples: a point-excited spherical shell submerged in water and a satellite structure subject to a diffuse sound pressure field excitation.

KEYWORDS

boundary element method, finite element method, greedy algorithm, implicit parameter dependence, reduced basis, structural acoustic interaction

1 | INTRODUCTION

Assessing the vibroacoustic behavior of structures is an important aspect of designing quiet machines and vehicles.¹ With the advances in numerical modeling techniques, vibroacoustic quantities such as radiated sound power and transmission loss of complex structures can be accurately predicted ahead of manufacturing. In the low frequency range, when the modes are still well separated, the underlying equations of motion are typically addressed by the finite element method (FEM)² and the boundary element method (BEM).^{3,4} The structural domain is usually discretized by finite elements whereas either FEM or BEM is used for discretizing the acoustic domain. Since the BEM reduces the problem's dimension by one, that is, only the sound radiating surface has to be discretized instead of the surrounding acoustic volume, the BEM features an inherent advantage for unbounded acoustic domains.⁴ This contribution focuses on structural acoustic problems with an unbounded acoustic domain in the low frequency region and hence a FEM-BEM approach is employed.

Including vibroacoustic quantities in design optimization and uncertainty analyses has become a common engineering practice in recent decades.^{5,6} However, when using a FEM-BEM approach, the repeated evaluation of these vibroacoustic quantities poses a significant computational challenge. In general, the structural acoustic system has to be

This is an open access article under the terms of the Creative Commons Attribution-NonCommercial-NoDerivs License, which permits use and distribution in any medium, provided the original work is properly cited, the use is non-commercial and no modifications or adaptations are made.

© 2021 The Authors. *International Journal for Numerical Methods in Engineering* published by John Wiley & Sons Ltd.

solved for each change in the design variables which usually includes the reassembly of the system matrices. Different techniques have been proposed to accelerate the evaluations for solely frequency dependent but also general parameter dependent problems.

Modal superposition is a popular choice for solely frequency dependent structural acoustic systems.⁷ Solving the corresponding eigenvalue problem yields the eigenfrequencies and modes of the structural acoustic problem and the time-harmonic responses can be estimated by superposing the modes. The computational complexity mainly depends on the type of the structural acoustic problem and the discretization method of choice. Bounded acoustic domains discretized by the FEM yield linear eigenvalue problems^{8,9} whereas unbounded acoustic domains generally yield nonlinear eigenvalue problems. An exception is given in the latter case by a particular choice of finite elements.^{10,11} In contrast, boundary element discretizations yield nonlinear eigenvalue problems in both cases due to the implicit frequency dependence of the boundary element matrices.^{12,13} A remedy can be found in a frequency approximation of the boundary element matrix.^{7,14} Alternatively, the nonlinear eigenvalue problem can be solved, for example, by contour integral methods^{15,16} and rational approximation.¹⁷

When considering parameter dependent structural acoustic problems, the aforementioned approach of modal reduction becomes infeasible. In these cases, parametric model order reduction (pMOR)^{18,19} can be employed to generate a reduced order model (ROM). A broad range of reduction techniques exists for affine parameter dependence, see Reference 20 for a detailed overview. Parameters with a low-rank impact on the system matrix are a special type of affine parameters. For those, a parametric ROM can be build that preserves all parameters by employing conventional non-parametric MOR techniques.²¹ Van Ophem et al.²² reduced a finite element discretized fully coupled structural acoustic problem based on Krylov subspace projection and a second order Arnoldi scheme. Their frequency dependent problem features additional parameters which correspond to locally added structural mass and hence can be described as low-rank updates of the mass matrix. For nonaffine parameterized systems such as linear systems with implicit frequency dependent boundary element matrices, the discrete empirical interpolation method (DEIM)²³ can be used. The DEIM yields an affine approximation of the linear system in a given parameter domain based on a small number of evaluations of the original linear system. Negri et al.²⁴ applied the matrix variant of the DEIM to a finite element discretized acoustic problem with a five-dimensional parameter domain. They optimize the shape of an acoustic horn in a frequency range by varying four geometry parameters. Casenave et al.²⁵ applied the DEIM to a solely frequency dependent boundary element discretized acoustic scattering problem. Applications to FEM-BEM structural acoustic problems have not yet been reported up to the authors' knowledge.

An alternative MOR technique are reduced basis methods which utilize that the solutions of parameterized linear systems are often members of lower-dimensional manifolds.²⁶ Hence, linear combinations of a small number of basis vectors can accurately approximate the solutions.²⁷ Most reduced basis methods follow an offline-online paradigm. In the offline stage, the reduced basis is built using solutions of the parameterized linear system. Usually either a proper orthogonal decomposition (POD) or greedy algorithms are employed. In the former approach, the parameter domain is sampled without prior knowledge of optimal points and a singular value decomposition (SVD) of the corresponding solutions determines the basis.²⁸ In contrast, greedy algorithms meticulously select parameter samples based on a pre-defined optimality criterion and the basis vectors coincide with the corresponding solutions.²⁹ In the online stage, the approximate solutions at new parameter values are found by linear combinations of the basis vectors.³⁰ Casenave et al.³¹ employed a greedy reduced basis scheme in conjunction with the BEM to find the solution of a parameterized acoustic scattering problem. Boundary element discretized electromagnetic problems can be solved in a similar way.²⁶ In our previous work,³² we proposed a greedy reduced basis scheme for the solution of fully coupled FEM-BEM structural acoustic problems at predefined frequency points. The reduced basis is expanded iteratively and the vectors spanning the reduced basis are simply the solutions of the linear system at some of these frequency points. The points are chosen based on a greedy approach, namely, the next basis vector is computed at the frequency point at which the solution is currently worst approximated. Although the study underlines the computational efficiency of the scheme, its memory requirements prevent the application to large-scale problems.

In this contribution, the greedy reduced basis scheme of Reference 32 is extended to general implicitly parameter dependent structural acoustic problems. The algorithm finds the solution specifically at predefined parameter points by a linear combination of reduced basis vectors. It builds and utilizes the reduced basis simultaneously in contrast to algorithms following the offline-online paradigm. While a high-dimensional parameter domain makes the previously reported greedy strategy infeasible due to prohibitive memory requirements, this issue is addressed here by an adaptively enriching technique similar to Reference 33. The scheme uses a small subset of the full parameter set to build the reduced basis. This introduces a bound on the memory usage and allows to apply the greedy strategy to large-scale problems

with possibly high-dimensional parameter domains. In contrast to Reference 33, the size of the subset is held small to allow storing the corresponding full order linear systems. This eliminates the need of reassembling and reduces the computational effort at an a priori known increase of the required memory. Furthermore, a variation of the scheme for problems with many right-hand sides is introduced. The efficiency of the adaptively enriching greedy reduced basis algorithm is verified based on the solution of two structural acoustic problems.

2 | COUPLED FEM-BEM FORMULATION FOR STRUCTURAL ACOUSTIC INTERACTION

The underlying equations of the structural acoustic interaction problem are given by the equations of linear time-harmonic elastodynamics and acoustics. Discretizing the former with FEM and the latter with BEM yields the system of linear equations for the structural and acoustic domains^{4,5}

$$(\mathbf{K}(\lambda) - \omega^2 \mathbf{M}(\lambda)) \mathbf{u} = \mathbf{f}_s + \mathbf{f}_f, \quad (1)$$

and

$$\mathbf{H}(\omega) \mathbf{p} = \mathbf{G}(\omega) (\mathbf{v}_s - \mathbf{v}_f^i) + \mathbf{H}(\omega) \mathbf{p}^i. \quad (2)$$

The vectors $\mathbf{u} \in \mathbb{C}^{n_s}$ and $\mathbf{p} \in \mathbb{C}^{n_f}$ contain the unknown displacement and sound pressure degrees of freedom (dofs) at the nodes, where n_s and n_f denote the corresponding numbers of degrees of freedom, respectively. The stiffness and mass matrices of the structure are denoted as $\mathbf{K}(\lambda) \in \mathbb{R}^{n_s \times n_s}$ and $\mathbf{M}(\lambda) \in \mathbb{R}^{n_s \times n_s}$. Both depend implicitly or explicitly on $d - 1$ parameters which are concatenated into the vector

$$\lambda = [\lambda_1, \dots, \lambda_{d-1}]. \quad (3)$$

We restrict the following derivations to parameters that do not affect the geometry of the sound radiating boundary. Hence, the boundary element matrices $\mathbf{H}(\omega) \in \mathbb{C}^{n_f \times n_f}$ and $\mathbf{G}(\omega) \in \mathbb{C}^{n_f \times n_f}$ only depend on the angular frequency $\omega = 2\pi f$, where f is the frequency in Hz. The boundary element matrices arise from a collocation discretization of the Kirchhoff-Helmholtz integral equation and relate the sound pressure to the structural particle velocity $\mathbf{v}_s \in \mathbb{C}^{n_f}$. The acoustic field is excited by an incident sound pressure field $\mathbf{p}^i \in \mathbb{C}^{n_f}$ and the corresponding incident particle velocity $\mathbf{v}_f^i \in \mathbb{C}^{n_f}$. The structure is excited by nodal forces $\mathbf{f}_s \in \mathbb{C}^{n_s}$ as well as an acoustic loading $\mathbf{f}_f \in \mathbb{C}^{n_s}$ due to the acoustic sound pressure on the sound radiating boundary. The particle velocity \mathbf{v}_s is the time derivative of the normal displacement on this boundary. Therefore, the coupling conditions

$$\mathbf{f}_f = \mathbf{C}_{sf} \mathbf{p} \quad \text{and} \quad \mathbf{v}_s = -i\omega \mathbf{C}_{fs} \mathbf{u}, \quad (4)$$

hold, with the imaginary unit i and the mesh coupling matrices $\mathbf{C}_{sf} \in \mathbb{R}^{n_s \times n_f}$ and $\mathbf{C}_{fs} \in \mathbb{R}^{n_f \times n_s}$. Both are obtained by a Galerkin projection.³⁴ Putting Equation (4) into Equations (1) and (2), the fully coupled system of linear equations reads

$$\begin{bmatrix} \mathbf{K}(\lambda) - \omega^2 \mathbf{M}(\lambda) & -\mathbf{C}_{sf} \\ i\omega \mathbf{G}(\omega) \mathbf{C}_{fs} & \mathbf{H}(\omega) \end{bmatrix} \begin{bmatrix} \mathbf{u} \\ \mathbf{p} \end{bmatrix} = \begin{bmatrix} \mathbf{f}_s \\ -\mathbf{G}(\omega) \mathbf{v}_f^i + \mathbf{H}(\omega) \mathbf{p}^i \end{bmatrix}. \quad (5)$$

This system can be solved at the current stage or reduced beforehand. Forming the Schur complement with respect to the pressure dofs is a common strategy especially when considering heavy fluid loading or lightweight structures since the system matrix of Equation (5) is generally ill-conditioned.^{16,35,36} The Schur complement reads

$$\left[i\omega \mathbf{G}(\omega) \mathbf{C}_{fs} (\mathbf{K}(\lambda) - \omega^2 \mathbf{M}(\lambda))^{-1} \mathbf{C}_{sf} + \mathbf{H}(\omega) \right] \mathbf{p} = \hat{\mathbf{f}}_s(\omega, \lambda), \quad (6)$$

with

$$\hat{\mathbf{f}}_s(\omega, \lambda) := -i\omega \mathbf{G}(\omega) \mathbf{C}_{fs} (\mathbf{K}(\lambda) - \omega^2 \mathbf{M}(\lambda))^{-1} \mathbf{f}_s - \mathbf{G}(\omega) \mathbf{v}_f^i + \mathbf{H}(\omega) \mathbf{p}^i. \quad (7)$$

In many applications of interest, the system matrix of Equation (6) is well conditioned and the corresponding linear system can be efficiently solved since the finite element matrix $\mathbf{K}(\lambda) - \omega^2 \mathbf{M}(\lambda)$ admits a sparse LU factorization. In this contribution, all time-harmonic structural acoustic problems are solved by finding the solution of Equation (6). In the following, the linear system (6) is abbreviated by

$$\mathbf{A}(\boldsymbol{\mu})\mathbf{x}(\boldsymbol{\mu}) = \mathbf{b}(\boldsymbol{\mu}), \quad (8)$$

introducing the d -dimensional parameter vector

$$\boldsymbol{\mu} = [\lambda, \omega] = [\lambda_1, \dots, \lambda_{d-1}, \omega]. \quad (9)$$

The system matrix $\mathbf{A}(\boldsymbol{\mu}) \in \mathbb{C}^{n \times n}$, the solution vector $\mathbf{x}(\boldsymbol{\mu}) \in \mathbb{C}^n$ and the right-hand side vector $\mathbf{b}(\boldsymbol{\mu}) \in \mathbb{C}^n$ implicitly depend on d parameters in the present case and feature n degrees of freedom.

3 | ALGORITHMS FOR STRUCTURAL ACOUSTIC PROBLEMS IN A D -DIMENSIONAL PARAMETER DOMAIN

We are interested in the solution of Equation (8) for specific parameter samples $\boldsymbol{\mu}$ located in the parameter domain \mathcal{P} . This domain is a d -dimensional box, that is,

$$\mathcal{P} := [\lambda_1^l, \lambda_1^u] \times \dots \times [\lambda_{d-1}^l, \lambda_{d-1}^u] \times [\omega^l, \omega^u], \quad (10)$$

with the lower and upper bounds, $(\cdot)^l$ and $(\cdot)^u$, in each dimension, respectively. Each interval k is discretized with n_k points, where $k = 1, \dots, d$. These sample points are denoted as $\lambda_{k,1}, \dots, \lambda_{k,n_k}$ for $k = 1, \dots, d-1$ and $\omega_1, \dots, \omega_{i_d}$ for $k = d$. The solution is sought at all possible combinations of these points which are summed up in the parameter set P , that is,

$$P = \{(\lambda_{1,i_1}, \dots, \lambda_{d-1,i_{d-1}}, \omega_{i_d}) : 1 \leq i_k \leq n_k \text{ for } k = 1, \dots, d\}. \quad (11)$$

Hence the solution of Equation (8) is sought for a total of $m = \prod_{k=1}^d n_k$ parameter samples. Instead of solving the linear system for each sample within P , we propose to apply a reduced basis approach. For this, a greedy algorithm for frequency dependent structural acoustic systems³² is extended to problems with high-dimensional parameter domains in Section 3.1. This is followed by an adaption of the algorithm to address the high memory requirements in Section 3.2.

3.1 | Greedy reduced basis algorithm

In each iteration j of the greedy algorithm, a set of parameter samples $P_j \subseteq P$ is given as

$$P_j = \{\boldsymbol{\mu}^{(1)}, \dots, \boldsymbol{\mu}^{(j)}\}. \quad (12)$$

A reduced basis \mathbf{X}_j is generated by concatenating the solutions at these parameter samples, that is,

$$\mathbf{X}_j = [\mathbf{x}(\boldsymbol{\mu}^{(1)}), \dots, \mathbf{x}(\boldsymbol{\mu}^{(j)})] \in \mathbb{C}^{n \times j}. \quad (13)$$

This basis is used to approximate the solution at an arbitrary parameter sample $\boldsymbol{\mu} \in P$ by

$$\mathbf{x}(\boldsymbol{\mu}) = \mathbf{x}(\boldsymbol{\mu}^{(1)})y_1(\boldsymbol{\mu}) + \dots + \mathbf{x}(\boldsymbol{\mu}^{(j)})y_j(\boldsymbol{\mu}) = \mathbf{X}_j \mathbf{y}(\boldsymbol{\mu}), \quad (14)$$

where $\mathbf{y}(\boldsymbol{\mu}) \in \mathbb{C}^j$ is the solution of the least squares problem

$$\min_{\mathbf{y}(\boldsymbol{\mu}) \in \mathbb{C}^j} \|\mathbf{A}(\boldsymbol{\mu})\mathbf{X}_j \mathbf{y}(\boldsymbol{\mu}) - \mathbf{b}(\boldsymbol{\mu})\|_2^2. \quad (15)$$

The next parameter sample $\boldsymbol{\mu}^{(j+1)}$ is chosen by a greedy approach, that is, at the parameter sample where the current approximation (14) yields the largest relative residual,

$$\boldsymbol{\mu}^{(j+1)} = \arg \max_{\boldsymbol{\mu} \in P} \|\mathbf{A}(\boldsymbol{\mu})\mathbf{X}_j \mathbf{y}(\boldsymbol{\mu}) - \mathbf{b}(\boldsymbol{\mu})\|_2 / \|\mathbf{b}(\boldsymbol{\mu})\|_2. \quad (16)$$

The next basis vector of the new iteration is determined by solving the underlying linear system

$$\mathbf{A}(\boldsymbol{\mu}^{(j+1)})\mathbf{x}(\boldsymbol{\mu}^{(j+1)}) = \mathbf{b}(\boldsymbol{\mu}^{(j+1)}). \quad (17)$$

The greedy reduced basis in Equation (13) is extended by one vector in each iteration which provides an improved approximation (14) of the solution at the remaining parameter samples in the parameter set. This is repeated until a convergence criterion is met for all $\boldsymbol{\mu} \in P$. The presented scheme is computationally superior to the explicit solution at each sample whenever a small number of iterations $q \ll m$ yields a sufficiently accurate approximation of the solution at all parameter samples. This is attainable if the solution matrix $\mathbf{X} = [\mathbf{x}(\boldsymbol{\mu}_1), \dots, \mathbf{x}(\boldsymbol{\mu}_m)] \in \mathbb{C}^{n \times m}$ is of low rank and its singular values follow an exponential decay. This has been proven for analytical parameter dependencies by Kressner and Tobler³⁷ and holds for the herein presented structural acoustic problems.

The computational cost of the greedy algorithm lies in the solution of q linear systems (17), repeatedly solving the least squares problem (15) for all the yet unconverged solutions and assessing the accuracy of the approximations by evaluating the relative residual (16). Although the number of least squares solutions is of order $\mathcal{O}(qm)$, each solution is rather inexpensive since $\mathbf{A}(\boldsymbol{\mu}_i)\mathbf{X}_q$ features only a few columns given that $q \ll m$ holds. However, the scheme requires the storage of all m system matrices which can lead to excessive memory requirements in the case of large parameter sets and/or large-scale problems. This issue can be addressed from two different sides: running the scheme in parallel in a high-performance computing environment or adapting the scheme, such that only a limited amount of system matrices need to be stored in the main memory at the same time. The latter is outlined in Section 3.2 whereas the former is described by Baydoun et al.³² Therein, the authors suggest to solve the least squares problem (15) in a distributed memory environment and to evaluate the linear system (17) in a shared memory environment.

The greedy reduced basis algorithm is outlined in Algorithm 1. The prescribed value of ϵ_{tol} defines a relative tolerance on the residual of the solution at parameter samples within the parameter set. The initial parameter sample $\boldsymbol{\mu}^{(1)}$ can be chosen randomly and is the first element within the set of solved parameter samples P_{sol} . At the end of the algorithm, a solution for each parameter sample within P is established either by explicitly solving the corresponding linear system or finding a sufficiently accurate linear approximation. Explicitly storing the least squares matrices $\mathbf{A}(\boldsymbol{\mu}_i)\mathbf{X}_j$ and only concatenating the new column $\mathbf{A}(\boldsymbol{\mu}_i)\mathbf{x}(\boldsymbol{\mu}^{(j)})$ in each iteration avoids additional computational effort. Whenever a solution for a parameter sample $\boldsymbol{\mu}_i$ is found, the corresponding matrices $\mathbf{A}(\boldsymbol{\mu}_i)$ and $\mathbf{A}(\boldsymbol{\mu}_i)\mathbf{X}_j$ are no longer required and freed from the memory.

3.2 | Adaptively enriching greedy reduced basis algorithm

The main disadvantage of Algorithm 1 is the need of assembling and storing the system matrices and right-hand sides for all parameter samples within the parameter set. This becomes prohibitive for large m , that is, high dimensional parameter domains and/or large numbers of parameter samples. As a remedy, we modify the greedy algorithm by introducing the adaptively enriching technique presented by Hesthaven et al.³³

The main idea of the adaptively enriching greedy algorithm is to start the algorithm on a small training set $P_{\text{train}} \subset P$ of size $m_{\text{train}} \ll m$ and to subsequently replace parameter samples for which a converged solution has been generated by parameter samples for which a solution has not been found yet. This reduces the memory requirements significantly, since only up to m_{train} assembled linear systems have to be stored at the same time. However, the small size of the subset implies a reduced richness and the iteratively performed greedy choice of the next basis vector is only depending on the residuals in P_{train} and not on all residuals in P . Hence, the algorithm will usually generate a larger basis than Algorithm 1 which implies an increase in the number of iterations.

Algorithm 1. Greedy algorithm for the solution of parameter dependent linear systems

```

1: input
2:   system matrices  $\mathbf{A}(\boldsymbol{\mu}_i)$  and right-hand sides  $\mathbf{b}(\boldsymbol{\mu}_i)$  for all  $\boldsymbol{\mu}_i \in P$ 
3:   relative residual tolerance  $\varepsilon_{\text{tol}}$ 
4:   parameter sample for first iteration  $\boldsymbol{\mu}^{(1)} \in P$ 
5: initialization
6:    $j := 1$ 
7:    $\mathbf{r}(\boldsymbol{\mu}_i) := \mathbf{b}(\boldsymbol{\mu}_i) \forall \boldsymbol{\mu}_i \in P$ 
8:   solve  $\mathbf{A}(\boldsymbol{\mu}^{(1)})\mathbf{x}(\boldsymbol{\mu}^{(1)}) = \mathbf{b}(\boldsymbol{\mu}^{(1)})$ 
9:    $\mathbf{X}_1 := [\mathbf{x}(\boldsymbol{\mu}^{(1)})]$ 
10:   $P_{\text{sol}} := \{\boldsymbol{\mu}^{(1)}\}$ 
11: while  $\exists \boldsymbol{\mu}_i \in P : \|\mathbf{r}(\boldsymbol{\mu}_i)\|_2 / \|\mathbf{b}(\boldsymbol{\mu}_i)\|_2 > \varepsilon_{\text{tol}}$  do
12:   for each  $\boldsymbol{\mu}_i \in P \setminus P_{\text{sol}}$  do
13:     solve  $\min_{\mathbf{y}(\boldsymbol{\mu}_i) \in \mathbb{C}^j} \|\mathbf{A}(\boldsymbol{\mu}_i)\mathbf{X}_j\mathbf{y}(\boldsymbol{\mu}_i) - \mathbf{b}(\boldsymbol{\mu}_i)\|_2^2$ ,    $\mathbf{r}(\boldsymbol{\mu}_i) := \mathbf{A}(\boldsymbol{\mu}_i)\mathbf{X}_j\mathbf{y}(\boldsymbol{\mu}_i) - \mathbf{b}(\boldsymbol{\mu}_i)$ 
14:     if  $\|\mathbf{r}(\boldsymbol{\mu}_i)\|_2 / \|\mathbf{b}(\boldsymbol{\mu}_i)\|_2 < \varepsilon_{\text{tol}}$  then
15:        $\mathbf{x}(\boldsymbol{\mu}_i) := \mathbf{X}_j\mathbf{y}(\boldsymbol{\mu}_i)$ ,    $P_{\text{sol}} := P_{\text{sol}} \cup \{\boldsymbol{\mu}_i\}$ 
16:     end if
17:   end for
18:   if  $\|\mathbf{r}(\boldsymbol{\mu}_i)\|_2 / \|\mathbf{b}(\boldsymbol{\mu}_i)\|_2 < \varepsilon_{\text{tol}} \forall \boldsymbol{\mu}_i \in P$  then
19:     break
20:   end if
21:    $\boldsymbol{\mu}^{(j+1)} := \operatorname{argmax}_{\boldsymbol{\mu}_i \in P} \|\mathbf{r}(\boldsymbol{\mu}_i)\|_2 / \|\mathbf{b}(\boldsymbol{\mu}_i)\|_2$ 
22:   solve  $\mathbf{A}(\boldsymbol{\mu}^{(j+1)})\mathbf{x}(\boldsymbol{\mu}^{(j+1)}) = \mathbf{b}(\boldsymbol{\mu}^{(j+1)})$ 
23:    $\mathbf{X}_{j+1} := [\mathbf{X}_j, \mathbf{x}(\boldsymbol{\mu}^{(j+1)})] \in \mathbb{C}^{n \times (j+1)}$ ,    $P_{\text{sol}} := P_{\text{sol}} \cup \{\boldsymbol{\mu}^{(j+1)}\}$ 
24:    $j := j + 1$ 
25: output
26:    $\mathbf{x}(\boldsymbol{\mu}_i)$  with  $\|\mathbf{A}(\boldsymbol{\mu}_i)\mathbf{x}(\boldsymbol{\mu}_i) - \mathbf{b}(\boldsymbol{\mu}_i)\|_2 / \|\mathbf{b}(\boldsymbol{\mu}_i)\|_2 < \varepsilon_{\text{tol}} \forall \boldsymbol{\mu}_i \in P$ 

```

At the beginning of the adaptively enriching greedy algorithm, an initial subset P_{train} is randomly chosen from the full set P based on the prescribed size m_{train} . With each iteration j , the reduced basis \mathbf{X}_j is extended by the basis vector $\mathbf{x}(\boldsymbol{\mu}^{(j)})$ as in Equation (13). This basis is used to approximate the solution at all remaining parameter samples within P_{train} , that is, the linear least squares problem (15) is solved for all $\boldsymbol{\mu} \in P_{\text{train}}$. Each parameter sample for which a sufficiently accurate solution is found—either by solving the corresponding linear system or by linear superposition of the basis vectors—is added to the set of solved parameter samples P_{sol} and removed from the training set P_{train} . Whenever a parameter sample is removed, the allocated memory of the corresponding linear system as well as the linear least squares system is freed. Further, a parameter sample for which a solution has not been generated yet, that is $\boldsymbol{\mu} \in P \setminus (P_{\text{sol}} \cup P_{\text{train}})$, is added to the training set. The linear system of the newly added parameter sample is assembled and stored in the main memory. In addition, the current basis is used to approximate its solution. If the approximation is sufficiently accurate, the newly added parameter sample is replaced right away. This procedure is repeated until the convergence criterion fails on all solutions of the newly added parameter samples within the training set. At this stage, the next parameter sample $\boldsymbol{\mu}^{(j+1)}$ is chosen in a greedy approach within the training set, that is,

$$\boldsymbol{\mu}^{(j+1)} = \operatorname{argmax}_{\boldsymbol{\mu} \in P_{\text{train}}} \|\mathbf{A}(\boldsymbol{\mu})\mathbf{X}_j\mathbf{y}(\boldsymbol{\mu}) - \mathbf{b}(\boldsymbol{\mu})\|_2 / \|\mathbf{b}(\boldsymbol{\mu})\|_2, \quad (18)$$

and the next basis vector is generated by solving the linear system (17). The full algorithm is outlined in Algorithm 2 and the scheme for replacing parameter samples in the training set is presented in Algorithm 3. Note that replacing a parameter sample in Line 19 updates the training set while looping over it. The implementation places new parameter samples at the end of the training set such that the loop in Line 15 is also executed for each new parameter sample.

Algorithm 2. Adaptively enriching greedy algorithm for the solution of parameter dependent linear systems

```

1: input
2:   parameter set  $P$ 
3:   initial training set  $P_{\text{train}} \subset P$  with  $|P_{\text{train}}| = m_{\text{train}}$ 
4:   system matrices  $\mathbf{A}(\boldsymbol{\mu}_i)$  and right-hand sides  $\mathbf{b}(\boldsymbol{\mu}_i)$  with  $\boldsymbol{\mu}_i \in P_{\text{train}}$ 
5:   relative residual tolerance  $\varepsilon_{\text{tol}}$ 
6:   parameter sample for first iteration  $\boldsymbol{\mu}^{(1)} \in P_{\text{train}}$ 
7: initialization
8:    $j := 1$ 
9:    $\mathbf{r}(\boldsymbol{\mu}_i) := \mathbf{b}(\boldsymbol{\mu}_i) \forall \boldsymbol{\mu}_i \in P_{\text{train}}$ 
10:  solve  $\mathbf{A}(\boldsymbol{\mu}^{(1)})\mathbf{x}(\boldsymbol{\mu}^{(1)}) = \mathbf{b}(\boldsymbol{\mu}^{(1)})$ 
11:   $\mathbf{X}_1 := [\mathbf{x}(\boldsymbol{\mu}^{(1)})]$ 
12:   $P_{\text{sol}} := \{\boldsymbol{\mu}^{(1)}\}$ 
13:   $P_{\text{train}} := \text{ALGORITHM 3}(P, P_{\text{train}}, P_{\text{sol}}, \boldsymbol{\mu}^{(1)})$ 
14: while  $|P_{\text{train}}| > 0$  do
15:   for each  $\boldsymbol{\mu}_i \in P_{\text{train}}$  do
16:    solve  $\min_{\mathbf{y}(\boldsymbol{\mu}_i) \in \mathbb{C}^j} \|\mathbf{A}(\boldsymbol{\mu}_i)\mathbf{X}_j\mathbf{y}(\boldsymbol{\mu}_i) - \mathbf{b}(\boldsymbol{\mu}_i)\|_2^2$ ,    $\mathbf{r}(\boldsymbol{\mu}_i) := \mathbf{A}(\boldsymbol{\mu}_i)\mathbf{X}_j\mathbf{y}(\boldsymbol{\mu}_i) - \mathbf{b}(\boldsymbol{\mu}_i)$ 
17:    if  $\|\mathbf{r}(\boldsymbol{\mu}_i)\|_2 / \|\mathbf{b}(\boldsymbol{\mu}_i)\|_2 < \varepsilon_{\text{tol}}$  then
18:       $\mathbf{x}(\boldsymbol{\mu}_i) := \mathbf{X}_j\mathbf{y}(\boldsymbol{\mu}_i)$ ,    $P_{\text{sol}} := P_{\text{sol}} \cup \{\boldsymbol{\mu}_i\}$ 
19:       $P_{\text{train}} := \text{ALGORITHM 3}(P, P_{\text{train}}, P_{\text{sol}}, \boldsymbol{\mu}_i)$ 
20:    end if
21:   end for
22:   if  $P_{\text{train}} = \emptyset$  then
23:     break
24:   end if
25:    $\boldsymbol{\mu}^{(j+1)} := \operatorname{argmax}_{\boldsymbol{\mu}_i \in P_{\text{train}}} \|\mathbf{r}(\boldsymbol{\mu}_i)\|_2 / \|\mathbf{b}(\boldsymbol{\mu}_i)\|_2$ 
26:   solve  $\mathbf{A}(\boldsymbol{\mu}^{(j+1)})\mathbf{x}(\boldsymbol{\mu}^{(j+1)}) = \mathbf{b}(\boldsymbol{\mu}^{(j+1)})$ 
27:    $\mathbf{X}_{j+1} := [\mathbf{X}_j, \mathbf{x}(\boldsymbol{\mu}^{(j+1)})] \in \mathbb{C}^{n \times (j+1)}$ ,    $P_{\text{sol}} := P_{\text{sol}} \cup \{\boldsymbol{\mu}^{(j+1)}\}$ 
28:    $P_{\text{train}} := \text{ALGORITHM 3}(P, P_{\text{train}}, P_{\text{sol}}, \boldsymbol{\mu}^{(j+1)})$ 
29:    $j := j + 1$ 
30: output
31:    $\mathbf{x}(\boldsymbol{\mu}_i)$  with  $\|\mathbf{A}(\boldsymbol{\mu}_i)\mathbf{x}(\boldsymbol{\mu}_i) - \mathbf{b}(\boldsymbol{\mu}_i)\|_2 / \|\mathbf{b}(\boldsymbol{\mu}_i)\|_2 \leq \varepsilon_{\text{tol}} \forall \boldsymbol{\mu}_i \in P$ 

```

Algorithm 3. Algorithm for replacing an element from the training set

```

1: input
2:   full parameter set  $P$ 
3:   current training set  $P_{\text{train}} \subset P$ 
4:   set  $P_{\text{sol}} \subset P$  with samples at which a solution is known
5:   parameter sample  $\boldsymbol{\mu}_i$  to be removed from  $P_{\text{train}}$ 
6:    $P_{\text{train}} := P_{\text{train}} \setminus \{\boldsymbol{\mu}_i\}$ 
7:   free memory of system matrix  $\mathbf{A}(\boldsymbol{\mu}_i)$  and right-hand side  $\mathbf{b}(\boldsymbol{\mu}_i)$ 
8:   if  $(P_{\text{train}} \cup P_{\text{sol}}) \neq P$  then
9:     randomly pick  $\boldsymbol{\mu}_k \in P \setminus (P_{\text{train}} \cup P_{\text{sol}})$ 
10:     $P_{\text{train}} := P_{\text{train}} \cup \{\boldsymbol{\mu}_k\}$ 
11:    assemble system matrix  $\mathbf{A}(\boldsymbol{\mu}_k)$  and right-hand side  $\mathbf{b}(\boldsymbol{\mu}_k)$ 
12:   end if
13: output
14:   updated training set  $P_{\text{train}}$ 

```

Throughout the algorithm, the size of the training set is bounded by m_{train} . Therefore, the memory requirements for the storage of the system matrices and the least squares matrices are of order $\mathcal{O}(m_{\text{train}}(n^2 + jn))$, assuming that the system matrix is fully populated. Note that the quadratic complexity in n could be removed by always applying the full order model (FOM) systems on-the-fly. However, reassembling the FOM systems within the training set in each iteration significantly increases the computational time in the case of coupled vibroacoustic problems due to the implicitly frequency dependent BE matrices. The overall computational efficiency of the algorithm depends on the size of the training set. Very small values of m_{train} lead to a higher number of iterations due to the limited range of the training set. In contrast, large values of m_{train} result in training sets which represent the full parameter set more accurately. This implies significantly higher memory requirements but results in a reduced number of iterations. In the case of $m_{\text{train}} = m$, the adaptively enriching greedy algorithm (Algorithm 2) is identical to the greedy algorithm (Algorithm 1).

3.3 | Adaptively enriching greedy reduced basis algorithm for linear systems with many right-hand sides

In some cases, the response to more than just one excitation is of interest, for example, when optimizing high-intensity focused ultrasound transducers³⁸ or when determining the response to diffuse incident sound pressure fields.³⁹ The corresponding system of linear equations features many right-hand sides and reads

$$\mathbf{A}(\boldsymbol{\mu})\mathbf{X}(\boldsymbol{\mu}) = \mathbf{B}(\boldsymbol{\mu}), \quad (19)$$

with the solution matrix $\mathbf{X}(\boldsymbol{\mu}) = [\mathbf{x}_1(\boldsymbol{\mu}), \dots, \mathbf{x}_{n_{\text{rhs}}}(\boldsymbol{\mu})]$, the right-hand side matrix $\mathbf{B}(\boldsymbol{\mu}) = [\mathbf{b}_1(\boldsymbol{\mu}), \dots, \mathbf{b}_{n_{\text{rhs}}}(\boldsymbol{\mu})]$ and the number of right-hand sides n_{rhs} . The vectors $\mathbf{x}_l(\boldsymbol{\mu})$ denote the individual solutions to the corresponding right-hand sides $\mathbf{b}_l(\boldsymbol{\mu})$ with $l = 1, \dots, n_{\text{rhs}}$.

Equation (19) can be understood as a sequence of n_{rhs} linear systems, which may be successively addressed by Algorithm 2 in order to obtain the solutions to each forcing vector individually. Such an approach requires n_{rhs} separate runs of the algorithm and generates n_{rhs} independent reduced bases. Since the system matrix of Equation (19) remains unchanged within the sequence, it is to be expected that the reduced bases share a common subspace. If this holds, it is more efficient to generate only one reduced basis for all solution vectors \mathbf{x}_l .

Implementing this strategy requires only slight modifications of the existing algorithm. In iteration j , all n_{rhs} linear systems are solved given the current parameter sample $\boldsymbol{\mu}^{(j)}$. Then, the basis is extended by adding the solution matrix \mathbf{X} to it. Alternatively, when dealing with a large number of right-hand sides, the matrix \mathbf{X} can be truncated in order to avoid an excessive increase of the reduced basis. This is particularly efficient when the n_{rhs} solutions span a low-dimensional subspace. Subsequent to extending the reduced basis, the solution for each right-hand side and for each parameter sample in the training set is determined as usual by the least squares solver. The adaptively enriching greedy algorithm for linear systems with many right-hand sides is outlined in Algorithm 4. The algorithm coincides with Algorithm 2 in the case of $n_{\text{rhs}} = 1$.

A broad variety of methods is available for truncating the system responses before extending the basis \mathbf{X}_j . In the first iteration, that is, $j = 1$, a truncated singular value decomposition (SVD) of the solution matrix is performed which yields the best approximation in the spectral norm within a prescribed accuracy.⁴⁰ It reads

$$\mathbf{X}(\boldsymbol{\mu}^{(1)}) \approx \mathbf{U}_1 \boldsymbol{\Sigma}_1 \mathbf{V}_1^*, \quad (20)$$

with $\boldsymbol{\Sigma}_1 = \text{diag}(\sigma_1^{(1)}, \sigma_2^{(1)}, \dots, \sigma_t^{(1)})$ storing the first t singular values of $\mathbf{X}(\boldsymbol{\mu}^{(1)})$ on its diagonal. The matrices \mathbf{U}_1 and \mathbf{V}_1 contain the first t left and right singular vectors as columns, respectively, and $(\cdot)^*$ denotes the complex conjugate transpose. Large values of t lead to more precise approximations with $t = \min\{n_{\text{rhs}}, n\}$ leading to an exact decomposition. Based on the decomposition in Equation (20), the first t left singular vectors are added to the reduced basis \mathbf{X}_1 . In all subsequent iterations $j > 1$, the part of the solution matrix that already lies in the current reduced basis is removed before applying the truncated SVD, that is,

$$\mathbf{X}^\perp(\boldsymbol{\mu}^{(j)}) = \mathbf{X}(\boldsymbol{\mu}^{(j)}) - \mathbf{X}^\parallel(\boldsymbol{\mu}^{(j)}) \approx \mathbf{U}_j \boldsymbol{\Sigma}_j \mathbf{V}_j^*. \quad (21)$$

Algorithm 4. Adaptively enriching greedy algorithm for the solution of parameter dependent linear systems with many right-hand sides

```

1: input
2:   full parameter set  $P$ 
3:   initial training set  $P_{\text{train}} \subset P$  with  $|P_{\text{train}}| = m_{\text{train}}$ 
4:   system matrices  $\mathbf{A}(\boldsymbol{\mu}_i)$  and right-hand sides  $\mathbf{B}(\boldsymbol{\mu}_i) = [\mathbf{b}_1(\boldsymbol{\mu}_i), \dots, \mathbf{b}_{n_{\text{rhs}}}(\boldsymbol{\mu}_i)]$  with  $\boldsymbol{\mu}_i \in P_{\text{train}}$ 
5:   relative residual tolerance  $\varepsilon_{\text{tol}}$ 
6:   truncation tolerance  $\varepsilon_{\text{svd}}$ 
7:   parameter sample for first iteration  $\boldsymbol{\mu}^{(1)} \in P_{\text{train}}$ 
8: initialization
9:    $j := 1$ 
10:   $[\mathbf{r}_1(\boldsymbol{\mu}_i), \dots, \mathbf{r}_{n_{\text{rhs}}}(\boldsymbol{\mu}_i)] := \mathbf{B}(\boldsymbol{\mu}_i) \forall \boldsymbol{\mu}_i \in P_{\text{train}}$ 
11:  solve  $\mathbf{A}(\boldsymbol{\mu}^{(1)})\mathbf{X}(\boldsymbol{\mu}^{(1)}) = \mathbf{B}(\boldsymbol{\mu}^{(1)})$ 
12:  calculate  $\mathbf{X}(\boldsymbol{\mu}^{(1)}) \approx \mathbf{U}_1 \boldsymbol{\Sigma}_1 \mathbf{V}_1^*$  with  $t$  as in Equation (23)
13:   $\mathbf{X}_1 := [\mathbf{U}_1]$ 
14:   $P_{\text{sol}} := \{\boldsymbol{\mu}^{(1)}\}$ 
15:   $P_{\text{train}} := \text{ALGORITHM } 3(P, P_{\text{train}}, P_{\text{sol}}, \boldsymbol{\mu}^{(1)})$ 
16: while  $|P_{\text{train}}| > 0$  do
17:   for each  $\boldsymbol{\mu}_i \in P_{\text{train}}$  do
18:    solve  $\min_{\mathbf{Y}(\boldsymbol{\mu}_i)} \|\mathbf{A}(\boldsymbol{\mu}_i)\mathbf{X}_j \mathbf{Y}(\boldsymbol{\mu}_i) - \mathbf{B}(\boldsymbol{\mu}_i)\|_2^2$ 
19:     $[\mathbf{r}_1(\boldsymbol{\mu}_i), \dots, \mathbf{r}_{n_{\text{rhs}}}(\boldsymbol{\mu}_i)] := \mathbf{A}(\boldsymbol{\mu}_i)\mathbf{X}_j \mathbf{Y}(\boldsymbol{\mu}_i) - \mathbf{B}(\boldsymbol{\mu}_i)$ 
20:    if  $\|\mathbf{r}_l(\boldsymbol{\mu}_i)\|_2 / \|\mathbf{b}_l(\boldsymbol{\mu}_i)\|_2 < \varepsilon_{\text{tol}} \forall l \in \{1, \dots, n_{\text{rhs}}\}$  then
21:       $[\mathbf{x}_1(\boldsymbol{\mu}_i), \dots, \mathbf{x}_{n_{\text{rhs}}}(\boldsymbol{\mu}_i)] := \mathbf{X}_j \mathbf{Y}(\boldsymbol{\mu}_i), \quad P_{\text{sol}} := P_{\text{sol}} \cup \{\boldsymbol{\mu}_i\}$ 
22:       $P_{\text{train}} := \text{ALGORITHM } 3(P, P_{\text{train}}, P_{\text{sol}}, \boldsymbol{\mu}_i)$ 
23:    end if
24:   end for
25:   if  $P_{\text{train}} = \emptyset$  then
26:     break
27:   end if
28:    $\boldsymbol{\mu}^{(j+1)} := \underset{\boldsymbol{\mu}_i \in P_{\text{train}}}{\text{argmax}} \max_{l \in \{1, \dots, n_{\text{rhs}}\}} \|\mathbf{r}_l(\boldsymbol{\mu}_i)\|_2 / \|\mathbf{b}_l(\boldsymbol{\mu}_i)\|_2$ 
29:   solve  $\mathbf{A}(\boldsymbol{\mu}^{(j+1)})\mathbf{X}(\boldsymbol{\mu}^{(j+1)}) = \mathbf{B}(\boldsymbol{\mu}^{(j+1)})$ 
30:   calculate  $\mathbf{X}^\perp(\boldsymbol{\mu}^{(j+1)}) \approx \mathbf{U}_{j+1} \boldsymbol{\Sigma}_{j+1} \mathbf{V}_{j+1}^*$  with  $t$  as in Equation (23)
31:    $\mathbf{X}_{j+1} := [\mathbf{X}_j, \mathbf{U}_{j+1}]$ ,  $P_{\text{sol}} := P_{\text{sol}} \cup \{\boldsymbol{\mu}^{(j+1)}\}$ 
32:    $P_{\text{train}} := \text{ALGORITHM } 3(P, P_{\text{train}}, P_{\text{sol}}, \boldsymbol{\mu}^{(j+1)})$ 
33:    $j := j + 1$ 
34: output
35:    $\mathbf{x}_l(\boldsymbol{\mu}_i)$  with  $\|\mathbf{A}(\boldsymbol{\mu}_i)\mathbf{x}_l(\boldsymbol{\mu}_i) - \mathbf{b}_l(\boldsymbol{\mu}_i)\|_2 / \|\mathbf{b}_l(\boldsymbol{\mu}_i)\|_2 \leq \varepsilon_{\text{tol}} \forall \boldsymbol{\mu}_i \in P, \forall l \in \{1, \dots, n_{\text{rhs}}\}$ 

```

The singular values and vectors are determined with respect to $\mathbf{X}^\perp(\boldsymbol{\mu}^{(j)})$ which only contains the part of the solution that is orthogonal to the current reduced basis \mathbf{X}_{j-1} . The subspace spanned by $\mathbf{X}^\perp(\boldsymbol{\mu}^{(j)})$, on the other hand, is parallel to the subspace spanned by the reduced basis \mathbf{X}_{j-1} . Hence, its columns are the orthogonal projection of $\mathbf{X}(\boldsymbol{\mu}^{(j)})$ onto \mathbf{X}_{j-1} , that is,

$$\mathbf{X}^\perp(\boldsymbol{\mu}^{(j)}) = \mathbf{X}_{j-1} \left(\mathbf{X}_{j-1}^* \mathbf{X}_{j-1} \right)^{-1} \mathbf{X}_{j-1}^* \mathbf{X}(\boldsymbol{\mu}^{(j)}). \quad (22)$$

This ensures that the first t left singular vectors in Equation (21) are orthogonal to the reduced basis \mathbf{X}_{j-1} and that no redundant information is introduced when adding them to the reduced basis. Since the columns of the reduced basis are orthogonal to each other, Equation (22) simplifies to $\mathbf{X}^\perp(\boldsymbol{\mu}^{(j)}) = \mathbf{X}_{j-1} \mathbf{X}_{j-1}^* \mathbf{X}(\boldsymbol{\mu}^{(j)})$. In each iteration of the greedy algorithm, the value of t is determined by

$$t = \min_{l \in \mathbb{N}} \left\{ \sigma_{t+1}^{(j)} \leq \varepsilon_{\text{svd}} \sigma_1^{(j)} \right\}, \quad (23)$$

with a prescribed tolerance $\varepsilon_{\text{svd}} > 0$. Choosing a small truncation tolerance leads to large values of t and thus to an extension of the reduced basis by a larger quantity of left singular vectors in each iteration. In contrast, ε_{svd} close to one leads to small values of t and thus significantly limits the number of vectors added to the reduced basis in each iteration. Extending the basis by a smaller quantity of vectors in each iteration does not generally imply an overall smaller reduced basis since an essential characteristic of the system response might be cut off by the truncated singular value decomposition. This in turn would result in a larger number of iterations of the greedy algorithm.

4 | NUMERICAL EXAMPLES

4.1 | Point-excited spherical shell in water

The first example features a spherical shell submerged in water. The shell is made of steel and excited by a point force of $F = 1$ N. The geometry and material properties are summed up in Table 1. The finite element mesh consists of 384 eight-noded quadrilateral shell finite elements based on the Reissner–Mindlin plate theory. This corresponds to eight elements on a $\pi/2$ arc. A mesh conforming boundary element discretization is employed on the sound radiating boundary using discontinuous nine-noded quadrilateral boundary elements with four sound pressure degrees of freedom. Forming the Schur complement with respect to the pressure degrees of freedom, compare Equation (6), yields a system of linear equations with 1536 degrees of freedom. The parameter-independent mesh coupling matrices are obtained by a Galerkin projection.³⁴

The parameter domain is spanned by the frequency f and the Young's modulus E . A nonuniform sampling is employed in frequency direction using $n_1 = 89$ points between 1 and 100 Hz. In contrast, the Young's modulus is uniformly sampled with $n_2 = 11$ points ranging between 189 and 231 GPa. This results in a total of $m = 979$ parameter samples. Figure 1 shows the absolute sound pressure at an angle of π with respect to the point of excitation of the spherical shell throughout the parameter domain \mathcal{P} . The parameter samples are highlighted by red dots and the underlying solution is computed analytically.⁴¹ Six distinct resonances occur within the considered parameter domain and change with both frequency and Young's modulus. Storing the 979 linear systems requires 35.24 GB of memory. The conventional approach as well as the greedy algorithm (Algorithm 1) and the adaptively enriching greedy algorithm (Algorithm 2) are applied to this problem.

In the conventional approach, the generalized minimum residual method (GMRes) solves the Schur complement systems with a relative residual tolerance of $\varepsilon = 10^{-4}$. The solution for all parameter samples within the parameter set requires 224.89 s of wall clock time. This corresponds to an average of 0.23 s per system. The greedy algorithm requires 27 iterations to determine a solution with a relative residual of $\varepsilon_{\text{tol}} = 10^{-4}$ for each parameter sample. Generating the basis vectors takes 10.35 s which involves the solution of 27 linear systems using the GMRes solver within a relative tolerance of 10^{-7} . Setting up the least squares problems requires 20,086 matrix-vector multiplications which correspond to 148.96 s and solving the least squares problems takes 18.32 s. In total, the wall clock time equals 179.55 s and hence the greedy algorithm is 20.2% faster than the conventional approach.

The adaptively enriching greedy algorithm contains the additional parameter m_{train} which defines the size of the training set. The parameter samples within the initial training set are randomly chosen out of the full parameter set and the replacement algorithm (Algorithm 3) randomly picks a new parameter sample whenever a converged solution is determined. To address this random component of the algorithm, 10 individual runs are performed and the computational efficiency is evaluated based on the maximum, minimum, and average values of the wall clock time and number of

TABLE 1 Geometry of the sphere and material properties of steel and water

Radius of sphere	r	5 m
Shell thickness	t	0.05 m
Density of steel	ρ_s	7860 kg/m ³
Poisson's ratio	ν	0.3
Density of water	ρ_f	1000 kg/m ³
Speed of sound	c	1482 m/s

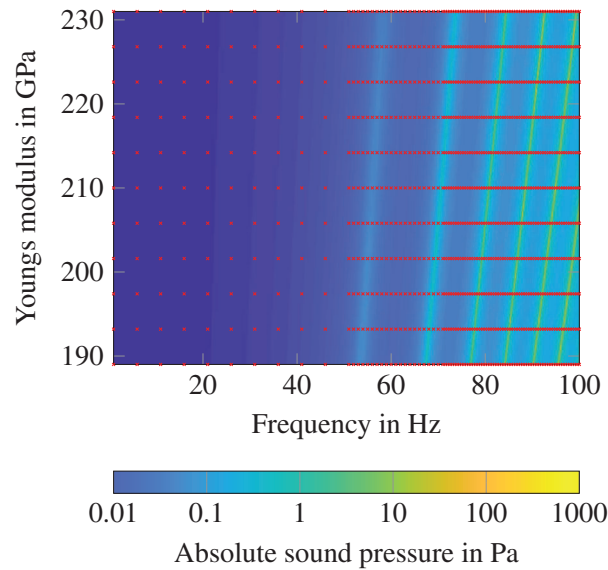


FIGURE 1 Analytical solution of the absolute sound pressure on the surface of the spherical shell at the opposite side of the point of excitation. The red dots mark the parameter samples

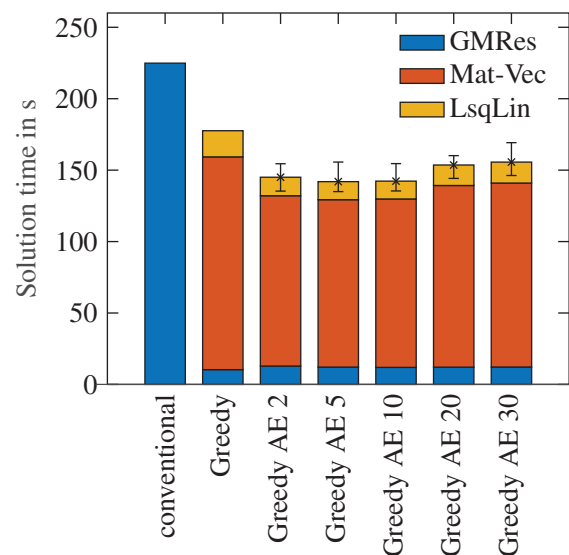


FIGURE 2 Wall-clock time for the solution process using the conventional approach, Algorithm 1 (Greedy) and Algorithm 2 (GreedyAE m_{train}) with varying values of m_{train} . Mean values for the solution time are marked by crosses whereas maximum and minimum values are given by the error bars

iterations, respectively. The adaptively enriching greedy algorithm with a training set size of $m_{\text{train}} = 10$ requires an average amount of 30.5 iterations which corresponds to an average run time of 142.32 s. The fastest and slowest runs require 29 and 32 iterations and take 134.79 and 153.83 s, respectively. Hence, Algorithm 2 solves the problem between 31.6% and 40.0% faster than the conventional approach and between 14.3% and 24.9% faster than the greedy algorithm. Although exhibiting a slightly higher number of iterations, the adaptively enriching technique manages to compute significantly less matrix-vector products. This is achieved by performing the linear approximation only on the small training set and by iteratively building the linear approximation for each new parameter sample. Figure 2 shows the individual timings for the conventional approach, the greedy algorithm (Greedy) and the adaptively enriching greedy algorithm (GreedyAE) with varying sizes of the training set. The adaptively enriching version solves a slightly higher number of linear systems but compensates the additional computational effort by a significantly reduced number of matrix-vector products and linear least squares solves. The results indicate that the choice of the training set size only has

a minor impact on the computational time. However, the impact on the memory requirements is significant. Doubling the size of the training set requires to assemble and store twice as many linear systems which can be a bottle neck for large-scale problems. Fortunately, Figure 2 shows that a small size seems to be a good choice in terms of computational time. The number of matrix-vector products is minimized at the cost of an increase in the number of iterations, that is, an increase in the dimension of the reduced basis, as shown in Figure 3.

Both greedy algorithms generate one basis vector in each iteration by evaluating the system response at the parameter sample which is currently approximated worse. Algorithm 1 assesses the quality of the approximation throughout the whole parameter set whereas Algorithm 2 takes only the small training set into account. Hence, the former leads to a global approximation of the solution and the latter leads to a local approximation. The markers in Figures 4 and 5 indicate the locations of the parameter samples which are chosen by the two greedy algorithms. The greedy algorithm

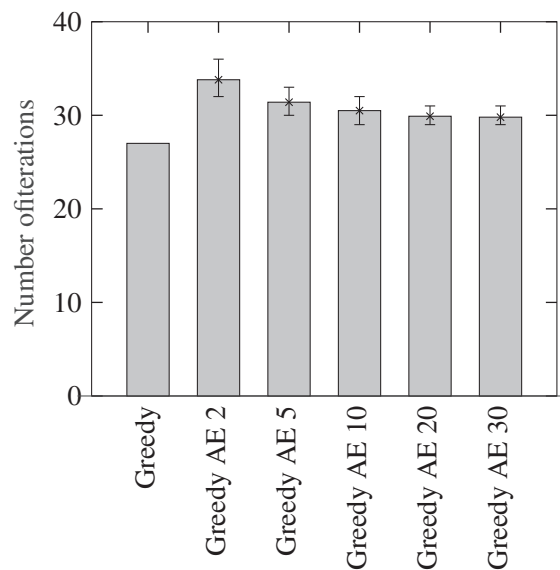


FIGURE 3 Number of iterations of Algorithm 1 (Greedy) and Algorithm 2 (GreedyAE m_{train}) with varying values of m_{train} . Mean values for the iteration numbers are marked by crosses whereas maximum and minimum values are given by the error bars

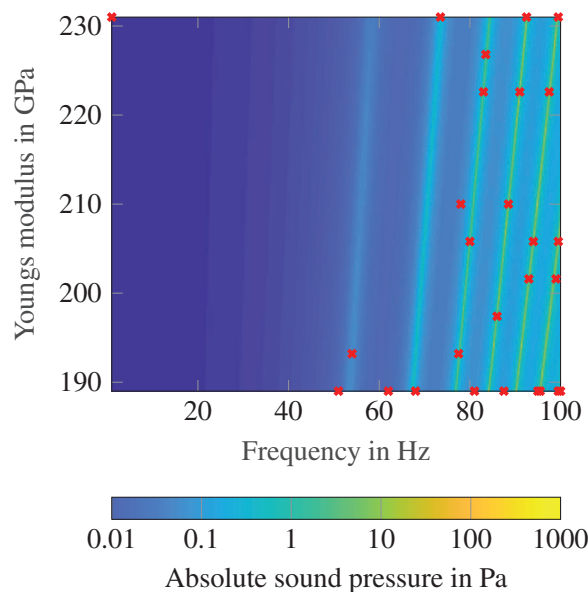


FIGURE 4 The red crosses mark the parameter samples at which the greedy algorithm (Algorithm 1) generates the basis vectors. The contour displays the analytical solution of the absolute sound pressure on the surface of the spherical shell at the opposite side of the point of excitation

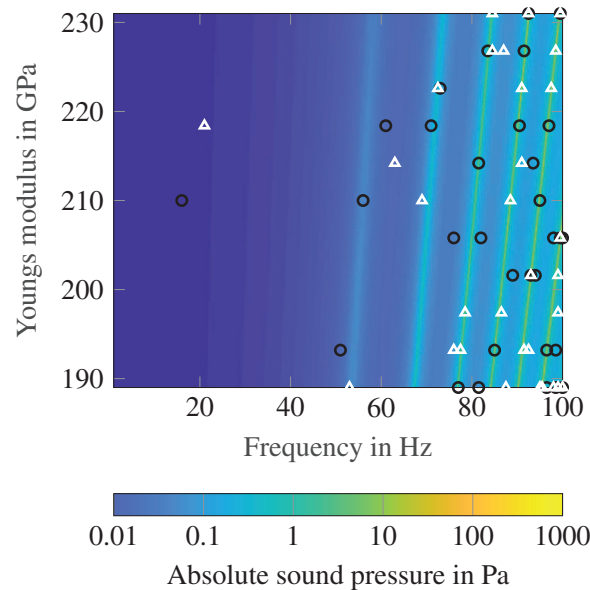


FIGURE 5 The black circles and white triangles mark the parameter samples chosen by the adaptively enriching greedy algorithm (Algorithm 2) in two different runs with $m_{\text{train}} = 10$. The contour displays the analytical solution of the absolute sound pressure on the surface of the spherical shell at the opposite side of the point of excitation

(Algorithm 1) generates a majority of the basis vectors in close proximity to resonances as presented in Figure 4. Note that this choice is based on the greedy approach in conjunction with the residual and not based on solving the corresponding nonlinear eigenvalue problem. The adaptively enriching greedy algorithm (Algorithm 2) leads to a similar selection of parameter samples. Although, an increased number of basis vectors are evaluated at parameter points apart from resonances, a significant number of samples are still located close to resonance peaks. Despite the small training set size, the algorithm selects parameter samples with high approximation power, some of which even coincide with the ones chosen by Algorithm 1.

For the purpose of analyzing the convergence behavior of the two greedy algorithms, Figures 6 and 7 show the relative residual within the parameter domain at iterations 1, 9, 14, and 20, respectively. Let us first discuss the convergence behavior of the adaptively enriching greedy algorithm depicted in Figure 6. The first basis vector is generated at a randomly chosen parameter sample among the $m_{\text{train}} = 10$ samples within the training set. In this specific run, the first parameter sample lies between two resonances at 93.5 Hz and 214.2 GPa as indicated in the top left plot of Figure 6. Solving the linear least squares problems yields the depicted relative residual with a maximum value of 0.9988 at the top left corner of the parameter domain (1 Hz, 231 GPa). Note that for the sake of the analysis here, the relative residual is explicitly calculated throughout the full parameter set, although in an actual application, the adaptively enriching greedy algorithm would only compute them for the parameter samples within the training set. The second basis vector is generated at 16 Hz and 210 GPa since this parameter point is associated with the largest relative residual among the current training set. The corresponding relative residual equals 0.9983. A total of nine basis vectors are available subsequent to the ninth iteration. The evaluated parameter samples are highlighted in the top right plot of Figure 6 together with the relative residual of the linear approximation. Adding the system response of a parameter sample to the reduced basis increases the quality of the linear approximation along certain lines within the parameter domain. These lines follow the direction of the nearby resonance peaks of the underlying solution which indicates that the system responses are similar along these lines. This behavior stems from the low rank property of the solution within the parameter domain which allows to build a sufficiently accurate solution by superposing adequately chosen system responses. When reaching iteration 14, the adaptively enriching greedy algorithm has found a sufficiently accurate solution throughout a large part of the parameter domain, compare the bottom left plot of Figure 6. Converged solutions are found in the proximity of the evaluated parameter samples and along the aforementioned lines. Large relative residuals still exist at the higher frequency end of the parameter domain. After 20 iterations, a solution is found for the majority of the parameter samples. By adding further system responses to the reduced basis, the algorithm finds a sufficiently accurate solution once reaching iteration 31. The standard greedy algorithm exhibits a similar convergence behavior as depicted in Figure 7.

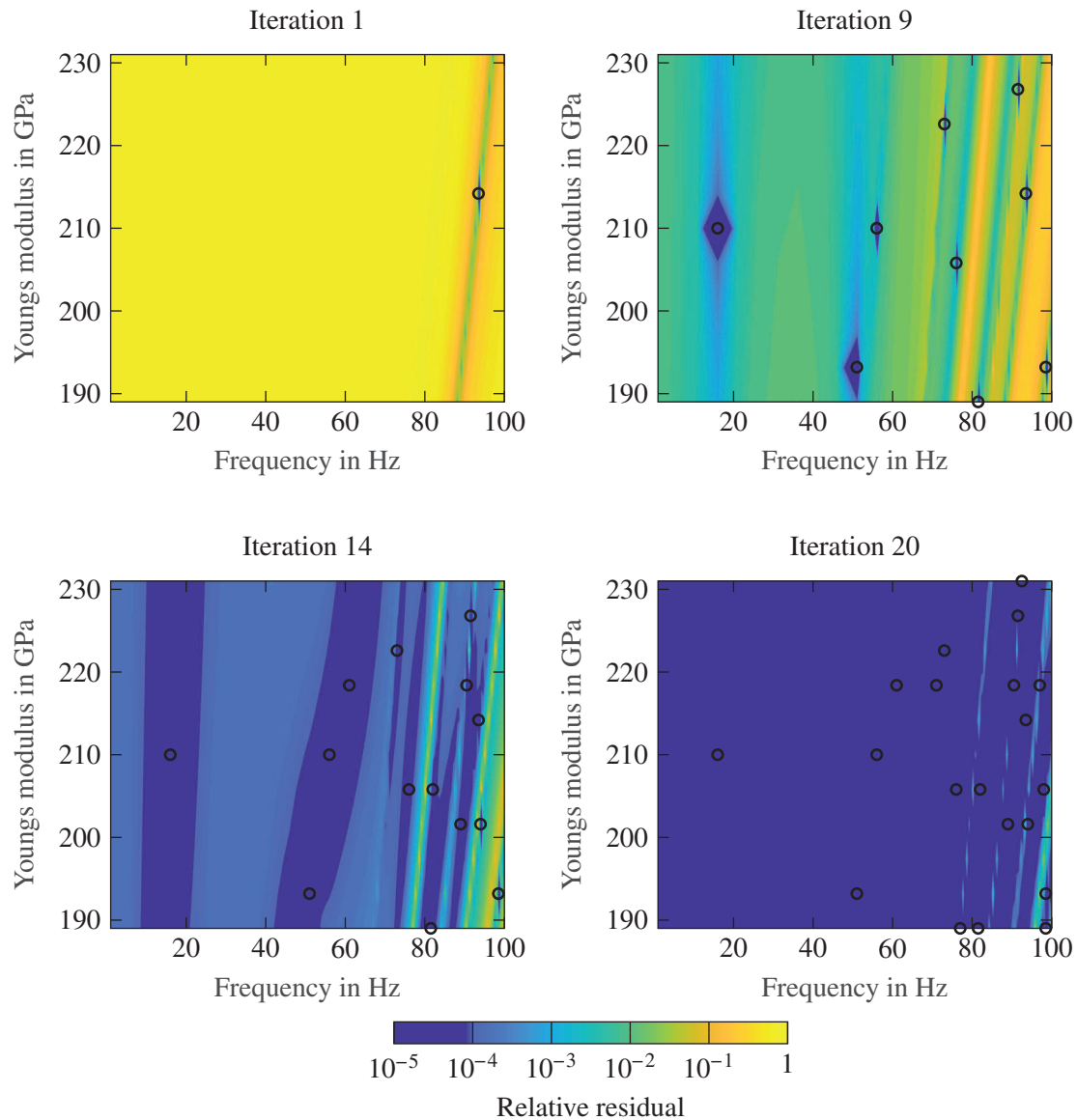


FIGURE 6 Relative residuals of the solution after iteration 1, 9, 14, and 20 (top left, top right, bottom left, and bottom right) for the solution of the submerged spherical shell using the adaptively enriching greedy algorithm (Algorithm 2). The relative residual tolerance is $\varepsilon_{\text{tol}} = 10^{-4}$ and $m_{\text{train}} = 10$. Black circles mark the parameter samples at which basis vectors are generated

However, a comparison between the two greedy strategies provides a rather unexpected result: The relative residuals in iterations 14 and 20 are larger than in the adaptively enriching version, compare bottom left and right subplots. This may seem nonintuitive, since the standard greedy algorithm chooses the basis vectors according to the relative residual in the whole parameter set, while the adaptively enriching version is limited to a small training set. An immediate interpretation of this result is that the standard greedy choice does not necessarily yield the basis vectors with the highest approximation power, that is, those basis vectors, which are capable of covering large portions of the parameter domain. Indeed, the greedy strategy is most efficient when the basis vectors with the highest approximation power are added to the basis as early as possible.

This issue is addressed from another point of view in Figure 8. The plot shows the number of parameter samples for which the approximate solution is found using a certain number of basis vectors. The bars of zero basis vectors belong to linear systems which are solved by GMRes. On average, the solution at a specific parameter sample requires significantly less basis vectors when using the adaptively enriching variant instead of the standard algorithm. For example, after iteration 15, both the standard and the adaptively enriching algorithms have built a reduced basis containing 15 basis vectors. In the case of the standard greedy algorithm, the linear combination of these basis vectors is only capable of providing

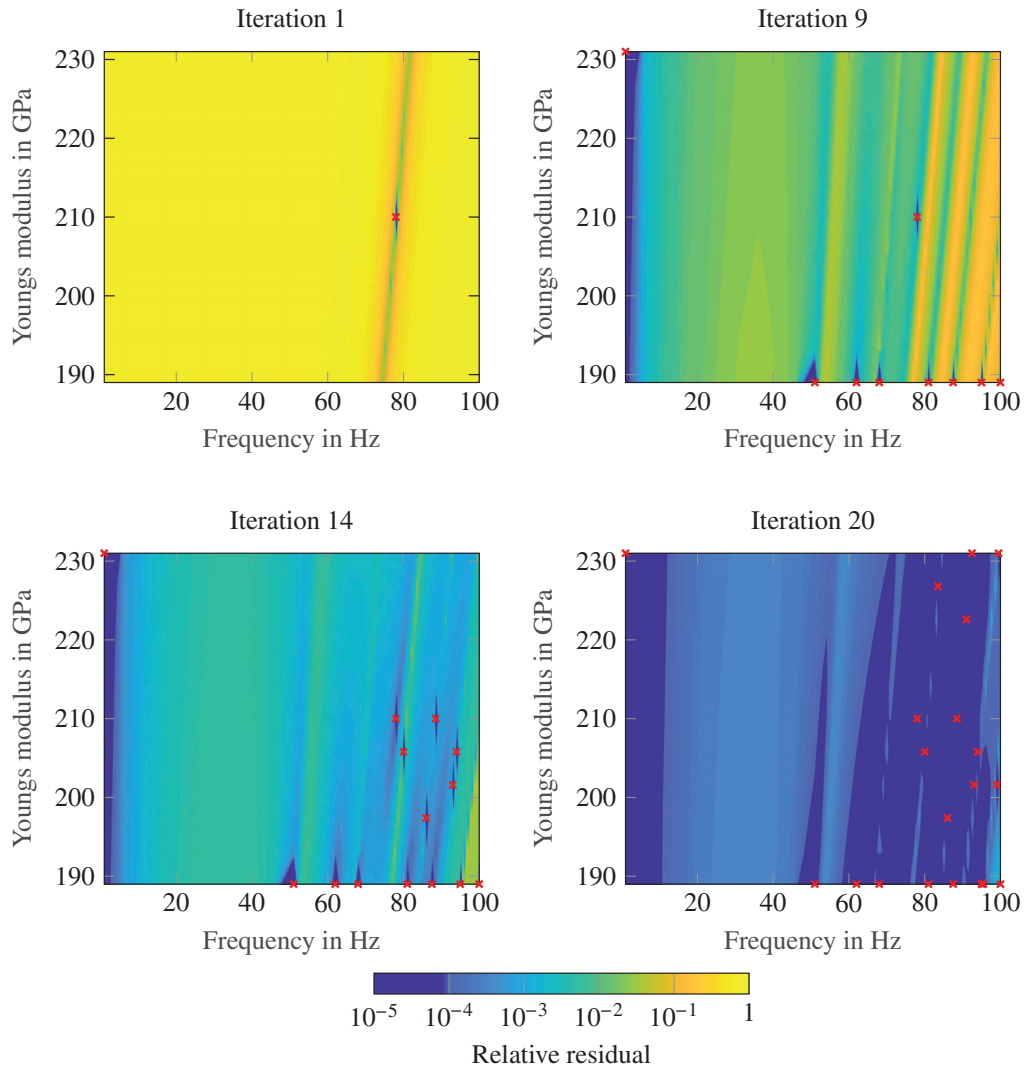


FIGURE 7 Relative residuals of the solution after iteration 1, 9, 14, and 20 (top left, top right, bottom left, and bottom right) for the solution of the submerged spherical shell using the standard greedy algorithm (Algorithm 1). The relative residual tolerance is $\epsilon_{tol} = 10^{-4}$. Red crosses mark the parameter samples at which basis vectors are generated

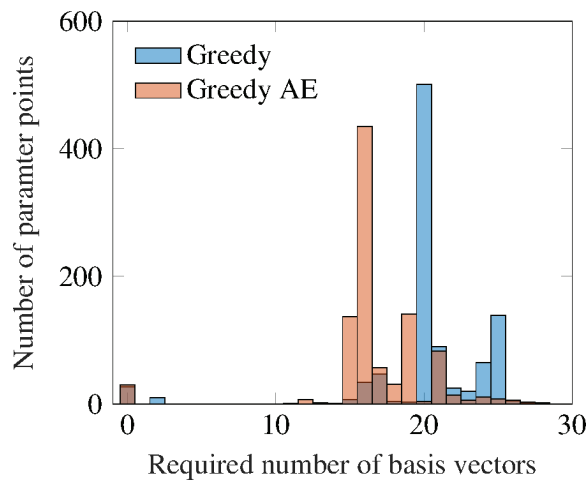


FIGURE 8 Number of basis vectors required to approximate the solution at a number of parameter points for Algorithm 1 (Greedy) and Algorithm 2 (GreedyAE). The bars of zero basis vectors belong to linear systems which are solved by GMRes. The bars of nonzero basis vectors indicate the number of parameter points at which a sufficiently accurate solution is found based the specified number of basis vectors

the solution at 17 other parameter points. In contrast, the reduced basis of the adaptively enriching greedy algorithm yields accurate enough solutions at 148 other parameter points. This behavior also stretches out to higher iteration numbers and is the main reason for the computational efficiency of the adaptively enriching greedy algorithm. Calculating a sufficiently accurate solution at the majority of parameter samples with a smaller number of basis vectors significantly reduces the number of matrix-vector products and linear least squares solutions. The top right subplot of Figure 7 shows that up until the ninth iteration, the standard greedy algorithm exclusively chooses parameter samples which are located at the boundary of the parameter domain. Apparently, these points are associated with the largest relative residuals but do not necessarily yield basis vectors with the highest approximation power. On the other hand, the random choice of the training set in the adaptively enriching strategy yields parameter samples which are better distributed across the whole parameter domain.

Analyzing the maximum value of the relative residuals within the parameter domain provides a further view on the convergence behavior. Figure 9 shows the maximum relative residual over the number of greedy iterations. The maximum values decrease monotonically in the case of the greedy algorithm (Greedy). In contrast, the residuals decrease nonmonotonically within the adaptively enriching greedy algorithm (GreedyAE). It assesses the residuals only locally within the training set P_{train} which results in fluctuations since the parameter samples are repeatedly removed from the set and replaced. When assessing the relative residuals globally within the full parameter set P , a monotonic decrease of the maximum relative residual is reported (GreedyAE global). Note that this information is not readily available within the GreedyAE algorithm and only postprocessed for the purpose of visualization.

4.2 | Satellite structure

Space telescopes for astronomical observations are subject to heavy acoustic loading during the launch of the carrier rocket. Sound pressure levels up to 180 dB account for the main load case determining the design of the payload. During launch, scientific instruments such as cameras are usually enclosed by a primary structure made of honeycomb sandwich panels. Therefore, it is crucial to accurately predict the structural acoustic behavior of such sandwich closures, which often feature gaps and slits to address thermal expansion.

In this second numerical example, a simplified radiator structure made of aluminum honeycomb panels is considered. Its geometry is shown in Figure 10. The structure consists of six sandwich panels and is rigidly mounted at four locations on the bottom panel. All panels are connected with each other by either rigid or elastic joints.

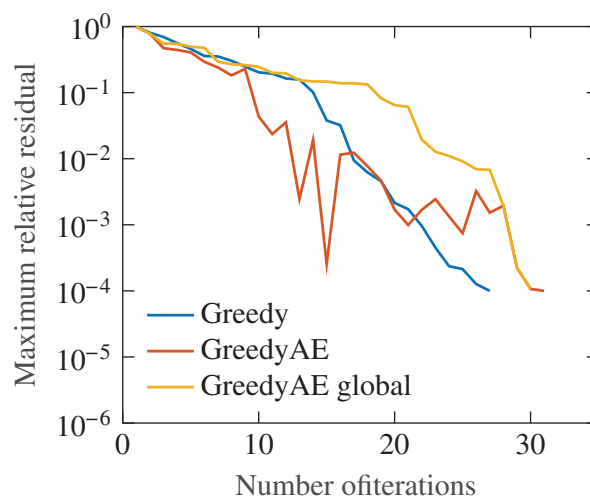


FIGURE 9 Maximum relative residual in each iteration of the greedy algorithm (Greedy) and adaptively enriching greedy algorithm with $m_{\text{train}} = 10$. The relative residuals are assessed either locally within the training set (GreedyAE) or globally at all parameter samples (GreedyAE global)

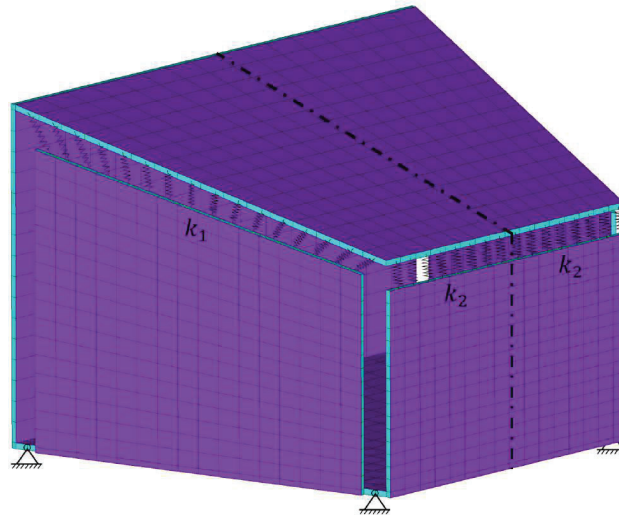


FIGURE 10 Satellite structure made of six sandwich panels. The geometry and boundary conditions are symmetric along the dash-dotted plane. The structure is rigidly mounted at four nodes on the bottom panel and partly connected with elastic joints which are modeled by series of springs with stiffness values k_1 and k_2 . The face sheets are purple whereas the cores are teal

TABLE 2 Properties of the face sheets and the core

Aluminum face sheet		
Thickness	t	0.28 mm
Density	ρ_a	26,600 kg m ⁻³
Young's modulus	E_a	70 GPa
Poisson's ratio	ν_a	0.34
Foam core		
Thickness	h	29 mm
Density	ρ_c	80 kg m ⁻³
Young's modulus	E_c	50 MPa
Poisson's ratio	ν_c	0.1

The latter are numerically modeled by a series of springs along the edges of the panels with a node-to-node contact formulation. Each spring features a translational stiffness in all three dimensions. The value k_1 is used on the side panel joints and k_2 is used on the front panel joints. Every sandwich panel consists of a 29 mm thick foam core and two 0.28 mm thick aluminum face sheets. Both materials are isotropic and their mechanical properties are given in Table 2. The surrounding air has a density of $\rho_f = 1.225 \text{ kg m}^{-3}$ and speed of sound of $c = 340 \text{ m s}^{-1}$. The face sheets are discretized by eight-noded quadrilateral Reissner-Mindlin shell finite elements whereas the cores are discretized by twenty-noded hexahedral solid finite elements. This results in a total of 68,802 displacement dofs. Quadrilateral boundary elements with linear discontinuous sound pressure approximation are employed for the discretization of the surrounding acoustic domain which yields 4024 sound pressure dofs. The structural and acoustic meshes are nonconforming on the face sheets and coupled by a Galerkin projection.³⁴ Comparing the radiated sound power in the frequency range of interest to the results obtained with a finer mesh featuring four times the acoustic pressure dofs yields a difference of less than 0.51 dB.

A diffuse incident sound pressure field excites the satellite structure during the liftoff of the carrier rocket. Following the approach of Rafaely,³⁹ a total of 50 individual right-hand sides are calculated to represent this excitation. Additional structural forces are neglected. Each right-hand side is given by a summation of 1145 random incident plane waves with uniformly distributed directions in space. The final vibro-acoustic response is the mean of the system responses to all 50

right-hand sides. The dynamical behavior of the satellite structure subject to the diffuse sound pressure field excitation is investigated in the frequency range between 10 and 50 Hz. This study analyzes different combinations of stiffness values k_1 and k_2 which lie in the interval of 103 and 104 N m⁻¹, and represent different types of elastic joints. The influence of modifying the elastic joint on the front edge, that is modifying k_2 , while keeping the elastic joint on the side edges unmodified is presented in Figures 11 and 12. The former shows the total kinetic energy of the satellite structure whereas the latter shows the radiated sound power. The three dimensional parameter domain is spanned by the frequency f and the stiffness values k_1 and k_2 . A uniform sampling with 81 frequency points and five stiffness values each yield a total of $m = 2025$ parameter samples. Storing a single linear system requires 1.8 GB of memory and hence, applying Algorithm 1 is infeasible on standard desktop computers due to memory limitations. However, assuming a memory size of 64 GB, Algorithm 4 can be run with a training set size of $n_{\text{train}} \approx 30$. This estimation also includes the memory required for storing the greedy basis \mathbf{X}_j and the least squares system matrices $\mathbf{A}(\mu_i)\mathbf{X}_j$ as well as a conservative estimation of the number of iterations.

A training set size of $m_{\text{train}} = 10$ is chosen based on the results of the first numerical example. The block generalized minimum residual method (BGMRes) is employed within the algorithm to solve Equation (19) with a relative tolerance of 10^{-7} . The BGMRes method significantly reduced the solution time for linear systems with multiple right-hand sides compared to the standard GMRes method.⁴² The adaptively enriching greedy algorithm terminates when a

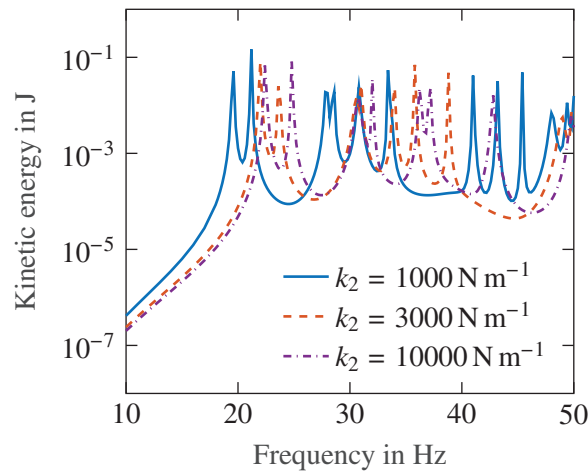


FIGURE 11 Total kinetic energy (in Joule) of the satellite structure under diffuse sound pressure field excitation with $k_1 = 1000 \text{ N m}^{-1}$ and varying values of k_2

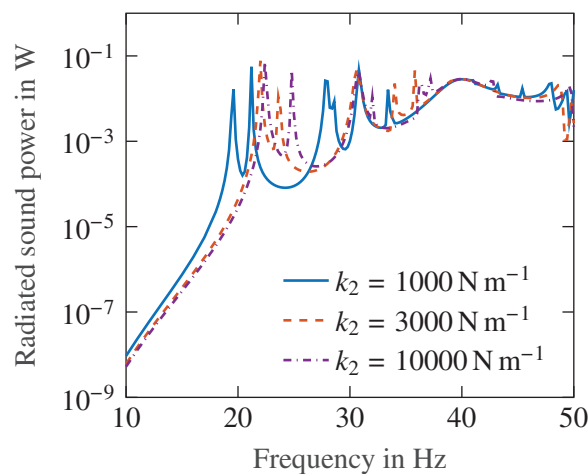


FIGURE 12 Radiated sound power (in Watt) of the satellite structure under diffuse sound pressure field excitation with $k_1 = 1000 \text{ N m}^{-1}$ and varying values of k_2

solution is found within a relative tolerance of $\epsilon_{\text{tol}} = 10^{-4}$ for every parameter sample. In each iteration, the t left singular vectors \mathbf{U}_j of the system responses extend the reduced basis, compare Lines 12 and 30 of Algorithm 4. The value of t is determined by Equation (23) given the tolerance $\epsilon_{\text{svd}} = 0.01$. The study assesses the performance by means of an average of 10 runs.

The adaptively enriching greedy algorithm with $\epsilon_{\text{svd}} = 0.01$ finds a solution within an average of 19.5 iterations which corresponds to a run time of 7.5 h. Setting up the linear least squares problems requires the most time with 6.5 h whereas their solution only takes 3.3 min. The BGMRes method solves an average of 19.5 linear systems in 56.5 min and the final reduced basis consists of 135.3 vectors on average. The fastest and slowest runs require 18 and 22 iterations, build a reduced basis with 126 and 139 vectors and take 7.1 and 8.0 h, respectively. In contrast, solving the linear systems of all 2025 parameter samples by BGMRes with the same accuracy would take a run time of 51.5 h.

Figures 13 and 14 visualize the impact of the truncation tolerance ϵ_{svd} on the solution time and, respectively, on the number of iterations and the size of the reduced basis. As expected, Figure 14 shows that smaller values of ϵ_{svd} lead to less iterations of the greedy algorithm. However, a smaller number of iterations does not necessarily imply a smaller reduced basis. In fact, Figure 14 even shows that the algorithm builds a significantly larger basis featuring an average of 163.5 and 194.5 vectors. This leads to an increased number of matrix-vector products and hence to further computational effort. In this case, the time spent on performing the additional matrix-vector products outweighs the reduction in system evaluations and the total run time increases. The runs take an average of 8.0 and 9.2 h, respectively. When increasing the truncation tolerance instead, the reduced basis is extended by a smaller quantity of vectors in each iteration. This leads to an increase in the number of iterations while decreasing the size of the reduced basis. For $\epsilon_{\text{svd}} = 0.1$, the algorithm builds a basis with 116.3 vectors in 34.6 iterations on average. Although this setting leads to the smallest reduced basis, the number of matrix-vector products does not significantly change compared to the $\epsilon_{\text{svd}} = 0.01$ runs. Since the number of system evaluations doubles, the average run time is increased to 8.1 h with 6.4 h spent on matrix-vector products and 1.7 h spent on solving the linear systems.

The run time analysis shows that the choice of the truncation tolerance ϵ_{svd} imposes a tradeoff between the computational effort of matrix-vector products and solutions of the high-fidelity systems via BGMRes. This is similar to the choice of the training set size m_{train} in Section 4.1. In the present example, a truncation tolerance of $\epsilon_{\text{svd}} = 0.01$ yields the fastest solution time. Decreasing the truncation tolerance yields a steady increase in the reduced basis size and a decrease in the number of iterations. Apparently, explicitly evaluating the solution at only 9 parameter samples gathers enough information to find a solution at all parameter samples for each of the 50 right-hand sides. On average, the basis is extended by 3.4, 7.0, 13.0, and 20.1 vectors in each iteration when prescribing a truncation tolerance of 0.1, 0.01, 0.001, and 0.0001, respectively.

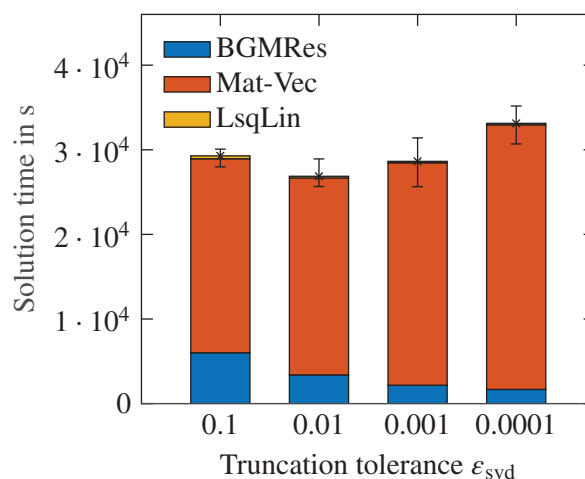


FIGURE 13 Wall-clock time for the solution process using the adaptively enriching greedy algorithm (Algorithm 4) with a fixed training set size of $m_{\text{train}} = 10$ and a varying truncation tolerance ϵ_{svd} . Mean values for the solution time are marked by crosses whereas maximum and minimum values are given by the error bars

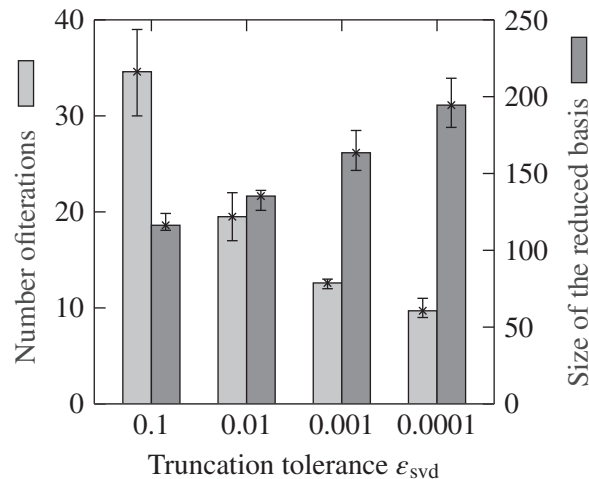


FIGURE 14 Number of iterations of the adaptively enriching greedy algorithm (Algorithm 4) in light gray and the size of the determined reduced basis in gray. The training set size is $m_{\text{train}} = 10$ and the truncation tolerance ϵ_{SVD} is varied. Mean values are marked by crosses whereas maximum and minimum values are given by the error bars

5 | CONCLUSION AND FUTURE WORK

An adaptively enriching greedy reduced basis scheme has been proposed for the solution of structural acoustic systems with parameter and implicit frequency dependence. The algorithm starts on a small subset of the discretized parameter domain and iteratively builds a reduced basis by adding the system response at the parameter sample where the approximation is currently worst. Working on a small subset allows to solve large-scale problems with a possibly high-dimensional parameter domain. Whenever the solution at a parameter sample is found, the sample is removed from the small subset and a parameter sample at which a solution has not yet been found is added. The first numerical example, the submerged elastic sphere, has indicated that working with a small training parameter set instead of the full parameter set is computationally more efficient. The run time analysis illustrated that the algorithm works best on very small subsets in the presented case. It has been shown that assessing the residual allows to choose parameter samples which yield basis vectors with high approximation power despite working on a small subset. A significant speedup has been documented for the example presented in this work when compared to both the conventional solution strategy and the globally working greedy algorithm. The algorithm has been adapted to vibro-acoustic problems featuring many right-hand sides. Instead of extending the basis by all system responses, only a few left singular vectors of the responses are added which are determined by a truncated singular value decomposition. The truncation is based on a comparison of the singular values of the system responses to a scaled reference singular value. The algorithm has been applied to a second numerical example, a satellite structure subject to a diffuse sound pressure field excitation. The impact of the scaling factor, that is, the truncation tolerance, has been studied and a region of optimal values has been identified. In both case studies, a linear combination of the system responses at a few parameter samples has led to a sufficiently accurate solution at all parameter samples.

The adaptively enriching greedy algorithm randomly chooses the initial subset as well as the parameter samples replacing samples at which a solution is found. This aspect was considered by presenting the results of 10 individual runs. In both numerical examples, the run time varied within a single digit percentage of the mean value and the above drawn conclusions are also valid for the run that performed worst. However, diminishing this random aspect by introducing a semideterministic way of choosing samples for the subset is part of future work. Analyzing the distribution of the samples within the parameter domain and limiting the choice to certain parts of the parameter domain might be a good starting point. Employing a multigrid scheme, that is, starting the algorithm on a coarse discretization of the parameter domain and introducing subsequent refining steps is also a possibility.⁴³ Furthermore, incorporating the greedy reduced basis scheme into a nongradient based optimization algorithm might be beneficial. These algorithms usually require repeated evaluations of a parameter dependent system. Although in this case, the parameter samples are not chosen based on the residual but an underlying cost function, it might be beneficial to combine the system responses in order to approximate the solution by linear combinations. Solving a linear least

squares problem and assessing the residual can be more efficient than explicitly solving the system at the parameter sample. Finally, a suitable a priori error estimator would accelerate the greedy algorithm and improve the choice of basis vectors

ACKNOWLEDGMENTS


The contributions of Christopher Jelich, Suhaib Koji Baydoun, Matthias Voigt, and Steffen Marburg to this work were supported by the German Research Foundation (DFG) in the context of the priority program 1897 “Calm, Smooth and Smart - Novel Approaches for Influencing Vibrations by Means of Deliberately Introduced Dissipation.” This research has been carried out while the third author was affiliated with Universität Hamburg and Technische Universität Berlin. Their support is gratefully acknowledged.

DATA AVAILABILITY STATEMENT

The data that support the findings of this study are available from the corresponding author upon reasonable request.

ORCID

Christopher Jelich  <https://orcid.org/0000-0002-2617-3116>

Suhaib Koji Baydoun  <https://orcid.org/0000-0002-1184-065X>

REFERENCES

- Koopmann GH, Fahnlone JB. *Designing Quiet Structures*. Elsevier; 1997.
- Zienkiewicz OC, Taylor RL, Fox D. *The Finite Element Method for Solid and Structural Mechanics*. Butterworth-Heinemann; 2014.
- von Estorff O, ed. *Boundary Elements in Acoustics: Advances and Applications*. WIT Press; 2000.
- Marburg S. Boundary element method for time-harmonic acoustic problems. In: Kaltenbacher M, ed. *Computational*. Springer; 2018.
- Marburg S. Developments in structural-acoustic optimization for passive noise control. *Arch Comput Methods Eng*. 2002;9(4):291-370.
- Sepahvand K, Scheffler M, Marburg S. Uncertainty quantification in natural frequencies and radiated acoustic power of composite plates: analytical and experimental investigation. *Appl Acoust*. 2015;87:23-29.
- Peters H, Kessissoglou N, Marburg S. Modal decomposition of exterior acoustic-structure interaction. *J Acoust Soc Am*. 2013;133(5):2668-2677.
- Petyt M, Lea J, Koopmann G. A finite element method for determining the acoustic modes of irregular shaped cavities. *J Sound Vib*. 1976;45(4):495-502.
- Nefske D, Wolf JA, Howell L. Structural-acoustic finite element analysis of the automobile passenger compartment: a review of current practice. *J Sound Vib*. 1982;80(2):247-266.
- Marburg S. Normal modes in external acoustics. Part III: sound power evaluation based on superposition of frequency-independent modes. *Acta Acust United Acust*. 2006;92:296-311.
- Moheit L, Marburg S. Normal modes and modal reduction in exterior acoustics. *J Theor Comput Acoust*. 2018;26(3):1850029.
- El-Guide M, Międlar A, Saad Y. A rational approximation method for solving acoustic nonlinear eigenvalue problems. *Eng Anal Bound Elem*. 2020;111:44-54. <https://doi.org/10.1016/j.enganabound.2019.10.006>
- Baydoun SK, Marburg S. Investigation of radiation damping in sandwich structures using finite and boundary element methods and a nonlinear eigensolver. *J Acoust Soc Am*. 2020;147(3):2020-2034. <https://doi.org/10.1121/10.0000947>
- Kirkup SM, Amini S. Solution of the Helmholtz eigenvalue problem via the boundary element method. *Int J Numer Methods Eng*. 1993;36(2):321-330.
- Kimeswenger A, Steinbach O, Unger G. Coupled finite and boundary element methods for fluid-solid interaction eigenvalue problems. *SIAM J Numer Anal*. 2014;52(5):2400-2414.
- Zheng CJ, Bi CX, Zhang C, Gao HF, Chen HB. Free vibration analysis of elastic structures submerged in an infinite or semi-infinite fluid domain by means of a coupled FE-BE solver. *J Comput Phys*. 2018;359:183-198.
- Baydoun SK, Voigt M, Goderbauer B, Jelich C, Marburg S. A subspace iteration eigensolver based on Cauchy integrals for vibroacoustic problems in unbounded domains. *Int J Numer Methods Eng*. 2021. <https://doi.org/10.1002/nme.6701>
- Weile DS, Michielssen E, Grimme E, Gallivan K. A method for generating rational interpolant reduced order models of two-parameter linear systems. *Appl Math Lett*. 1999;12(5):93-102. [https://doi.org/10.1016/s0893-9659\(99\)00063-4](https://doi.org/10.1016/s0893-9659(99)00063-4)
- Li YT, Bai Z, Su Y, Zeng X. Model order reduction of parameterized interconnect networks via a two-directional Arnoldi process. *IEEE Trans Comput-Aided Des Integr Circuits Syst*. 2008;27(9):1571-1582. <https://doi.org/10.1109/tcad.2008.927768>
- Benner P, Gugercin S, Willcox K. A survey of projection-based model reduction methods for parametric dynamical systems. *SIAM Rev*. 2015;57(4):483-531. <https://doi.org/10.1137/130932715>
- Yue Y, Meerbergen K. Parametric model order reduction of damped mechanical systems via the block Arnoldi process. *Appl Math Lett*. 2013;26(6):643-648. <https://doi.org/10.1016/j.aml.2013.01.006>

22. van Ophem S, Deckers E, Desmet W. Parametric model order reduction without a priori sampling for low rank changes in vibro-acoustic systems. *Mech Syst Signal Process*. 2019;130:597-609. <https://doi.org/10.1016/j.ymssp.2019.05.035>
23. Chaturantabut S, Sorensen DC. Nonlinear model reduction via discrete empirical interpolation. *SIAM J Sci Comput*. 2010;32(5):2737-2764. <https://doi.org/10.1137/090766498>
24. Negri F, Manzoni A, Amsallem D. Efficient model reduction of parametrized systems by matrix discrete empirical interpolation. *J Comput Phys*. 2015;303:431-545.
25. Casenave F, Ern A, Lelièvre T. A nonintrusive reduced basis method applied to aeroacoustic simulations. *Adv Comput Math*. 2014;41(5):961-986. <https://doi.org/10.1007/s10444-014-9365-0>
26. Fares M, Hesthaven JS, Maday Y, Stamm B. The reduced basis method for the electric field integral equation. *J Comput Phys*. 2011;230(14):5532-5555. <https://doi.org/10.1016/j.jcp.2011.03.023>
27. Quarteroni A, Manzoni A, Negri F. *Reduced Basis Methods for Partial Differential Equations*. Springer International Publishing; 2016.
28. Liang YC, Lee HP, Lim SP, Lin WZ, Lee KH, Wu CG. Proper orthogonal decomposition and its applications—Part I: theory. *J Sound Vib*. 2002;252(3):527-544. <https://doi.org/10.1006/jsvi.2001.4041>
29. Binev P, Cohen A, Dahmen W, DeVore R, Petrova G, Wojtaszczyk P. Convergence rates for greedy algorithms in reduced basis methods. *SIAM J Math Anal*. 2011;43(3):1457-1472.
30. Buffa A, Maday Y, Patera AT, Prud'homme C, Turinici G. A priori convergence of the greedy algorithm for the parametrized reduced basis method. *ESAIM Math Model Numer Anal*. 2012;46:595-603.
31. Casenave F, Ern A, Lelièvre T. Accurate and online-efficient evaluation of the a posteriori error bound in the reduced basis method. *ESAIM Math Model Numer Anal*. 2014;48(1):207-229. <https://doi.org/10.1051/m2an/2013097>
32. Baydoun SK, Voigt M, Jelich C, Marburg S. A greedy reduced basis scheme for multifrequency solution of structural acoustic systems. *Int J Numer Methods Eng*. 2020;121(2):187-200. <https://doi.org/10.1002/nme.6205>
33. Hesthaven JS, Stamm B, Zhang S. Efficient greedy algorithms for high-dimensional parameter spaces with applications to empirical interpolation and reduced basis methods. *ESAIM Math Model Numer Anal*. 2014;48(1):259-283. <https://doi.org/10.1051/m2an/2013100>
34. Peters H, Marburg S, Kessissoglou N. Structural-acoustic coupling on non-conforming meshes with quadratic shape functions. *Int J Numer Methods Eng*. 2012;91(1):27-38.
35. Liang T, Wang J, Xiao J, Wen L. Coupled BE-FE based vibroacoustic modal analysis and frequency sweep using a generalized resolvent sampling method. *Comput Methods Appl Mech Eng*. 2019;345:518-538.
36. Fritze D, Marburg S, Hardtke HJ. FEM—BEM-coupling and structural—acoustic sensitivity analysis for shell geometries. *Comput Struct*. 2005;83(2-3):143-154. <https://doi.org/10.1016/j.compstruc.2004.05.019>
37. Kressner D, Tobler C. Low-rank tensor Krylov subspace methods for parametrized linear systems. *SIAM J Matrix Anal Appl*. 2011;32(4):1288-1316.
38. van Wout E, Gélat P, Betcke T, Arridge S. A fast boundary element method for the scattering analysis of high-intensity focused ultrasound. *J Acoust Soc Am*. 2015;138(5):2726-2737. <https://doi.org/10.1121/1.4932166>
39. Rafaely B. Spatial-temporal correlation of a diffuse sound field. *J Acoust Soc Am*. 2000;107(6):3254-3258. <https://doi.org/10.1121/1.429397>
40. Eckart C, Young G. The approximation of one matrix by another of lower rank. *Psychometrika*. 1936;1(3):211-218. <https://doi.org/10.1007/bf02288367>
41. Junger MC, Feit D. *Sound, Structures, and Their Interaction*. MIT Press; 1986.
42. Golub GH, Van Loan CF. *Matrix Computations*. 2nd ed. Johns Hopkins University Press; 1989.
43. Baur U, Benner P. Model reduction for parametric systems using balanced truncation and interpolation. *Automatisierungstechnik*. 2009;57(8):411-419. <https://doi.org/10.1524/auto.2009.0787>

How to cite this article: Jelich C, Koji Baydoun S, Voigt M, Marburg S. A greedy reduced basis algorithm for structural acoustic systems with parameter and implicit frequency dependence. *Int J Numer Methods Eng*. 2021;122(24):7409-7430. doi: 10.1002/nme.6835

A.3 Paper C

Efficient solution of block Toeplitz systems with multiple right-hand sides arising from a periodic boundary element formulation

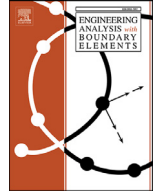
Christopher Jelich, Mahmoud Karimi, Nicole Kessissoglou and Steffen Marburg

Reprinted from C. Jelich, M. Karimi, N. Kessissoglou and S. Marburg. Efficient solution of block Toeplitz systems with multiple right-hand sides arising from a periodic boundary element formulation. *Engineering Analysis with Boundary Elements*, 130:135–144, 2021. Copyright © 2021 Elsevier. Reprinted with permission.



Contents lists available at ScienceDirect

Engineering Analysis with Boundary Elements

journal homepage: www.elsevier.com/locate/enganabound

Efficient solution of block Toeplitz systems with multiple right-hand sides arising from a periodic boundary element formulation

Christopher Jelich^{a,*}, Mahmoud Karimi^b, Nicole Kessissoglou^c, Steffen Marburg^a^a Chair of Vibroacoustics of Vehicles and Machines, Technical University of Munich, Boltzmannstrasse 15, Garching 85748, Germany^b Centre for Audio, Acoustics and Vibration, University of Technology Sydney, Sydney, New South Wales, Australia^c School of Mechanical and Manufacturing Engineering, The University of New South Wales, Sydney, New South Wales, Australia

ARTICLE INFO

Keywords:

Sequence of linear systems
Global Krylov solver
Block Krylov solver
Block Toeplitz matrix
Boundary element method

ABSTRACT

Block Toeplitz matrices are a special class of matrices that exhibit reduced memory requirements and a reduced complexity of matrix-vector multiplications. We herein present an efficient computational approach to solve a sequence of block Toeplitz systems arising from a block Toeplitz system with multiple right-hand sides. Two different numerical schemes are implemented for the solution of the sequence of block Toeplitz systems based on global and block variants of the generalized minimal residual (GMRES) method. The performance of the schemes is assessed in terms of the wall clock time of the iterative solution process, the number of multiplications with the block Toeplitz system matrix and the peak memory usage. To demonstrate the method, two numerical examples are presented. In the first case study, aeroacoustic prediction of an airfoil in turbulent flow is examined, which requires multiple solutions of the wall pressure field beneath the turbulent boundary layer. The fluctuating pressure on the surface of the airfoil is synthesized in terms of uncorrelated wall plane waves, whereby each realization of the wall pressure field is an input to the acoustic solver based on the boundary element method (BEM). The total acoustic response from the airfoil in turbulent flow is then obtained from an ensemble average for the number of realizations considered. The number of realizations to yield a converged solution for the wall pressure field leads to a sequence of block Toeplitz systems. The second case study examines the nonlinear eigenvalue analysis of a sonic crystal barrier composed of locally resonant C-shaped sound-hard scatterers. The periodicity of the sound barrier leads to a block Toeplitz system matrix whereas the nonlinear eigenvalue problem requires the solution of sequences of linear systems. The combined technique to solve the sequences of block Toeplitz systems using the proposed variants of the GMRES is shown to yield a computationally efficient approach for flow noise prediction and nonlinear eigenvalue analysis.

1. Introduction

A block Toeplitz matrix is a special block matrix which contains constant blocks along each diagonal, and is one of the most well-studied classes of structured matrices [1]. A system of linear equations in which the system matrix is a block Toeplitz matrix is called a block Toeplitz system [1,2]. Block Toeplitz systems arise in a diversity of disciplines including applied mathematics [3,4], physical sciences and engineering [5–10], and signal processing and control [11]. Karimi et al. [12] found that applying the BEM to periodic structures leads to the formation of a block Toeplitz matrix due to the translational invariance of the free-space Green's function. The method is termed the periodic boundary element method and has been applied to problems with multi-directional periodicity [13], problems involving rotational symmetry [14] and aeroacoustic predictions of airfoils [15,16]. In the latter

case, sequences of linear block Toeplitz systems are considered which are block Toeplitz systems with many right-hand sides. Sequences of linear block Toeplitz systems can also be found in Gaussian process modeling [17], electromagnetics [18,19] and data analysis [20].

Direct or iterative solvers are generally employed to solve a Toeplitz system. Direct solution schemes for Toeplitz systems as well as multilevel and block Toeplitz systems have been extensively studied, for example, see [21–26]. Direct solution schemes generally exhibit a complexity of $\mathcal{O}(N^2)$, with N denoting the number of degrees of freedom. Recently, stable direct solvers with complexities below $\mathcal{O}(N^2)$ have been proposed, for example, see [27–29] and references therein. However, the high memory requirements of direct solvers still prevent their application to large-scale problems. Iterative solvers generally require less memory than direct solvers and can be implemented without additional effort [30–32]. Employing an iterative solver for the solution of a sin-

* Corresponding author.

E-mail address: c.jelich@tum.de (C. Jelich).

gle linear block Toeplitz system was shown to exhibit a complexity of $\mathcal{O}(N \log^2(N))$. A prominent variant of an iterative solver is the conjugate gradient algorithm, which has been applied to symmetric positive definite Toeplitz systems employing circulant preconditioners [33,34]. Using this algorithm, several parallelization techniques were implemented to solve multilevel Toeplitz systems [35]. Further, the minimum residual method and the generalized minimal residual method (GMRES) were used to solve indefinite and non-symmetric Toeplitz systems [36,37]. Barrowes et al. [8] demonstrated efficient solution of an electromagnetic scattering problem involving multilevel block Toeplitz matrices using the biconjugate gradient stabilized method together with one-dimensional fast Fourier transforms.

The aforementioned iterative solution schemes belong to the class of Krylov subspace methods and can be grouped as seed/recycling, global or block Krylov subspace methods [38]. Using seed methods, a single system within the sequence of linear systems is selected and solved. Subsequently, the Krylov subspace of the seed system is reused in the solution process of the other linear systems. For m linear systems, the residuals of the remaining $m - 1$ linear systems are projected onto the Krylov subspace of the seed system. This often leads to a good approximation of the solution of the remaining non-seed systems [38,39]. Seed methods can be improved further by introducing augmentation and/or deflation, which are referred to as recycling methods [40,41]. Recycling methods have been applied to solve the Helmholtz equation discretized by the finite element method [42] as well as Maxwell’s equations discretized by the boundary element method [43,44]. In contrast, global and block methods efficiently solve all linear systems within the sequence simultaneously. As such, the solution and right-hand side vectors are concatenated into matrices. This allows matrix-matrix multiplications to be efficiently performed within the global and block iterative schemes. A further benefit of global and block methods is that they build a much larger Krylov subspace which usually yields a solution within less iterations [45,46]. Malhotra et al. [47] applied block methods to solve exterior acoustic problems using the finite element method (FEM). Block methods have also been employed using the FEM for applications in exterior acoustics to address waveform inversion [48] and for uncertainty analysis [42].

The current work extends the capability in exterior acoustics by employing global and block iterative solvers to accelerate the solution process of a block Toeplitz system with many right-hand sides. Both global and block variants of the GMRES are employed to solve a sequence of block Toeplitz systems arising from a BEM formulation. Two numerical examples are considered. In the first case study, the aeroacoustic prediction of flow-induced noise from an airfoil in low Mach number turbulent flow is considered. A small segment of the airfoil was selected as a unit cell. Using a periodic BEM formulation, the acoustic problem results in a block Toeplitz system. An uncorrelated wall plane wave technique is used to synthesize the fluctuating pressures on the surface of the structure. Each realization of the synthesized wall pressure field corresponds to an input to the acoustic problem, i.e., to a right-hand side of the periodic BEM model of the airfoil. Taking a number of realizations into account results in a sequence of block Toeplitz systems. The acoustic response of each realization is predicted by solving this sequence. The final acoustic response due to flow-induced noise from the flat plate is then obtained from an ensemble average of the individual acoustic response of the realizations. In the second case study, the eigenvalues and eigenvectors of a periodic sound barrier design are analyzed. Applying the periodic BEM formulation leads to a block Toeplitz system that is implicitly frequency dependent. This yields a nonlinear eigenvalue problem which can be solved efficiently by contour integral methods [49–51]. These methods allow extraction of the eigenvalues within a pre-defined contour but require the solution of sequences of linear systems at multiple frequency points along the contour. For both case studies, the performance of global and block variants of the GMRES to solve the sequence of block Toeplitz systems is evaluated in terms of computation time and memory requirements. Both the global and block GMRES

methods are shown to significantly reduce the overall computational effort of the solution process, yielding an efficient approach for exterior acoustic problems.

2. Sequence of block Toeplitz systems

A sequence of linear systems is given by

$$\mathbf{T}\mathbf{x}^{(i)} = \mathbf{b}^{(i)}, \quad i = 1, \dots, m, \tag{1}$$

where \mathbf{T} is a complex-valued system matrix and $\mathbf{b}^{(i)}$, $\mathbf{x}^{(i)}$ respectively denote the complex-valued right-hand side vector and solution vector of the i -th linear system within the sequence of m linear systems. When the system matrix \mathbf{T} is a block Toeplitz matrix, the linear systems within Eq. (1) are called block Toeplitz systems [1,2]. An $N \times N$ matrix \mathbf{T} is a block Toeplitz matrix if it has constant blocks along each diagonal. Hence, a block Toeplitz matrix has the form

$$\mathbf{T} = \begin{pmatrix} \mathbf{T}_0 & \mathbf{T}_{-1} & \dots & \dots & \mathbf{T}_{1-s} \\ \mathbf{T}_1 & \mathbf{T}_0 & \mathbf{T}_{-1} & \dots & \mathbf{T}_{2-s} \\ \vdots & \mathbf{T}_1 & \ddots & \ddots & \vdots \\ \vdots & \vdots & \ddots & \ddots & \mathbf{T}_{-1} \\ \mathbf{T}_{s-1} & \mathbf{T}_{s-2} & \dots & \mathbf{T}_1 & \mathbf{T}_0 \end{pmatrix}, \tag{2}$$

where each \mathbf{T}_j is an $n \times n$ matrix. In order to solve block Toeplitz systems by means of global and block Krylov solvers, the sequence of linear systems given by Eq. (1) is reformulated into

$$\mathbf{TX} = \mathbf{B}, \tag{3}$$

where the solution and right-hand side vectors are concatenated to form the solution matrix $\mathbf{X} = [\mathbf{x}^{(1)}, \dots, \mathbf{x}^{(m)}]$ and right-hand side matrix $\mathbf{B} = [\mathbf{b}^{(1)}, \dots, \mathbf{b}^{(m)}]$.

An efficient scheme to calculate block Toeplitz matrix products is implemented using the following procedure: (i) calculate the unique entries of the block Toeplitz matrix, (ii) construct the first block column of a block circulant matrix, (iii) calculate the discrete Fourier transform (DFT) of this first block column, and (iv) store the DFT of the first block column as a block diagonal matrix. The unique elements of the block Toeplitz matrix in Eq. (2) are the first block row and first block column. Concatenating the unique blocks column-wise yields the following $n \times (2s - 1)n$ matrix

$$\mathbf{Q} = (\mathbf{T}_0 \quad \mathbf{T}_{-1} \quad \dots \quad \mathbf{T}_{1-s} \quad \mathbf{T}_{s-1} \quad \dots \quad \mathbf{T}_2 \quad \mathbf{T}_1). \tag{4}$$

The \mathbf{Q} matrix defines the first block row of the block circulant matrix \mathbf{C} . A block circulant matrix is a special type of block Toeplitz matrix in which each block row is a rightward circular shift of the first block row [2,52]. Therefore, rightward circular shifts of \mathbf{Q} form the block circulant matrix \mathbf{C} , i.e.

$$\mathbf{C} = \begin{pmatrix} \mathbf{T}_0 & \mathbf{T}_{-1} & \dots & \mathbf{T}_2 & \mathbf{T}_1 \\ \mathbf{T}_1 & \mathbf{T}_0 & \mathbf{T}_{-1} & \dots & \mathbf{T}_2 \\ \vdots & \mathbf{T}_1 & \ddots & \ddots & \vdots \\ \mathbf{T}_{-2} & \vdots & \ddots & \ddots & \mathbf{T}_{-1} \\ \mathbf{T}_{-1} & \mathbf{T}_{-2} & \dots & \mathbf{T}_1 & \mathbf{T}_0 \end{pmatrix}. \tag{5}$$

By embedding the block Toeplitz matrix into a block circulant matrix, matrix products become circular convolutions that can be quickly computed using the discrete Fourier transform (DFT) or the fast Fourier transform (FFT). A matrix product can be obtained by multiplying the block Toeplitz matrix \mathbf{T} with an arbitrary matrix \mathbf{V} , which is equivalently expressed in terms of a block circulant matrix \mathbf{C} as follows [14]

$$\mathbf{TV} = \mathbf{Z} \quad \equiv \quad \mathbf{C}\tilde{\mathbf{V}} = \tilde{\mathbf{Z}}, \tag{6}$$

with $\tilde{\mathbf{V}}$ and $\tilde{\mathbf{Z}}$ being extended versions of \mathbf{V} and \mathbf{Z} , respectively. Introducing the block DFT operator \mathfrak{F} and its corresponding inverse operator \mathfrak{F}^{-1} , the block circulant matrix in Eq. (6) is given by

$$\mathbf{C} = \mathfrak{F}^{-1}\mathbf{A}\mathfrak{F}, \tag{7}$$

where Λ is a block diagonal matrix. This block diagonal matrix stores the block DFT of the first block column of the block circulant matrix, that is

$$\Lambda = \text{diag} \left(\hat{\mathbf{T}}_0, \hat{\mathbf{T}}_1, \dots, \hat{\mathbf{T}}_{-2}, \hat{\mathbf{T}}_{-1} \right), \quad (8)$$

where $[\hat{\mathbf{T}}_0 \hat{\mathbf{T}}_1 \dots \hat{\mathbf{T}}_{-2} \hat{\mathbf{T}}_{-1}] = \mathfrak{F} [\mathbf{T}_0 \mathbf{T}_1 \dots \mathbf{T}_{-2} \mathbf{T}_{-1}]$. The forward block DFT operator is given by the Kronecker product \otimes of the $(2s - 1) \times (2s - 1)$ Fourier matrix \mathbf{F}_{2s-1} and the $n \times n$ identity matrix \mathbf{I}_n , that is

$$\mathfrak{F} = \mathbf{F}_{2s-1} \otimes \mathbf{I}_n. \quad (9)$$

Analogously, the inverse of the forward block DFT operator is defined by

$$\mathfrak{F}^{-1} = \mathbf{F}_{2s-1}^{-1} \otimes \mathbf{I}_n. \quad (10)$$

The definition of the Fourier matrix and its inverse can be found in Golub and Van Loan [1].

The extended matrices $\tilde{\mathbf{V}}$ and $\tilde{\mathbf{Z}}$ in the matrix-vector product of Eq. (6) include additional unknowns. A further acceleration is achieved by only computing the necessary terms, i.e. by computing

$$\tilde{\mathbf{C}}\mathbf{V} = \mathbf{Z}. \quad (11)$$

The $sn \times sn$ matrix $\tilde{\mathbf{C}}$ is defined by

$$\tilde{\mathbf{C}} = \mathfrak{F}^{-1} \Lambda \mathfrak{F}, \quad (12)$$

with the incomplete block DFT operators

$$\tilde{\mathfrak{F}} = \tilde{\mathbf{F}}_{2s-1} \otimes \mathbf{I}_n \quad \text{and} \quad \tilde{\mathfrak{F}}^{-1} = \tilde{\mathbf{F}}_{2s-1}^{-1} \otimes \mathbf{I}_n. \quad (13)$$

The incomplete Fourier matrix $\tilde{\mathbf{F}}_{2s-1}$ contains the first s columns of \mathbf{F}_{2s-1} , whereas the incomplete inverse Fourier matrix $\tilde{\mathbf{F}}_{2s-1}^{-1}$ contains the first s rows of \mathbf{F}_{2s-1}^{-1} .

3. Krylov subspace solvers

3.1. Block Krylov subspace solver

Block Krylov subspace solvers can be derived from standard Krylov subspace solvers by modifying the way the Krylov subspace is built. Block Krylov methods generate an approximate solution $\mathbf{X}_k \in \mathbb{C}^{N \times m}$ in each iteration k such that the following relation holds

$$\mathbf{X}_k - \mathbf{X}_0 \in \mathcal{K}_k^{\square}(\mathbf{T}, \mathbf{R}_0). \quad (14)$$

Here, $\mathbf{X}_0 \in \mathbb{C}^{N \times m}$ is an arbitrary initial estimate of the solution matrix, $\mathbf{R}_0 = \mathbf{B} - \mathbf{T}\mathbf{X}_0$ is the initial residual and $\mathcal{K}_k^{\square}(\mathbf{T}, \mathbf{R}_0)$ is the block Krylov subspace of iteration k . The superscript (\square) denotes the block nature of the subspace and is given by Gutknecht [38]

$$\mathcal{K}_k^{\square}(\mathbf{T}, \mathbf{R}_0) = \left\{ \sum_{i=0}^{k-1} \mathbf{T}^i \mathbf{R}_0 \boldsymbol{\gamma}_i ; \boldsymbol{\gamma}_i \in \mathbb{C}^{m \times m} \right\}. \quad (15)$$

Eq. (15) shows that every column of the matrix $\mathbf{X}_k - \mathbf{X}_0$ is approximated by a linear combination of every column of the matrices spanning the block Krylov subspace $\mathcal{K}_k^{\square}(\mathbf{T}, \mathbf{R}_0)$. Compared to standard Krylov subspace solvers, the block Krylov subspace is of much larger size. Each iteration adds up to m additional Krylov vectors to the subspace instead of just a single vector in the case of standard Krylov solvers. As such, a greater number of Krylov vectors is available for the approximation of the solution in each iteration and convergence is generally reached in less iterations [38]. However, the computational efficiency comes at the cost of additional memory requirements. Further, linearly or nearly linearly dependent columns in the block Krylov subspace lead to a breakdown of the solver. Deflation techniques which detect and delete linearly dependent columns prevent this breakdown [38]. In addition, linearly dependent right-hand side vectors can be detected upfront. An elegant implementation was introduced by Langou [43], comprising the performance of a singular value decomposition (SVD) of the right-hand side matrix of Eq. (3) and truncating the SVD at a prescribed tolerance.

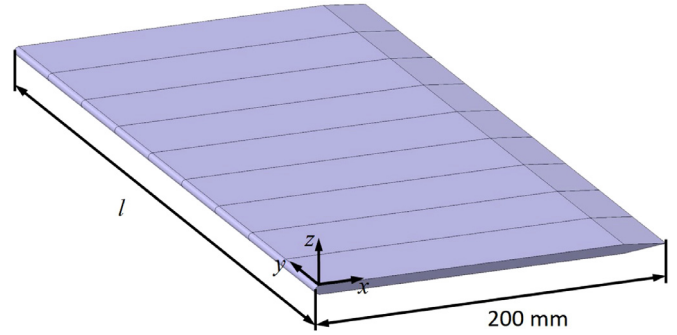


Fig. 1. Flat plate airfoil divided into small segments in the spanwise direction. The local coordinates in the streamwise and spanwise directions are denoted by x and y respectively.

This leads to a dimension reduction of the right-hand side matrix, thus reducing the computational effort.

The block variant of the GMRES introduced by Vital [53] is herein employed. The block GMRES uses a block Arnoldi process to build the block-orthogonal basis of $\mathcal{K}_k^{\square}(\mathbf{T}, \mathbf{R}_0)$. Similar to the standard GMRES, this orthogonal basis is stored and extended within every iteration. As such, the block GMRES requires a significant amount of memory which increases linearly with k . Remedies to the large memory requirements are restarting the algorithm [54] and applying preconditioning techniques [48,55].

3.2. Global Krylov subspace solver

Global Krylov subspace solvers generate an approximate solution \mathbf{X}_k in each iteration k such that the following relation holds

$$\mathbf{X}_k - \mathbf{X}_0 \in \mathcal{K}_k(\mathbf{T}, \mathbf{R}_0). \quad (16)$$

In contrast to block methods, global methods rely on a matrix Krylov subspace $\mathcal{K}_k(\mathbf{T}, \mathbf{R}_0)$ that is extended in each iteration k as follows

$$\mathcal{K}_k(\mathbf{T}, \mathbf{R}_0) = \left\{ \sum_{i=0}^{k-1} \mathbf{T}^i \mathbf{R}_0 \gamma_i ; \gamma_i \in \mathbb{C} \right\}. \quad (17)$$

Using the global Krylov subspace, the entire matrix $\mathbf{X}_k - \mathbf{X}_0$ is approximated by a linear combination of the matrices which span the matrix Krylov subspace. This clearly differs from block methods which rely on the block Krylov subspace in Eq. (15) and approximate each column of $\mathbf{X}_k - \mathbf{X}_0$ independently. Consequently, the search space of global methods is smaller than the search space of block methods, yielding slower convergence [38].

The global variant of the GMRES method introduced by Jbilou et al. [56] employs the global Arnoldi algorithm. This algorithm creates F -orthonormal matrices \mathbf{V}_i , i.e. $\text{tr}(\mathbf{V}_i^* \mathbf{V}_j) = 0$ for $i \neq j$ and $i, j = 0, \dots, k - 1$ in its k -th iteration. Here, $\text{tr}(\cdot)$ denotes the trace and $(\cdot)^*$ denotes the conjugate transpose. Linear dependence of the matrices spanning the Krylov subspace does not occur. However, linear dependent right-hand sides can be handled following the aforementioned approach of Vital [53].

4. Numerical examples

4.1. Aeroacoustic prediction of an airfoil in turbulent flow

In the first numerical example, aeroacoustic prediction of an airfoil in turbulent flow is examined. An incompressible flow passes a flat plate with a Reynolds number based on chord $Re_c = 4.9 \times 10^5$ and Mach number $M = 0.1$. At this Reynolds number, the flow is in a turbulent unsteady regime. The plate has a chord length of 200 mm, a variable span l and a thickness of 5 mm, as shown in Fig. 1. The leading edge is circular

with a diameter of 5 mm while the trailing edge is a symmetric wedge shape with an apex angle of 12°.

Assuming a time-harmonic dependence of the form $e^{-i\omega t}$, where $i = \sqrt{-1}$, $\omega = 2\pi f$ is the circular frequency, f is the frequency in Hz and t is time, the Helmholtz equation is given by

$$\Delta p(\mathbf{x}, \omega) + k_a^2 p(\mathbf{x}, \omega) = -q(\mathbf{x}, \omega). \quad (18)$$

$p(\mathbf{x}, \omega)$ is the acoustic pressure at point \mathbf{x} , Δ is the Laplacian operator, $k_a = \omega/c$ is the acoustic wave number, c is the speed of sound and q is the source term. The plate is divided into segments in the spanwise direction as shown in Fig. 1, where each segment corresponds to a unit cell. Applying the boundary element method to the flat plate, the following block Toeplitz system is obtained [12,13]

$$\mathbf{T}\mathbf{p} = \mathbf{p}_{\text{inc}}, \quad (19)$$

where \mathbf{T} is a complex-valued, non-symmetric block Toeplitz matrix in the form of Eq. (2). Each block within the block Toeplitz matrix is of dimension $n \times n$, with n denoting the number of degrees of freedom of the unit cell. Considering s plate segments, \mathbf{T} is of dimension $N \times N$ with $N = ns$ denoting the total number of degrees of freedom. In Eq. (19), \mathbf{p}_{inc} and \mathbf{p} represent the incident acoustic pressure and response acoustic pressure at discrete nodal points on the boundary of the flat plate. In contrast to the underlying geometry, the incident and response pressures do not need to fulfill periodicity.

The incident acoustic pressure originates from the pressure beneath a turbulent boundary layer arising from turbulent flow around the plate. This incident pressure is called the wall pressure field (WPF) and can be calculated using the uncorrelated wall plane wave (UWPW) technique [57,58]. Different realizations of the random WPF are generated, where each realization is an input to an acoustic solver based on the BEM. The WPF for the l -th realization can be represented by a set of UWPWs at a node of the boundary element mesh as follows [16,57]

$$p_{\text{inc}}^{(l)}(\mathbf{x}, \omega) = \sum_{i=1}^{N_x} \sum_{j=1}^{N_y} \sqrt{\frac{\phi_{pp}(k_x, k_y, \omega) \delta k_x \delta k_y}{4\pi^2}} e^{i(k_x x + k_y y + \varphi_{ij}^{(l)})}, \quad (20)$$

where δk_x and δk_y are the wavenumber resolutions in streamwise and spanwise directions of the wavenumber space, respectively, and N_x, N_y are the number of points considered along the k_x and k_y directions, respectively. The phase φ is sampled from a uniform random distribution within $[0, 2\pi]$. The cross spectral density of the WPF denoted by ϕ_{pp} can be expressed in terms of the auto spectral density Ψ_{pp} of the WPF and the normalized cross spectral density $\tilde{\phi}_{pp}$ of the WPF as follows [57,59]

$$\phi_{pp}(k_x, k_y, \omega) = \Psi_{pp}(\omega) \left(\frac{U_c}{\omega}\right)^2 \tilde{\phi}_{pp}(k_x, k_y, \omega), \quad (21)$$

where U_c denotes the convective velocity. Using Eqs. (20) and (21), a deterministic acoustic load is calculated for each realization.

Taking a total of m realizations into account, the block Toeplitz system of Eq. (19) is reformulated into a sequence of block Toeplitz systems as

$$\mathbf{TP} = \mathbf{P}_{\text{inc}}, \quad (22)$$

where the matrix $\mathbf{P} = [\mathbf{p}^{(1)}, \dots, \mathbf{p}^{(m)}]$ contains the acoustic pressure of each realization and the right-hand side matrix $\mathbf{P}_{\text{inc}} = [\mathbf{p}_{\text{inc}}^{(1)}, \dots, \mathbf{p}_{\text{inc}}^{(m)}]$ contains the incident pressure of each realization. Solving the sequence in Eq. (22) corresponds to calculating the acoustic pressure on the boundary of the flat plate for each realization. The far-field acoustic pressure $\mathbf{p}_f = [p_f^{(1)}, \dots, p_f^{(m)}]$ at a single field point \mathbf{x}_f for each realization is then computed by

$$\mathbf{p}_f = -\mathbf{h}_f \mathbf{P}, \quad (23)$$

where \mathbf{h}_f is the far-field boundary element matrix as defined in Marburg [60]. Finally, the scattered acoustic response at each frequency is obtained from an ensemble average of the far-field acoustic pressure of all realizations as follows

$$S_{pp}(\mathbf{x}, \omega) = \mathbf{E} \left[p_f^{(l)}(\mathbf{x}, \omega) \left(p_f^{(l)}(\mathbf{x}, \omega) \right)^* \right]_{l \in \{1, \dots, m\}}, \quad (24)$$

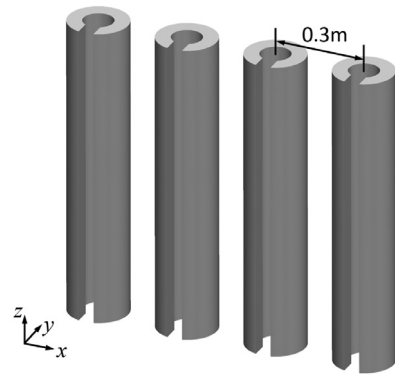


Fig. 2. Sonic crystal barrier design with four C-shaped cylinders.

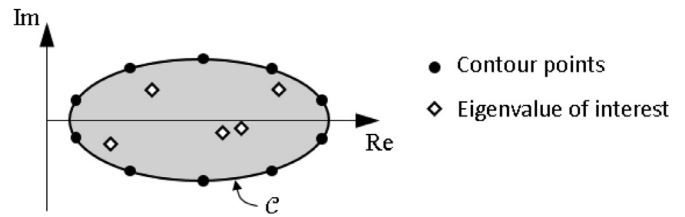


Fig. 3. Contour points z_j on the contour C that encloses all eigenvalues of interest.

where $\mathbf{E}[\]$ represents the ensemble average over the number of realizations.

4.2. Eigenvalue analysis of a locally resonant sonic crystal barrier

Sonic crystals are periodic arrangements of sound scatterers, and have been receiving growing interest in their potential for use as a noise barrier [61,62]. Significant sound attenuation in the shadow zone of a sonic crystal barrier is shown to occur in broad and narrow frequency bands respectively attributed to the periodicity and local resonance of the scatterers [63,64]. The second numerical example considers a finite sonic crystal composed of four C-shaped cylindrical shells as shown in Fig. 2. Each cylinder corresponds to a periodic segment and has a height of 1 m, an outer radius of 0.1 m, inner radius of 0.05 m and a slit width of 0.05 m. The ground is assumed to be sound-hard and the distance between the centers of neighboring C-shaped cylinders is 0.3 m.

Applying the periodic boundary element method yields a block Toeplitz system similar to Eq. (22) with an $N \times N$ block Toeplitz matrix \mathbf{T} that has constant $n \times n$ matrix blocks along its diagonal. Setting the right-hand side to zero yields the following nonlinear eigenvalue problem

$$\mathbf{T}(\tilde{\omega})\Phi = \mathbf{0}, \quad (25)$$

with the complex eigenvalue parameter $\tilde{\omega}$ and the nonzero eigenvector Φ . The real part of $\tilde{\omega}$ corresponds to the eigenfrequency whereas the imaginary part describes the damping of the corresponding mode. The eigenfrequencies and modal damping of the periodic structure are of interest since sound attenuation occurs around the eigenfrequencies and the mode shapes provide valuable insight on the effects leading to the attenuation. For infinite periodic arrangements, an eigenvalue analysis of a single unit cell is sufficient [65]. However, for small periodic arrangements, the entire geometry needs to be considered [66].

Contour integral methods are an efficient measure to solve the nonlinear eigenvalue problem in Eq. (25). All eigenvalues and corresponding eigenvectors are extracted within a predefined contour in the complex plane, as shown in Fig. 3. A specific contour integral method is the block Sakurai Sugiura (block-SS) method [49]. It involves transforming the nonlinear eigenvalue problem into the smaller generalized eigen-

value problem given by

$$(\mathbf{H}_2 - \hat{\omega}\mathbf{H}_1)\hat{\Phi} = \mathbf{0}, \quad (26)$$

with the $KL \times KL$ Hankel matrices \mathbf{H}_1 and \mathbf{H}_2 , where K and L denote parameters of the eigenvalue solver. The solution of Eq. (26) yields the complex eigenvalue parameters $\hat{\omega}$ which coincide with those eigenvalue parameters $\tilde{\omega}$ of the original nonlinear eigenvalue problem that lie inside the contour C . The Hankel matrices are formed by

$$\mathbf{H}_1 = [\mathbf{M}_{i+j-2}]_{i,j=1}^K \quad \text{and} \quad \mathbf{H}_2 = [\mathbf{M}_{i+j-1}]_{i,j=1}^K, \quad (27)$$

based on the positive integer K and the sequence of moments

$$\mathbf{M}_k = \frac{1}{2\pi i} \oint_C z^k \mathbf{V}^* \mathbf{T}(z)^{-1} \mathbf{V} dz, \quad k = 0, 1, \dots, 2K - 1, \quad (28)$$

of size $L \times L$. Calculating the moments involves an integration along the contour C with complex coordinate z and a random $n \times L$ matrix \mathbf{V} with its conjugate transpose denoted by \mathbf{V}^* . Integrating Eq. (28) with the trapezoidal rule along a circular contour yields

$$\mathbf{M}_k \approx \frac{1}{N_c} \sum_{j=0}^{N_c-1} \rho \left(\frac{z_j - \gamma}{\rho} \right)^{k+1} \mathbf{V}^* \mathbf{T}(z_j)^{-1} \mathbf{V}, \quad (29)$$

where $z_j = \gamma + \rho e^{i\theta_j}$ is one of the N_c contour points [49]. The complex value of z_j is given in polar coordinates in terms of angle θ_j , center γ and radius ρ of the circular contour. Once the small eigenvalue problem given by Eq. (26) is set up and solved, the eigenvalue parameters $\hat{\omega}$ and eigenvectors $\hat{\Phi}$ can be projected back to the original problem. The reader is referred to [49,67] for details on the solution techniques for Eq. (26) and the back transformation.

The accuracy of the eigenvalue solver is mainly determined by the number of contour points N_c and the value of L . A large value of N_c leads to a more accurate approximation of Eq. (28) whereas a large value of L results in a larger subspace, i.e. a larger generalized eigenvalue problem given by Eq. (26). The calculation of $\mathbf{T}(z_j)^{-1}\mathbf{V}$ in Eq. (29) is performed once for each of the N_c contour points and involves the $n \times L$ matrix \mathbf{V} as the right-hand side. Hence, highly accurate eigenvalue estimates require the solution of a large number of linear systems with many right-hand sides. A sophisticated choice of the iterative solver to calculate $\mathbf{T}(z_j)^{-1}\mathbf{V}$ has great potential to reduce the overall computational cost of the nonlinear eigenvalue solver. Note that the structure of Eq. (29) is not unique to the block-SS method but also occurs in other contour integral methods such as the block-SS with resolvent sampling [68] or nonlinear FEAST algorithms [51].

5. Numerical results

5.1. Aeroacoustic prediction of an airfoil in turbulent flow

Both block and global variants of the GMRES are applied to solve the sequence of block Toeplitz systems defined in Eq. (22), arising from the prediction of the aeroacoustic response of a flat plate excited by turbulent flow using the periodic boundary element formulation in conjunction with the UWPW technique. In this example, each periodic segment of the plate sketched in Fig. 1 is discretized using 376 linear discontinuous boundary elements. This yields a total of $n = 1504$ degrees of freedom per segment. Four different cases are studied in which the span length l of the flat plate is varied by varying the number of segments s . Here, 25, 50, 75 and 100 segments are considered, corresponding to numerical models with a total of 37,600, 75,200, 112,800 and 150,400 degrees of freedom, respectively. The analyses were performed at a frequency of $f = 2600$ Hz unless specified otherwise. The plate is in air with sound speed of $c = 340$ m/s.

A total of $m = 30$ realizations need to be taken into account to achieve an average error of the scattered acoustic pressure of less than 1 dB [16,57]. The solution of the acoustic system with 60 and 90

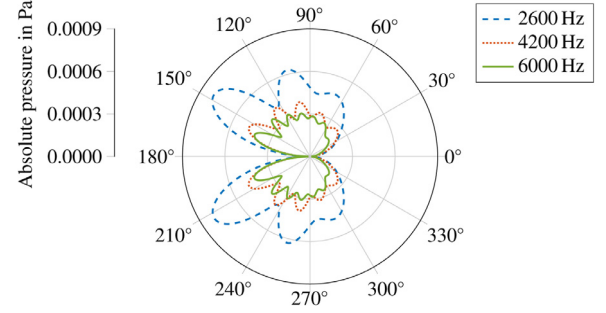


Fig. 4. Directivity of the scattered absolute acoustic pressure (in Pascal) on a circle with radius 585 mm located in the $x - z$ -plane with its center at $(x, y, z) = (100 \text{ mm}, 75 \text{ mm}, -2.5 \text{ mm})$, for a plate with span length $l = 150$ mm. The downstream and upstream directions of the flow correspond to 0° and 180° , respectively.

realizations has also been considered in order to investigate the complexity of the linear solvers with respect to different numbers of right-hand sides. The performances of both block GMRES and global GMRES are compared to the performance of the standard GMRES algorithm by examining the total time to solution, the number of equivalent matrix-vector products and the required memory. The global and block GMRES solve the full sequence of block Toeplitz systems of Eq. (22) whereas the standard GMRES solves each of the m block Toeplitz systems independently. The accuracy of the solution of each block Toeplitz system is tracked by computing the norm of the relative residual in each iteration. For the global GMRES, the Frobenius norm of the residual matrix \mathbf{R} is calculated, whereas for the GMRES and block GMRES, the l^2 -norm of the residual of each individual block Toeplitz system is calculated. Convergence is achieved whenever a relative tolerance of 10^{-8} is met for all systems. Preliminary studies showed that for the case study presented here, linear dependence of the basis vectors does not occur within the solution process. Therefore, deflation techniques are not included. Furthermore, no restarting and no preconditioning is applied. The calculations were performed using MATLAB R2018b on a desktop PC with 128 GB of RAM and 6 physical cores running at 3.5 GHz.

5.1.1. Acoustic response

The acoustic response of the flat plate airfoil subject to incompressible flow was calculated using Eq. (24) at 400 field points located on a circle circumscribing the flat plate. The circle has a radius of 585 mm, lies in the $x - z$ -plane and is centered at $(x, y, z) = (100 \text{ mm}, l/2, -2.5 \text{ mm})$. Fig. 4 shows the directivity of the scattered field at frequencies of 2600 Hz, 4200 Hz and 6000 Hz for a plate with span length $l = 150$ mm. Only a limited amount of noise is radiated in the downstream and upstream direction of the flow which corresponds to 0° and 180° , respectively. The absolute pressure is symmetric with respect to the $x - y$ -plane and the phase of the acoustic waves on the top side are shifted by half a wavelength with respect to the acoustic waves on the bottom side. The noise that propagates in the upstream direction is reduced due to destructive interference of the acoustic waves which are diffracted at the leading edge. Further, acoustic waves which are scattered by the trailing edge are backscattered by the leading edge and cause multiple lobes in the directivity plot. The complexity of the acoustic directivity increases with increasing frequency as indicated by the increasing number of lobes, with a corresponding decrease in amplitude.

5.1.2. Computational effort

The performances of all three Krylov solvers are initially investigated by comparing the time of the iterative solution processes. Fig. 5 presents the wall clock time as a function of the considered number of right-hand sides for a plate comprising 75 segments, corresponding to 112800 degrees of freedom. The solution times for all three variants of GMRES scale linearly with the number of right-hand sides. The block GMRES

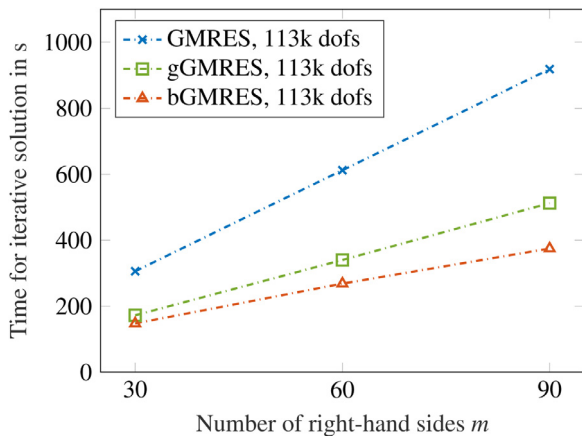


Fig. 5. Wall clock time (in seconds) for solving the sequence of block Toeplitz systems with 112800 degrees of freedom (dofs) using GMRES, global GMRES (gGMRES) and block GMRES (bGMRES) for 30, 60 and 90 right-hand sides.

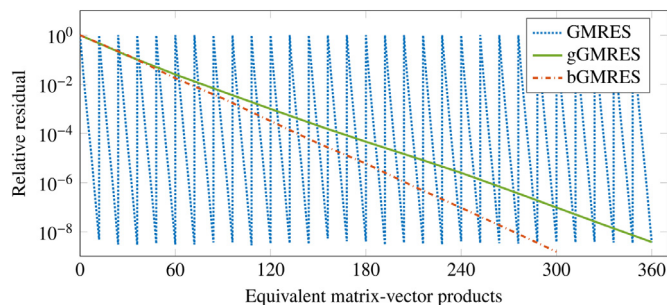


Fig. 6. Convergence of the relative residual of the solutions calculated using standard GMRES, global GMRES (gGMRES) and block GMRES (bGMRES) for a plate model with 112,800 degrees of freedom and 30 right-hand sides. Multiplications of the system matrix with another matrix are expressed in terms of equivalent matrix-vector products.

algorithm is the fastest in each case followed by the global GMRES algorithm, and both are significantly faster than standard GMRES. A beneficial deviation from linear scaling in time is observed for the block variant attributed to the varying number of iterations until convergence is reached. To solve the block Toeplitz systems with 30, 60 and 90 right-hand sides, the block GMRES performs 10, 9 and 8 iterations, respectively. The size of the block Krylov subspace increases with an increased number of right-hand sides and convergence is reached in less iterations compared to the other Krylov solvers. This capability is unique to block Krylov subspace methods. In contrast, the global GMRES performed 12 iterations to solve the full sequence of block Toeplitz systems, and the GMRES performed 360 iterations to solve the block Toeplitz systems, independent of the number of right-hand sides.

For all three solvers, the convergence behavior of the solution of the plate model with 112800 degrees of freedom and 30 right-hand sides is presented in Fig. 6. Multiplications of the system matrix are expressed in terms of equivalent matrix-vector products, i.e., multiplying the $N \times N$ system matrix with an $N \times m$ matrix corresponds to m equivalent matrix-vector products. The standard GMRES solves each of the 30 block Toeplitz systems consecutively, resulting in a total of 360 matrix-vector products. The convergence plot resembles a sawtooth profile, where each tooth represents the convergence of the solution of a single system. As such, using the standard GMRES, the solution of each block Toeplitz system is equally expensive in terms of matrix multiplications. The global and block GMRES solve all block Toeplitz systems simultaneously, yielding a single monotonically decreasing curve for both cases. A total of 12 iterations are required in the case of the global GMRES whereas only 10 iterations of the block GMRES are performed until

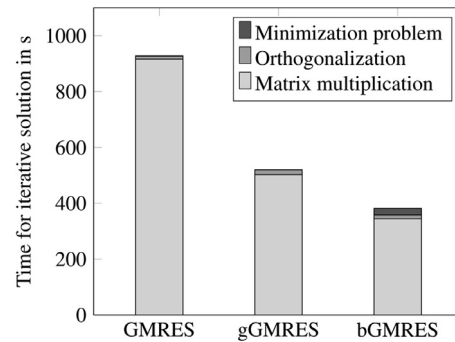


Fig. 7. Wall clock time (in seconds) for solving the sequence of block Toeplitz systems with 112,800 degrees of freedom and 90 right-hand sides using standard GMRES, global GMRES (gGMRES) and block GMRES (bGMRES). The total time is separated into time spent for system matrix multiplication, orthogonalizing the new basis and solving a minimization problem.

convergence is reached. This corresponds to 360 and 300 equivalent matrix-vector products, respectively.

Solving a linear system in less iterations usually comes at the cost of additional computational effort in other parts of the solution process. In the present case, the duration of each iteration can be separated into three parts: system matrix multiplication, orthogonalization of the new basis and solution of a minimization problem. Fig. 7 compares the time each solver spends on these operations while solving the block Toeplitz system of a plate model with 112800 degrees of freedom and 90 right-hand sides. The first step involving multiplication of the system matrix is the most costly operation, which respectively takes up to 98.7%, 96.6% and 90.3% of the total solution time for the GMRES, global GMRES and block GMRES. For the case of 90 right-hand sides, GMRES and global GMRES perform a total of 1080 equivalent matrix-vector products. Although both solvers require the same amount of equivalent matrix-vector products, the time both solvers spend performing these products differs by a factor of 1.81. This is mainly related to the benefit of performing matrix-matrix multiplications in the global GMRES instead of matrix-vector multiplications in GMRES. This benefit also occurs within the block GMRES, where 8 iterations are performed until convergence is reached which corresponds to 720 equivalent matrix-vector products. An additional reduction in computational time is achieved since the block GMRES requires less iterations in total, which accounts for the difference in the solution time of the global and block variants. The aforementioned additional computational effort arises in orthogonalizing the new basis and solving the minimization problem. The global GMRES requires slightly more time during the orthogonalization process. In the block GMRES, more time is spent solving the minimization problem. However, the additional effort is only minor since the matrix multiplications take up the largest fraction of the solution time.

Finally, the solution time for different widths of the plate is investigated. Different values of the span length l are obtained by modifying the number of segments s . The number of segments selected here are 25, 50, 75 and 100 corresponding to a total of 37,600, 75,200, 112,800 and 150,400 degrees of freedom. In Fig. 8, the solution time is compared for both block and global GMRES considering all four plate models. The solution time scales linear for both variants with the aforementioned deviations occurring for block GMRES. Applying global GMRES leads to a higher wall clock time in all four cases. The average speedup of the block variant compared to the global variant is about 1.31. Compared to the standard GMRES, the average speedup is 2.34. In Fig. 8, a tendency towards higher speedup rates for block Toeplitz systems with increasing number of right-hand sides is observed. This especially holds for the plate model with 150400 degrees of freedom where the maximum speedup rates of 1.42 with respect to global GMRES and 2.53 with respect to standard GMRES are observed.

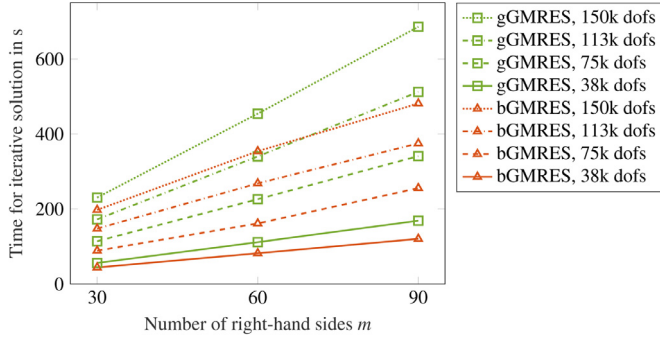


Fig. 8. Wall clock time (in seconds) for solving the sequence of block Toeplitz systems using global GMRES and block GMRES taking 30, 60 and 90 right-hand sides and plate models with 37,600, 75,200, 112,800 and 150,400 degrees of freedom (dofs).

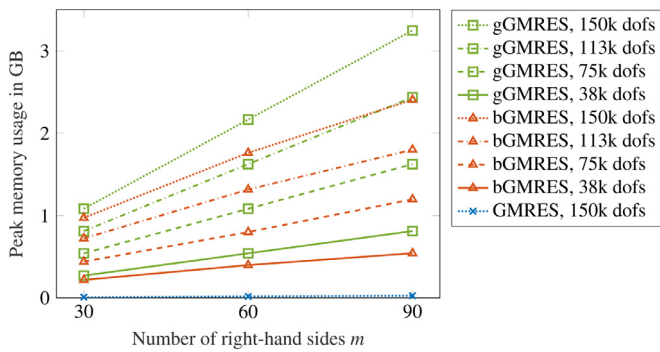


Fig. 9. Peak memory usage (in gigabyte) of GMRES, global GMRES and block GMRES for solving block Toeplitz systems with 30, 60 and 90 right-hand sides considering plate models with 37,600, 75,200, 112,800 and 150,400 degrees of freedom (dofs).

5.1.3. Memory requirements

The memory requirements of all three solvers is herein examined. The peak memory usage is shown in Fig. 9. Since standard GMRES solves each linear system within the sequence subsequently, the memory usage is independent of the number of right-hand sides, scaling $\mathcal{O}(N(k + 5))$ with the number of iterations k . In the case of 150400 degrees of freedom, the standard GMRES uses a total of 36 MB of memory. In contrast, the memory requirements of the global and block variants scale $\mathcal{O}(Nm(k + 5))$ and therefore exhibit linear scaling with both the number of degrees of freedom N and the number of right-hand sides m . The deviation from linear scaling in Fig. 9 is due to the varying number of iterations until convergence is reached using block GMRES. For the solution of the numerical case study considered in this work, a standard desktop computer is adequate for the memory requirement. For problems exhibiting slower convergence or higher numbers of degrees of freedom, the memory requirements may become impracticable. To address this issue, restarting the solver as well as preconditioning can be employed.

5.2. Eigenvalue analysis of a locally resonant sonic crystal barrier

The second case study is an eigenvalue analysis of a periodic sound barrier design. Applying the periodic boundary element method leads to a nonlinear eigenvalue problem which can be solved by contour integral methods. In this work, the nonlinear eigenvalue solver block-SS is employed [49]. The scheme requires the solution of N_c linear systems with L right-hand sides along a predefined contour C according to Eq. (29). Both block and global variants of GMRES are applied to these sequences of linear equations to accelerate the eigenvalue computations. The sonic crystal barrier design comprising four C-shaped cylin-

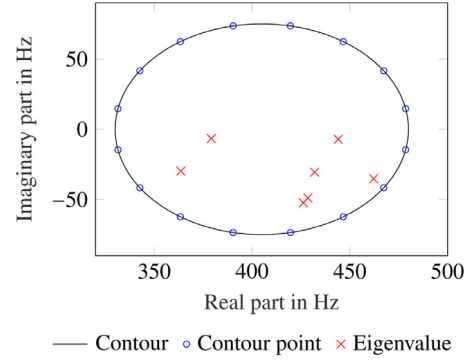


Fig. 10. Contour and contour points used in the block-SS method. The calculated eigenvalues lie inside the contour and are highlighted by red crosses.

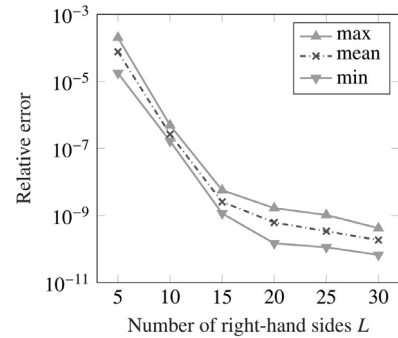


Fig. 11. Convergence of the eigenvalues $\tilde{\omega}$ and eigenvectors Φ with respect to the parameter L for $N_c = 16$ contour points. The relative error is given by $|\mathbf{T}(\tilde{\omega})\Phi|/|\Phi|$.

ders as shown in Fig. 2 is examined. Each cylinder is discretized with 2800 boundary elements featuring 11,200 pressure degrees of freedom. This leads to a total of 44,800 pressure degrees of freedom. The design of Fig. 2 features resonances at the Helmholtz frequency of the C-shaped cross section which is estimated at 382.0 Hz based on a two-dimensional finite element analysis of a single C-shaped cross section. The circular contour of the eigenvalue solver has a center point at 405 Hz and a radius of 75 Hz and as such, encloses the estimated Helmholtz frequency. The contour is discretized with $N_c = 16$ contour points shown in Fig. 10 and a value of $K = 4$ is chosen. Six different runs of the block-SS are compared where the value of L is varied between 5 and 30. This influences the accuracy of the solution and the computational effort. The accuracy of an eigenvalue $\tilde{\omega}$ and corresponding eigenvector Φ is quantified by the relative error $|\mathbf{T}(\tilde{\omega})\Phi|/|\Phi|$.

5.2.1. Eigenvalues and eigenvectors

Fig. 10 shows the eigenvalues of the C-shaped sonic crystal within the contour. All eigenvalues have a negative imaginary part and are calculated with a relative error of less than 10^{-8} using $L = 20$. The accuracy of the solution changes significantly with the parameter L as shown in Fig. 11. Each mode is numbered in ascending order according to the real part of its eigenvalue, i.e. its eigenfrequency. Fig. 12 visualizes the first, third and fifth eigenvector on the boundary of the sonic crystal, with corresponding eigenfrequencies of 363.6 Hz, 426.3 Hz and 432.0 Hz. Resonances within each C-shaped cylinder can be observed. In the case of the first eigenvector, the resonances of the first and fourth cylinder are in-phase and shifted by π with respect to the resonances in the second and third cylinder. This changes for the third eigenfrequency, where the resonance of the first two cylinders and the last two cylinders share the same phase. The resonances resemble the pressure distribution of a Helmholtz resonator in the cutting planes parallel to the xy -plane where the sound pressure is nearly constant. The sound pressure varies

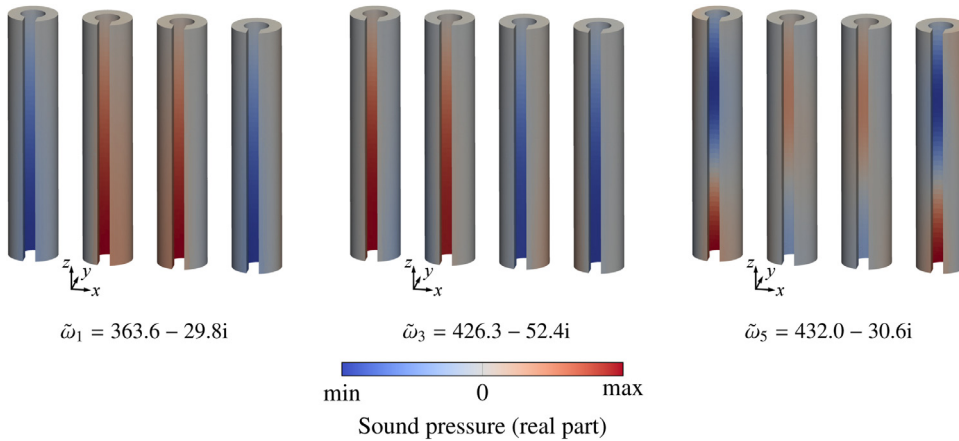


Fig. 12. Real part of the eigenvectors of the first, third and fifth eigenfrequency (from left to right).

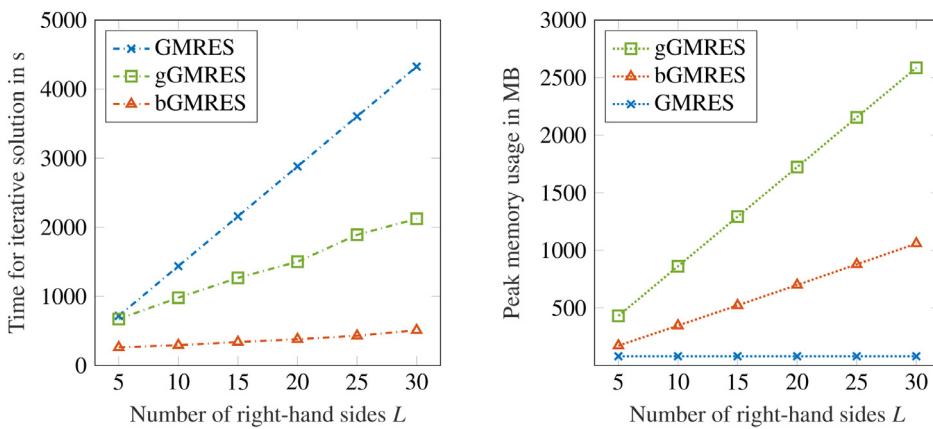


Fig. 13. Comparison of the performance of GMRES, global GMRES (gGMRES) and block GMRES (bGMRES) based on the solution of a single sequence of block Toeplitz systems in the block-SS method. Values of L between 5 and 30 are considered which leads to block Toeplitz systems with 5 to 30 right-hand sides.

(a) Wall clock time (in seconds) for the iterative solution

(b) Peak memory usage (in megabyte)

along the height of the C-shaped cylinders due to the opening at the top. Three quarters of a wave forms within the resonators in the case of the fifth eigenvector with less pronounced magnitudes in the second and third cylinders. The large imaginary parts of the calculated eigenvalues indicate high attenuation of the sound waves that excite the corresponding modes. This is in good agreement with the study of Karimi et al. [13], in which significant insertion loss between 350 Hz to 480 Hz was reported for a comparable C-shaped sound barrier design.

5.2.2. Computational effort and memory requirements

The performance of all three Krylov solvers is evaluated and compared in terms of their solution time and peak memory usage. Fig. 13(a) presents the time spent for the iterative solution of a single block Toeplitz system within the block-SS method, i.e. for computing the term $\mathbf{T}(z_j)^{-1}\mathbf{V}$ in Eq. (29). The results are based on the solution at $z_1 = 478.56 + 14.63i$ but also hold for every other contour point shown in Fig. 10. The value of L defines the accuracy of the eigenvalue solver and corresponds to the number of columns of \mathbf{V} , that is, the number of right-hand sides of the block Toeplitz system. The solution time of the GMRES method scales linear with L and takes 718 s for $L = 5$ and 4325 s for $L = 30$. An average of 106.2 iterations is performed per right-hand side. The global GMRES is up to two times faster and requires between 115 and 119 iterations in total. The number of iterations is slightly higher than in the GMRES method since the Frobenius norm of the residual matrix \mathbf{R} is used to calculate the relative error of the intermediate solutions. This norm slightly overestimates the actual relative error of each individual solution vector which is given by its l^2 -norm. The fastest solver is the block GMRES method which only requires 44 iterations in the case of $L = 5$ and generates a solution 2.74 times faster

than GMRES. The number of block GMRES iterations reduces with an increase in L . Only 28 iterations are performed in the case of $L = 30$ which takes 510 s and corresponds to a speedup of 8.48 compared to GMRES and 4.16 compared to global GMRES. As shown in the previous case study, this speedup comes at the cost of higher memory requirements. Fig. 13(b) compares the peak memory usage of all three solvers with respect to L . Since GMRES solves the block Toeplitz system for each right-hand side subsequently, the memory usage is constant in L with only 80.5 MB. For $L = 30$, the global and block GMRES require additional memory of up to 2584 MB and 1059 MB, respectively. However, the additional memory usage is well within the bounds of modern desktop computers. In the case of the block variant, the speedup is in good relation with the additional memory requirements. For $L = 20$, a speedup of 7.6 comes at an increase of the memory usage by 8.7.

The convergence of the relative error within the solution process is presented in Fig. 14 for all three solvers and $L = 20$ right-hand sides. The GMRES method solves each block Toeplitz system subsequently without taking information of previous solution processes into account. GMRES takes a total of 2123 matrix-vector products to solve the full sequence. In contrast, the global GMRES performs matrix-matrix products and solves the system for all right-hand sides simultaneously. The matrix-matrix products are expressed in terms of equivalent matrix-vector products in Fig. 14. Applying the global GMRES method does not yield faster convergence. In fact, a few additional equivalent matrix-vector products are computed. However, significant speedup is achieved due to performing matrix-matrix products which can be computed more efficiently than matrix-vector products. The fastest convergence is achieved using the block GMRES method. It solves the full sequence at once and builds a very large Krylov subspace. In the present case, con-

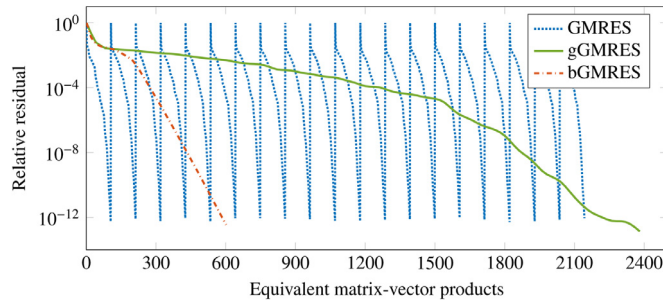


Fig. 14. Convergence of the relative residual of the solutions calculated using GMRES, global GMRES (gGMRES) and block GMRES (bGMRES) for the eigenvalue analysis with $L = 20$ right-hand sides. Multiplications of the system matrix with another matrix are expressed in terms of equivalent matrix-vector products.

vergence is achieved in 30 iterations computing 600 equivalent matrix-vector products.

6. Conclusions

In this work, global and block GMRES methods were employed to solve block Toeplitz systems with many right-hand sides. Such systems can be understood as sequences of block Toeplitz systems and arise in various fields. In the present study, boundary element discretized Helmholtz problems of periodic structures are considered. Employing global and block GMRES significantly reduces the time of the iterative solution, thus providing an efficient approach for exterior acoustic problems. To demonstrate the approach, two case studies were presented. In the first case study, the evaluation of aeroacoustic noise from turbulent flow around a flat plate airfoil was examined. The block Toeplitz matrix arises from a periodic boundary element formulation applied to the geometric model divided into unit cells. The acoustic excitation was assessed by synthesizing the wall pressure field underneath the turbulent boundary layer in terms of uncorrelated wall plane waves. A number of realizations of the wall pressure field to yield a converged solution was taken into account which leads to a sequence of block Toeplitz systems. In the second case study, an eigenvalue analysis of a sonic crystal barrier was performed. Applying the periodic boundary element method yields a block Toeplitz system which is solved at various frequencies within a nonlinear eigenvalue solver in order to extract the eigenvalues and eigenvectors within a predefined contour. The block Toeplitz system features many right-hand sides and its solution accounts for the major part of the computational time spent by the nonlinear eigenvalue solver. Both numerical examples presented here show that employing global and block GMRES significantly reduces the time of the iterative solution of the sequences of block Toeplitz systems. The solution times of both methods exhibit more favorable scaling with respect to the number of right-hand sides, leading to higher speedup rates for problems with an increasing number of right-hand sides. The speedup rates arise from performing matrix-matrix products within global and block GMRES instead of matrix-vector products with standard GMRES. A further speedup is achieved using block GMRES since the method requires less iterations. The significant reduction in solution time comes at the cost of increased memory requirements. Further acceleration of the solution process can be achieved by reducing the complexity of the matrix multiplications. In the case of aeroacoustic noise prediction, this may be done by incorporating the fast multipole BEM into the periodic boundary element formulation. For problems which feature poor convergence behavior, different preconditioning techniques based on the block Toeplitz structure of the system matrix could be applied. In addition, the block GMRES solver can be applied to other acoustic BEM problems in which many right-hand sides arise. This might include problems which do not feature block Toeplitz matrices such as the optimization of high-intensity focused ultrasonic transducer arrays [69,70].

Declaration of Competing Interest

The authors declare that they have no known competing financial interest or personal relationship that could have appeared to influence the work reported in this paper.

Acknowledgments

The second author gratefully acknowledges the financial support by the Australian Government through the Australian Research Council's Discovery Early Career Project funding scheme (project DE190101412).

References

- [1] Golub GH, Van Loan CF. *Matrix computations*. 2nd ed. Johns Hopkins University Press; 1989.
- [2] Gray RM. Toeplitz and circulant matrices: a review. *Found Trends Commun Inf Theory* 2005;2(3):155–239. doi:10.1561/0100000006.
- [3] Strang G. The discrete cosine transform. *SIAM Rev* 1999;41(1):135–47. doi:10.1137/s0036144598336745.
- [4] Haupt J, Bajwa WU, Raz G, Nowak R. Toeplitz compressed sensing matrices with applications to sparse channel estimation. *IEEE Trans Inf Theory* 2010;56(11):5862–75. doi:10.1109/tit.2010.2070191.
- [5] Antoine X, Chniti C, Ramdani K. On the numerical approximation of high-frequency acoustic multiple scattering problems by circular cylinders. *J Comput Phys* 2008;227(3):1754–71. doi:10.1016/j.jcp.2007.09.030.
- [6] Amirkulova FA, Norris AN. Negative refraction of acoustic waves in phononic crystals using recursive algorithms for block Toeplitz matrices. *J Acoust Soc Am* 2015;138(3):1751. doi:10.1121/1.4933533.
- [7] Czuprynski KD, Fahnline JB, Shontz SM. *Parallel boundary element solutions of block circulant linear systems for acoustic radiation problems with rotationally symmetric boundary surfaces*. In: *Proceedings of inter-noise 2012*; 2012.
- [8] Barrowes BE, Teixeira FL, Kong JA. Fast algorithm for matrix-vector multiply of asymmetric multilevel block-Toeplitz matrices in 3-D scattering. *Microwave Opt Technol Lett* 2001;31(1):28–32. doi:10.1002/mop.1348.
- [9] Zeng W-J, Xu W. Fast estimation of sparse doubly spread acoustic channels. *J Acoust Soc Am* 2012;131(1):303–17. doi:10.1121/1.3665992.
- [10] Zhang Q, Abeida H, Xue M, Rowe W, Li J. Fast implementation of sparse iterative covariance-based estimation for array processing. In: *Conference record of the forty fifth asilomar conference on signals, systems and computers (ASILOMAR)*. IEEE; 2011. p. 2031–5. doi:10.1109/acssc.2011.6190383.
- [11] Özbay H, Tannenbaum A. A skew Toeplitz approach to the H^∞ optimal control of multivariable distributed systems. *SIAM J Control Optim* 1990;28(3):653–70. doi:10.1137/0328038.
- [12] Karimi M, Croaker P, Kessissoglou N. Boundary element solution for periodic acoustic problems. *J Sound Vib* 2016;360:129–39. doi:10.1016/j.jsv.2015.09.022.
- [13] Karimi M, Croaker P, Kessissoglou N. Acoustic scattering for 3D multi-directional periodic structures using the boundary element method. *J Acoust Soc Am* 2017;141(1):313–23. doi:10.1121/1.4973908.
- [14] Karimi M, Croaker P, Peake N, Kessissoglou N. Acoustic scattering for rotational and translational symmetric structures in nonuniform potential flow. *AIAA J* 2017;55(10):3318–27. doi:10.2514/1.j055844.
- [15] Karimi M, Croaker P, Kinns R, Kessissoglou N. Effect of a serrated trailing edge on sound radiation from nearby quadrupoles. *J Acoust Soc Am* 2017;141(5):2997–3010. doi:10.1121/1.4982201.
- [16] Karimi M, Croaker P, Skvortsov A, Moreau D, Kessissoglou N. Numerical prediction of turbulent boundary layer noise from a sharp-edged flat plate. *Int J Numer Methods Fluids* 2019;90(10):522–43. doi:10.1002/flid.4733.
- [17] Chen J, Li TLH, Anitescu M. A parallel linear solver for multilevel Toeplitz systems with possibly several right-hand sides. *Parallel Comput* 2014;40(8):408–24. doi:10.1016/j.parco.2014.06.004.
- [18] Bleszynski E, Bleszynski M, Jaroszewicz T. AIM: Adaptive integral method for solving large-scale electromagnetic scattering and radiation problems. *Radio Sci* 1996;31(5):1225–51. doi:10.1029/96rs02504.
- [19] Cavillot J, Tihon D, Craeye C, de Lera Acedo E, Razavi-Ghods N. Fast simulation technique for antenna installed on a finite ground plane. In: *2019 International conference on electromagnetics in advanced applications (ICEAA)*. IEEE; 2019. p. 0742–5. doi:10.1109/iceaa.2019.8879358.
- [20] Kalantzi V, Malossi ACI, Bekas C, Curioni A, Gallopoulos E, Saad Y. A scalable iterative dense linear system solver for multiple right-hand sides in data analytics. *Parallel Comput* 2018;74:136–53. doi:10.1016/j.parco.2017.12.005.
- [21] Levinson N. The Wiener RMS error criterion in filter design and prediction. *J Math Phys* 1946;25(1-4):261–78. doi:10.1002/sapm1946251261.
- [22] Trench WF. Solution of systems with Toeplitz matrices generated by rational functions. *Linear Algebra Appl* 1986;74:191–211. doi:10.1016/0024-3795(86)90122-9.
- [23] Gohberg I, Kailath T, Koltracht I. Efficient solution of linear systems of equations with recursive structure. *Linear Algebra Appl* 1986;80:81–113. doi:10.1016/0024-3795(86)90279-x.
- [24] Kalouptsidis N, Carayannis G, Manolakis D. Fast algorithms for block Toeplitz matrices with Toeplitz entries. *Signal Process* 1984;6(1):77–81. doi:10.1016/0165-1684(84)90053-7.

- [25] Chandrasekaran S, Sayed AH. A fast stable solver for nonsymmetric Toeplitz and quasi-Toeplitz systems of linear equations. *SIAM J Matrix Anal Appl* 1998;19(1):107–39. doi:10.1137/s0895479895296458.
- [26] Brent RP, Gustavson FG, Yun DYY. Fast solution of Toeplitz systems of equations and computation of Padé approximants. *J Algorithms* 1980;1(3):259–95. doi:10.1016/0196-6774(80)90013-9.
- [27] Chandrasekaran S, Gu M, Sun X, Xia J, Zhu J. A superfast algorithm for Toeplitz systems of linear equations. *SIAM J Matrix Anal Appl* 2008;29(4):1247–66. doi:10.1137/040617200.
- [28] Martinsson PG, Rokhlin V, Tygert M. A fast algorithm for the inversion of general Toeplitz matrices. *Comput Math Appl* 2005;50(5-6):741–52. doi:10.1016/j.camwa.2005.03.011.
- [29] Stewart M. A superfast Toeplitz solver with improved numerical stability. *SIAM J Matrix Anal Appl* 2003;25(3):669–93. doi:10.1137/s089547980241791x.
- [30] Chan RH-F, Jin X-Q. An introduction to iterative Toeplitz solvers. Society for Industrial and Applied Mathematics; 2007. doi:10.1137/19780898718850.
- [31] Strang G. A proposal for Toeplitz matrix calculations. *Stud Appl Math* 1986;74(2):171–6. doi:10.1002/sapml1986742171.
- [32] Jin X-Q. *Developments and applications of block Toeplitz iterative solvers*. Springer Netherlands; 2003. ISBN 1402008309.
- [33] Chan RH, Tang PTP. Fast band-Toeplitz preconditioners for Hermitian Toeplitz systems. *SIAM J Sci Comput* 1994;15(1):164–71. doi:10.1137/0915011.
- [34] Bini D, Benedetto F. A new preconditioner for the parallel solution of positive definite Toeplitz systems. In: Proceedings of the second annual ACM symposium on Parallel algorithms and architectures - SPAA '90. ACM Press; 1990. p. 220–3. doi:10.1145/97444.97688.
- [35] Chen J, Li TLH. Parallelizing the conjugate gradient algorithm for multilevel Toeplitz systems. *Procedia Comput Sci* 2013;18:571–80. doi:10.1016/j.procs.2013.05.221.
- [36] Saad Y, Schultz MH. GMRES: a generalized minimal residual algorithm for solving nonsymmetric linear systems. *SIAM J Sci Stat Comput* 1986;7(3):856–69. doi:10.1137/0907058.
- [37] Saad Y. *Iterative Methods for Sparse Linear Systems*. Society for Industrial and Applied Mathematics; 2003. doi:10.1137/19780898718003.
- [38] Gutknecht MH. *Block Krylov space methods for linear systems with multiple right-hand sides: an introduction*. In: Siddiqi AH, Duff I, Christensen O, editors. *Modern mathematical models, methods and algorithms for real world systems*. Anamaya Publishers; 2007. p. 1–22.
- [39] Chan TF, Wan WL. Analysis of projection methods for solving linear systems with multiple right-hand sides. *SIAM J Sci Comput* 1997;18(6):1698–721. doi:10.1137/s1064827594273067.
- [40] Parks ML, de Sturler E, Mackey G, Johnson DD, Maiti S. Recycling Krylov subspaces for sequences of linear systems. *SIAM J Sci Comput* 2006;28(5):1651–74. doi:10.1137/040607277.
- [41] Gaul A. *Recycling Krylov Subspace Methods for Sequences of Linear Systems*. TU Berlin; 2014. Ph.D. thesis. doi:10.14279/depositonce-4147
- [42] Elman HC, Ernst OG, O’Leary DP, Stewart M. Efficient iterative algorithms for the stochastic finite element method with application to acoustic scattering. *Comput Methods Appl Mech Eng* 2005;194(9-11):1037–55. doi:10.1016/j.cma.2004.06.028.
- [43] Langou J. *Iterative Methods for Solving Linear Systems with Multiple Right-Hand Sides*. L’Institut National des Sciences Appliquées de Toulouse; 2003. Ph.D. thesis.
- [44] Giraud L, Gratton S, Martin E. Incremental spectral preconditioners for sequences of linear systems. *Appl Numer Math* 2007;57(11-12):1164–80. doi:10.1016/j.apnum.2007.01.005.
- [45] El Guennouni A, Jbilou K, Sadok H. A block version of BiCGSTAB for linear systems with multiple right-hand sides. *Electron Trans Numer Anal* 2003;16(129-142):2.
- [46] Puzryev V, Cela JM. A review of block Krylov subspace methods for multisource electromagnetic modelling. *Geophys J Int* 2015;202(2):1241–52. doi:10.1093/gji/ggv216.
- [47] Malhotra M, Freund RW, Pinsky PM. Iterative solution of multiple radiation and scattering problems in structural acoustics using a block quasi-minimal residual algorithm. *Comput Methods Appl Mech Eng* 1997;146(1-2):173–96. doi:10.1016/s0045-7825(96)01227-3.
- [48] Calandra H, Gratton S, Lago R, Vasseur X, Carvalho LM. A modified block flexible GMRES method with deflation at each iteration for the solution of non-Hermitian linear systems with multiple right-hand sides. *SIAM J Sci Comput* 2013;35(5):S345–67. doi:10.1137/120883037.
- [49] Asakura J, Sakurai T, Tadano H, Ikegami T, Kimura K. A numerical method for nonlinear eigenvalue problems using contour integrals. *JSIAM Lett* 2009;1(0):52–5. doi:10.14495/jsiaml.1.52.
- [50] Beyn W-J. An integral method for solving nonlinear eigenvalue problems. *Linear Algebra Appl* 2012;436(10):3839–63. doi:10.1016/j.laa.2011.03.030.
- [51] Gavin B, Międlar A, Polizzi E. FEAST eigensolver for nonlinear eigenvalue problems. *J Comput Sci* 2018;27:107–17. doi:10.1016/j.jocs.2018.05.006.
- [52] Davis PJ. *Circulant matrices*. Chelsea, New York: AMS Chelsea Publishing Series; 1994.
- [53] Vital B. *Etude de Quelques Méthodes de Résolution de Problèmes Linéaires de Grande Taille sur Multiprocesseur*. Université de Rennes; 1990. Ph.D. thesis.
- [54] Morgan RB. GMRES with deflated restarting. *SIAM J Sci Comput* 2002;24(1):20–37. doi:10.1137/s1064827599364659.
- [55] Baker AH, Dennis JM, Jessup ER. On improving linear solver performance: a block variant of GMRES. *SIAM J Sci Comput* 2006;27(5):1608–26. doi:10.1137/040608088.
- [56] Jbilou K, Messaoudi A, Sadok H. Global FOM and GMRES algorithms for matrix equations. *Appl Numer Math* 1999;31(1):49–63. doi:10.1016/s0168-9274(98)00094-4.
- [57] Maxit L. Simulation of the pressure field beneath a turbulent boundary layer using realizations of uncorrelated wall plane waves. *J Acoust Soc Am* 2016;140(2):1268–85. doi:10.1121/1.4960516.
- [58] Karimi M, Croaker P, Maxit L, Robin O, Skvortsov A, Marburg S, Kessissoglou N. A hybrid numerical approach to predict the vibrational responses of panels excited by a turbulent boundary layer. *J Fluids Struct* 2020;92:102814. doi:10.1016/j.jfluidstructs.2019.102814.
- [59] Graham WR. A comparison of models for the wavenumber-frequency spectrum of turbulent boundary layer pressures. *J Sound Vib* 1997;206(4):541–65. doi:10.1006/jsvi.1997.1114.
- [60] Marburg S. *Boundary element method for time-harmonic acoustic problems*. Computational acoustics. Kaltenbacher M, editor. Wien: Springer; 2018.
- [61] Martínez-Sala R, Sancho J, Sánchez JV, Gómez V, Llinares J, Meseguer F. Sound attenuation by sculpture. *Nature* 1995;378(6554):241. doi:10.1038/378241a0.
- [62] Fredianelli L, Pizzo AD, Licitra G. Recent developments in sonic crystals as barriers for road traffic noise mitigation. *Environments* 2019;6(2):14. doi:10.3390/environments6020014.
- [63] Montiel F, Chung H, Karimi M, Kessissoglou N. An analytical and numerical investigation of acoustic attenuation by a finite sonic crystal. *Wave Motion* 2017;70:135–51. doi:10.1016/j.wavemoti.2016.12.002.
- [64] Melnikov A, Maeder M, Friedrich N, Pozhanka Y, Wollmann A, Scheffler M, Oberst S, Powell D, Marburg S. Acoustic metamaterial capsule for reduction of stage machinery noise. *J Acoust Soc Am* 2020;147(3):1491–503. doi:10.1121/10.0000857.
- [65] Eilford DP, Chalmers L, Kusmartsev FV, Swallowe GM. Matryoshka locally resonant sonic crystal. *J Acoust Soc Am* 2011;130(5):2746–55. doi:10.1121/1.3643818.
- [66] Moheit L, Anthis S, Heinz J, Kronowetter F, Marburg S. Analysis of scattering by finite sonic crystals in free field with infinite elements and normal modes. *J Sound Vib* 2020;476:115291. doi:10.1016/j.jsv.2020.115291.
- [67] Zheng C-J, Gao H-F, Du L, Chen H-B, Zhang C. An accurate and efficient acoustic eigensolver based on a fast multipole BEM and a contour integral method. *J Comput Phys* 2016;305:677–99. doi:10.1016/j.jcp.2015.10.048.
- [68] Yokota S, Sakurai T. A projection method for nonlinear eigenvalue problems using contour integrals. *JSIAM Lett* 2013;5(0):41–4. doi:10.14495/jsiaml.5.41.
- [69] Gavrilov LR, Hand JW. A theoretical assessment of the relative performance of spherical phased arrays for ultrasound surgery. *IEEE Trans Ultrason Ferroelectr Freq Control* 2000;47(1):125–39. doi:10.1109/58.818755.
- [70] van Wout E, Gélât P, Betcke T, Arridge S. A fast boundary element method for the scattering analysis of high-intensity focused ultrasound. *J Acoust Soc Am* 2015;138(5):2726–37. doi:10.1121/1.4932166.